APPLICATION OF HYBRID METHODOLOGY TO ROTORS IN STEADY AND MANEUVERING FLIGHT

A Dissertation
Presented to
The Academic Faculty

by

Nischint Rajmohan

In Partial Fulfillment
of the Requirements for the Degree
Doctor of Philosophy in the
School of Aerospace Engineering

Georgia Institute of Technology
August 2010

APPLICATION OF HYBRID METHODOLOGY TO ROTORS IN STEADY AND MANEUVERING FLIGHT

Approved by:

Dr. Lakshmi N. Sankar, Advisor
School of Aerospace Engineering
Georgia Institute of Technology

Dr. Stephen M. Ruffin
School of Aerospace Engineering
Georgia Institute of Technology

Dr. Olivier Bauchau
School of Aerospace Engineering
Georgia Institute of Technology

Dr. Hormoz Tadghighi
Integrated Defense System - IDS
The Boeing Company

Dr. Mark Costello
School of Aerospace Engineering
Georgia Institute of Technology

Date Approved: [July 6, 2010]

Dedicated to my parents,

Rajmohan and Nitya

and my brother and sister-in-law

Nitin and Priti

for their selfless encouragement and support

ACKNOWLEDGEMENTS

First and foremost, I would like to thank my advisor, Dr.Sankar, for his support and guidance. His patience, support and kindness helped me throughout my years as a student and research assistant at Georgia Tech.

I would like to thank Dr.Stephen Ruffin, Dr.Olivier Bauchau and Dr. Mark Costello for agreeing to be on my thesis committee. Their valuable comments and suggestions helped me produce research material worthy of archival. I would like to specially thank Dr.Hormoz Tadghighi at Boeing Mesa for his valuable feedback on my work.

I am very grateful to Alan Egolf, who for all practical purposes was like my co-advisor on my research. His suggestions and comments have gone a long way in shaping my thesis and helped me develop a robust computational tool which has gained a lot of respect in the rotorcraft community. I would like to thank all our industry partners, Mark Wasikowski, Edward Reed and Ram Janakiram for their valuable comments on my research work.

My stint at Georgia Tech would have been extremely mundane if not for my colleagues Sujeet Phanse, Sarun Benjanirat, Mina Zaki, Nandita Yeshala, Susheel Sekhar and Kyle Collins. I would like to specially thank Byung-Young Min and Jeremy Bain for their valuable insights and suggestions.

I would like to thank the Airloads Workshop community for collaborating on all our research activities. I would like to express my gratitude to Mike Rutkowski and the Center for Rotorcraft Innovation (CRI) for their continued support and funding of my

research work. I am extremely grateful to Robert Kufeld and Hyeonsoo Yeo for making the UH-60A flight test airloads readily available for our perusal.

Last but not the least; I have to say, I am greatly indebted to my parents who have been the pillars of support throughout my life; and their selfless love and affection has been a great source of strength and confidence. I dedicate this thesis work to them and hopefully, I will get many more opportunities like this to express my love and gratitude.

TABLE OF CONTENTS

LIST OF TABLES

Page

LIST OF FIGURES

Page

NOMENCLATURE

a	Speed of sound
A, B, C	Flux Jacobian matrices
b	Wing semi-span
c	Chord
$C_n M^2$	Normal force coefficient ($N/\left(\frac{1}{2}\rho a^2 c_{ref}\right)$)
$C_m M^2$	Pitching Moment coefficient ($PM/\left(\frac{1}{2}\rho a^2 c_{ref}^2\right)$)
C_p	Specific heat at constant pressure, Pressure coefficient ($(p - p_\infty)/q_{ref}$)
C_T	Thrust coefficient ($T/\left(\rho_\infty A V_{tip}^2\right)$)
d	Distance from the wall
D	Drag force
D'	Sectional drag force
e	Flapping hinge offset.
EN	Energy per unit volume
E, F, G	Inviscid flux matrices
E_v, F_v, G_v	Viscous flux matrices
F/M	Force and moment
F_1	Aerodynamic force
F_c	Chord-wise force
F_z	Force along z-direction
g	Acceleration of gravity
h_0	Specific total enthalpy
I	Identity matrix

J	Jacobian of transformation
k	Thermal conductivity, Reduced frequency
k_β	Hinge spring constant
l	Length
L	Lift force, Reference length, Load, Rotational matrix
L'	Sectional lift force
L, D, U	Lower, diagonal and upper block triangular matrix
L, M N	Moments about helicopter center of mass
m	Mass
M	Million
M	Mach number
max	Maximum
M_z	Yaw moment
n	Number of harmonics
N	Normal force
N_b	Number of blade
n_t	Grid velocity in the surface normal direction
n_x, n_y, n_z	Surface normal vector
p	Pressure
P	Per-revolution
Pr	Prandtl number
Psi	Azimuth angle
q	Primitive variable
q_{ref}	Dynamic pressure ($\frac{1}{2}\rho_\infty V_{tip}^2$ for rotor analysis)

Q	State variable vector, Vorticity and strain rate balance, Torque
r	Radial location
Re	Reynolds number
RHS	Shorthand notation for the terms on the right hand side for any equation
s	Sectional span length
S	Vorticity
S_{ij}	Strain rate
t	Time, Thickness
T	Temperature, Thrust
u, v, w	Cartesian components of velocity
U, V, W	Contravariant velocity
V	Velocity
$\forbar{V}$	Volume
w	Weight function
x, y, z	Cartesian coordinates
y^+	Viscous sub-layer length scale ($y\sqrt{\rho\tau_w}/\mu$)

Greek Symbols

α	Angle of attack
α_s	Shaft tilt angle
β	Flapping angle
δ	Central difference operator
Δ	Difference, Grid spacing
ε	Turbulent dissipation
ϕ	Limiter function, Phase angle

$\Delta\phi, \Delta\theta, \Delta\psi$	Euler angles
γ	Specific heat ratio
Γ	Vortex strength
κ	Turbulent kinetic energy
λ	Eigen value
μ	Viscosity, Advance ratio
μ_l	Molecular viscosity
μ_t	Turbulent viscosity
θ	Pitch angle
ρ	Density
σ	Solidity
τ_{ij}	Shear stress tensor component
ω	Turbulent specific dissipation
ξ, η, ζ	Curvilinear coordinates
ψ, Ψ	Azimuth angle
Ω	Rotational speed
ψ_{MR}	rotational speed

Subscripts

0	Amplitude of zero-th harmonic
$1c, 1s$	Amplitude of first harmonic
i, j, k	Indices in three coordinate directions
LL	Lifting line
L, R	Left and right sides of the cell faces

max	Maximum
n	Normal direction
p	Pressure
t	Derivative with respect to time
$wall$	Variable on the wall surface
x, y, z	Derivatives with respect to Cartesian coordinates
ξ, η, ζ	Derivatives with respect to curvilinear coordinates
∞, inf, ref	Reference value

Superscripts

-1	Inverse matrix
l, r	Left and right sides of the cell faces
m, m+1	Sub-iteration level
n, n+1	Time level
sgs	Sub-grid scale
*	Non-dimensional variable
∧	Dimensional variable
–	Matrix in the computational domain
~	Roe-averaged quantity
+	Positive eigen value
-	Negative eigen value
'	Fluctuation quantity after average

Acronyms and Abbreviations

2-D	Two Dimensional
3-D	Three Dimensional
AFMC	Aeromechanics / Flight mechanics Coupling
BC	Boundary Condition
BVI	Blade Vortex Interaction
CFD	Computational Fluid Dynamics
CSD	Computational Structural Dynamics
DES	Detached Eddy Simulation
ENO	Essentially Non-Oscillatory
FDS	Flux Difference Splitting
FSI	Fluid Structure Interface
GCL	Geometric Conservation Law
HRKES	Hybrid RANS-KES
KES	Kinetic Eddy Simulation
LES	Large Eddy Simulation
LC	Loose Coupling
LU-SGS	Lower-Upper Symmetric Gauss Seidel
MUSCL	Monotone Upstream-centered Scheme for Conservation Laws
PDE	Partial Differential Equation
RANS	Reynolds Averaged Navier-Stokes
RHS	Right Hand Side
rpm	Rotation-per-minute
SA	Spalart-Allmaras
SST	Shear Stress Transform
T.E	Trailing Edge

TC	Tight Coupling
VLES	Very Large Eddy Simulation

SUMMARY

Helicopters are versatile flying machines that have capabilities that are unparalleled by fixed wing aircraft, such as operating in hover, performing vertical take-off and landing on unprepared sites. This makes their use especially desirable in military and search-and-rescue operations. However, modern helicopters still suffer from high levels of noise and vibration caused by the physical phenomena occurring in the vicinity of the rotor blades. Therefore, improvement in rotorcraft design to reduce the noise and vibration levels requires understanding of the underlying physical phenomena, and accurate prediction capabilities of the resulting rotorcraft aeromechanics. The goal of this research is to study the aeromechanics of rotors in steady and maneuvering flight using hybrid Computational Fluid Dynamics (CFD) methodology. The hybrid CFD methodology uses the Navier-Stokes equations to solve the flow near the blade surface but the effect of the far wake is computed through the wake model. The hybrid CFD methodology is computationally efficient and its wake modeling approach is non-dissipative making it an attractive tool to study rotorcraft aeromechanics.

Several enhancements were made to the CFD methodology and it was coupled to a Computational Structural Dynamics (CSD) methodology to perform a trimmed aeroelastic analysis of a rotor in forward flight. The coupling analyses, both loose and tight were used to identify the key physical phenomena that affect rotors in different steady flight regimes. The modeling enhancements improved the airloads predictions for a variety of flight conditions. It was found that the tightly coupled method did not impact

the loads significantly for steady flight conditions compared to the loosely coupled method.

The coupling methodology was extended to maneuvering flight analysis by enhancing the computational and structural models to handle non-periodic flight conditions and vehicle motions in time accurate mode. The flight test control angles were employed to enable the maneuvering flight analysis. The fully coupled model provided the presence of three dynamic stall cycles on the rotor in maneuver.

It is important to mention that analysis of maneuvering flight requires knowledge of the pilot input control pitch settings, and the vehicle states. As the result, these computational tools cannot be used for analysis of loads in a maneuver that has not been duplicated in a real flight. This is a significant limitation if these tools are to be selected during the design phase of a helicopter where its handling qualities are evaluated in different trajectories. Therefore, a methodology was developed to couple the CFD/CSD simulation with an inverse flight mechanics simulation to perform the maneuver analysis without using the flight test control input. The methodology showed reasonable convergence in steady flight regime and control angles predictions compared fairly well with test data. In the maneuvering flight regions, the convergence was slower due to relaxation techniques used for the numerical stability. The subsequent computed control angles for the maneuvering flight regions compared well with test data. Further, the enhancement of the rotor inflow computations in the inverse simulation through implementation of a Lagrangean wake model improved the convergence of the coupling methodology.

CHAPTER 1

INTRODUCTION

The most versatile flying machines in existence today are helicopters. They have capabilities that are unparalleled by fixed wing aircraft, such as operating in hover, performing vertical take-off and landing on unprepared sites. This makes their use especially desirable in military and search-and-rescue operations. However, modern helicopters still suffer from high levels of noise and vibration caused by the physical phenomena occurring in the vicinity of the rotor blades, and by their interaction with the blades themselves. Therefore, improvement in rotorcraft design to reduce the noise and vibration levels requires understanding of the underlying physical phenomena, and accurate prediction capabilities of the resulting rotor dynamics.

1.1 Rotorcraft Aeromechanics

Low fidelity computational tools have traditionally been used for design of helicopters. Although these tools are valuable, they are limited in their capabilities to predict complex physical phenomena. These limitations force the design process to be expensive and time consuming since full scale models need to be built and tested several times to determine the optimal configuration. Figure 1.1 shows the different physical phenomena occurring during a steady flight operation of a helicopter, all of which affect the handling qualities and structural integrity of the vehicle. The capabilities of the computational tools are evaluated based on how well they can accurately and efficiently model all these distinct physical phenomena. The prediction of physical phenomena affecting rotorcraft is highly complicated because the flow field is inherently unsteady

and three dimensional. On the advancing side, the combination of rotational speed and forward flight velocity may cause the flow in the tip region to be transonic with associated formation of supersonic pockets and shock waves. Thus, shock induced separation and shock motion along the chord of the blade may occur. Because the inboard section of the retreating blade operates in a reversed flow condition that grows in size with increasing forward flight velocity, the outboard stations are required to operate at increasingly high angles of attack to generate sufficient lift, which may cause dynamic stall. At low advance ratios, strong tip vortices in the rotor wake dominate the flow field and produce an unsteady and non-uniform induced velocity field at the rotor disk. The loads on a given blade are often impulsively modified by the passage of vortices shed by the other blades, a phenomenon known as blade-vortex interaction (BVI).

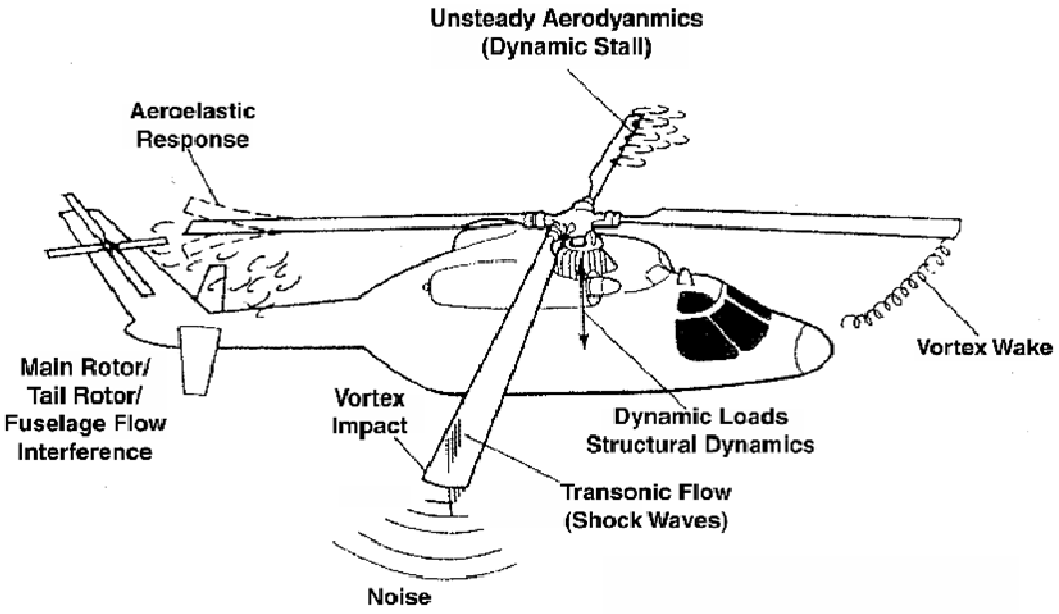

Figure 1.1 Physical phenomena experienced in forward flight by helicopters, Reference [2]

Flow dynamics around the rotor is not the only aspect under consideration in rotorcraft design. The rotor blades and hub form a dynamic system, which is harmonically excited by motion dependent forces and unsteady aerodynamic loads. The rotor blades are long, slender and flexible therefore, they respond to this periodic excitation by motions in axial, chordwise bending, flapwise bending and torsional directions. The torsional motions of the blade consist of a rigid motion caused by pilot input controls in addition to the elastic deformations caused by the unsteady aerodynamic forcing function. Finally, the influence of the fuselage, which is often neglected, can produce significant modifications in the flow field around the blades. Thus, the problem of modeling rotors in forward flight is multi-disciplinary. The rotor loads are due to the nonlinear interaction between the rotor aerodynamics, trim, aeroelasticity and blade dynamics. As stated by Landgrebe [1], the accurate prediction of airloads and the many aerodynamic interaction effects that may influence the performance and dynamic loading of the vehicle, has been the challenge in rotor aerodynamics.

Helicopters operate in different flight modes including hover, steady level flight and maneuvers. In hover, the blades experience steady flow-field characteristics at all azimuthal locations. The wake system from the blades is convected by local wake induced velocity components. The rotor aeromechanics in hover is relatively simpler due to symmetric flow-field and non-varying controls, although the effect of the wake is significant on rotor performance. In forward flight, the asymmetric velocity variation around the rotor disk together with cyclic pitch angles and complex inflow distribution generate higher harmonic air loads, 3/rev and higher. In order to highlight the complexity associated with advanced rotor design in forward flight, a typical scenario is given, for

example, a velocity variation of zero and 1/rev creates a zero, 1 and 2/rev variation in the square of velocity, which when multiplied with 1/rev cyclic angles generates zero, 1, 2 and 3/rev airloads. The steady components of the airloads are used to trim the vehicle, the 1/rev components are required for control, and the higher harmonics give rise to rotor vibration. At certain flight conditions, significant higher harmonic air loads are generated creating unacceptable rotor vibration - e.g., tip vortex induced airloads in transition flight, dynamic stall airloads in high thrust flight, unsteady transonic air loads in high speed flight. A combination of all of the above phenomena occurs in maneuvering flight making it the most difficult flight mode to study using computational tools. One of the most important and, at the same time, difficult challenges for rotorcraft design is the accurate prediction of limit loads and the design envelope for helicopters in severe maneuvers. Therefore, computational tools must be accurate and efficient to enable the designer to perform advanced rotorcraft design and analysis.

1.2 Previous Work

1.2.1 Rotorcraft Comprehensive Analysis Methods

Helicopter industries traditionally used comprehensive helicopter analyses that contain phenomenological models for the blade aerodynamics and the wake, coupled to linear structural dynamics models. The basis for the aerodynamic modeling in these analyses was blade element theory. This method can offer a good understanding of the rotor aerodynamic performance. In forward flight analyses, Theodorsen's unsteady two dimensional airfoil theory [2] is often applied in rotor analysis. Loewy [3] extended the classical Theodorsen technique to rotors via a lift deficiency function that accounts for the influence of the vortex sheets underneath the rotor disk. The disadvantage of simple

momentum theory based methods is that they cannot give details of the aerodynamic field. The complicated three dimensional, skewed wake geometry and periodically varying free stream velocity in forward flight make the analysis of rotors quite different from fixed wings. A semi-empirical unsteady aerodynamic model developed by Leishman and Beddoes [4] is usually included for modeling unsteady aerodynamics, separated flow and dynamic stall. In the 1970s, dissatisfaction with the first generation computer programs for predicting helicopter performance and dynamic behavior motivated the development of CAMRAD (Comprehensive Analytical Model of Rotorcraft Aerodynamics and Dynamics) [5,6], and later the development of 2GCHAS (Second Generation Comprehensive Helicopter Analysis System) [7]. The rotorcraft industries also developed their own comprehensive analyses codes (e.g. Sikorsky's Rotorcraft System Dynamic Analysis (RDYNE) [8]). The last two decades have seen the development of comprehensive analysis tools with sophisticated non-linear finite element methods that model geometrically exact configurations and multi-body dynamics techniques that allow the modeling of arbitrary topologies. CAMRAD II [9,10], developed by Johnson Aeronautics is a multi-body dynamics code that uses finite element analysis along the blades. It uses geometrically exact non-linear finite elements and assumes moderate deflections. It incorporates an internal free wake and dynamic inflow models, simplified aerodynamics, and a trim model. The current research effort utilizes DYMORE [11], a code developed at the Georgia Institute of Technology. This multi-body code uses geometrically exact finite elements, does not make assumptions about the size of the deflections, and uses an autopilot trimmer. UMARC [12], developed at the University of Maryland, uses finite element analysis to solve the equations of motion of

the rotor blades. The finite elements used assume moderate deflections. It also incorporates different aerodynamic and inflow models, as well as being capable of trim analysis. The trim model used solves six force balance equations for a target setting. The Rotorcraft Comprehensive Analysis System (RCAS) [13] is a comprehensive multi-disciplinary, computer software system for predicting rotorcraft aerodynamics, performance, stability and control, aeroelastic stability, loads, and vibration. RCAS was developed by the Aeroflightdynamics Directorate, US Army Aviation and Missile Research, Development, and Engineering Center (RDE-COM), to provide state-of-the-art rotorcraft modeling and analysis technology for government, industry, and academia. In Europe, HOST [14], developed through the combined effort of ONERA, Eurocopter, and DLR, incorporates the features of the S80 and R53 first-generation codes, and includes expanded features for trim, aerodynamic, and inflow analysis. The trim analysis is based on computations from a harmonic representation of movement and internal state. Although all these comprehensive analysis tools use sophisticated finite element methods for structural analysis, the aerodynamic models are not general enough to model the non-linear and unsteady effects in the flow.

1.2.2 Rotorcraft CFD Analysis Methods

With the advent of high speed computers, higher fidelity computational techniques like CFD gained a lot of traction. In the 1970s, several potential flow methodologies were developed for rotorcraft analysis. In potential flow methods, the effect of the wake is introduced as an inflow correction from an external wake methodology. Trim is also achieved externally by coupling the aerodynamic analysis with comprehensive analyses. Caradonna and Isom [15] developed the first transonic small disturbance solver for rotor flows. The

potential flow code called FDR by Chattot [16] was coupled to a comprehensive code. The effect of the wake and trim were input to the solver as a table of angle of attack corrections. Sankar and Prichard [17] developed unsteady full potential flow based rotor solvers, named RFS2. In these analyses, the flow results were coupled to CAMRAD in an open-loop fashion. RFS2, with the velocity transpiration approach of Sankar and Malone [18] was used by Hassan et al [19] and Tadghighi et al [20] to study self-generated blade-vortex interactions. The potential flow methods had limited ability in capturing the effects of compressibility or flow separation but were popular for their minimal computational requirements.

The 1980s saw the emergence of Euler and Navier-Stokes (NS) based methodologies. Sankar *et al.* [21,22] developed the first Euler analysis for rotors in hover and forward flight. Other Euler analyses for rotors were reported by Murman *et al* [23], Agarwal *et al.* [24] , and Chang [25]. Srinivasan *et al.* [26,27] developed a widely used NS solver for isolated rotors in hover called TURNS (Transonic Unsteady Rotor Navier-Stokes). The first NS solution of isolated rotor blades was reported by Wake and Sankar [28], and was followed by Srinivasan and McCroskey [29], and Agarwal and Deese [30]. Wake and Baeder [31] used a 3^{rd} order N-S approach to study the UH-60A rotor using a computational domain with a million grid points. Hariharan and Sankar [32] developed a 7^{th} order spatially accurate ENO (essentially non-oscillatory) methodology and assessed its advantages over a previous 5^{th} order spatial ENO scheme. Bangalore and Sankar [33] used a NS solver to study a UH-60A configuration and a leading edge slatted rotor in forward flight. Ahmad and Duque [34] also studied forward flight flow fields using a version of the NASA Ames code OVERFLOW with an embedded overset grid technique. Ekaterinaris *et al*. [35] used a Navier-Stokes flow solver with a variety of turbulence models for a 2-D dynamic stall problem, and emphasized the importance of turbulence

models. Narramore and Sankar [36] applied a three dimensional Navier-Stokes solver to study the retreating blade stall for a rotor configuration.

1.2.3 Rotorcraft Hybrid CFD Methodology

CFD solvers using wake capturing methods like OVERFLOW have been employed for loose coupling studies for the UH-60A rotor in forward flight. These class of solvers generally use fine meshes and try to capture the far wake computationally by solving Reynolds averaged Navier–Stokes equations. The wake capturing methods suffer from numerical dissipation in far wake and large computational times. Considerable expertise and time are needed for Chimera grid and embedded grid system manipulation to control the numerical diffusion of the vortical wake. It takes significantly longer times for studying rotors in maneuvering flight. A hybrid methodology based CFD solver uses near body meshes whereas the far wake is incorporated using a wake model. The hybrid methodology is shown to achieve comparable solution quality with faster turnaround times making it an efficient tool for studying helicopters in time varying maneuvering flight conditions. Hybrid methodologies employ the most appropriate numerical models in different flow regions to retain solution quality, with a large reduction in computer time.

Sankar *et al.* [37] developed a hybrid method that combines a Navier-Stokes solver (inner region) with a full potential solver (outer region) to reduce computational time. The hybrid solver was demonstrated for a fixed wing and hovering rotor, and showed the same level of accuracy as a full Navier-Stokes solver, while requiring almost half the computational time. Berezin and Sankar [38] developed a hybrid rotor solver using Navier-Stokes equations near the blades and a potential flow model elsewhere.

Only the near wake was captured. The viscous region near the blade is needed to capture flow separation, shock waves, and the tip vortex formation. This hybrid solver was coupled to a comprehensive code called RDYNE to properly account for the far wake and trim effects through angle of attack corrections. Berkman and Sankar [39] improved the hybrid technique by modeling the entire wake from first principles, and obtained good results for rotors in hover. Yang and Sankar [40,41] improved the efficiency of the hybrid technique by using phenomenological modeling for the far field wake and obtained results for the AH-1G and UH-60A rotors in forward flight. The hybrid CFD based methodology that was used in this study is an enhancement of the aforementioned hybrid CFD methodologies.

1.2.4 Aeroelastic Coupling Methods

Most of the rotorcraft comprehensive codes developed to predict aeroelastic response initially used phenomenological models for the wake structure and geometry, the induced velocity calculation and the blade aerodynamics. A quasi-steady strip theory approximation was commonly used. The dynamic inflow wake modeling [42] was usually employed for capturing low frequency, unsteady rotor wake effects. These approaches were inadequate for calculating higher harmonic airloads and aeroelastic stability near stall. It is important that the models used for the various parts of aeroelastic analysis have a consistent level of sophistication. Unfortunately, in rotor forward flight, many rotor aeroelastic analyses used a complex structural model but a simple quasi-steady, two dimensional aerodynamic theory. Unlike the fixed wing, the rotor blades encounter the oscillatory aerodynamic loads even in steady forward flight. An appropriate unsteady aerodynamic model capturing detailed flow physics was needed. This

requirement led to the coupling of rotor dynamics analyses with highly detailed CFD methods.

Historically, there have been two ways researchers have tried to couple CFD based aerodynamics into rotor structural analysis. The first method, often referred to as loose coupling (LC), involves transfer of information between the structural dynamic analysis and CFD analysis periodic intervals. The second method, which is the tight coupling (TC) approach, performs a simultaneous time integration of both structural dynamic and fluid dynamic equations. In essence, there is transfer of information between both analyses at every time step. The loose coupling method has the inherent advantage that a trim solution can also be achieved along with the convergence of structural dynamic response. But, because some of the frequencies of interest in the rotor system are much larger than the rotor rotational frequency (which is the same as the frequency of information exchange), often the credibility of the vibration predictions by this approach is suspect. The tight coupling is a more rigorous aeroelastic analysis from a fundamental point of view; however, the practicality of the approach is limited because of the inherent numerical challenges of ensuring both trim state and a periodic response solution.

One of the earliest successful efforts which used the loose coupling approach was by Tung, Caradonna and Johnson [43] who coupled the comprehensive rotor analysis code CAMRAD to FDR. Strawn and Tung [44,45] used the Full Potential Rotor (FPR) code, a successor to FDR and improved the coupling approach by extending the computational region to the full 360 degrees of azimuth rather than just at advancing blade azimuths. Yamauchi et al. [46] used a similar approach (i.e., FPR/CAMRAD) to predict structural bending and aerodynamic loads on an advanced geometry rotor blade of

a SA349/2 Gazelle helicopter and showed good correlation with flight test data. A study by Murthy et al [47] used the airloads obtained from a parallel adaptive finite element Euler solver, coupled with DYMORE. The computational structural dynamics (CSD) code determined the displacements along spanwise locations and provided new rotor blade geometry at each time step. A deforming mesh algorithm was used to account for the geometry changes and the resulting mesh was supplied to the CFD solver. The research efforts on developing a tightly coupled approach was initiated by Bauchau and Ahmad [48] who coupled the CFD code OVERFLOW with an overset grid to DYMORE for studying the aeroelastic effects on rotors in forward flight. Results were obtained for a four-bladed UH-60A rotor in forward flight and compared with flight test measurements. Other studies include research by Chopra [49,50]. In their work, the aerodynamic analysis was done by a potential flow code, and coupled to a structural dynamic analysis of the rotor blade.

The last decade has seen a lot of progress in application of CFD/CSD coupling to study rotorcraft aeromechanics. Sitaraman [51] used CFD (TURNS) computations with CSD (UMARC) in an open-loop coupled approach to investigate unsteady rotor airloads for the UH-60A in steady level flight and reported excellent agreement with test data. Datta *et al*. [52] used CFD (TURNS) computations with CSD (UMARC) in an open-loop coupled approach to gain a fundamental understanding of rotor vibratory loads in different steady flight conditions. Datta [53] also studied the dynamic stall loads in high altitude flight for the UH-60A rotor. Potsdam *et al.* [54] conducted a similar open-loop coupled CFD (OVERFLOW-D) - CSD (CAMRADII) study and obtained predictions for UH-60A airloads for a range of different flight conditions and found good agreement

with test data. Phanse [55,56] tested and validated tight coupling between hybrid methodology based GT-Hybrid and DYMORE and loose coupling between GT-Hybrid and CAMRADII. Makinen *et al.* [57,58] used the loose coupling methodology between DYMORE and GT-Hybrid to study thrust sweeps of UH-60A flight conditions. Duque *et al.* [59] demonstrated the application of aeroelastic coupling methodology for prediction of rotor noise.

1.2.5 Maneuvering Flight

Maneuvering flight introduces additional challenges that need to be addressed by the computational tools: aperiodic rotor airloads and structural response; and dependence of rotor response on vehicle dynamics. The rotor response in maneuvering flight conditions is aperiodic and often occurs over several rotor revolutions. Typically in maneuvers, rotor blade airfoils operate close to the stall region, large blade elastic deflections intensify aeroelastic phenomena and the operating environment is highly unsteady, and non-periodic. Computational analysis of maneuvering flight conditions has not been attempted until the last decade. This is because the traditional comprehensive rotorcraft analysis tools have been found to be inadequate in predicting the aerodynamic environment even in steady flight conditions. These approaches lacked the capability to predict the complex yet fundamental aerodynamic events occurring over the rotor disk. The last couple of years have seen attempts to extend the CFD/CSD coupling methodology to maneuvering flight. Bhagwat *et al.* [60] extended the coupling methodology to maneuvers by performing tightly coupled simulations with OVERFLOW-2 and RCAS for calculation of rotor airloads and structural loads in the Utility Tactical Transport Aerial System (UTTAS) pull-up maneuver for the UH-60A

rotor. Silbaugh [61] studied staggered and time accurate tight coupling between TURNS and UMARC for the 11029 maneuver. Abhishek *et. al.* [62] used UMARC to do a comprehensive analysis of UH-60A blade loads in maneuvering flight. The current state of the art in CFD/CSD coupling simulations for maneuvering flight use pilot controls from flight test database.

Apart from aeromechanics, rotorcraft maneuvering flight has been a significant area of research in the field of flight dynamics, inverse simulation and trajectory optimization. Researchers have tried to use high fidelity airloads or structural dynamics in vehicle dynamics simulations. Fusato and Celi [63] performed a design optimization study by accounting for both rotor dynamics and flight dynamics simultaneously. Bottasso and Bauchau [64-66] attempted to model helicopter maneuvering flight as an optimal control problem using DYMORE to simulate the maneuvering multi-body dynamics. Bridges *et al.* [67] studied the effect of ship wake captured by CFD code on the flight dynamics of the helicopter. Neill *et al.* [68] developed a 6 DOF rigid body dynamics solver for a non inertial finite-element inviscid CFD solver. The conventional approach adopted in flight simulation is to calculate the response of a modeled vehicle to prescribed control inputs. This is achieved by integrating the differential equations of motion, allowing the vehicle's trajectory to be computed in response to a defined pilot control sequence. Interest in an alternative approach, known as inverse simulation, is a growing area of research. This form of simulation involves calculating the pilot inputs required for a modeled vehicle to a prescribed trajectory or maneuver. Inverse simulation is particularly useful in studies of flight involving precision maneuvering. There are different numerical techniques used for inverse simulation. The vast majority of the

published literature focuses on a technique called “differentiation inverse” method. The “differentiation inverse” method begins by differentiating the algebraic equations that describe the flight path, so as to obtain the desired aircraft velocity components and accelerations. Then the equations of motion are “inverted” to obtain the controls that generate those velocity components and accelerations. The method was originally developed by Thomson and Bradley [69,70]. A similar technique was used by Whalley [71] in a study that included a validation through pilot-in-the-loop simulations. Earlier, a hybrid method in which the differentiated equations were used to reduce the number of equations to be integrated; had been proposed by Kato and Sugiura [72]. In an alternate method proposed by Hesset al. [73], called “integration inverse” technique, the trajectory is divided into small steps. For each step the initial controls are known, and the controls at the end of the step are computed using a Newton-Raphson technique to reduce to zero, the difference between actual and prescribed trajectories. The current state of the art in inverse simulation methods use simple linearized aerodynamic models to compute the rotor airloads.

1.3 Research Objectives and Scope

The goal of this research is to study the aeromechanics of rotors in steady and maneuvering flight using hybrid CFD methodology. The hybrid CFD methodology is computationally efficient and its wake modeling approach is non-dissipative making it an attractive tool to study rotorcraft aeromechanics. This work primarily focuses on the UH-60A rotor for all its computational studies primarily because of the NASA – Army UH-60A Airloads Program [74] which provides a highly repeatable and accurate set of flight test data that includes pilot input, vehicle attitudes, blade airloads and structural loads.

This test data enables a comprehensive validation of the CFD and CSD tools, helping in evaluating the capabilities of the tools and identifying the various aeroelastic mechanisms that determine observed physical phenomena.

The feasibility of using the hybrid CFD methodology for rotorcraft simulations is established through detailed validation studies. Validation studies include 2-D airfoil studies and 3-D rotor simulations using prescribed blade motions. Several enhancements are made to the hybrid CFD methodology that help in capturing key physical phenomena in an efficient way. These enhancements include parallelization of the solver, implementation of full span wake and shed wake models, implementation of geometric conservation law and higher order spatial and temporal schemes.

Loose coupling and tight coupling methodologies are implemented between hybrid CFD and CSD methodologies to study the airloads and structural loads of UH-60A rotor in several steady flight conditions chosen from the UH-60A Flight Test Database. These test cases include a high speed forward flight condition c8534 where vibratory loads (> 2 per rev) play a key role; moderate speed, high altitude flight conditions c9017 and c9020 which are characterized by deep dynamic stall cycles; low speed flight condition c8513 which is characterized by impulsive BVI loading. The vehicle experiences maximum vibration in c8534 and c8513 which directly affects the maintenance costs. The dynamic stall phenomena observed in c9017 and c9020 cases cause severe load cycles on the rotor structural components. These steady flight conditions have been carefully chosen to study a wide spectrum of physical phenomena that affect rotors in forward flight.

The unsteadiness encountered in maneuvering flight impose severe demands on the rotor structure and often dictates the overall sizing and structural properties of the helicopter rotor. Thus, the capability to accurately predict the airloads and structural loads encountered during maneuvers is critical from a rotorcraft designer's perspective. Therefore, the coupling methodologies used for steady flight analysis are now extended to maneuvering flight. Both loose coupling and tight coupling is used to study the distinct physical phenomena that affect the UH-60A rotor in UTTAS 11029 pull-up maneuver. The entire maneuver is over 40 rotor revolutions but the CFD/CSD coupling is used for first five revolutions which correspond to steady flight conditions and revs 15-17 where the vehicle experiences the maximum load factor.

The analysis of maneuvering flight requires knowledge of the instantaneous control pitch settings, the vehicle velocity components, attitudes, and the pitch, roll, and yaw rates and accelerations as a function of time. This data is readily available for the UH-60A rotor from the flight test database. The current state-of-the-art in maneuvering flight simulation require the pilot control inputs from the database. But this means that these computational tools cannot be used for analysis of loads in a maneuver that has not been flown. This is a significant limitation if these tools are to be used during the design phase of a helicopter where its handling qualities are evaluated in different trajectories. A new methodology developed in the final part of this study tries to address this limitation by integrating the flight mechanics of a helicopter in forward flight with the aeroelastic coupling framework, eliminating the need to know pilot control input a priori. This is performed by integrating an inverse flight dynamics simulation with the CFD/CSD coupling tools. The inverse simulation is a technique used to estimate the pilot input

based on vehicle states in a maneuver. The current inverse simulation tools use low fidelity aerodynamics to predict the pitch input. The use of CFD hub loads for the rotor in the inverse simulation is expected to improve the solution quality. Thus the coupling between flight dynamics and CFD/CSD tools is beneficial to both analyses.

1.4 Organization of Dissertation

This dissertation deals with study of rotorcraft aeromechanics using a hybrid CFD methodology. The background and the motivation of this dissertation are introduced in chapter 1. The main objectives of the present work are proposed after the brief introduction.

Chapter 2 contains the mathematical and numerical formulation of the hybrid methodology based CFD flow solver. The principle behind the Lagrangean wake model and the coupling between the wake model and Navier-Stokes methodology is explained. A brief description of the CSD methodology is also presented.

Chapter 3 details all the enhancements made to the GT-Hybrid CFD methodology to improve the aerodynamic modeling of rotors in forward flight. These enhancements include improvements to the wake model, implementation of higher order spatial and temporal schemes in the Navier-Stokes methodology and parallelization of the CFD methodology

Chapter 4 discusses the 2-D and 3-D validation studies of the hybrid CFD methodology and its enhancements. 2-D studies include a high speed and a dynamic stall case. Rotor simulations are performed using the CFD methodology with application of prescribed controls and elastic deformations obtained from an external CFD/CSD coupling framework.

Chapter 5 focuses on the study of aeroelastic phenomena that affect the UH-60A rotor in various steady flight conditions. The phenomena are studied through CFD/CSD coupling simulations. The CFD/CSD loose and tight coupling methodologies are explained and airloads and structural load predictions are compared with flight test data.

Chapter 6 focuses on the extension of the validated loose and tight CFD/CSD coupling methodologies to the analysis of maneuvering flight. The modifications made to the CFD and CSD methodology for maneuvering flight analysis are listed. Results obtained from coupling simulations for selected revolutions of UTTAS 11029 maneuver are discussed.

Chapter 7 introduces a new methodology that was developed to couple the CFD/CSD coupling framework with an inverse simulation so that the CFD airloads in the maneuver can be estimated without using the flight test data for pitch inputs. Results obtained using this coupling methodology for selected revolutions of a maneuver are discussed. The final chapter summarizes the main conclusions drawn from this work and provides some recommendations for future research.

CHAPTER 2

COMPUTATIONAL METHODOLOGY

In this chapter, the mathematical and numerical formulation of the hybrid methodology based CFD flow solver will be discussed. The principle behind the Lagrangean wake model and the coupling between the wake model and Navier-Stokes methodology is explained. A brief description of the CSD methodology is also presented.

2.1 Mathematical Formulation of CFD Methodology

GT-Hybrid is a finite volume based 3-D compressible Navier-Stokes (NS) solver. The following sections contain the mathematical formulation for the discretized 3-D Navier-Stokes equations.

2.1.1 Governing Equations in Cartesian Coordinates

The differential form of Navier Stokes equations in Cartesian coordinates without body forces or external heat addition can be written as

$$\frac{\partial Q}{\partial t}+\frac{\partial F}{\partial x}+\frac{\partial G}{\partial y}+\frac{\partial H}{\partial z}=\frac{\partial R}{\partial x}+\frac{\partial S}{\partial y}+\frac{\partial T}{\partial z} \tag{2.1}$$

Here Q is the flow vector given by:

$$Q=\begin{Bmatrix}\rho\\ \rho u\\ \rho v\\ \rho w\\ e\end{Bmatrix} \tag{2.2}$$

where ρ is fluid density, *u*,*v*,*w* are fluid velocity components in three Cartesian directions, and *e* is the total energy per unit volume (the sum of internal energy and kinetic energy per unit volume) defined by

$$e = \frac{p}{\gamma - 1} + \frac{1}{2}\rho(u^2 + v^2 + w^2) \tag{2.3}$$

where *p* is the static pressure and γ is the specific heat ratio of the fluid.

The inviscid flux terms shown in equation are given by

$$F = \begin{Bmatrix} \rho \\ \rho u^2 + p \\ \rho uv \\ \rho uw \\ u(e+p) \end{Bmatrix} \mathrm{G} = \begin{Bmatrix} \rho \\ \rho uv \\ \rho v^2 + p \\ \rho vw \\ v(e+p) \end{Bmatrix} \mathrm{H} = \begin{Bmatrix} \rho \\ \rho uw \\ \rho vw \\ \rho w^2 + p \\ w(e+p) \end{Bmatrix} \tag{2.4}$$

The viscous flux vectors in equation are defined as:

$$\mathrm{R} = \begin{Bmatrix} 0 \\ \tau_{xx} \\ \tau_{yx} \\ \tau_{zx} \\ EN_x \end{Bmatrix} \mathrm{S} = \begin{Bmatrix} 0 \\ \tau_{xy} \\ \tau_{yy} \\ \tau_{zy} \\ EN_y \end{Bmatrix} \mathrm{T} = \begin{Bmatrix} 0 \\ \tau_{xz} \\ \tau_{yz} \\ \tau_{zz} \\ EN_z \end{Bmatrix} \tag{2.5}$$

The stress terms are evaluated based on Stokes' hypothesis in which the bulk viscosity λ is set equal to $-\frac{2}{3}\mu$.

$$\tau_{xx} = \frac{2}{3}\mu\left(2\frac{\partial u}{\partial x} - \frac{\partial v}{\partial y} - \frac{\partial w}{\partial z}\right) \tag{2.6}$$

$$\tau_{xy} = \mu\left(\frac{\partial u}{\partial y} + \frac{\partial v}{\partial x}\right)$$

$$\tau_{xz} = \mu\left(\frac{\partial u}{\partial z} + \frac{\partial w}{\partial x}\right)$$

$$\tau_{yy} = \frac{2}{3}\mu\left(2\frac{\partial v}{\partial y} - \frac{\partial u}{\partial x} - \frac{\partial w}{\partial z}\right)$$

$$\tau_{yz} = \mu\left(\frac{\partial v}{\partial z} + \frac{\partial w}{\partial y}\right)$$

$$\tau_{zz} = \frac{2}{3}\mu\left(2\frac{\partial w}{\partial z} - \frac{\partial u}{\partial x} - \frac{\partial v}{\partial y}\right)$$

Based on Fourier's Law, the viscous terms in the energy equation can be written as:

$$\begin{aligned} EN_x &= u\tau_{xx} + v\tau_{xy} + w\tau_{xz} + k\frac{\partial T}{\partial x} \\ EN_y &= u\tau_{xy} + v\tau_{yy} + w\tau_{yz} + k\frac{\partial T}{\partial y} \\ EN_z &= u\tau_{xz} + v\tau_{yz} + w\tau_{zz} + k\frac{\partial T}{\partial z} \end{aligned} \tag{2.7}$$

where *k* is the thermal conductivity

$$k = \frac{\mu C_P}{Pr} = \frac{\mu\gamma R}{Pr(\gamma - 1)} \tag{2.8}$$

and Pr is the Prandtl number ($\approx$0.72 for air).

2.1.2 Non-dimensionalized Governing Equations

The governing equations are non-dimensionalized to maintain solver generality. The reference parameters used for non-dimensionalization are:

$l_{ref} = c_{75\%}$: Chord of the rotor blade at 75% radial station

$v_{ref} = a_\infty$: Freestream speed of sound

$\rho_{ref} = \rho_\infty$: Freestream density

$\mu_{ref} = \mu_\infty$: Freestream viscosity

$T_{ref} = T_\infty$: Freestream temperature

The non-dimensional flow variables are expressed as follows:

$$\langle x^*, y^*, z^* \rangle = \frac{\langle x, y, z \rangle}{l_{ref}}$$

$$\langle u^*, v^*, w^* \rangle = \frac{\langle u, v, w \rangle}{l_{ref}}$$

$$\langle p^*, e^* \rangle = \frac{\langle p, e \rangle}{\rho_\infty a_\infty^2}$$

$$t^* = \frac{t}{l_{ref}/a_\infty} \; ; \; \rho^* = \frac{\rho}{\rho_\infty}$$

$$\mu^* = \frac{\mu}{\mu_\infty} \; ; \; T^* = \frac{T}{T_\infty}$$

where the asterisk denotes a dimensionless variable. When this non-dimensionalization is applied to Eqn. (2.1), a similar equation with the non-dimensional state vector, inviscid and viscous fluxes are obtained.

$$\frac{\partial \boldsymbol{Q}^*}{\partial \boldsymbol{t}} + \frac{\partial \boldsymbol{F}^*}{\partial \boldsymbol{x}} + \frac{\partial \boldsymbol{G}^*}{\partial \boldsymbol{y}} + \frac{\partial \boldsymbol{H}^*}{\partial \boldsymbol{z}} = \frac{\boldsymbol{M}}{\boldsymbol{Re}}\left[\frac{\partial \boldsymbol{R}^*}{\partial \boldsymbol{x}} + \frac{\partial \boldsymbol{S}^*}{\partial \boldsymbol{y}} + \frac{\partial \boldsymbol{T}^*}{\partial \boldsymbol{z}}\right] \tag{2.9}$$

2.1.3 Governing Equations in Generalized Coordinates

It is difficult to obtain solutions for rotor configurations with arbitrary geometries, by solving the governing equations in Cartesian coordinates. Therefore the physical coordinate system (x, y, z, t) is expressed in terms of a generalized non-orthogonal curvilinear coordinate system (ξ, η, ζ, τ) as follows:

$$\tau = \tau(t)$$

$$\xi = \xi(x, y, z, t)$$

$$\eta = \eta(x, y, z, t)$$

$$\zeta = \zeta(x, y, z, t)$$

By applying the generalized transformation using the chain rule of differentiation to Eqn. (2.9), the transformed non-dimensional governing equations in generalized curvilinear system can be expressed as:

$$\frac{\partial \hat{Q}}{\partial \tau} + \frac{\partial \hat{F}}{\partial \xi} + \frac{\partial \hat{G}}{\partial \eta} + \frac{\partial \hat{H}}{\partial \zeta} = \frac{M}{Re}\left[\frac{\partial \hat{R}}{\partial \xi} + \frac{\partial \hat{S}}{\partial \eta} + \frac{\partial T}{\partial \zeta}\right] \tag{2.10}$$

in which the transformed vectors are related to their Cartesian counterparts through the metrics and Jacobians of the transformation.

In Eqn. (2.10), the transformed conserved flow variable vector becomes

$$\hat{Q} = \frac{Q}{J} = \frac{1}{J}\begin{Bmatrix} \rho \\ \rho u \\ \rho v \\ \rho w \\ e \end{Bmatrix} \tag{2.11}$$

The transformed inviscid fluxes $\hat{F}, \hat{G}, \hat{H}$ and the transformed viscous fluxes $\hat{R}, \hat{S}, \hat{T}$ are related to their counterparts F, G, H and R, S, T as follows:

$$\begin{aligned}
\hat{F} &= \frac{1}{J}\left(F\xi_x + G\xi_y + H\xi_z + q\xi_t\right) \\
\hat{G} &= \frac{1}{J}\left(F\eta_x + G\eta_y + H\eta_z + q\eta_t\right) \\
\hat{H} &= \frac{1}{J}\left(F\zeta_x + G\zeta_y + H\zeta_z + q\zeta_t\right) \\
\hat{R} &= \frac{1}{J}\left(R\xi_x + S\xi_y + T\xi_z\right) \\
\hat{S} &= \frac{1}{J}\left(R\eta_x + S\eta_y + T\eta_z\right) \\
\hat{T} &= \frac{1}{J}\left(R\zeta_x + S\zeta_y + T\zeta_z\right)
\end{aligned} \tag{2.12}$$

where J is the Jacobian of transformation defined by

$$\begin{aligned}
J \equiv \frac{\partial(x,y,z)}{\partial(\xi,\eta,\zeta)} &\equiv \begin{bmatrix} x_\xi & y_\xi & z_\xi \\ x_\eta & y_\eta & z_\eta \\ x_\zeta & y_\zeta & z_\zeta \end{bmatrix} \\
&= \frac{1}{x_\xi\left(y_\eta z_\zeta - y_\zeta z_\eta\right) + x_\eta\left(y_\zeta z_\xi - y_\xi z_\zeta\right) + x_\zeta\left(y_\xi z_\eta - y_\eta z_\xi\right)}
\end{aligned} \tag{2.13}$$

Physically, the Jacobian is the ratio of the volume of a grid cell in the computational domain divided by its volume in the physical domain. The quantities ξ_x, ξ_y, ξ_z, ξ_t etc. appearing in Eqn. (2.13) are called the metrics of transformation and are computed by:

$$\xi_x = J(y_\eta z_\zeta - y_\zeta z_\eta) \qquad \eta_x = J(y_\zeta z_\xi - y_\xi z_\zeta) \qquad \zeta_x = J(y_\xi z_\eta - y_\eta z_\xi)$$
$$\xi_y = J(x_\zeta z_\eta - x_\eta z_\zeta) \qquad \eta_y = J(x_\xi z_\zeta - x_\zeta z_\xi) \qquad \zeta_y = J(x_\eta z_\xi - x_\xi z_\eta) \qquad (2.14)$$
$$\xi_z = J(x_\eta y_\zeta - x_\zeta y_\eta) \qquad \eta_z = J(x_\zeta y_\xi - x_\xi y_\zeta) \qquad \zeta_z = J(x_\xi y_\eta - x_\eta y_\xi)$$

The contravariant velocity components *U*, *V*, and *W* are defined in the generalized coordinates as:

$$U = \xi_t + u\xi_x + v\xi_y + w\xi_z \qquad (2.15)$$
$$V = \eta_t + u\eta_x + v\eta_y + w\eta_z$$
$$W = \zeta_t + u\zeta_x + v\zeta_y + w\zeta_z$$

where

$$\xi_t = -x_\tau\xi_x - y_\tau\xi_y - z_\tau\xi_z$$
$$\eta_t = -x_\tau\eta_x - y_\tau\eta_y - z_\tau\eta_z \qquad (2.16)$$
$$\zeta_t = -x_\tau\zeta_x - y_\tau\zeta_y - z_\tau\zeta_z$$

where x_τ, y_τ, and z_τ represent the velocity components of the grid in an inertial frame. The contravariant velocity components *U*, *V*, and *W* are in directions normal to the constant ξ, η, and ζ surfaces, respectively.

The transformed inviscid and viscous flux vectors in Eqn. (2.10) may be rewritten as

$$\hat{F} = \begin{Bmatrix} \rho U \\ \rho uU + \xi_x p \\ \rho vU + \xi_y p \\ \rho wU + \xi_z p \\ U(e+p) - \xi_t p \end{Bmatrix} \hat{G} = \begin{Bmatrix} \rho V \\ \rho uV + \eta_x p \\ \rho vV + \eta_y p \\ \rho wV + \eta_z p \\ V(e+p) - \eta_t p \end{Bmatrix} \hat{H} = \begin{Bmatrix} \rho W \\ \rho uW + \zeta_x p \\ \rho vW + \zeta_y p \\ \rho wW + \zeta_z p \\ W(e+p) - \zeta_t p \end{Bmatrix} \tag{2.17}$$

$$\hat{R} = \begin{Bmatrix} 0 \\ \xi_x \tau_{xx} + \xi_y \tau_{xy} + \xi_z \tau_{xz} \\ \xi_x \tau_{yx} + \xi_y \tau_{yy} + \xi_z \tau_{yz} \\ \xi_x \tau_{zx} + \xi_y \tau_{zy} + \xi_z \tau_{zz} \\ \xi_x EN_x + \xi_y EN_y + \xi_z EN_z \end{Bmatrix}, \hat{S} = \begin{Bmatrix} 0 \\ \eta_x \tau_{xx} + \eta_y \tau_{xy} + \eta_z \tau_{xz} \\ \eta_x \tau_{yx} + \eta_y \tau_{yy} + \eta_z \tau_{yz} \\ \eta_x \tau_{zx} + \eta_y \tau_{zy} + \eta_z \tau_{zz} \\ \eta_x EN_x + \eta_y EN_y + \eta_z EN_z \end{Bmatrix}, \tag{2.18}$$

$$\hat{T} = \begin{Bmatrix} 0 \\ \zeta_x \tau_{xx} + \zeta_y \tau_{xy} + \zeta_z \tau_{xz} \\ \zeta_x \tau_{yx} + \zeta_y \tau_{yy} + \zeta_z \tau_{yz} \\ \zeta_x \tau_{zx} + \zeta_y \tau_{zy} + \zeta_z \tau_{zz} \\ \zeta_x EN_x + \zeta_y EN_y + \zeta_z EN_z \end{Bmatrix}$$

where the stresses terms and heat transfer terms in the transformed coordinates may now be written as follows:

$$\begin{aligned} \tau_{xx} &= \frac{2}{3}\mu\big[2\big(u_\xi \xi_x + u_\eta \eta_x + u_\zeta \zeta_x\big) - \big(v_\xi \xi_y + v_\eta \eta_y + v_\zeta \zeta_y\big) - (w_\xi \xi_z + w_\eta \eta_z \\ &\quad + w_\zeta \zeta_z)\big] \\ \tau_{yy} &= \frac{2}{3}\mu\big[2\big(v_\xi \xi_y + v_\eta \eta_y + v_\zeta \zeta_y\big) - (w_\xi \xi_z + w_\eta \eta_z + w_\zeta \zeta_z) \\ &\quad - \big(u_\xi \xi_x + u_\eta \eta_x + u_\zeta \zeta_x\big)\big] \\ \tau_{zz} &= \frac{2}{3}\mu\big[2(w_\xi \xi_z + w_\eta \eta_z + w_\zeta \zeta_z) - \big(u_\xi \xi_x + u_\eta \eta_x + u_\zeta \zeta_x\big) \\ &\quad - \big(v_\xi \xi_y + v_\eta \eta_y + v_\zeta \zeta_y\big)\big] \\ \tau_{xy} &= \tau_{yx} = \mu\big(u_\xi \xi_y + u_\eta \eta_y + u_\zeta \zeta_y + v_\xi \xi_x + v_\eta \eta_x + v_\zeta \zeta_x\big) \end{aligned} \tag{2.19}$$

$$\tau_{yz} = \tau_{zy} = \mu\left(w_\xi \xi_y + w_\eta \eta_y + w_\zeta \zeta_y + v_\xi \xi_z + v_\eta \eta_z + v_\zeta \zeta_z\right)$$

$$\tau_{zx} = \tau_{xz} = \mu\left(w_\xi \xi_x + w_\eta \eta_x + w_\zeta \zeta_x + u_\xi \xi_z + u_\eta \eta_z + u_\zeta \zeta_z\right)$$

$$EN_x = u\tau_{xx} + v\tau_{xy} + w\tau_{xz} + \frac{\mu C_P}{Pr}\left(\xi_x \frac{\partial T}{\partial \xi} + \eta_x \frac{\partial T}{\partial \eta} + \zeta_x \frac{\partial T}{\partial \zeta}\right)$$

$$EN_y = u\tau_{xy} + v\tau_{yy} + w\tau_{yz} + \frac{\mu C_P}{Pr}\left(\xi_y \frac{\partial T}{\partial \xi} + \eta_y \frac{\partial T}{\partial \eta} + \zeta_y \frac{\partial T}{\partial \zeta}\right) \tag{2.20}$$

$$EN_z = u\tau_{xz} + v\tau_{yz} + w\tau_{zz} + \frac{\mu C_P}{Pr}\left(\xi_z \frac{\partial T}{\partial \xi} + \eta_z \frac{\partial T}{\partial \eta} + \zeta_z \frac{\partial T}{\partial \zeta}\right)$$

2.2 Numerical Formulation of CFD Methodology

The starting point for the numerical formulation is a semi-discrete finite difference approximation to Eqn. (2.10) given by

$$\left(\frac{\partial \hat{Q}}{\partial \tau}\right)_{i,j,k} + \frac{\hat{F}_{i+\frac{1}{2},j,k} - \hat{F}_{i-\frac{1}{2},j,k}}{\Delta\xi} + \frac{\hat{G}_{i,j+\frac{1}{2},k} - \hat{G}_{i,j-\frac{1}{2},k}}{\Delta\eta} + \frac{\hat{H}_{i,j,k+\frac{1}{2}} - \hat{H}_{i,j,k-\frac{1}{2}}}{\Delta\zeta}$$

$$= \frac{M}{Re}\left(\frac{\hat{R}_{i+\frac{1}{2},j,k} - \hat{R}_{i-\frac{1}{2},j,k}}{\Delta\xi} + \frac{\hat{S}_{i+\frac{1}{2},j,k} - \hat{S}_{i-\frac{1}{2},j,k}}{\Delta\eta} + \frac{\hat{T}_{i+\frac{1}{2},j,k} - \hat{T}_{i-\frac{1}{2},j,k}}{\Delta\zeta}\right) \tag{2.21}$$

here,

$$\Delta\xi = \xi_{i+\frac{1}{2},j,k} - \xi_{i-\frac{1}{2},j,k} = 1$$

$$\Delta\eta = \eta_{i,j+\frac{1}{2},k} - \eta_{i,j-\frac{1}{2},k} = 1 \tag{2.22}$$

$$\Delta\zeta = \zeta_{i,j,k+\frac{1}{2}} - \zeta_{i,j,k-\frac{1}{2}} = 1$$

The central difference operator δ is now introduced such that:

$$\delta_\xi \hat{F}_{i,j,k} = \frac{\hat{F}_{i+\frac{1}{2},j,k} - \hat{F}_{i-\frac{1}{2},j,k}}{\Delta\xi}$$

$$\delta_\eta \hat{G}_{i,j,k} = \frac{\hat{G}_{i,j+\frac{1}{2},k} - \hat{G}_{i,j-\frac{1}{2},k}}{\Delta\eta} \tag{2.23}$$

$$\delta_\zeta \hat{H}_{i,j,k} = \frac{\hat{H}_{i,j,k+\frac{1}{2}} - \hat{H}_{i,j,k-\frac{1}{2}}}{\Delta\zeta}$$

For the viscous fluxes, $\delta_\xi \hat{R}_{i,j,k}$, $\delta_\eta \hat{S}_{i,j,k}$, $\delta_\zeta \hat{T}_{i,j,k}$ are also defined in a similar manner.

With this notation, the Eqn. (2.21) then can be written as:

$$\frac{\partial \hat{Q}}{\partial \tau} = -\left(\delta_\xi \hat{F} + \delta_\eta \hat{G} + \delta_\zeta \hat{H}\right) + \frac{M}{Re}\left(\delta_\xi \hat{R} + \delta_\eta \hat{S} + \delta_\zeta \hat{T}\right) \tag{2.24}$$

Eqn. (2.24) is now an ODE in time for the flow properties Q that may be advanced in time until a steady state solution (or a limit cycle periodic solution in time) is obtained.

2.2.1 Calculation of Inviscid Fluxes

The fluxes F, G, H represent fluxes of mass, momentum, and energy carried by acoustic, vortical, and entropy waves. While computing these terms, attention must be paid to the direction in which information is propagated. To account for the wave propagation nature of the flow, a variety of flux-vector splitting and flux-difference

splitting schemes [75-79] have been proposed that split the flux into contributions from the individual waves.

In the present work, Roe's approximate Riemann solver [81] is used. The flux $\hat{F}$ is computed as:

$$\hat{F}_{i+\frac{1}{2},j,k} = \frac{1}{2}\left\{\left(\hat{F}_L + \hat{F}_R\right) - \left|\tilde{A}\right|(q_R - q_L)\right\} \tag{2.25}$$

In Eqn. (2.25), q_R and q_L may be considered as q at $(i+\frac{1}{2}, j, k)$ node just to the right and to the left sides of $(i\pm\frac{1}{2}$ or $j\pm\frac{1}{2}$ or $k\pm\frac{1}{2})$, respectively, and defined as:

$$q_L = \begin{Bmatrix} \rho_L \\ u_L \\ v_L \\ w_L \\ p_L \end{Bmatrix} \quad q_R = \begin{Bmatrix} \rho_R \\ u_R \\ v_R \\ w_R \\ p_R \end{Bmatrix} \tag{2.26}$$

The quantities $\hat{F}_L$ and $\hat{F}_R$, the physical fluxes, are fluxes $\hat{F}$ evaluated at the half node $(i+\frac{1}{2}, j, k)$ using the flow properties from left and right of the cell face as shown in Figure 2.1.

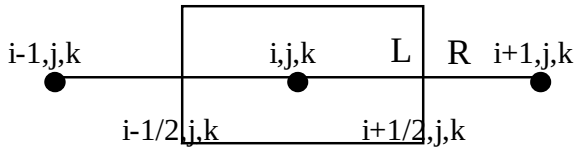

Figure 2.1 Nodal construction

The fluxes $\hat{F}_L$ and $\hat{F}_R$ can be evaluated as:

$$\hat{F}_L = \begin{Bmatrix} \rho_L U_L \\ \rho_L U_L u_L + p_L n_x \\ \rho_L U_L v_L + p_L n_y \\ \rho_L U_L w_L + p_L n_z \\ \rho_L U_L h_{0L} - p_L n_t \end{Bmatrix} \quad \hat{F}_R = \begin{Bmatrix} \rho_R U_R \\ \rho_R U_R u_R + p_R n_x \\ \rho_R U_L v_R + p_R n_y \\ \rho_R U_L w_R + p_R n_z \\ \rho_R U_R h_{0R} - p_R n_t \end{Bmatrix} \tag{2.27}$$

Here, the quantities $U, h_0,$ and n_t are the contravariant velocity, specific total enthalpy, and the grid velocity of the coordinate surface $(i+\frac{1}{2}, j, k)$ in the normal direction of the surface, respectively. These terms are defined as:

$$\mathrm{U} = \left(\vec{\mathrm{V}} - \vec{\mathrm{V}}_{\mathrm{G}}\right).\frac{\vec{\nabla}\xi}{\mathrm{J}} \;;\; \mathrm{h}_0 = \frac{\mathrm{e+p}}{\rho} \;;\; \eta_{\mathrm{t}} = -\left(\vec{\mathrm{V}}_{\mathrm{G}}.\frac{\vec{\nabla}\xi}{\mathrm{J}}\right) \tag{2.28}$$

where $\vec{V}_G$ is the grid velocity at the cell face $(i+\frac{1}{2}, j, k)$ defined by $\vec{V}_G = x_\tau \vec{i} + y_\tau \vec{j} + z_\tau \vec{k}$. The fluxes at other half-points $(i, j+\frac{1}{2}, k)$ etc. can be defined in a similar way.

The term $\left|\tilde{A}\right|(q_R - q_L)$ on the right hand side of Eqn. (2.29) is referred to as a "numerical viscosity" or "diffusion term". The numerical viscosity term, calculated as a sum of simple wave contributions depending on their wave speeds, is needed to filter out high frequency non-physical oscillations in the solution. The term $\left|\tilde{A}\right| = \left|\partial\hat{F} / \partial\hat{q}\right|$, the flux Jacobian matrix, is evaluated using "Roe-averaged" flow properties from left and right of the cell face.

To simplify the numerical computations, the matrix elements of the numerical term $\left|\tilde{A}\right|(q_R - q_L)$ are computed by an approach presented by Vinokur and Liu [82]:

$$\left|\tilde{A}\right|(q_R - q_L) = \left|\tilde{\lambda}_1\right| \begin{Bmatrix} \Delta\rho \\ \Delta\rho u \\ \Delta\rho v \\ \Delta\rho w \\ \Delta e \end{Bmatrix} + \delta_1 \begin{Bmatrix} \tilde{\rho} \\ \tilde{\rho}\tilde{u} \\ \tilde{\rho}\tilde{v} \\ \tilde{\rho}\tilde{w} \\ \tilde{\rho}\widetilde{h_0} \end{Bmatrix} + \delta_2 \begin{Bmatrix} 0 \\ \eta_x \\ \eta_y \\ \eta_z \\ \widetilde{U_c} \end{Bmatrix} \tag{2.29}$$

Where

$$\delta_1 = C_1 \frac{\Delta p}{\tilde{\rho}\tilde{a}^2} + \frac{1}{2} C_2 \frac{\Delta U_C}{\tilde{a}}$$

$$\delta_1 = C_1\tilde{\rho}\Delta U_C + \frac{1}{2}C_2\frac{\Delta p}{\tilde{a}} \tag{2.30}$$

$$C_1 = -\left|\widetilde{\lambda_1}\right| + 0.5\left(\left|\widetilde{\lambda_2}\right| + \left|\widetilde{\lambda_3}\right|\right)$$

$$C_2 = -\left|\widetilde{\lambda_2}\right| - \left|\widetilde{\lambda_3}\right|$$

Here the operator Δ is defined as a jump across the cell face. The characteristic wave speeds and the contravariant velocity are defined by

$$\widetilde{\lambda_1} = \tilde{U}$$

$$\widetilde{\lambda_2} = \tilde{U} + a$$

$$\widetilde{\lambda_3} = \tilde{U} - a$$

$$\tilde{U} = \eta_t + \eta_x\tilde{u} + \eta_y\tilde{v} + \eta_z\tilde{w} = (\vec{V} - \overrightarrow{V_G}).\vec{\eta} \tag{2.31}$$

$$\widetilde{U_c} = \eta_x\tilde{u} + \eta_y\tilde{v} + \eta_z\tilde{w} = \vec{V}.\vec{\eta}$$

$$\Delta U_c = \eta_x(u_R - u_L) + \eta_y(v_R - v_L) + \eta_z(w_R - w_L)$$

Again, $\vec{n} = n_x\vec{i} + n_y\vec{j} + n_z\vec{k} = \frac{\vec{\nabla}\xi}{J}$, is a unit normal vector to the surface ξ = constant, multiplied by area associated with the cell interface $(i+\frac{1}{2}, j, k)$, at which the flux is calculated. All the quantities with a tilde sign over represent the "Roe-averaged" quantities [83] which are given by:

$$R = \sqrt{\frac{\rho_R}{\rho_L}}$$

$$\tilde{\rho} = \sqrt{\rho_R \rho_L}$$

$$\tilde{u} = u_L\left(\frac{1}{1+R}\right) + u_R\left(\frac{R}{1+R}\right)$$

$$\tilde{v} = v_L\left(\frac{1}{1+R}\right) + v_R\left(\frac{R}{1+R}\right) \tag{2.32}$$

$$\tilde{w} = w_L\left(\frac{1}{1+R}\right) + w_R\left(\frac{R}{1+R}\right)$$

$$\tilde{e} = e_L\left(\frac{1}{1+R}\right) + e_R\left(\frac{R}{1+R}\right)$$

$$\tilde{a} = \sqrt{\gamma(\gamma-1)\left[\frac{e}{\rho} - \frac{1}{2}(\tilde{u}^2 + \tilde{v}^2 + \tilde{w}^2)\right]}$$

In this present work, an interpolation method called the Monotone Upstream-centered Scheme for Conservation Laws (MUSCL) is used. In general, the MUSCL scheme [84] can be written as:

$$q_L = \left\{1 + \frac{[(1-k)\nabla + (1+\mathrm{k})\Delta]}{4}\right\}\mathrm{q_i}$$

$$q_R = \left\{1 - \frac{[(1+k)\nabla + (1-\mathrm{k})\Delta]}{4}\right\}\mathrm{q_{i+1}} \tag{2.33}$$

Here Δ and ∇ are the forward- and backward-difference operators, respectively, defined as:

$$\Delta(\quad)_i = (\quad)_{i+1} - (\quad)_i$$

$$\nabla(\quad)_i = (\quad)_i - (\quad)_{i-1}$$

The choice of k determines the spatial accuracy of the scheme. For example, $k=-1$ yields a second-order fully upwind scheme, while $k=1$ yields a second-order central difference scheme. In the present work, $k=\frac{1}{3}$ is chosen, and a third-order accurate upwind scheme is obtained. Eqn. (2.33) can be rewritten as:

$$\begin{aligned} q_L &= q_i + \frac{1}{6}(q_i - q_{i-1}) + \frac{1}{3}(q_{i+1} - q_i) \\ q_R &= q_{i+1} - \frac{1}{3}(q_{i+1} - q_i) - \frac{1}{6}(q_{i+2} - q_{i+1}) \end{aligned} \tag{2.34}$$

Figure 2.2 shows the three-point stencils for computing left and right primitive variables in the third-order MUSCL scheme.

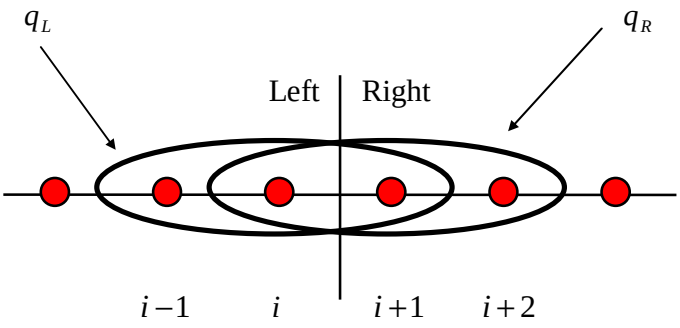

Figure 2.2 Three point stencil

The high-order scheme must be reduced to a lower order in regions with large flow gradients and discontinuities (e.g. shocks), to maintain stability and to eliminate spurious numerical oscillations in the solution. This can be accomplished by use of a flux limiter. A limiter is a non-linear algorithm that reduces the high-derivative content of a subgrid interpolant in order to make it non-oscillatory. It yields the interface

reconstructions which are within the bounds of the adjacent cell averages. By applying the flux limiter ϕ, Eqn. (2.34) can be expressed generally as:

$$\begin{aligned} q_L &= \left\{1+\phi^l[(1-k)\nabla+(1+k)\Delta]/4\right\}q_i \\ q_R &= \left\{1-\phi^r[(1+k)\nabla+(1-k)\Delta]/4\right\}q_{i+1} \end{aligned} \tag{2.35}$$

where ϕ^l and ϕ^r are designed such that they become zero in the vicinity of the high gradients.

In the present methodology, the modified Van Albada flux limiter [85] is used, which is defined by:

$$\begin{aligned} \phi^l &= \frac{2(\nabla q_i)(\Delta q_i)+\varepsilon}{(\nabla q_i)^2+(\Delta q_i)^2+\varepsilon} \\ \phi^r &= \frac{2(\nabla q_{i+1})(\Delta q_{i+1})+\varepsilon}{(\nabla q_{i+1})^2+(\Delta q_{i+1})^2+\varepsilon} \end{aligned} \tag{2.36}$$

Also, ε is a small parameter that prevents indeterminacy in regions of zero gradients, i.e. where $(\nabla q_i)=(\Delta q_i)=0$.

2.2.2 Calculation of Viscous Fluxes

At each time step the viscous fluxes $(\hat{R},\hat{S},\hat{T})$ in Eqn. (2.24) are computed and added to the inviscid flux contributions on the right hand side of the equation. The viscous fluxes are computed using a symmetric second order central difference scheme. The viscous fluxes contain derivatives of the velocity components, such as u_ξ, which can be computed as:

$$u_\xi\Big|_{i+\frac{1}{2},j,k} = \frac{u_{i+1,j,k}-u_{i,j,k}}{\Delta\xi} \qquad u_\xi\Big|_{i-\frac{1}{2},j,k} = \frac{u_{i,j,k}-u_{i-1,j,k}}{\Delta\xi} \tag{2.37}$$

and the metrics needed at the half point can be directly calculated.

2.2.3 Time Marching Scheme

Since the governing equations are parabolic in time, a stable dissipative time marching scheme is needed to advance the solution. In this study, the following semi-implicit scheme is used with first order backward differencing.

$$\left.\frac{\partial \hat{q}}{\partial \tau}\right|^{n+1} = -(\delta_\xi \hat{F} + \delta_\eta \hat{G} + \delta_\zeta \hat{H})\Big|^{n+1} + \frac{M}{\mathrm{Re}}(\delta_\xi \hat{R} + \delta_\eta \hat{S} + \delta_\zeta \hat{T})\Big|^{n} \tag{2.38}$$

where the superscripts refer to time step *n* and *n+1*. Here, δ_ξ, δ_η, δ_ζ are standard central difference operators. The inviscid fluxes and viscous fluxes are computed at the half-points $(i \pm \frac{1}{2}, j \pm \frac{1}{2}, k \pm \frac{1}{2})$ as discussed earlier.

The discretization of term $\frac{\partial \hat{q}}{\partial \tau}$ in Eqn. (2.38) is given by:

$$\left.\frac{\partial \hat{q}}{\partial \tau}\right|^{n+1} = \frac{\hat{q}^{n+1} - \hat{q}^{n}}{\Delta \tau} + O(\Delta \tau) \tag{2.39}$$

As a result, Eqn. (2.38) can be expressed as:

$$\hat{q}^{n+1} = \hat{q}^{n} - \Delta\tau(\delta_\xi \hat{F}^{n+1} + \delta_\eta \hat{G}^{n+1} + \delta_\zeta \hat{H}^{n+1}) + \Delta\tau \frac{M}{\mathrm{Re}}(\delta_\xi \hat{R}^{n} + \delta_\eta \hat{S}^{n} + \delta_\zeta \hat{T}^{n}) \tag{2.40}$$

It is to be noted that $\hat{q}$ contains the jacobian term which is not a constant for deforming grids. The effect of variable jacobians is dealt in next chapter. Eqn. (2.40) gives a system of non-linear algebraic equations since the inviscid terms are being handled implicitly. Therefore, to obtain a linear system of equations, the implicit inviscid terms must be linearized. Linearization is performed using Taylor series expansion:

$$\begin{aligned} \hat{F}^{n+1} &= \hat{F}^{n} + [A^{n}](\hat{q}^{n+1} - \hat{q}^{n}) \\ \hat{G}^{n+1} &= \hat{G}^{n} + [B^{n}](\hat{q}^{n+1} - \hat{q}^{n}) \\ \hat{H}^{n+1} &= \hat{H}^{n} + [C^{n}](\hat{q}^{n+1} - \hat{q}^{n}) \end{aligned} \tag{2.41}$$

where $[A^n]$, $[B^n]$ and $[C^n]$ are the 5x5 Jacobian matrices defined as:

$$[A] = \hat{A} = \frac{\partial \hat{F}}{\partial \hat{q}} \qquad [B] = \hat{B} = \frac{\partial \hat{G}}{\partial \hat{q}} \qquad [C] = \hat{C} = \frac{\partial \hat{H}}{\partial \hat{q}} \tag{2.42}$$

The viscous terms are treated explicitly, and no linearization is needed.

The Jacobian matrices can be evaluated analytically and are given by Pulliam and Steger [86]. The detailed forms of these matrices are shown below:

$$[A] = \begin{bmatrix} \xi_t & \xi_x & \xi_y & \xi_z & 0 \\ \xi_x\phi^2 - u\theta & \Theta - \xi_x(\gamma-2)u & \xi_y u - \sigma\xi_x v & \xi_z u - \sigma\xi_x w & \xi_x\sigma \\ \xi_y\phi^2 - v\theta & \xi_x v - \sigma\xi_y u & \Theta - \xi_y(\gamma-2)v & \xi_z v - \sigma\xi_y w & \xi_y\sigma \\ \xi_z\phi^2 - w\theta & \xi_x w - \sigma\xi_z u & \xi_y w - \sigma\xi_z v & \Theta - \xi_z(\gamma-2)w & \xi_z\sigma \\ \theta(\phi^2 - E) & \xi_x E - \sigma u\theta & \xi_y E - \sigma v\theta & \xi_z E - \sigma w\theta & \xi_t + \gamma\theta \end{bmatrix} \tag{2.43}$$

where

$$\begin{aligned} \phi^2 &= (\gamma-1)(u^2+v^2+w^2)/2 \\ \theta &= \xi_x u + \xi_y v + \xi_z w \\ \sigma &= \gamma - 1 \\ \Theta &= \xi_t + \theta \\ E &= \frac{\gamma e}{\rho} - \phi^2 \end{aligned} \tag{2.44}$$

The matrices $[B]$ and $[C]$ can be similarly evaluated by using η and ζ in the above equations, respectively, instead of ξ.

Now Eqn. (2.40) can be rearranged as:

$$[I + \Delta\tau(\delta_\xi \hat{A}^n + \delta_\eta \hat{B}^n + \delta_\zeta \hat{C}^n)]\Delta\hat{q}^{n+1} = [RHS]^n \tag{2.45}$$

where $\Delta\hat{q}^{n+1} = \hat{q}^{n+1} - \hat{q}^n$, I is the identity matrix. The term [*RHS*], referred to as the residual, is given by:

$$[RHS]^n = -\Delta\tau(\delta_\xi \hat{F}^n + \delta_\eta \hat{G}^n + \delta_\zeta \hat{H}^n) + \Delta\tau \frac{M}{\mathrm{Re}}(\delta_\xi \hat{R}^n + \delta_\eta \hat{S}^n + \delta_\zeta \hat{T}^n) \tag{2.46}$$

In steady-state problems, the residual should be reduced to an acceptable small value for the calculation to be considered converged. In time dependent or unsteady problems, however, the residual does not need to reach a minimum value and may vary with time depending on the flow situation.

Eqn. (2.46) may be viewed as a matrix system

$$[M]\{\Delta\hat{q}\} = [RHS] \tag{2.47}$$

Solution of Eqn. (2.47) is computationally expensive because the unfactored coefficient matrix [*M*], which is a seven-diagonal matrix, requires vast computer storage and computing time to invert. In order to reduce the computational work, this sparse matrix [*M*] is approximately factored into three sparse matrices using a Lower-Upper Symmetric Gauss-Seidel (LU-SGS) implicit scheme proposed by Yoon and Jameson [87]. The LU-SGS method ensures that the matrix is diagonally dominant. This scheme is widely used to solve the compressible Navier-Stokes equations.

In this method, Eqn. (2.47) is first expressed as

$$(L + D + U)\Delta\hat{q}^{n+1} = [RHS]^n \tag{2.48}$$

where *L* is a lower block triangular matrix with null matrices on the diagonal, *D* is a block diagonal matrix formed out of both positive and negative flux Jacobian matrices, and *U* is an upper block triangular matrix with null matrices on the diagonal. For the case of non-singular matrix D, Eqn. (2.48) may be written as:

$$D(D^{-1}L + I + D^{-1}U)\Delta\hat{q}^{n+1} = [RHS]^n \tag{2.49}$$

Using LU- factorization, Eqn. (2.49) can be approximated as

$$D(I + D^{-1}L)(I + D^{-1}U)\Delta\hat{q}^{n+1} = [RHS]^n \tag{2.50}$$

or

$$(D + L)D^{-1}(D + U)\Delta\hat{q}^{n+1} = [RHS]^n \tag{2.51}$$

These matrices may be expressed as

$$\begin{aligned}
(D+L) &= I - \Delta\tau\left(\frac{\hat{A}^-}{\Delta\xi} - \delta_\xi^-\hat{A}^+ + \frac{\hat{B}^-}{\Delta\eta} - \delta_\eta^-\hat{B}^+ + \frac{\hat{C}^-}{\Delta\zeta} - \delta_\zeta^-\hat{C}^+\right) \\
D &= I + \frac{\Delta\tau}{\Delta\xi}\left(\hat{A}^+ - \hat{A}^-\right) + \frac{\Delta\tau}{\Delta\eta}\left(\hat{B}^+ - \hat{B}^-\right) + \frac{\Delta\tau}{\Delta\zeta}\left(\hat{C}^+ - \hat{C}^-\right) \\
(D+U) &= I + \Delta\tau\left(\frac{\hat{A}^+}{\Delta\xi} + \delta_\xi^+\hat{A}^- + \frac{\hat{B}^+}{\Delta\eta} + \delta_\eta^+\hat{B}^- + \frac{\hat{C}^+}{\Delta\zeta} - \delta_\zeta^+\hat{C}^-\right)
\end{aligned} \tag{2.52}$$

Here, δ_ξ^-, δ_η^- and δ_ζ^- are the first-order backward differences, while δ_ξ^+, δ_η^+ and δ_ζ^+ are the first-order forward difference operators.

Computing the matrices $\hat{A}^\pm$, $\hat{B}^\pm$ and $\hat{C}^\pm$ directly is very expensive. There are many ways to approximate the matrices $\hat{A}^\pm$, $\hat{B}^\pm$ and $\hat{C}^\pm$. In this present work, the following approach by Yoon and Jameson [87] is used.

$$\begin{aligned}
\hat{A}^\pm &= \frac{1}{2}(\hat{A} \pm r_A I) \\
\hat{B}^\pm &= \frac{1}{2}(\hat{B} \pm r_B I) \\
\hat{C}^\pm &= \frac{1}{2}(\hat{C} \pm r_C I)
\end{aligned} \tag{2.53}$$

where r_A, r_B, r_C are called the spectral radii or the largest eigenvalues of the flux Jacobian matrices $\hat{A}$, $\hat{B}$ and $\hat{C}$, respectively, and defined as:

$$\begin{aligned} r_A &= k_A \max(|\lambda_A|) \\ r_B &= k_B \max(|\lambda_B|) \\ r_C &= k_C \max(|\lambda_C|) \end{aligned} \tag{2.54}$$

Here, λ_A, λ_B and λ_C represent the eigenvalues of the matrices $\hat{A}$, $\hat{B}$ and $\hat{C}$, respectively. k_A, k_B and k_C are user-input constants, which are greater than or equal to 1 for stability. In this study, $k_A = k_B = k_C = 1$ is used, and Eqn. (2.54) can be evaluated as follows:

$$\begin{aligned} r_A &= |U| + a(\xi_x^2 + \xi_y^2 + \xi_z^2)^{1/2} \\ r_B &= |V| + a(\eta_x^2 + \eta_y^2 + \eta_z^2)^{1/2} \\ r_C &= |W| + a(\zeta_x^2 + \zeta_y^2 + \zeta_z^2)^{1/2} \end{aligned} \tag{2.55}$$

By substituting Eqn. (2.55) into Eqn. (2.52) gives:

$$\begin{aligned} (D+L) &= \left[1 + r_A \frac{\Delta\tau}{\Delta\xi} + r_B \frac{\Delta\tau}{\Delta\eta} + r_C \frac{\Delta\tau}{\Delta\zeta}\right] I - \frac{\Delta\tau}{\Delta\xi} A^+_{i-1,j,k} - \frac{\Delta\tau}{\Delta\eta} B^+_{i,j-1,k} - \frac{\Delta\tau}{\Delta\zeta} C^+_{i,j,k-1} \\ D &= \left[1 + r_A \frac{\Delta\tau}{\Delta\xi} + r_B \frac{\Delta\tau}{\Delta\eta} + r_C \frac{\Delta\tau}{\Delta\zeta}\right] I \\ (D+U) &= \left[1 + r_A \frac{\Delta\tau}{\Delta\xi} + r_B \frac{\Delta\tau}{\Delta\eta} + r_C \frac{\Delta\tau}{\Delta\zeta}\right] I + \frac{\Delta\tau}{\Delta\xi} A^-_{i+1,j,k} + \frac{\Delta\tau}{\Delta\eta} B^-_{i,j+1,k} + \frac{\Delta\tau}{\Delta\zeta} C^-_{i,j,k+1} \end{aligned} \tag{2.56}$$

From Eqn. (2.56) each of the factored matrices can be inverted and the system of equations can be solved to obtain $\Delta\hat{q}^{n+1}$ as detailed below:

$$\begin{aligned} (D+L)X &= [RHS]^n \\ D^{-1}Y &= X \\ (D+U)\Delta\vec{\hat{q}}^{n+1} &= Y \end{aligned} \tag{2.57}$$

where each matrix has either lower, or diagonal, or upper part only. The inversion of these matrices can be accomplished by backward or forward substitution, which requires less computational work than solving Eqn. (2.47). Finally, the new $\hat{q}^{n+1}$ can be obtained from $\hat{q}^{n+1} = \hat{q}^{n} + \Delta\hat{q}^{n+1}$.

2.3 Turbulence Modeling

The time-averaged Navier-Stokes equations lead to the Reynolds stress terms $\overline{u_i' u_j'}$, which cannot be solved directly and must be modeled. The Reynolds stresses, in tensor form, can be modeled using an eddy viscosity concept:

$$-\rho\overline{u_i' u_j'} = \mu_T\left[\frac{\partial \overline{u}_i}{\partial x_j} + \frac{\partial \overline{u}_j}{\partial x_i}\right] \qquad \text{for } i, j = 1,2,3 \tag{2.58}$$

where u_i', u_j' are the instantaneous velocity fluctuations about the mean velocity components $\overline{u}_i$ and $\overline{u}_j$, respectively, and $\overline{u_i' u_j'}$ is the time-averaged value of the product u_i' and u_j'. The eddy viscosity μ_T is used to account for the effect of turbulent flow. Turbulence models implemented in the solver are Baldwin-Lomax, Spalart-Allmaras (SA)/ Spalart-Allmaras-DES (SA-DES) and Kinetic Eddy Simulation (KES). SA-DES and KES turbulence models were used for all the rotor studies presented in this work.

2.3.1 Spalart-Allmaras Detached Eddy Simulation (SA-DES) model

Spalart and Allmaras [88] have proposed a one-equation transport model for eddy viscosity called the Spalart-Allmaras (SA) model. In this model, the eddy viscosity, μ_t, is computed from:

$$\mu_t = \rho\tilde{\nu} f_{v1} \tag{2.59}$$

Where the viscous damping function, f_{v1}, is given by:

$$f_{v1} = \frac{\chi^3}{\chi^3 + c_{v1}^3} \quad \text{and} \quad \chi = \frac{\tilde{\nu}}{\nu} \tag{2.60}$$

The damping function goes to zero at the wall and gradually rises to unity as the distance from the wall increases. The operating parameter $\tilde{\nu}$ is determined by the transport equation as follows:

$$\begin{aligned} \frac{D\tilde{\nu}}{Dt} &= c_{b1}[1 - f_{t2}]\tilde{S}\tilde{\nu} + \frac{1}{\sigma}\left[\nabla \cdot \left((\nu + \tilde{\nu})\nabla\tilde{\nu}\right) + c_{b2}(\nabla\tilde{\nu})^2\right] \\ &\quad - \left[c_{w1}f_w - \frac{c_{b1}}{\kappa^2}f_{t2}\right]\left[\frac{\tilde{\nu}}{d}\right]^2 + f_{t1}\Delta U^2 \end{aligned} \tag{2.61}$$

On the right hand-side, each term represents production, diffusion, dissipation, and trasition / trip effects, respectively. The individual components are defined as:

$$\begin{aligned} \tilde{S} &= S + \frac{\tilde{\nu}}{\kappa^2 d^2}f_{v2} & f_{v2} &= 1 - \frac{\chi}{1 + \chi f_{v1}} \\ f_w &= g\left[\frac{1 + c_{w3}^6}{g^6 + c_{w3}^6}\right]^{\frac{1}{6}} & g &= r + c_{w2}(r^6 - r) \\ r &= \frac{\tilde{\nu}}{\tilde{S}\kappa^2 d^2} & f_{t2} &= c_{t3}exp(-c_{t4}\chi^2) \\ f_{t1} &= c_{t1}g_t exp\left(-c_{t2}\frac{\omega_t^2}{\Delta U^2}[d^2 + g_t^2 d_t^2]\right) \end{aligned} \tag{2.62}$$

Where:

d_t is the distance from the field point to the trip point on the wall

ω_t is the wall vorticity at the trip

ΔU is the difference between velocity at the field point and that at the trip

$g_t \equiv min(0.1, \Delta U/\omega_t \Delta x_t)$

x_t is the grid spacing along the wall at the

And, the constants are:

$$c_{b1} = 0.1355 \qquad c_{b2} = 0.622 \qquad \sigma = 2/3 \qquad \kappa = 0.41$$

$$c_{w1} = \frac{c_{b1}}{\kappa^2} + \frac{(1 + c_{b2})}{\sigma} \qquad c_{w2} = 0.3 \qquad c_{w3} = 2 \qquad c_{v1} = 7.1$$

$$c_{t1} = 1 \qquad c_{t2} = 2 \qquad c_{t3} = 1.2 \qquad c_{t4} = 0.5$$

In the current study, the trip is not applied and the flow field is assumed to be turbulent everywhere.

Spalart and Allmaras also proposed a Detached Eddy Simulation (DES) model [89] to improve the SA model for separated flows. In the DES model, the turbulence length scale is computed in two different ways. In regions close to the wall the length scale is related to the closest distance to the wall. In regions away from the wall, this definition is replaced by the maximum cell size as follows:

$$\tilde{d} = min(d, C_{DES}\Delta), \qquad \Delta = max(\Delta x, \Delta y, \Delta z) \tag{2.63}$$

The distance, d, in the transport equation is replaced with $\tilde{d}$, and the model constant $C_{DES} = 0.65$ is used in this study.

2.3.2 Kinetic Eddy Simulation (KES) model

Kinetic Eddy Simulation (KES) model was developed by Fang and Menon [90] for large-eddy simulation (LES) of wall-bounded high Reynolds number flows. The model solves two PDEs, one of the sub-grid kinetic energy, k^{sgs}, and the other for $(kl)^{sgs}$ where l^{sgs} is the sub-grid length scale.

$$\frac{\partial \rho k^{sgs}}{\partial t} + \frac{\partial \rho u_i k^{sgs}}{\partial x_j} = \tau_{ij}\frac{\partial u_i}{\partial x_j} - C_k \rho \frac{(k^{sgs})^{3/2}}{l^{sgs}} + \frac{\partial}{\partial x_j}\left[\rho\left(\frac{\nu_l}{Pr} + \frac{\nu_t}{\sigma_k}\right)\frac{\partial k^{sgs}}{\partial x_j}\right] \tag{2.64}$$

$$\frac{\partial \rho (kl)^{sgs}}{\partial t} + \frac{\partial \rho u_i (kl)^{sgs}}{\partial x_j} = C_l l^{sgs} \tau_{ij} \frac{\partial u_i}{\partial x_j} - C_{kl} \rho (k^{sgs})^{\frac{3}{2}} + \frac{\partial}{\partial x_j}\left[\rho \left(\frac{\nu_l}{Pr} + \frac{\nu_t}{\sigma_{kl}}\right) \frac{\partial (kl)^{sgs}}{\partial x_j}\right] \tag{2.65}$$

Where:

$\sigma_k = 0.9$ $\quad$ $\sigma_{kl} = 2$ $\quad$ $C_k = 0.916$

$C_l = 1.06$ $\quad$ $C_{kl} = 0.58 + 2\frac{C_\nu}{\sigma_{kl}}\left(\frac{\partial l^{sgs}}{\partial x_j}\right)^2$ $\quad$ $C_\nu = 0.0667$

$\nu_l = \frac{\mu_l}{\rho}$ $\quad$ $\nu_t = \frac{\mu_t}{\rho}$ $\quad$ $Pr = 0.72$

The first term on the right-hand side of the Eqns. (2.64) and (2.65) represents production, and the second and third term represents dissipation and diffusion, respectively. The sub-grid eddy viscosity is computed from:

$$\mu_t = \rho C_\nu (k^{sgs})^{\frac{1}{2}} l^{sgs} \tag{2.66}$$

Both k^{sgs} and l^{sgs} are set to zero on the wall, and following formulation is used to determine the value on the first cell off the wall.

$$k^{sgs} = 0.25\nu (u_i u_i)_1^{0.5} / \Delta_1 \tag{2.67}$$

$$l^{sgs} = \sqrt{k^{sgs}} \Delta_1^2 / (0.53\nu) \tag{2.68}$$

When the length scale, l^{sgs}, is close to the computational grid size, Δ, the model approaches LES. When the computed length scale is much larger than the local grid size, the model smoothly approaches Very Large-Eddy Simulation (VLES). Thus, the model is considered a VLES-LES approach.

2.4 Rotor Inflow Modeling

In low speed operations, the rotor flow environment is strongly modified by the interaction between the rotor blade and the vortices shed from the neighboring blades. The ability to predict this wake is important, especially for blade-vortex interactions (BVI) in forward flight. In addition to the near wake, the rotor far wake that extends upto 4-6 rotor diameters needs to be captured or modeled to accurately predict the rotor inflow field. The requirement that the vortex core in the far wake be resolved without dissipation can make CFD wake capturing methods like OVERFLOW [54] computationally expensive. GT-Hybrid CFD solver utilizes a hybrid methodology where the flow field near the blade is resolved through the Navier-Stokes solution, whereas the influence of the other blades and of the trailing vorticity in the far field wake are accounted for by modeling them as a collection of piece-wise linear bound and trailing vortex elements. The near wake is captured inherently in the Navier-Stokes analysis. The use of such a hybrid Navier-Stokes / vortex modeling method allows for an accurate and economical modeling of viscous features near the blades, and an accurate "non-diffusive" modeling of the trailing wake in the far field.

2.4.1 Rigid/Free Wake Model

The vortex model is based on a Lagrangean wake approach where a collection of vortex elements are shed from the rotor blade trailing edge. This wake model is based on the assumption that all shed vorticity from blade coalesce downstream into a strong tip vortex. The convection of the tip vortex elements depends on differing approaches – rigid wake or free wake model. In the rigid wake model, the wake elements are non-distorting hence they maintain their initial helical structure and they are convected at a speed

determined by linear superposition of free stream velocity components and a uniform inflow velocity. This inflow velocity is determined using the Prandtl-Glauert's formula [2]. The convection velocity components in free/distorting wake model include velocity components induced by wake elements on each other in addition to above mentioned velocity components. The effect of bound vortex is also included for computation of self-induced velocity components. These self-induced velocity components are determined using Biot-Savart's law. Free wake methods provide more generality with a minimum dependence on experimental data but they are also computationally more expensive than rigid wake modeling. The rigid and free wake geometries are shown in Figure 2.3.

In the current implementation, the free/rigid wake model is initialized with prescribed wake geometry. The wake strengths are initialized using an analytical model developed by Mello et al. [91]. The number of revolutions of the wake preserved in the model is chosen by the user. In forward flight, 3 to 5 wake revolutions are chosen, depending on the advance ratio. In the hybrid method, the wake strength and geometry are assumed to vary periodically with blade azimuthal location. New wake filaments are added at the vortex shedding point as the rotor is advanced in the azimuthal direction. To keep the fixed number of wake elements small, the oldest age elements are dropped from the end of the wake. The induced velocity components and wake geometry distortion are updated for all wake elements each time new wake filaments are shed. Also, in order to reduce the computational cost, the frequency of updating the wake distortion can be controlled, permitting induced velocity and wake geometry updates at periodic azimuthal intervals. The free wake model is a better physical representation of the wake than rigid wake model, and therefore it is used for all the studies presented in this work.

2.4.2 Navier-Stokes/Wake Model Coupling

The wake model derives its vorticity strength from the Navier-Stokes solution. The effect of the wake model on the Navier-Stokes solution is accounted for by applying wake induced velocity components as a boundary condition on Navier-Stokes far-field boundaries. This coupling between the Navier-Stokes solution and wake model is explicit in nature. The effect of the wake lags the Navier-Stokes solution. The strength of the vortex elements in the tip vortex is set to be equal to the peak bound circulation on the rotor blade at the instant the element is shed. The peak bound circulation is obtained from airloads predicted by Navier-Stokes solution using Kutta-Joukowski theorem. The shedding point of the vortex element is based on the centroid of trailed circulation between the tip and location of peak bound circulation. The wake induced velocity components are computed at domain boundary points using Biot-Savart's law. The wake trailers used for boundary condition computation includes trailing and bound wake from all blades but neglects the contribution of the elements within the CFD volume grid trailed immediately from the blade. It is necessary to exclude the wake trailers inside the CFD volume grid to avoid double counting the vorticity already captured by the Navier-Stokes solution. The wake trailers inside the volume grid are excluded by constructing a bounding box as show in Figure 2.4. This bounding box is an imaginary box that is used to determine if wake markers are inside or outside the computational domain in an efficient way.

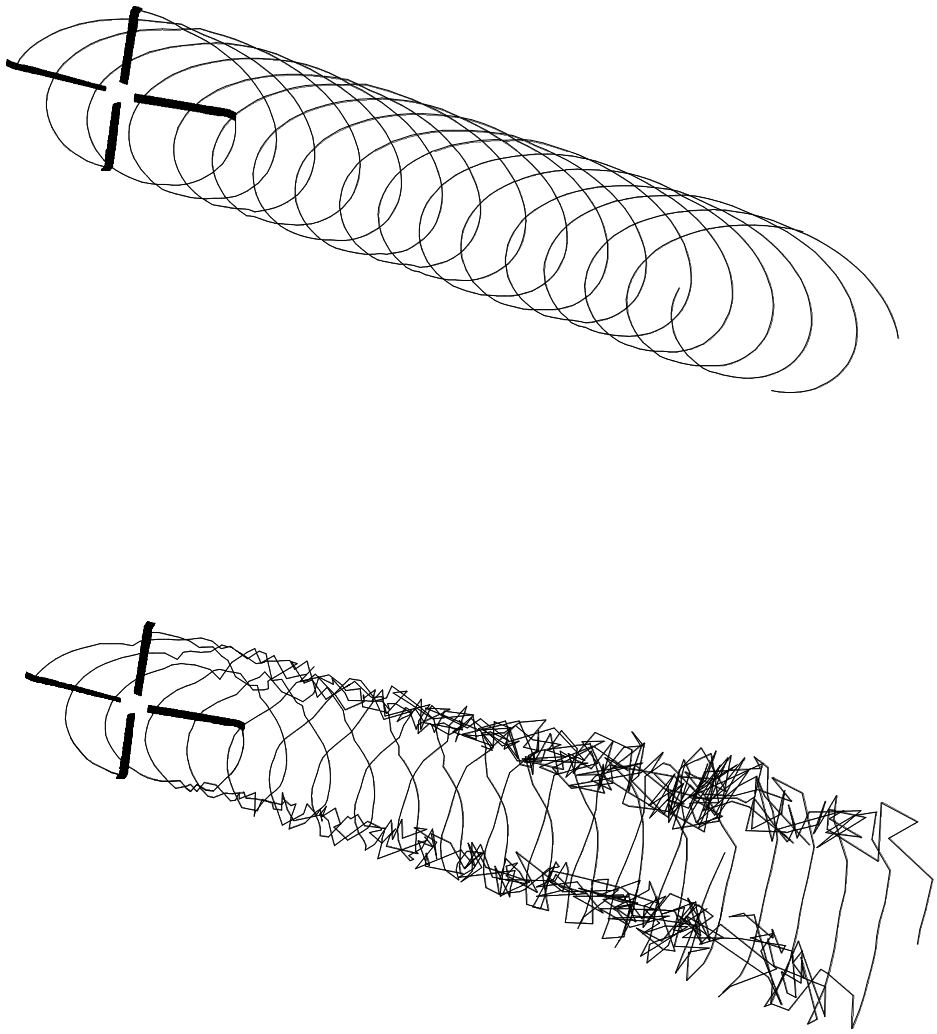

Figure 2.3 Rigid wake (upper) and free wake (lower) geometry in forward flight

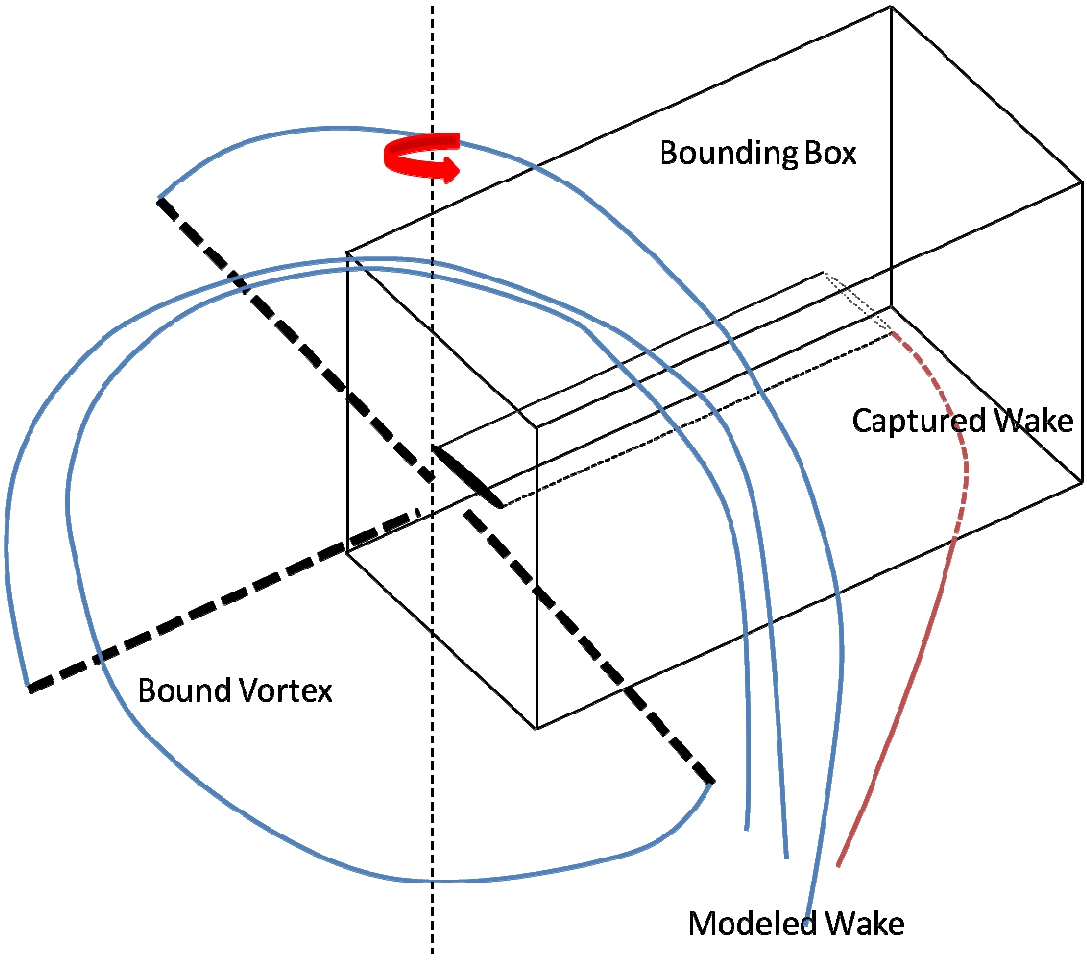

Figure 2.4 Wake model with bounding box

2.5 Initial and Boundary Conditions

2.5.1 Initial Conditions

In the beginning of the analysis, flow properties in the Navier-Stokes domain are initialized using flow conditions at rest:

$$\begin{aligned} \rho &= \rho_\infty \\ u &= 0 \\ v &= 0 \\ w &= 0 \\ p &= p_\infty \end{aligned} \tag{2.69}$$

2.5.2 Boundary Conditions

At solid walls, no-slip adiabatic wall temperature condition was applied. For this the following condition is satisfied.

$$\begin{aligned} \vec{V}_{wall} &= \vec{V}_{grid} \\ \left.\frac{\partial T}{\partial n}\right|_{wall} &= 0 \end{aligned} \tag{2.70}$$

Zero gradient of pressure at the wall was also assumed, i.e. $(\partial p/\partial n|_{wall} = 0)$.

At the outer boundaries including far-field, inboard, and outboard surfaces, characteristics based inflow/outflow boundary condition was applied to prevent non-physical wave reflection at the boundary. The details of this boundary condition may be found in several CFD text books [92]. In this boundary condition, Riemann invariants are written as:

$$\begin{aligned} R^+ &= \vec{V}_n + \frac{2a}{\gamma - 1} \\ R^- &= \vec{V}_n - \frac{2a}{\gamma - 1} \end{aligned} \tag{2.71}$$

And the characteristic velocity components are

$$\begin{aligned} \lambda_1 &= \vec{V}_n + a \\ \lambda_2 &= \vec{V}_n - a \end{aligned} \tag{2.72}$$

Here, $\vec{V}_n$ is the normal velocity directing outward from the computational domain. In the current hybrid method, the velocity at the outer boundary surface is defined as:

$$\vec{V} = \vec{V}_{wind} + \vec{V}_{wi} \tag{2.73}$$

Here, $\vec{V}_{wind}$ includes the freestream velocity components and velocity components due to movement of the grid, $\vec{V}_{wi}$ is the induced velocity by all the wake filaments and bound vorticity from other blades.

If $\vec{V}_n$ is a negative value, so is λ_2, therefore inflow condition is applied. In this case, if the value of λ_1 is also negative, all the information comes from the free stream. If λ_1 value is positive, one piece of information comes from the interior and others come from the free stream.

If $\vec{V}_n$ is a positive value, so is λ_1, then outflow condition is applied. In such a case, if the value of λ_2 is positive, all the information comes from the interior. If the value of λ_2 is negative, one piece of information comes from the free stream and others come from the interior of the domain. Detailed computation of flow properties may be found in Reference [92].

2.6 Computational Grid

The computational grid used in GT-Hybrid is based on C-H grid topology. The baseline grid has 131*75*65 nodes in chordwise, spanwise and normal directions, respectively. The blade surface has 91 chordwise points and 50 spanwise points. The far field boundary is located about nine chord lengths away from the blade surface. The normal grid spacing at the blade surface is about 1*10^-5c, where c is the reference chord length. This grid spacing corresponds to a y^+ of $O(1)$ for all the flight conditions tested in this study. The y^+ values for all the flight conditions are specified in Table 4.1. The grid is clustered near the tip and near the leading and trailing edges to handle regions of high

gradients. Grid sensitivity studies are performed in the next chapter. Figure 2.5 shows the computational grid used in the current study.

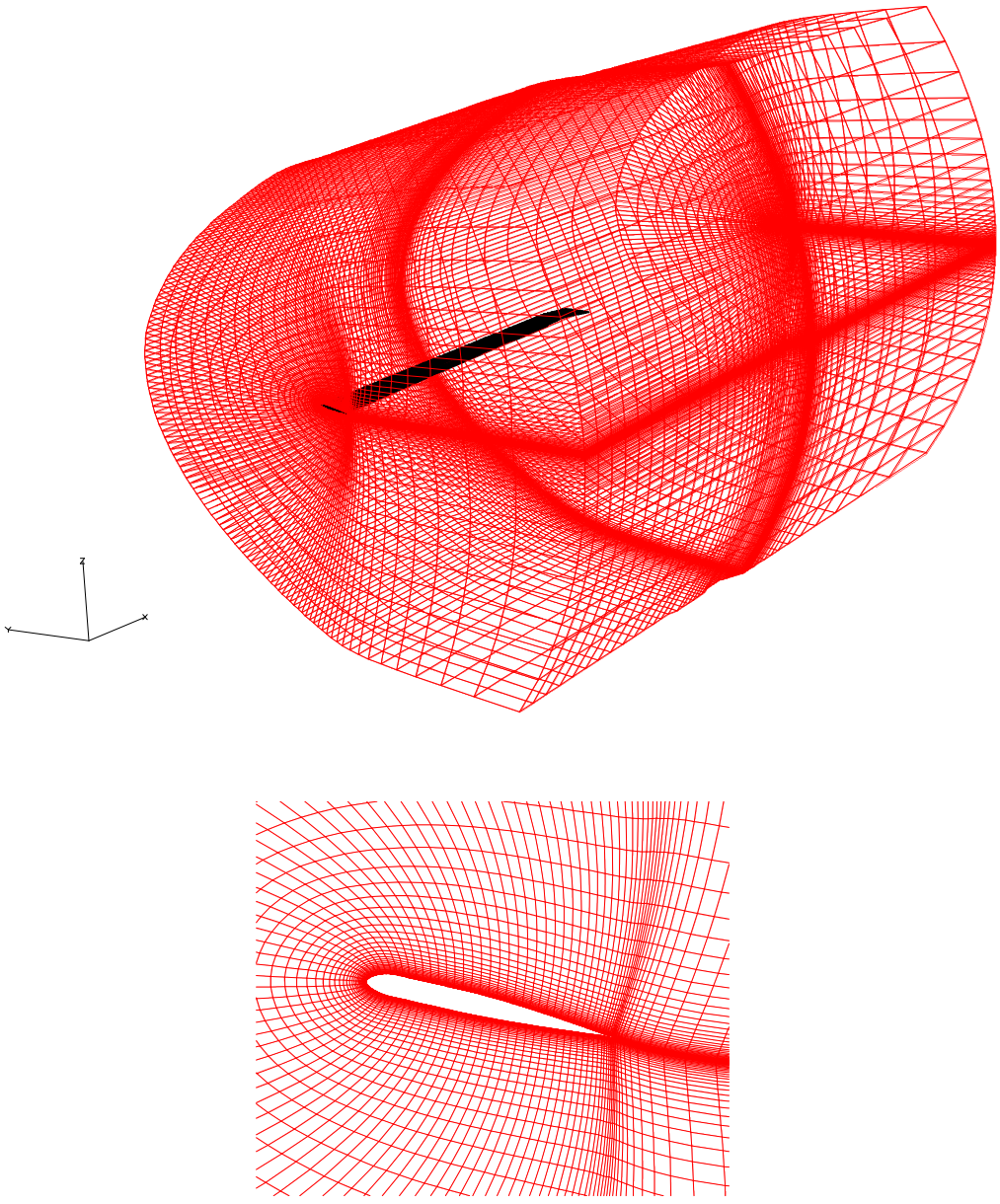

Figure 2.5 Baseline computational grid

2.7 Grid Deformation

Rotor blades are long, slender and flexible. This makes them extremely susceptible to structural deflections and deformations with three degrees of freedom. To compute the airloads on a rotor blade, the CFD methodology needs to account for these deformations. These deformations are applied to the computational grid using the methodology specified in this section.

The blade motions obtained from the CSD analysis includes linear (Δx, Δy, Δz) and rotational deformations ($\Delta\phi$, $\Delta\theta$, $\Delta\psi$). These deformations are written out as a function of azimuth and radial station. These blade motions are interpolated using a bi-linear interpolation scheme from CSD to CFD radial stations and to intermediate azimuthal points to match the CFD azimuthal time step. The rotational deformation is applied to the initial un-deformed grid following x-y-z sequence of the Euler angle rotation around the reference point as follows.

$$\begin{bmatrix} x \\ y \\ z \end{bmatrix}_r = L_r \left[\begin{bmatrix} x \\ y \\ z \end{bmatrix}_{initial} - \begin{bmatrix} x \\ y \\ z \end{bmatrix}_{ref} \right]$$

$$L_r = L_3(-\Delta\psi)L_2(-\Delta\theta)L_1(-\Delta\phi) \tag{2.74}$$

$$= \begin{bmatrix} CS \cdot CT & -SS \cdot CF + ST \cdot CS \cdot SF & SS \cdot SF + ST \cdot CS \cdot CF \\ SS \cdot CT & CS \cdot CF + SS \cdot ST \cdot SF & -CS \cdot SF + SS \cdot ST \cdot CF \\ -ST & CT \cdot SF & CT \cdot CF \end{bmatrix}$$

Where:

$$CS = \cos(\Delta\psi), CT = \cos(\Delta\theta), CF = \cos(\Delta\phi)$$
$$SS = \sin(\Delta\psi), ST = \sin(\Delta\theta), SF = \sin(\Delta\phi) \tag{2.75}$$

Here, $[x \quad y \quad z]^T_{initial}$ is the initial grid coordinates placed at 0 degree azimuth without pre-cone, elastic deformation, flapping and pitch control input, but with built-in

twist angle. The point, $[x \quad y \quad z]^T_{ref}$, is the reference point, where the deformations were obtained after interpolation. Note that the expression above represents rotation applied to the grid point with positive $\Delta\phi$, $\Delta\theta$, and $\Delta\psi$ angles. Thus, the angles in the rotational matrixes (L_1, L_2, L_3) for the axis have negative sign. The final grid at the desired azimuthal angle is then obtained after applying linear transformation, pre-cone angle and rotation to the azimuthal location as follows.

$$\begin{bmatrix} x \\ y \\ z \end{bmatrix} = L_{IB}\left[\begin{bmatrix} x \\ y \\ z \end{bmatrix}_r + \begin{bmatrix} x \\ y \\ z \end{bmatrix}_{ref} + \begin{bmatrix} \Delta x \\ \Delta y \\ \Delta z \end{bmatrix}\right]$$

$$L_{IB} = L_3(-\Psi)L_2(\theta_p) \tag{2.76}$$

$$= \begin{bmatrix} \cos\Psi\cos\theta_p & -\sin\Psi & -\cos\Psi\sin\theta_p \\ \sin\Psi\cos\theta_p & \cos\Psi & -\sin\Psi\sin\theta_p \\ \sin\theta_p & 0 & \cos\theta_p \end{bmatrix}$$

Where, Ψ is the azimuthal angle (+, counterclockwise from top view), and θ_p is the pre-cone angle (+, flap up). Again, note that the angles in the rotational matrixes have the opposite sign of the grid rotation. The positive pre-cone angle is defined as flap-up direction, which is the opposite of the right hand rule. Thus, its sign in the rotational matrix is positive.

The grid deformation may be gradually reduced from the blade surface to the outer boundary of the computational domain using a decay function, so that the outer boundary is remained un-deformed. However, deformations observed in this study were small, and the same deformations have been applied at a radial location throughout the constant spanwise plane.

2.8 CSD Methodology

DYMORE is a computational structural dynamics (CSD) solver used in this study. It is a multi-body finite element code for arbitrary non-linear elastic systems. The multi-body models are constructed by piecing together basic structural elements, the data for these elements are stored within an element library. Each of these elements has its own system of equations which when pieced together create larger and more complex equations.

DYMORE belongs to a class of solvers known as rotorcraft comprehensive codes which can perform a fully trimmed aeroelastic simulation of an isolated rotor configuration. This is accomplished by integration of structural, aerodynamic and trimming algorithms in a modular fashion. The structural module includes a library of elements from which models with arbitrarily complex topologies can be built. The element library includes rigid bodies, cables, composite capable beams and shells and joint models which can include generic spring and/or damper elements. Deformable bodies are modeled using the finite element method. The formulation of beams is geometrically exact i.e. arbitrarily large displacements and finite rotations are accounted for, but is limited to small strains. The equations of equilibrium are written in a Cartesian inertial frame. Constraints are modeled using the Lagrange multiplier technique, resulting in a system of differential/algebraic equations (DAE). These equations are then solved using a robust and efficient time integration algorithm. The theory and complete list of features in DYMORE are available in References [92-94]. DYMORE includes several simplified aerodynamics models to approximately predict the state of the rotor flow-field. A dynamic wake model is used for predicting rotor inflow. This inflow model is not as

accurate as a free wake model, but it does provide an averaged inflow distribution. The 2-D models within the original codes are approximate and are not able to handle all of the possible physical phenomena associated with rotor aerodynamics, but DYMORE provides options to include external airloads. This option enables the coupling of DYMORE with a CFD solver which can capture additional physical features that are not predicted using simplified aerodynamics. The development and validation of different types of coupling between DYMORE and GT-Hybrid for rotors in forward flight is one of the main highlights of this thesis and is explained in detail in the following chapters. Trim analysis is accomplished using DYMORE's internal auto pilot trim analysis. The auto pilot algorithm evaluates a trim Jacobian matrix and adjusts the blade collective and cyclic control to achieve the target rotor hub loads. This trimming methodology is restricted to CFD/CSD loose coupling because it is not computationally feasible for the tight coupling method.

CHAPTER 3

ENHANCEMENTS TO HYBRID CFD METHODOLOGY

This chapter enumerates all the enhancements made to the hybrid CFD methodology to improve the aerodynamic modeling of rotors in forward flight. These enhancements include improvements to the wake model, implementation of higher order spatial and temporal schemes in the Navier-Stokes methodology and parallelization of the CFD methodology.

3.1 Vorticity Core Modeling

Although the wake models are based on potential flow theory, the formation of wake behind any lifting surface must be considered as a viscous phenomenon. Therefore, we need to include semi-empirical models for the vortex core structure and core growth. BVI predictions are extremely sensitive to these empirical models. Several vortex core models have been researched in literature [95-97]. The simplest model for the swirl velocity inside a viscous vortex with a finite core is due to Rankine [96]. This model exhibits the key features of a viscous core, i.e. a solid-body like rotation near the vortex center and free vortex away from the center. It can be inferred from Figure 3.1 that Rankine core model exhibits a discontinuous velocity profile at the vortex core boundary. Among the velocity profiles seen for different core models, the Vatistas model [98,99] exhibits a smooth distribution and was found to provide the best agreement with experimental results [101]. Therefore this model was chosen for implementation in GT-Hybrid solver. The velocity $\bar{V}$ induced by a vortex with a Vatistas core model is given by Eqn. (3.1)

$$\vec{V} = \frac{\Gamma}{4\pi} \frac{\vec{r}_1 \times \vec{r}_2}{\left(\left| \vec{r}_1 \times \vec{r}_2 \right|^{2n} + \left(r_c r_0 \right)^{2n} \right)^{1/n}} \left[\vec{r}_0 \cdot \left(\frac{\vec{r}_1}{r_1} - \frac{\vec{r}_2}{r_2} \right) \right] \tag{3.1}$$

where n = 2 for Vatistas type core, Γ is circulation, $\vec{r_1}, \vec{r_2}$ are position vectors of the wake segment, $\vec{r_0}$ is the position vector of the point where the induced velocity is computed and $\vec{r_c}$ is viscous core radius.

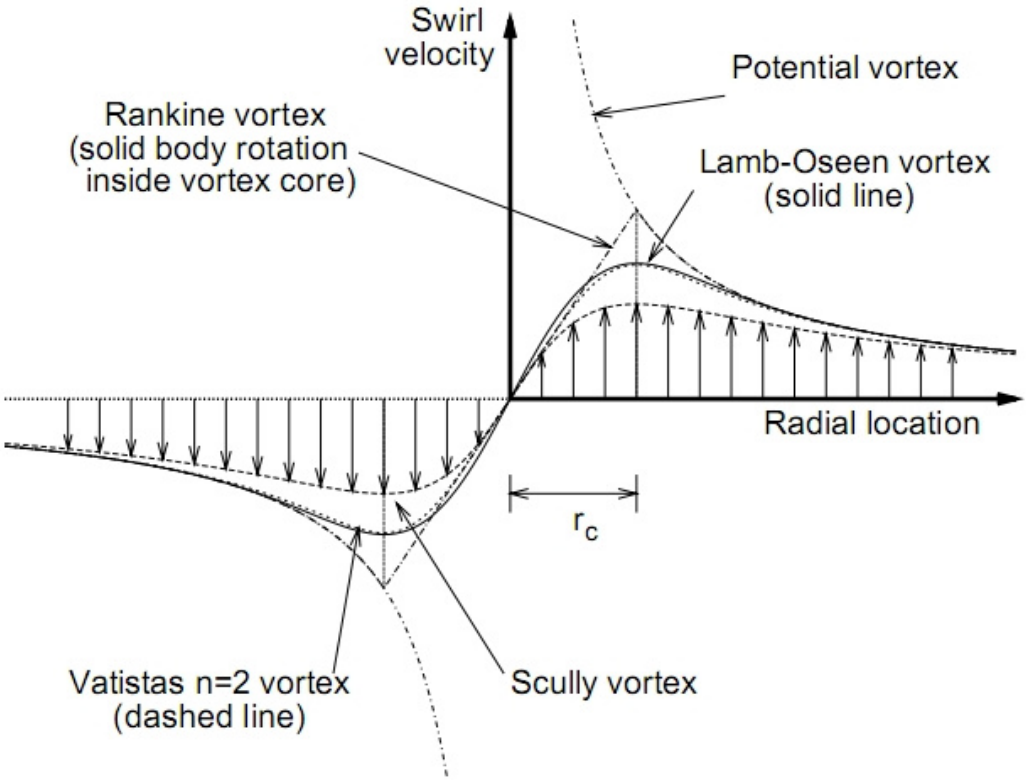

Figure 3.1 Viscous core velocity profiles, Ref. [101]

The viscous core model also needs to account for the diffusive growth of its core. In the Bhagwat – Leishman [101] core growth model, the viscous core growth was

modeled using an extension of the classic Lamb-Oseen model for the diffusion of laminar vortices. Turbulence in the tip vortex affects the diffusion of vorticity, and these effects were incorporated using an empirically validated correction for the average apparent or "eddy" viscosity. The vortex induced velocity profiles measured in experiments were found to exhibit strong self-similarity when using the vortex core radius as a length-scale, suggesting that a generalized model is possible. This model accounts for the effect of both laminar and turbulent viscosities on viscous core growth. The model was compared with velocity field measurements for both fixed-wing and rotating-wing tip vortices, with good agreement [101]. The analytical expression for the core growth is shown in Eqn.(3.2).

$$r_c = \sqrt{4\alpha\delta\nu\left(\frac{z+z_0}{V_\infty}\right)} \qquad (3.2)$$
$$\delta = 1 + a_1 \mathrm{Re}_\nu$$

where $\vec{r_c}$ is viscous core radius, a_1 and α are empirical parameters,V_∞ is freestream velocity.

3.2 Full Span Wake Model (FSWM)

The wake model described in the previous chapter assumes a single concentrated tip vortex trailing from a region near the blade tip. The model assumes that all inboard wake is either weak or coalesces into the tip vortex immediately that the effect of inboard wake can be easily ignored. This assumption would be appropriate for high speed flight but would be physically less accurate for rotors in low speed forward and descent flight since location and strength of the inboard vortices are critical for predicting blade vortex

interaction (BVI) phenomena. A full-span wake model (FSWM) was implemented in GT-Hybrid solver as an alternative to the tip vortex model to address this issue. The FSWM is based on Prandtl's lifting-line theory [102]. For a three dimensional blade, the bound vorticity, located at quarter chord line of the blade is trailed into the wake from the blade tip and root. Vorticity is also shed from the blade mid-span regions because of radial changes in the bound circulation. Therefore the single tip vortex is replaced by user specified number of multiple vortex segments trailed from all the blades. The trailers are equally distributed along the blade span. The strength of the vortex elements is based on radial gradient of bound circulation and number of wake trailers chosen by the user. The vorticity strength of first wake element of trailer n at any azimuthal position Ψ is given by Eqn. (3.3)

$$\Gamma_{tr}(\Psi, n) = \Gamma(\Psi, n+1) - \Gamma(\Psi, n) \tag{3.3}$$

Figure 3.2 shows the orthographic projections of the rotor wake geometry generated using the FSWM for the UH-60A rotor in forward flight. The distorted wake was modeled using 15 trailers. The x-z plane projection shows the convection of the rotor wake downwards due to a forward shaft tilt of the rotor which causes an effective downward velocity when added to the rotor inflow. The y-z plane projection shows the roll-up of vortices as they are convected away from the rotor disk. The x-y plane projection is a top view of the wake geometry. The wake geometry undergoes distortion at far wake as it evolves from a smooth helical structure near the blade surface because of the effect of self induced velocity components and change in circulation for each wake segment. The FSWM uses the viscous core growth models specified in the previous section. The use of FSWM significantly increases computational time since the

calculation of wake geometries scale approximately as n^2 where n is the number of wake trailers. The effect of the FSWM on airloads predictions will be addressed in the next chapter.

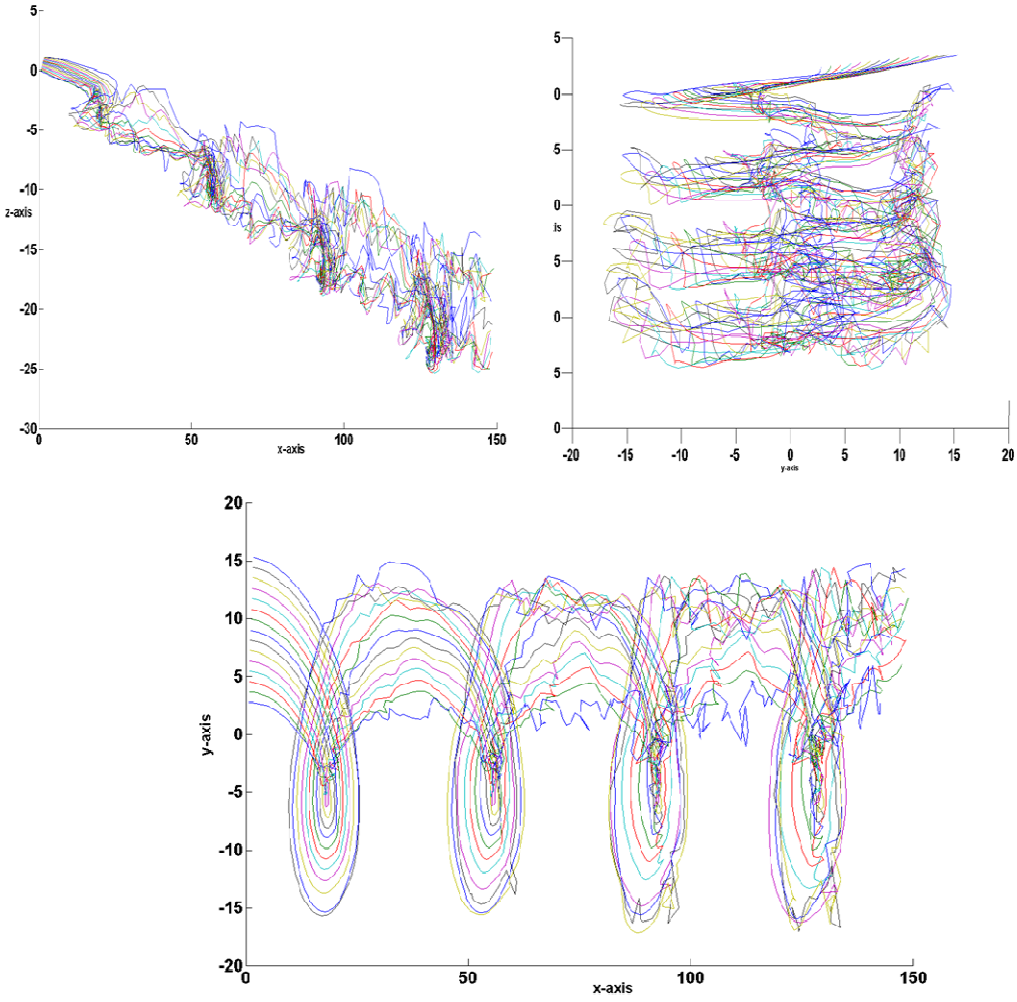

Figure 3.2 FSWM geometry for UH-60A rotor

3.3 Shed Wake model

The FSWM system of vortices described in the previous section does not include the wake shed due to temporal change in bound vorticity strength. According to Kelvin's

theorem [102], the circulation around a closed curve (which encloses the same fluid elements) moving with the fluid remains constant with time. This means a counter-rotating vortex is shed equal in magnitude to the change in bound circulation. This additional wake is modeled through a shed wake model. The wake system behind a blade is shown in Figure 3.3. The effect of the shed wake on the source blade is adequately captured by the Navier-Stokes solution but its effect on adjacent blades needs to be modeled. The vorticity strength of wake element shed between trailer n and n+1 at azimuthal Ψ is given by Eqn. (3.4).

$$\Gamma_{sh}(\Psi, n) = \Gamma(\Psi, n) - \Gamma(\Psi - \Delta\Psi, n) \tag{3.4}$$

Even though wake is shed continuously, new shed wake elements are created only at periodic azimuthal intervals for computational efficiency. The viscous core growth for shed wake elements is modeled in the same way as for the trailed wake elements. The effect of the shed wake model on airloads predictions will be addressed in the next chapter.

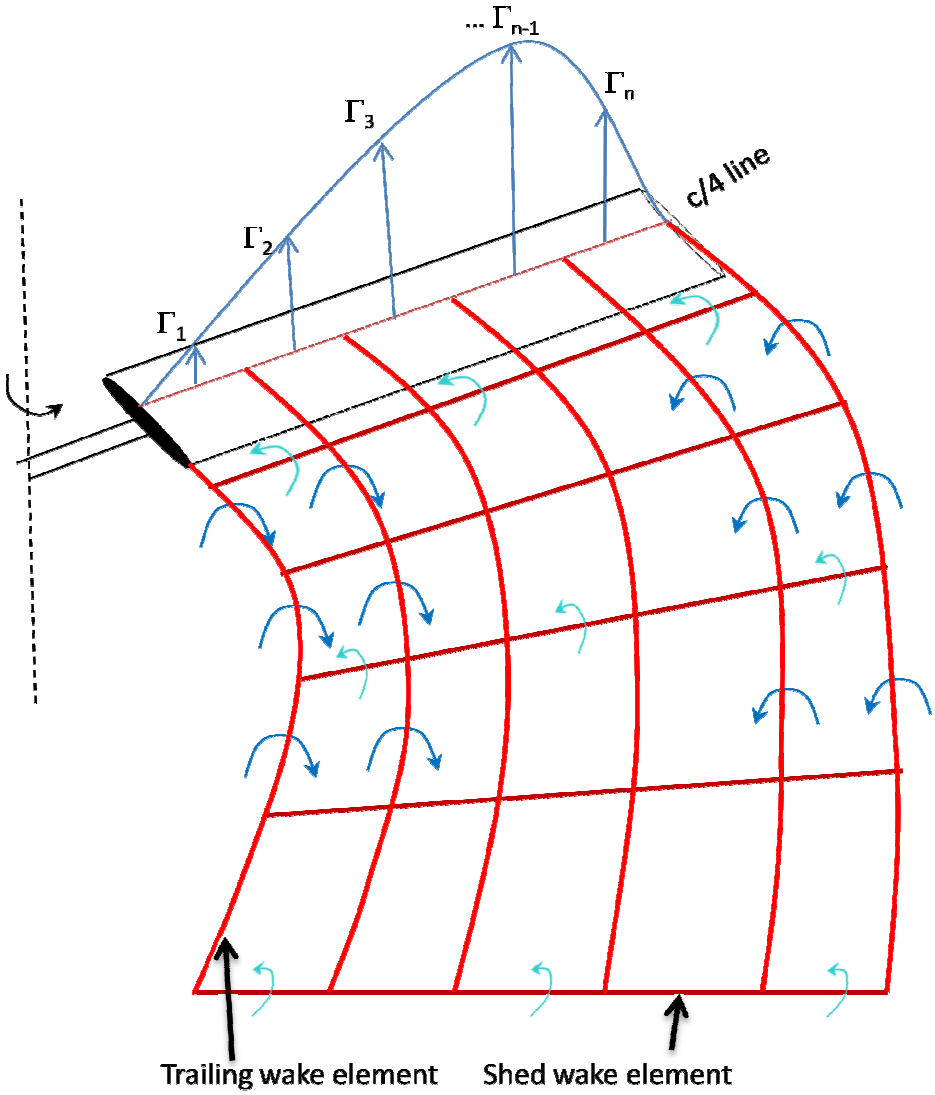

Figure 3.3 Schematic of a wake system behind rotor blade

3.4 Parallelization of CFD methodology

One of the primary advantages of using a hybrid methodology based CFD solver for rotor aerodynamic modeling is its fast turnaround time. This turnaround time decreases even more significantly with solver parallelization. Parallelization helps in utilization of additional computing resources available in the form of high performance clusters and multi-core processors. GT-Hybrid was parallelized based on the single

program multiple data (SPMD) approach where multiple autonomous processors simultaneously execute the same program at independent points, rather than in the lockstep that a single instruction multiple data (SIMD) approach imposes on different data. The data communication routines were coded using FORTRAN libraries that conform to Message Passing Interface (MPI) standard [103]. MPI is highly portable and provides a gamut of functionality using 115 routines. A lot of open source MPI implementations like MPICH are available for testing the parallelization.

A schematic of the blade spanwise parallelization is shown in Figure 3.4. The parallelization is based on peer communication method where all nodes are given equal processor time for the main computation but one processor denoted the master handles some serial processes too. When the solver is executed, the number of spanwise grid points is divided by the number of processors available for the execution. This gives the number of computational zones that will be executed simultaneously. The input variables are broadcast to all the processors from the master whereas each grid zone is communicated to the corresponding node and time simulations are initiated. The RANS simulations are carried out independently on each node with communication of flow variables at the zonal interface every time step. The number of grid points for which flow information needs to be exchanged depends on the chosen spatial accuracy of the solver. The interface communication happens in such a way that initially the processors with odd index send data and processors with even index receive them followed by even index processors sending data to the processors with odd index. This method prevents communication deadlocks which can occur if all processors try to send data simultaneously. The flow variables from all the nodes are communicated to the master at

specified intervals to compute the blade airloads. The wake model is executed in serial mode on the master, while the computation of induced velocity components on the computational boundary is parallelized. The parallelization routines are generic and platform independent and have been tested on both Windows and Linux machines.

Figure 3.5 shows the observed speedup based on simulations on a Linux based 2.2GHz AMD Opteron cluster with 1GB of physical memory available for each processor. The solver was tested multiple times on varying number of processors starting from 1 to 12. The baseline computational grid (131*75*65) was used in these tests. The wake model is serially executed and was excluded from the benchmarks. The physical tests are compared with the theoretical curve to assess the parallelization speedup. The observed values follows the theoretical curve as execution moves from serial to parallel mode till about six processors. A gradual decrease in parallelization efficiency is observed beyond six processors. The solver was observed to be ten times faster when it was executed in parallel on 12 processors. The first half of the curve indicates a good degree of parallelization. But this trend starts moderating since the MPI communication and serial data output time becomes comparable to the actual run time of the process. This communication overhead starts negating improvement in turnaround time and loss of parallelization efficiency is observed.

The number of spanwise grid points limits the number of processors that can be used for parallel execution to maintain the spatial and temporal accuracy of the solver. Since the solver can be run for multiple blade and coaxial rotor configurations, it will be useful to implement additional levels of parallelism to achieve faster turnaround times. Therefore a hierarchical MPI parallelization method is implemented to utilize the nested

parallelism in multi-rotor/blade configurations. An organizational chart of a hierarchical parallelization method can be seen in Figure 3.6. This method uses the configuration topology to allocate processors to each rotor/blade. In a hybrid CFD methodology, the wake information is not required by all the processors which means the communication modules are heterogeneous. Therefore the hierarchical parallelization method uses multiple communicators to address unique communication requirements between rotors and blades rather than using a generic multi-block communication. This communication paradigm ensures that data is transferred only between processors handling the relevant zones therefore reducing the communication overhead. Since the parallelized blocks are identical, load balancing is implicitly achieved ensuring maximum efficiency. The parallelization is automatic based on the rotor configuration and number of processors used. The number of processors that can be used for solver execution is restricted to an integral multiple of number of rotors and blades.

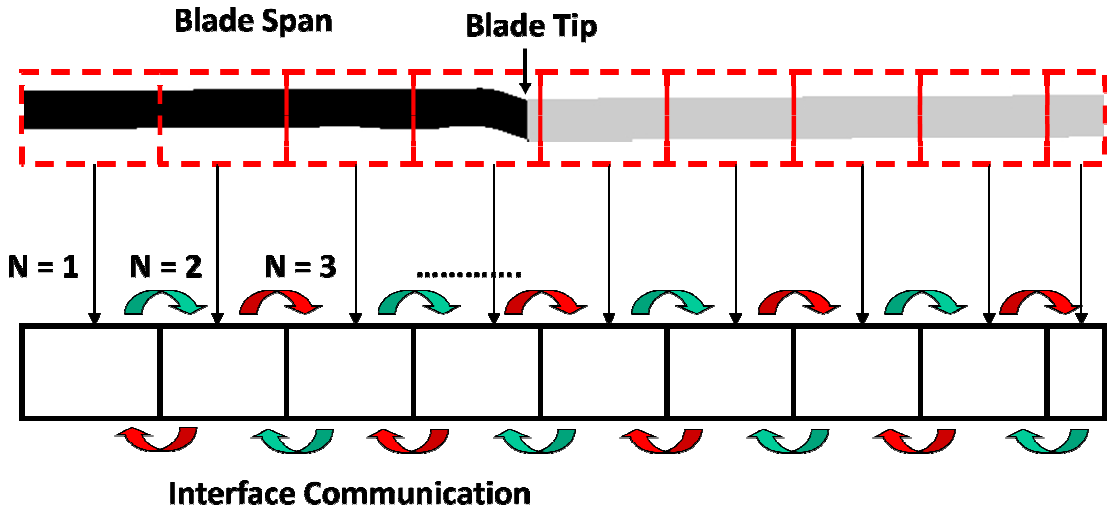

Figure 3.4 Schematic of blade spanwise parallelization

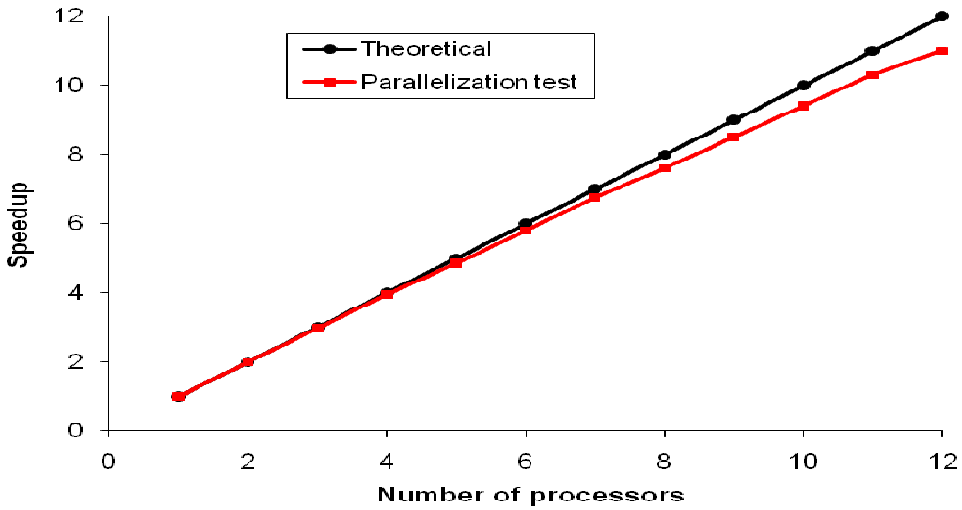

Figure 3.5 Parallelization benchmark results

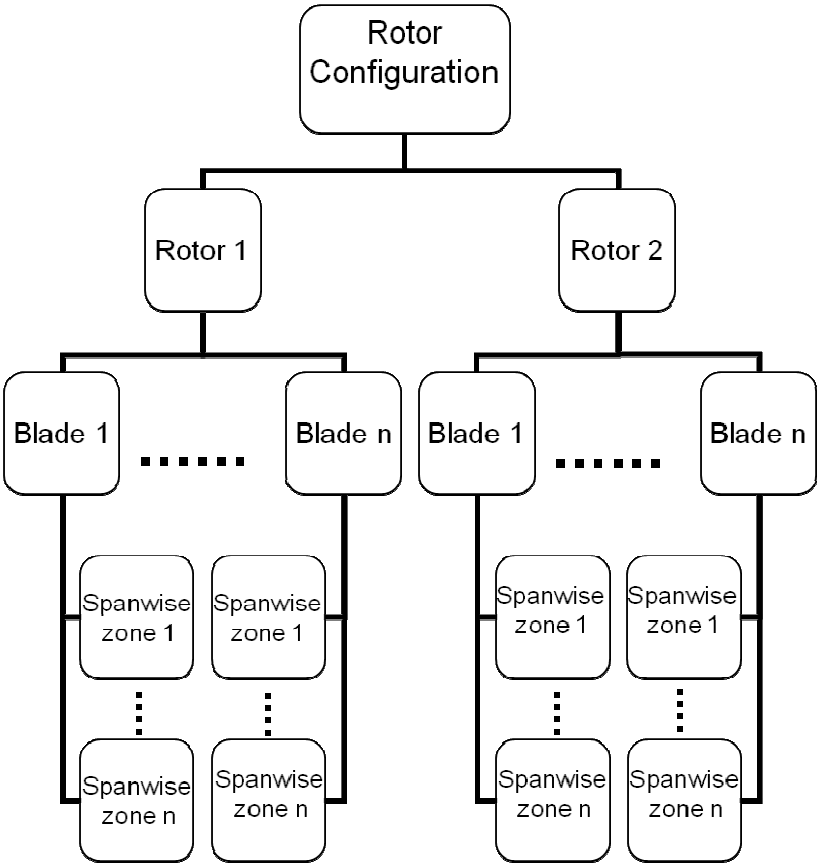

Figure 3.6 Hierarchical MPI Parallelization

3.5 Geometric Conservation Law (GCL)

The geometric conservation law (GCL) is used to satisfy the conservative relations of the surfaces and volumes of the control cells. In moving meshes, the GCL states that the volumetric increment of a moving cell must be equal to the sum of the changes along the surfaces that enclose the volume. Thomas and Lombard [104] formulated the differential form of the geometric conservation law. The GCL terms can be identified from the differential form of the Navier-Stokes equations in generalized coordinates.

Eqn. (3.5) gives the differential form of the Navier Stokes equations.

$$\frac{\partial VQ}{\partial t}+\frac{\partial \hat{F}}{\partial \xi}+\frac{\partial \hat{G}}{\partial \eta}+\frac{\partial \hat{H}}{\partial \zeta}=\frac{M}{Re}\left[\frac{\partial \hat{R}}{\partial \xi}+\frac{\partial \hat{S}}{\partial \eta}+\frac{\partial T}{\partial \zeta}\right] \tag{3.5}$$

Where V is the cell volume

$$V=\frac{1}{J}$$

This can be expressed as

$$\frac{V\partial Q}{\partial t}+\frac{Q\partial V}{\partial t}+\frac{\partial \hat{F}}{\partial \xi}+\frac{\partial \hat{G}}{\partial \eta}+\frac{\partial \hat{H}}{\partial \zeta}=\frac{M}{Re}\left[\frac{\partial \hat{R}}{\partial \xi}+\frac{\partial \hat{S}}{\partial \eta}+\frac{\partial T}{\partial \zeta}\right] \tag{3.6}$$

The term $Q\frac{\partial V}{\partial t}$ is known as the GCL term and can be expressed in term of generalized coordinates as

$$Q\frac{\partial V}{\partial t}=-Q[\frac{\partial}{\partial \xi}\left(\frac{\xi_t}{J}\right)+\frac{\partial}{\partial \eta}\left(\frac{\eta_t}{J}\right)+\frac{\partial}{\partial \zeta}\left(\frac{\zeta_t}{J}\right)]$$

The refined governing equation accounting for GCL term becomes

$$\frac{1}{\mathrm{J}}\frac{\partial Q}{\partial \mathrm{t}}+\frac{\partial F}{\partial \xi}+\frac{\partial G}{\partial \eta}+\frac{\partial G}{\partial \zeta}=\frac{\partial R}{\partial \xi}+\frac{\partial S}{\partial \eta}+\frac{\partial T}{\partial \zeta}+\mathrm{RHS_{GCL}}$$

where

$$\mathrm{RHS_{GCL}}=\ Q[\frac{\partial}{\partial \xi}\left(\frac{\xi_t}{J}\right)+\frac{\partial}{\partial \eta}\left(\frac{\eta_t}{J}\right)+\frac{\partial}{\partial \zeta}\left(\frac{\zeta_t}{J}\right)]$$

The significance of satisfying GCL in moving grid computations is illustrated in the next chapter.

3.6 Second Order Time Accuracy

GT-Hybrid uses an implicit two point backward difference scheme to advance the solution in time. This scheme is only first order in time. To assess the effects of temporal differencing scheme on the solutions, the analysis was enhanced with a 2nd order accurate time marching scheme, with Newton sub-iterations. The governing equation in implicit form is given as follows:

$$\left[\frac{(1+\phi)}{J\Delta t}I+\delta_\xi A+\delta_\eta B+\delta_\zeta C\right]\Delta Q^m=\frac{\phi\Delta Q^{n-1}}{J^{n-1}\Delta t}-\frac{(1+\phi)\left(Q^m-Q^n\right)}{J\Delta t}+R\left(Q^m\right) \tag{3.7}$$

Where:

$$\begin{aligned}
&\Delta Q^m=Q^{m+1}-Q^m\\
&\Delta Q^{n-1}=Q^n-Q^{n-1}\\
&A=\frac{\partial E}{\partial Q},B=\frac{\partial F}{\partial Q},C=\frac{\partial G}{\partial Q}\\
&R\left(Q^m\right)=RHS_{GCL}^m+RHS^m
\end{aligned} \tag{3.8}$$

If ϕ is 0, the discretization is 1st order in time, and if ϕ is 0.5, it becomes 2nd order accurate in time. The superscript *m* indicates the sub-iteration level. Use of Newton sub-iterations improves convergence and stability at the expense of computer time, because of the need to recompute the residual on the right hand side once every iteration.

3.7 Fifth Order Spatial Accuracy

A fifth order spatially accurate ENO based interpolation scheme [105]-[107] was implemented in GT-Hybrid solver. TVD formulations like MUSCL scheme described in the previous chapter automatically reduce to first order accuracy near the extrema of the solution. TVD formulations are based on limiting the fluxes near such extremes. ENO formulation is based on interpolating "smartly" i.e. use an adaptive stencil of points being sampled for the interpolation based on some measure of smoothness. Thus the methodology is less restrictive than TVD schemes and global higher order accuracy can be achieved. The central idea behind the ENO schemes is to avoid sampling across a discontinuity by shifting the stencil dynamically with the solution. Therefore a 5^{th} order stencil for flux computation at node $i + \frac{1}{2}$ can involve a combination of points starting from $i - 4$ to $i + 5$. Figure 3.7 illustrates a stencil that is part of all possible combinations of stencils that can be used. The numerical formulation for this scheme is available in reference [108]. This scheme uses significantly more computational resources than the MUSCL scheme since the correct stencil has to be chosen at each grid point.

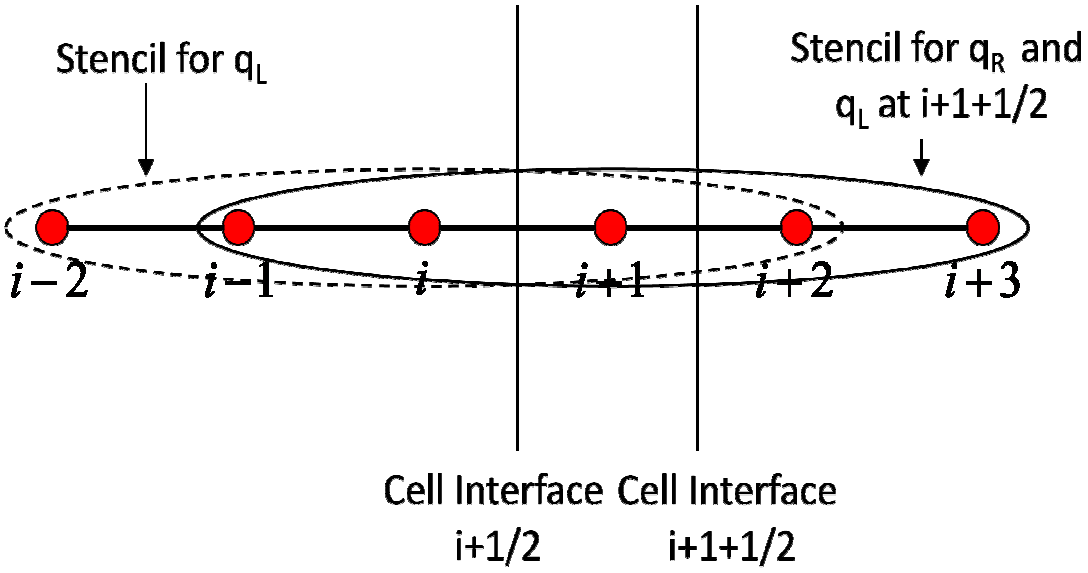

Figure 3.7 Schematic of a typical stencil for 5th order ENO scheme

CHAPTER 4

CFD VALIDATION STUDIES

In this chapter, GT-Hybrid CFD solver is validated and its enhancements are evaluated before the CFD/CSD coupling analysis is attempted. This chapter is divided into two main sections – 2-D airfoil studies and 3-D rotor CFD analysis using blade motions obtained from OVERFLOW/CAMRADII loose coupling.

4.1 2-D Airfoil Studies

4.1.1 RAE 2822 Airfoil

It is customary to present a 2-D test case with pressure coefficient validation before testing a CFD solver for 3-D cases. The test case chosen was that of the RAE 2822 airfoil as measured pressure distribution for SC1095 airfoil (found in the UH-60A rotor) was unavailable in literature. The data from pressure measurement for this case is from the AGARD test data base [109]. This test case is the accepted standard for CFD research code validation. The freestream Mach number is 0.729, at a Reynolds number of 6.5 million, and an angle of attack 2.31°. Figure 4.1 shows the C-type grid used for the computations. Airfoil studies in GT-Hybrid are not performed using 2-D grids; rather a 3-D grid with five identical spanwise planes (3^{rd} order spatial scheme) is created. The mid-span plane is used for the analysis and flow-field information from this plane is copied to the other planes. Figure 4.2 shows the plot of C_p vs. chord location on the airfoil. The salient features of the pressure field including the shock location are well captured. The lower surface pressure coefficient prediction shows excellent correlation with the

experimental data. The leading edge suction peak magnitude and location is well captured by both the turbulence models. The shock is predicted to occur slightly closer to the leading edge than that observed from measurements. This behavior is observed for both the turbulence models and can be attributed to the grid density. Adaptive or embedded grids may be required to precisely capture the shock location. Figure 4.3 shows the variation of skin friction coefficient along the chord line. The results from the validation studies match well with test data for both turbulence models.

4.1.2 NACA 0012 Airfoil

The hybrid CFD methodology was validated for an oscillating NACA 0012 airfoil. This validation is required for application of solver to rotor studies in high thrust conditions where dynamic stall is an observed phenomenon. The grid system used for the study is shown in Figure 4.4. The loads predictions are compared with experimental data by McAlister et al. [110]. The flow Mach number was 0.28 and Reynolds number was 3.52 million. The reduced frequency is 0.1. The airfoil angle of attack varies with time as:

$$\alpha = 14.8^{\circ} + 9.8^{\circ} \sin\left(2kM_{\infty}t + \frac{3}{2}\pi\right) \tag{4.1}$$

Lift and moment stall is seen to occur in regions of higher angle of attack. The predictions compare well with test data. The maximum lift, moment and drag is slightly over-predicted but the overall hysteresis loops match well with test data. KES shows marginally better peak values of lift than SA-DES.

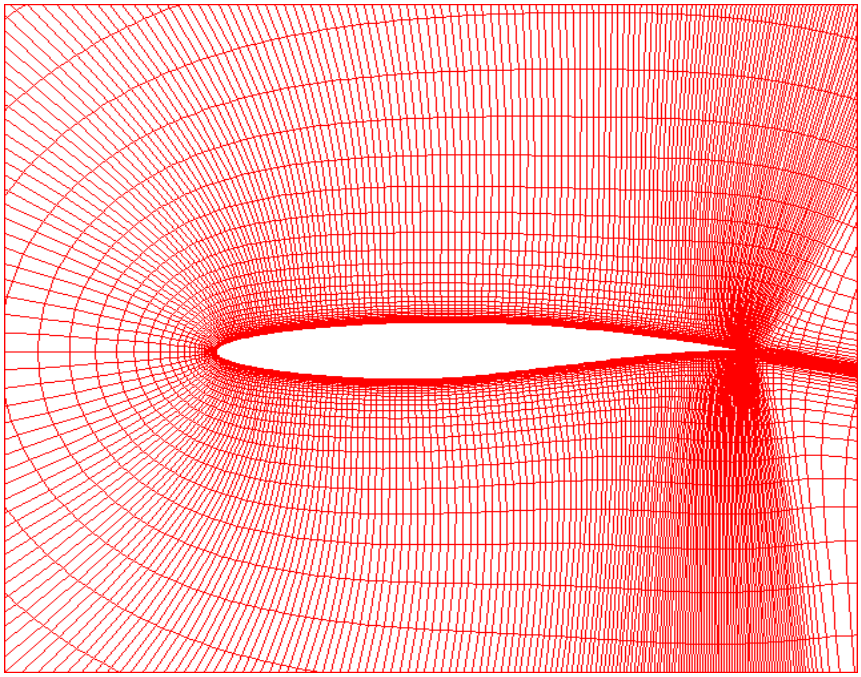

Figure 4.1 RAE 2822 computational grid [439*5*75]

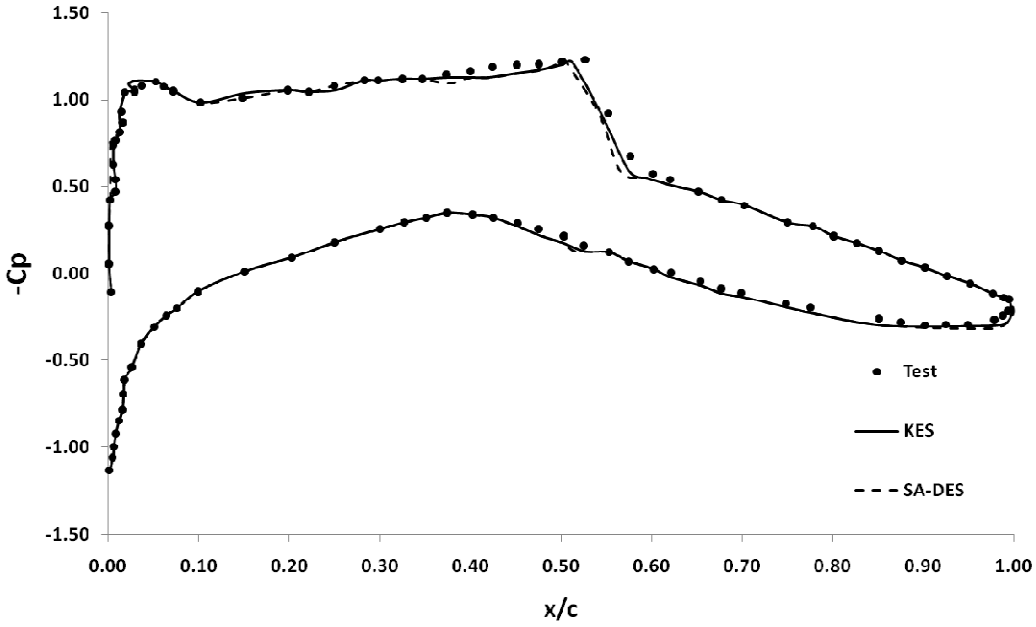

Figure 4.2 Surface C_p for RAE 2822 airfoil

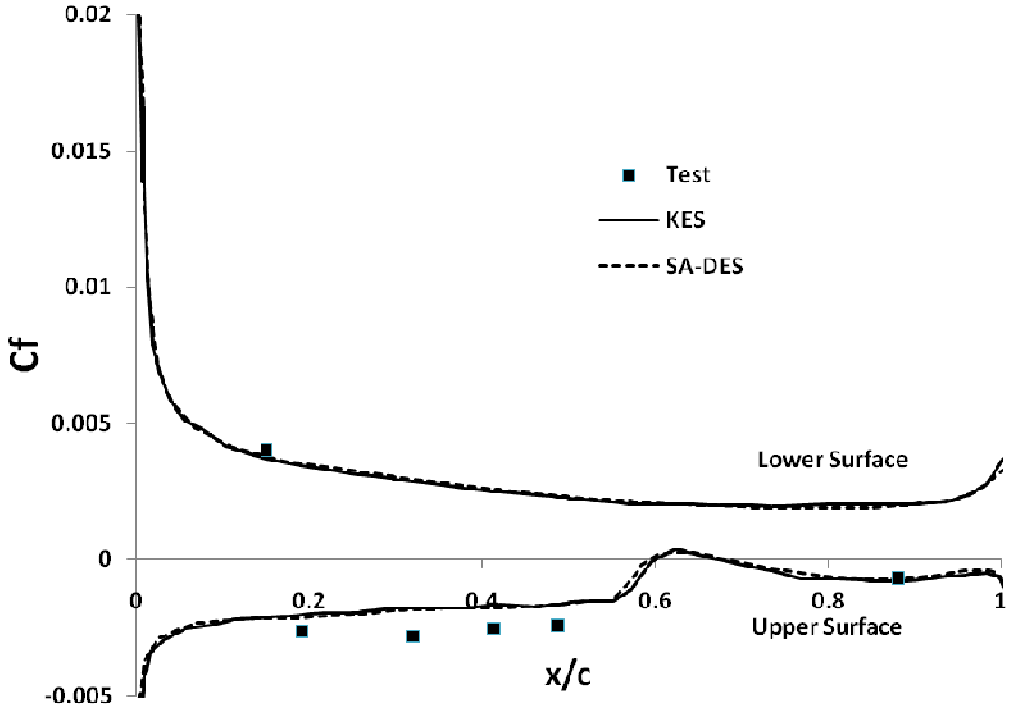

Figure 4.3 Surface C_f for RAE 2822 airfoil

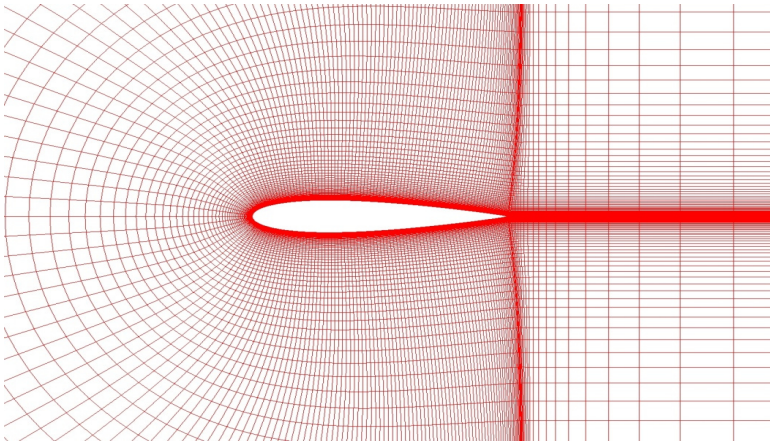

Figure 4.4 NACA0012 grid (257*5*129)

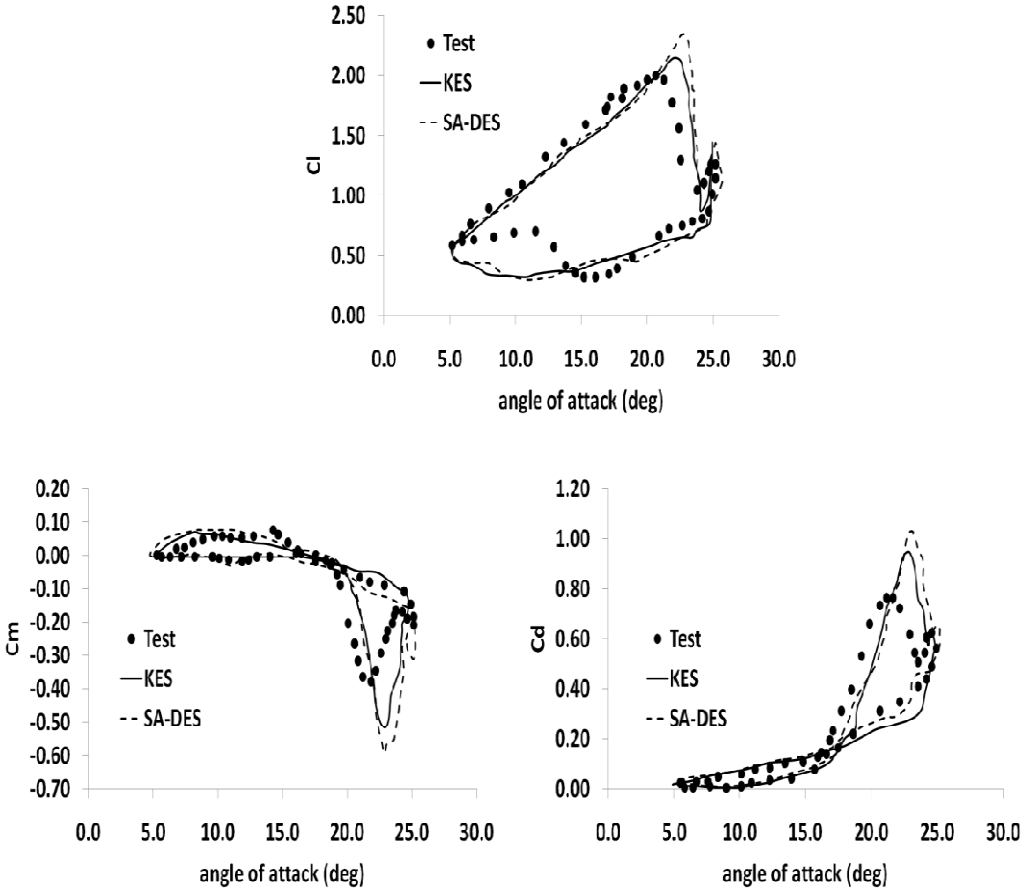

Figure 4.5 NACA0012 loads and moments in dynamic stall

4.2 Effect of GCL

The significance of the Geometric Conservation Law (GCL) was explained in section 3.5. The effect of satisfying the GCL can be illustrated by performing a CFD simulation using a grid without a physical surface that undergoes temporal change in cell volumes. This temporal change is effected through angular rotation of the grid in space and application of blade deflections and deformations. Figure 4.6 show the computational domain colored by density variation on the inflow boundary. The results are obtained in hovering conditions with $M_{tip} = 0.63$. The computational domain does not have a physical surface therefore theoretically; the absence of an object should preserve an unperturbed flow-field. The density surfaces should represent a uniform field with magnitude equal to the free stream condition value. When the GCL is not applied to the governing equation, a non-physical increase in density is seen on the outer boundary indicating an erroneous accumulation of mass. Since the volumes are not conserved when the cells are deformed, artificial sources and sinks are created. This mass disappears once the GCL term is computed indicating that Geometric Conservation Law has to be applied implicitly or explicitly in computations involving moving grids.

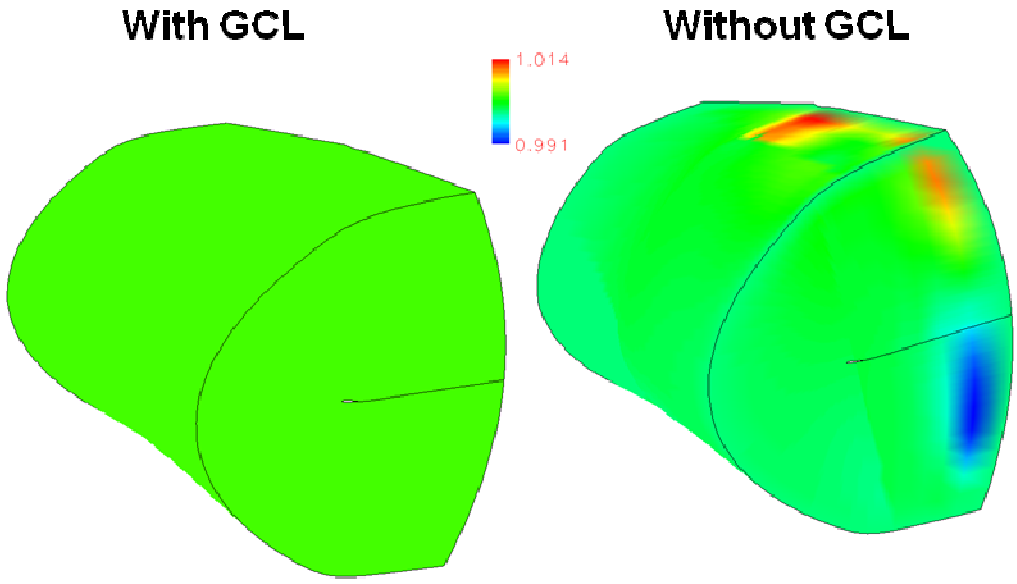

Figure 4.6 Density variation on far field boundary (no physical body)

4.3 UH-60A Rotor: 3-D CFD Studies using Prescribed Blade Motions

The hybrid CFD methodology needs to be validated independently for a trimmed rotor in steady forward flight before performing CFD/CSD coupling studies. The UH-60A rotor associated with the Black Hawk helicopter is the rotor configuration used for the 3-D validation studies. Lorber [111] has documented the flow over a UH-60A rotor for a number of hover and forward flight conditions. This rotor is a four-bladed configuration, typical of that found on a current generation army helicopter. It has a complex blade form that tends to complicate numerical analysis, especially in forward flight. The features of the blade include nonlinear twist distribution, several unsymmetrical airfoil sections, and tip sweep. Figure 4.7 shows a schematic representation of the model UH-60A rotor planform. The structural twist distribution reproduced from reference [111] is shown in

Figure 4.8. The blade has a rearward sweep of 20 degrees starting from the radius of 93%. The blade is made up of two airfoil sections SC1095 and SC1095R8 as seen in Figure 4.9.

UH-60A rotor is a fully-articulated system that exhibits all possible motions, and thus requires that all the hinge motions are modeled. The articulated motion consists of pitch, flap, and lead-lag components with non-zero higher harmonic content, as well as hinge offsets and shaft tilt. Substantial torsional deformation of the model was observed in the experiment and has been documented. This elastic deformation should be included in any forward flight analysis to validate the airloads predictions with test data. To independently validate the capabilities of the CFD solver, converged blade deformations obtained from OVERFLOW/CAMRAD II loose coupling [54] is used to account for the trim and aeroelastic effects. The test cases for the validation studies are chosen from the UH-60A Airloads database [74] . The flight conditions for these test cases are listed in Table 5.1. The validation results are presented as non-dimensional, sectional normal forces or pitching moment coefficients about quarter chord. The steady component is discarded from the airload comparisons to remove the effect of trim that might exist between different coupling frameworks.

4.3.1 Grid Sensitivity Studies

Grid sensitivity studies are required to determine the size and density of the computational grid to be used for CFD analysis. In the hybrid methodology, the inflow boundary conditions are applied based on far field assumptions with velocity perturbations introduced by wake model only. This assumption is valid only when the distance of the far field boundary from the blade surface is sufficiently large. To

determine the optimal location of the far field boundary, three computational grids with same number of chordwise and spanwise points but with different far field distances from blade surface are chosen. The nodes in the normal direction are scaled in the same ratio as farfield boundary distance from blade surface to maintain comparable grid spacing. The y^+ values for the 2-D and 3-D validation cases are listed in Table 4.1. The grid profiles are shown in Figure 4.10. A 3-D CFD simulation of the rotor blade with prescribed blade motions for high speed c8534 flight condition is run using the three grids and normal force coefficients as a function of azimuth are compared in Figure 4.11. It is observed that the results obtained using grid (a) and grid (b) are almost identical. Therefore, nine chord lengths is chosen as the far field distance for the baseline grid.

Sensitivity of the solution to near-wall grid density was studied using two sets of grid systems. The baseline C-type grid system has 131x75×65 grid points (0.638 Million) in chordwise, spanwise, and surface normal direction. The fine grid has doubled chordwise and surface normal direction grid points (261×75×130 = 2.544 Million), thus the computational time with the fine grid is about four times more than the baseline grid. Figure 4.12 compares the normal forces for c8534 flight condition for the baseline and fine grids. It is seen that there is essentially no difference in the predictions between the baseline and fine grid. Therefore, the baseline grid system was used for all the studies presented in the rest of this work.

4.3.2 Time Step Sensitivity

A time step convergence study has been performed to determine the time step size needed to obtain time step independent solution for a 3-D rotor simulation. Three different time steps with baseline hybrid method were tested for the c9017 flight

condition. The sectional normal forces at three radial locations are compared in Figure 4.13. The normal forces for $\Delta t = 0.05°$ and $0.025°$ are almost identical but a small deviation is observed when a time step of $0.01°$ is used. Unless specified otherwise, a time step of $0.05°$ is used for all the studies.

4.3.3 Effect of FSWM

The primary enhancement of FSWM over the single tip vortex model is accounting for the effect of inboard vortices. Therefore, the effect of FSWM on airloads predictions will be best observed for a low speed flight condition. C8513 is a low speed flight condition available in the UH-60A airloads database and is a good candidate to test the FSWM. The FSWM was run with 40 trailers with the wake geometry updated every 5°. The high number of trailers was primarily for validation purposes but 15 trailers was found to be sufficient to capture most of the inboard vorticity. The normal forces for c8513 flight condition obtained using the FSWM and single tip vortex model simulations are compared with flight test data in Figure 4.14. It is seen that the simulations performed using FSWM show much better predictions than the single tip vortex model. The impulsive loading seen in the fourth quadrant is partially captured by the FSWM. The single tip vortex model fails to capture this phenomenon effectively. The single tip vortex does not model the inboard vorticity therefore, fails to predict the impulsive loads accurately. Therefore, it can be concluded from these observations that the FSWM is more effective in capturing key physical phenomena characteristic to rotors in low speed forward or descent flight. Figure 4.15 shows the wake geometry for full span wake model in GT-Hybrid compared to a similar model used in CAMRADII [75].

4.3.4 Effect of Shed Wake Model

The shed wake model captures the effects of wake shed due to azimuthal changes in loading. Though the Navier-Stokes solution captures the shed vorticity within the computational domain, the effect of shed wake on preceding blades can be modeled only through the shed wake model. Generally the shed wake is significantly weaker than the tip vortex and is dissipated quickly before it reaches the preceding blade. But the shed vorticity tends to be strong in regions where the rotor blade experiences sharp azimuthal variation in airloads. This phenomenon is typically observed when the blade experiences deep dynamic stall cycles on the retreating side of the rotor. Therefore, the c9017 high thrust flight condition is chosen to test the effect of the shed wake model on rotor airloads predictions. The test case is run with 15 wake trailers preserving trailing and shed vorticity for four wake revolutions. Figure 4.16 shows the sectional lift and pitching moments for simulations with and without the shed wake model. The shed wake model improves the prediction of the second dynamic stall on the retreating side. The second dynamic stall is a consequence of high elastic torsion and lower induced downwash that increases the effective angle of attack. The shed wake model enhances the induced velocity field that helps in better prediction of phase and magnitude of dynamic stall cycles.

4.3.5 Effect of Spatial and Temporal Accuracy

The 5^{th} order order ENO scheme uses adaptive stencils to better capture the effect of shocks with reduced dissipation. This scheme is compared with baseline 3^{rd} order MUSCL scheme for the c8534 flight condition where transonic effects are observed on the advancing side. Figure 4.17 shows the comparison of normal force history for both

the schemes against flight test data. On the baseline grid described in section 2.6, the use of the 5th order scheme does not improve the airloads predictions significantly with some azimuthal regions experiencing a slight reduction in solution quality. While spatially high order schemes exhibit superior dissipation characteristics on uniform fine grids, they might have the opposite effect with highly stretched or distorted grids. This is primarily because the order of magnitude of error varies with grid spacing. Therefore, for a grid spacing greater than 1 unit, high order schemes might cause more numerical dissipation than lower order schemes.

The effect of 2nd order temporal scheme is tested for the c9017 flight condition since dynamic stall is a highly unsteady phenomenon. The effect of time accuracy on dynamic stall prediction for c9017 flight condition was minor when an azimuthal time step of 0.05° is used, as seen in Figure 4.18. The 2nd order temporal scheme with Newton sub-iterations allows for larger time steps with better convergence. However, a simulation with higher temporal accuracy is computationally more expensive even with larger time steps because of higher memory requirements. Therefore, the first order temporal scheme is used for all the steady flight simulations. The effect of temporal accuracy for maneuvering flight simulations is discussed in section 6.4.1.

4.4 Chapter Summary

In this chapter, the CFD methodology was validated for several 2-D airfoil and 3-D rotor simulations. The CFD methodology was tested for a transonic mach number condition with RAE-822 airfoil. Both KES and SA-DES turbulence models modeled the shock magnitude correctly though the shock position was predicted to occur closer to the leading edge. A dynamic stall case was run with NACA0012 airfoil. SA-DES slightly

over-predicts the lift compared to KES turbulence model, however the overall hysteresis loop was in good agreement.

The CFD methodology was tested and validated for the UH-60A rotor in steady flight conditions using prescribed deformations. The baseline grid size of 131*75*65 with far field boundary located 9 chord lengths from blade surface was found to be sufficient for rotor studies. The FSWM was shown to have a significant effect on airloads predictions for low speed conditions. The shed wake model improved the predictions for the dynamic stall condition. The 5^{th} order ENO scheme on the baseline grid did not impact the predictions significantly. The 2^{nd} order temporal scheme did not affect the airloads predictions for steady flight conditions. Based on these findings, the baseline computational parameters are defined in Table 4.2. These baseline parameters, unless specified otherwise, are used for all the CFD simulations.

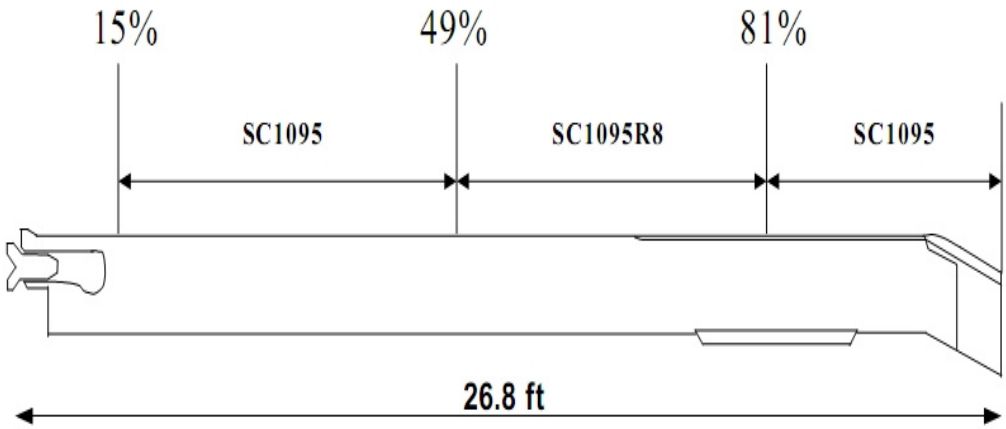

Figure 4.7 UH-60A blade planform

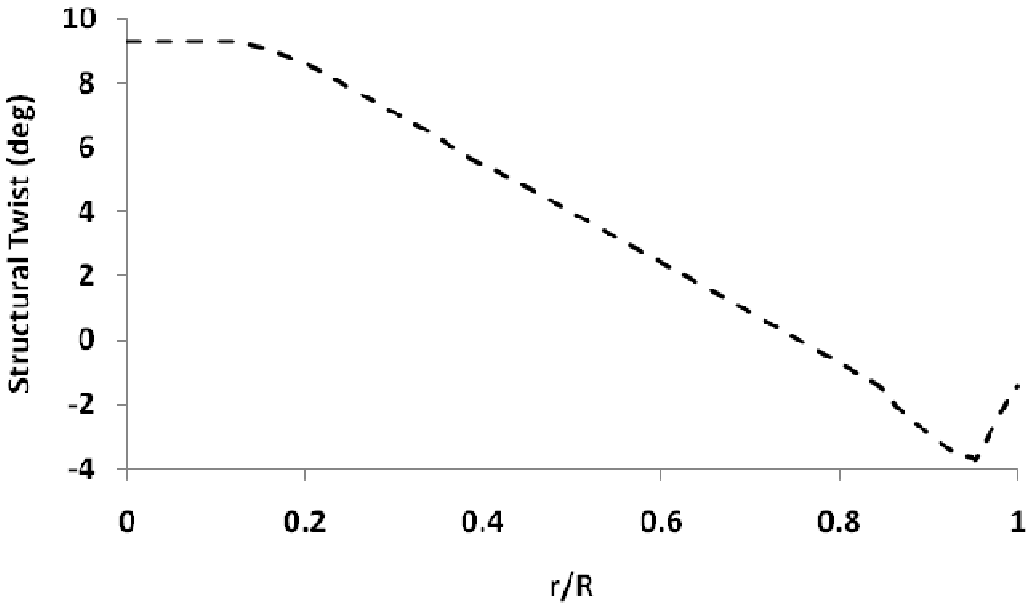

Figure 4.8 UH-60A twist distribution

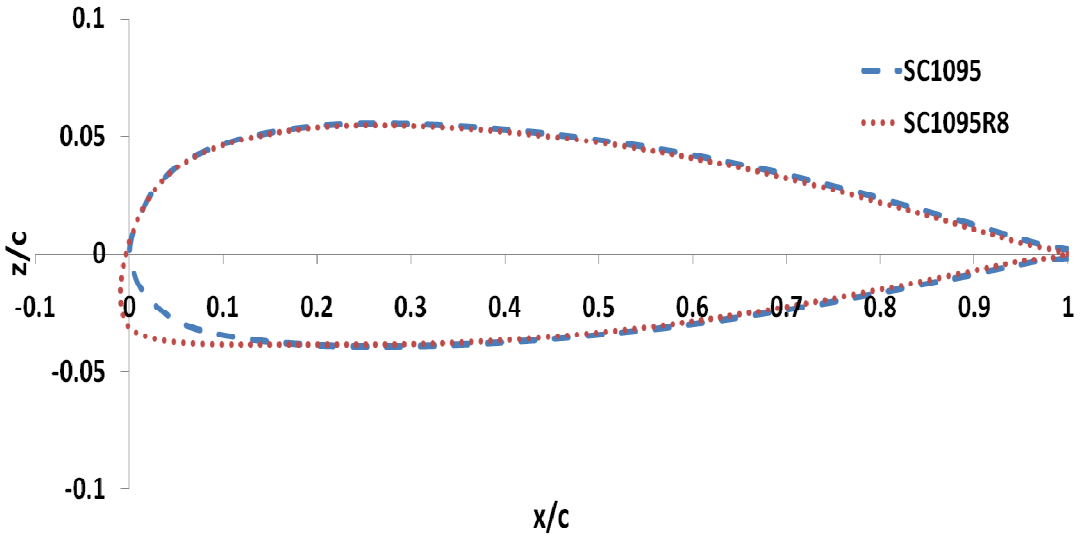

Figure 4.9 SC1095 and SC1095R8 airfoils

Table 4.1 CFD validation cases: y^+ values

Test case	**y^+**
RAE 2822	1.1
NACA 0012	1.4
UH-60A c8534	3.4
UH-60A c9017	2.3
UH-60A c8513	4.2

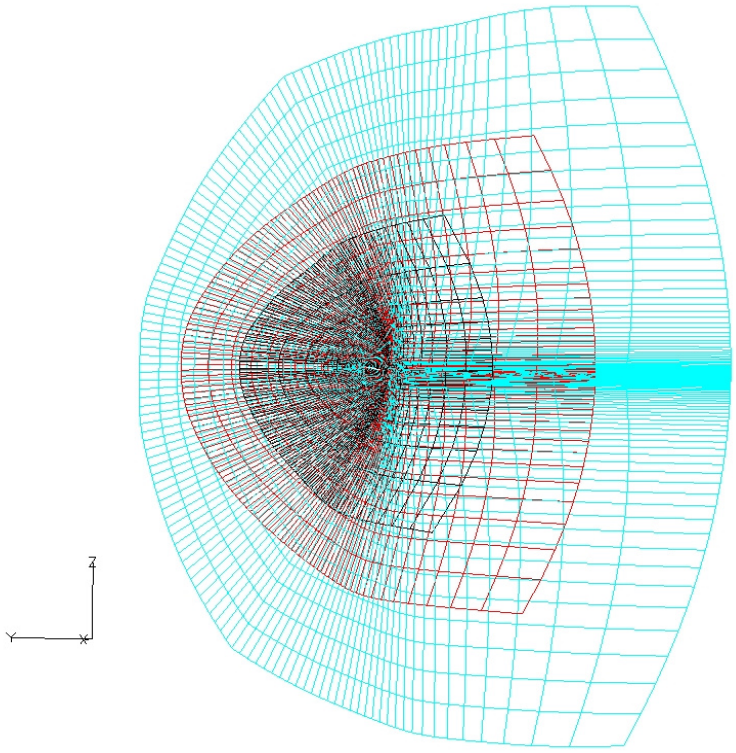

Figure 4.10 Computational grid with varying far field boundary distances
a) 14 chords (131*75*108) b) 9 chords (131*75*65) c) 4 chords (131*75*30)

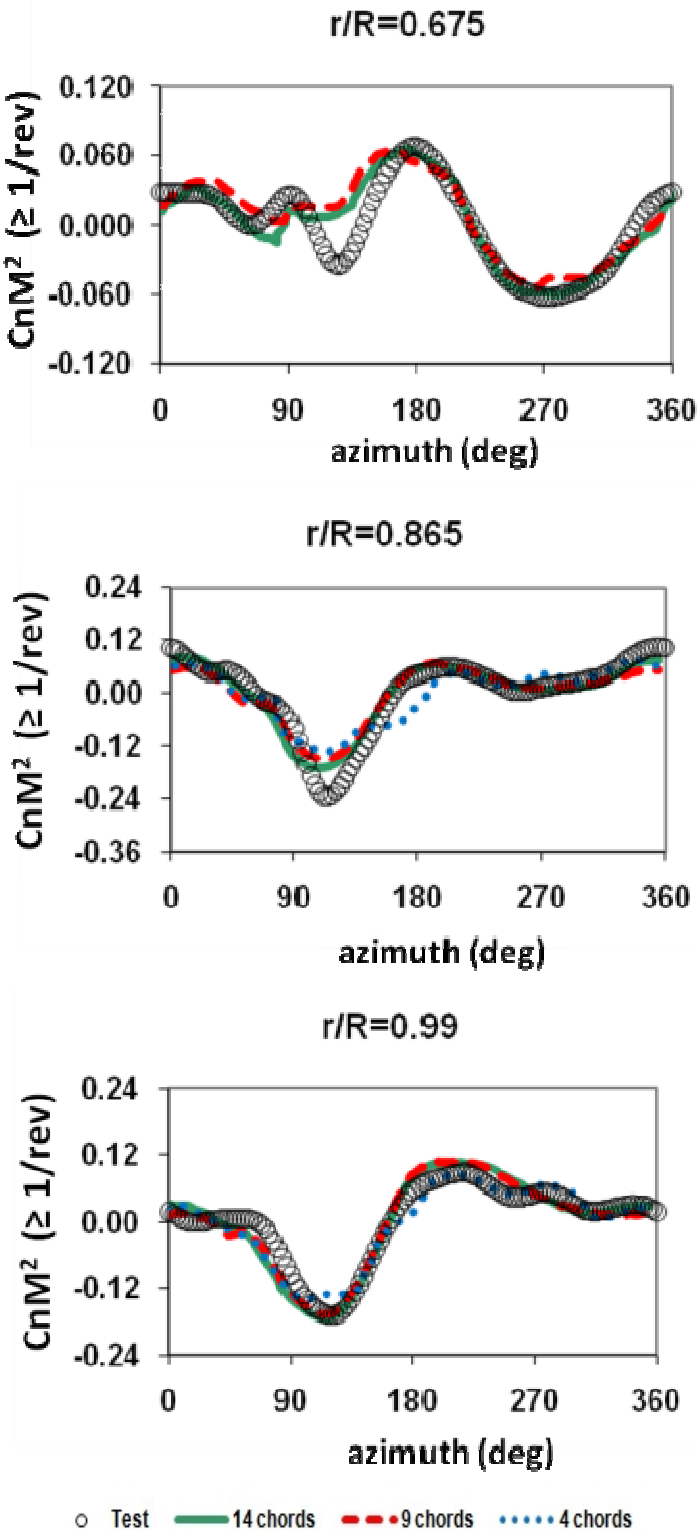

Figure 4.11 Flight counter 8534: Effect of location of far field boundary

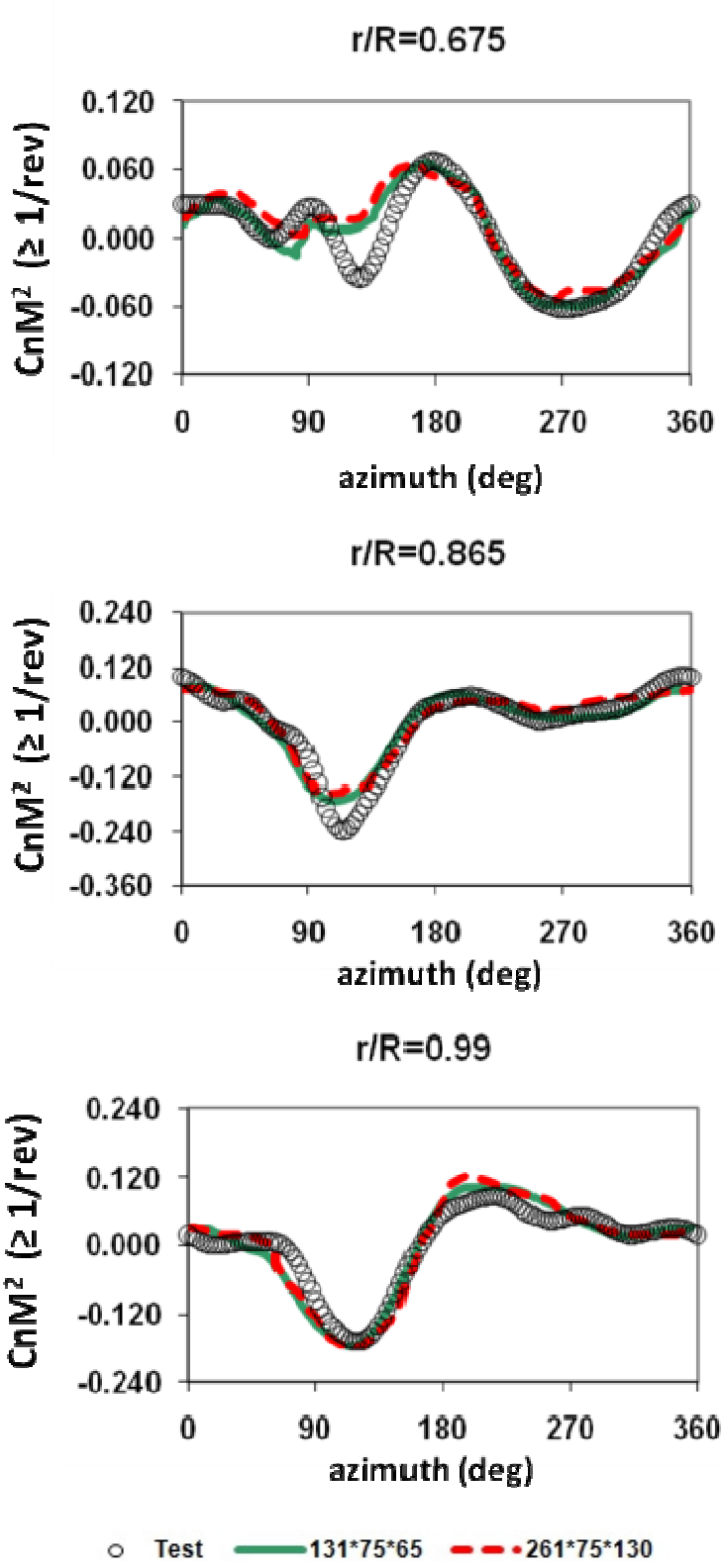

Figure 4.12 Flight counter 8534: Effect of grid density

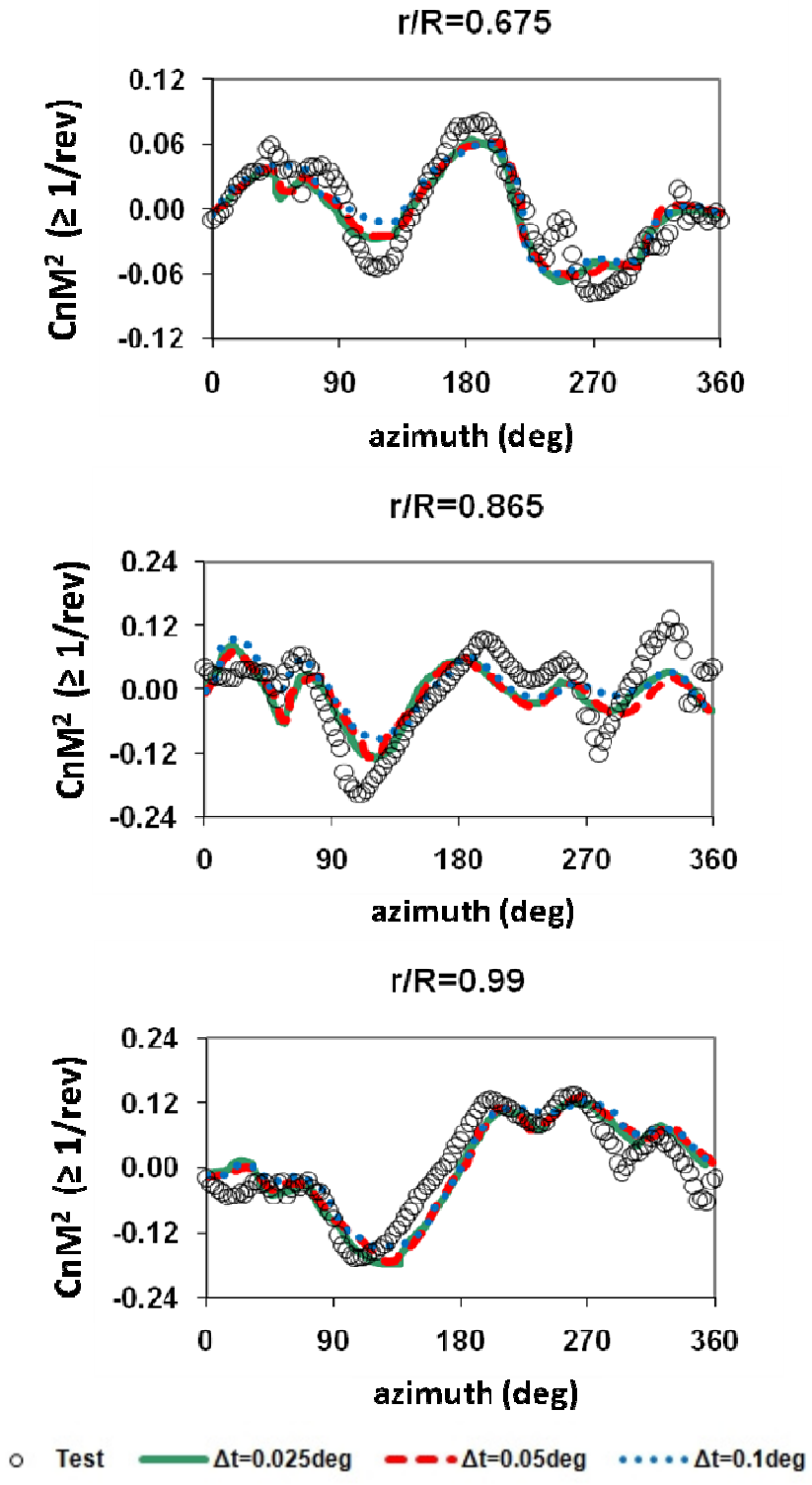

Figure 4.13 Flight counter 9017: Time step sensitivity

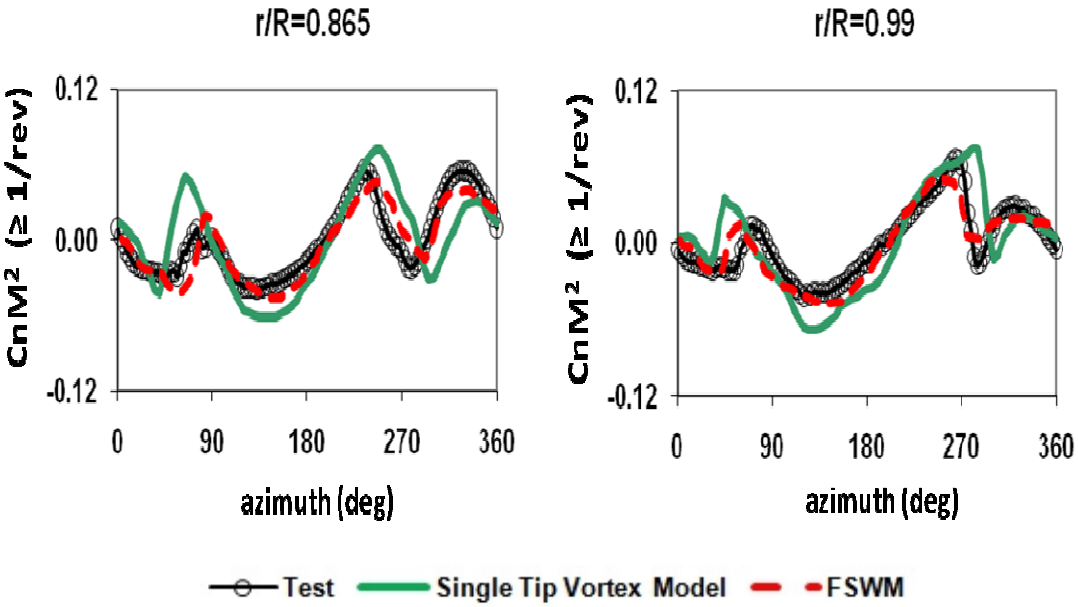

Figure 4.14 Flight counter 8513: Effect of FSWM

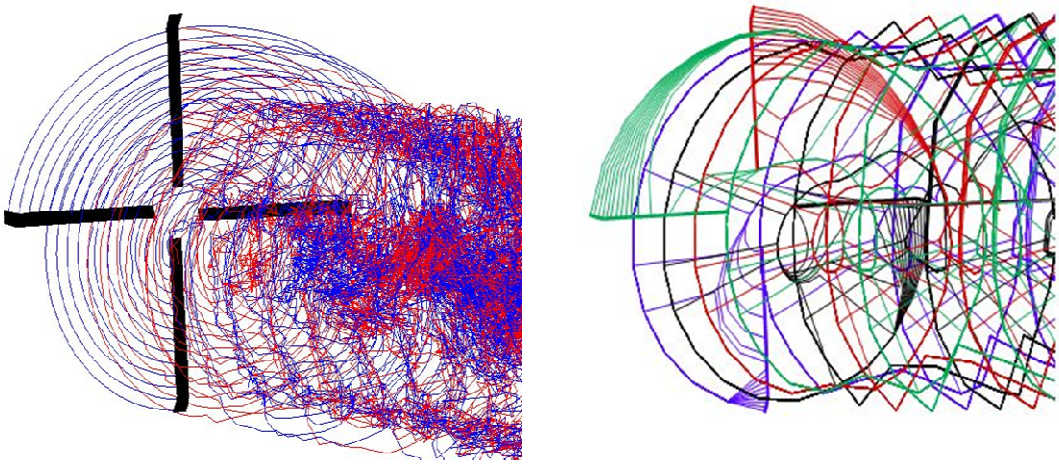

Figure 4.15 Comparison of full span wake model between GT-Hybrid (left) and CAMRADII (right)

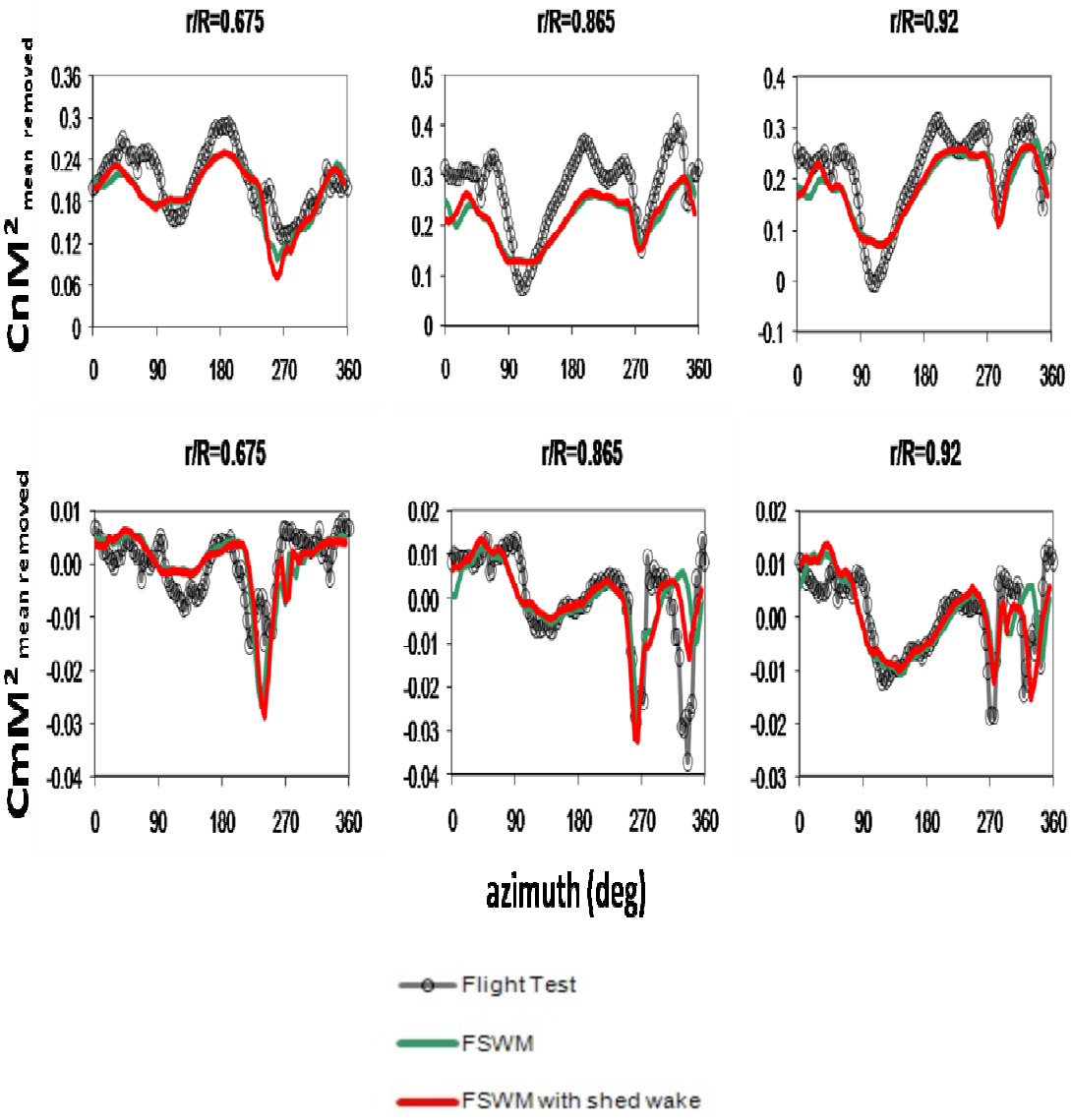

Figure 4.16 Flight counter 9017: Effect of shed wake model

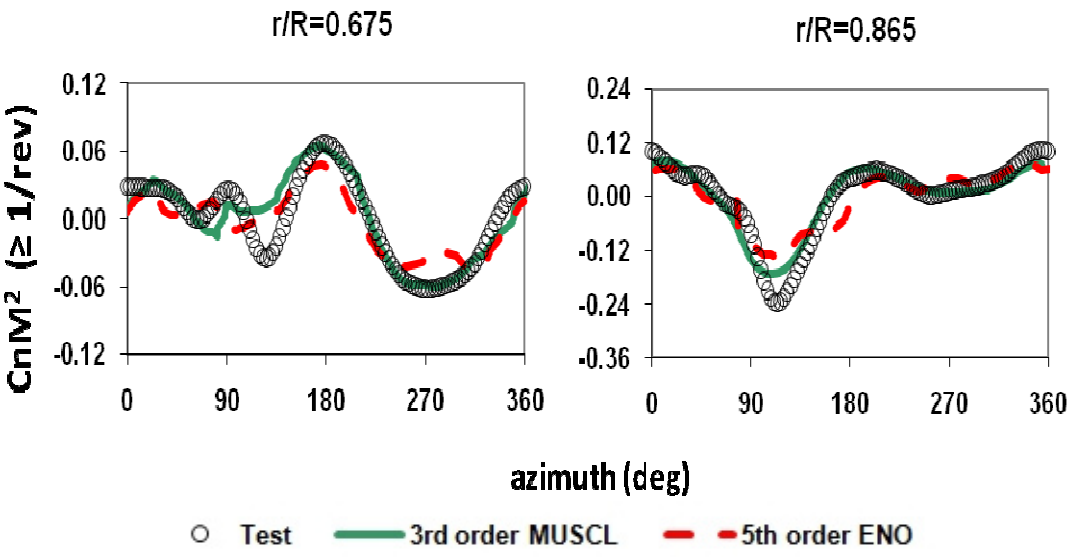

Figure 4.17 Flight counter 8534: 3rd order vs 5th order spatial accuracy

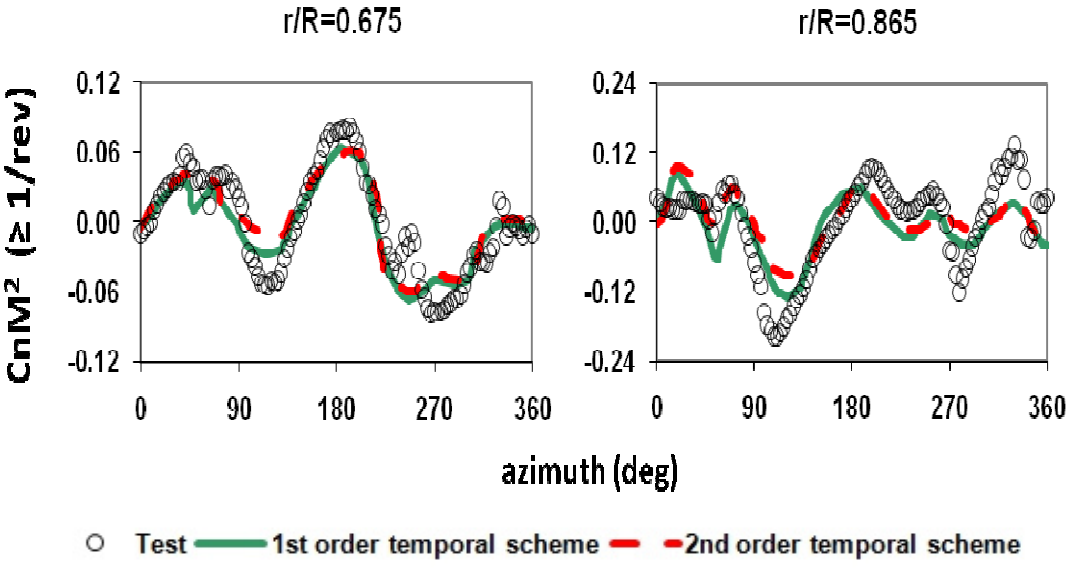

Figure 4.18 Flight counter 9017: 1st order vs. 2nd order temporal accuracy

Table 4.2 Baseline computational parameters

Computational Parameters	
Grid density	131*75*65
Temporal Accuracy	1st order
Spatial Accuracy	3rd order MUSCL
Time step size	0.05 degrees azimuth
Wake model	Single tip vortex
Turbulence model	SA-DES
Wake size	4 revolutions
Wake update frequency	5 degrees azimuth

CHAPTER 5

RESULTS PART I: CFD/CSD COUPLING FOR STEADY FLIGHT CONDITIONS

This chapter focuses on the study of aeroelastic phenomena that affect the UH-60A rotor in various steady flight conditions. The phenomena are studied through CFD/CSD coupling simulations. The study analyzes the airloads and structural loads comparisons between the predictions and flight test data. All the computational studies, unless specified otherwise, are performed for baseline CFD parameters listed in Table 4.2.

Four varied flight conditions were chosen from the UH-60A airloads database for the analyses – counter 8534, counter 9017, counter 8513 and counter 9020. Flight counter 8534 is a high speed flight condition. Vibratory loads (> 2 per rev) play a key role at this flight condition. Flight counter 9017 is a moderate speed, high altitude flight condition. This flight condition is characterized by high thrust dynamic stall cycles. Flight counter 8513 is a low speed flight condition characterized by impulsive BVI loading. Flight counter 9020 is similar to c9017 but has a lower thrust requirement making it less severe in terms of dynamic stall effects. The vehicle experiences maximum vibration in c8534 and c8513 which increases structural fatigue significantly. The limiting design loads, on the other hand occur during maneuvers which are characterized by dynamic stall cycles on retreating side very similar to what is seen in c9017 and c9020 flight conditions.

The four flight conditions are indicated on Mchugh's lift boundary chart in Figure 5.1. McHugh [112] reported the results of a wind tunnel experiment that used a rotor

model designed and constructed so that the aerodynamic limits of the rotor could be determined. Thus, during testing at one advance ratio for example, the collective pitch was increased until the rotor thrust reversed (because of stall). The limit conditions obtained were aerodynamic limits as opposed to structural limits as occurs in normal rotor tests. The flight conditions are listed in Table 5.1. The analysis in this chapter is presented as airloads and structural load comparisons with flight test data. The airloads are computed in the local airfoil section frame. The structural loads are computed with respect to the rotating blade frame. The quantities analyzed are shown in Figure 5.2.

5.1 UH-60A Structural Model

DYMORE model for the UH-60A helicopter rotor is modeled using basic structural elements. This model was designed and validated by Liu [113]. The construction of this model can be seen in Figure 5.3. The main blade and root connector elements are modeled using Euler-Bernoulli beam elements. The blade has ten 3^{rd} order finite elements, the root connectors each have two 3^{rd} order finite elements, and the hinges are modeled using revolute joints. In DYMORE, the four-bladed model consists of not only the blades, but also flap, lead-lag, and pitch hinges, a hydraulic lead-lag damper [114], an equivalent spring, and a hub component to tie it all together. The equivalent spring is included to represent the stiffness of the pitch-link and swash plate components, which have not been included. The associated lifting lines used for the aerodynamic computations contain 81 evenly spaced points that lie along the blade quarter chord. The geometry of the blade itself includes both the swept tip and the tab, which are applied through the lifting line data. The structural elements have structural twist data but no offsets from the beam axis.

Since this model uses a non-physical equivalent spring to represent the stiffness of the control linkages, the stiffness of this spring must be determined such that it represents as loosely as possible the stiffness of the control system. However, there is no experimental measure of the stiffness of the physical components of this system. Therefore, the value was determined to be 363 ft-lbs/deg in Ref. [114] by applying measured airloads on the structural system.

5.2 CFD-CSD Loose Coupling (LC) Methodology

The LC methodology for rotorcraft was first developed by Tung et al. [43]. In the LC methodology, distinct sets of fluid dynamics and structural dynamics equations are solved alternatively with occasional information transfer between software codes. The methodology can be applied to aircraft in steady flight, which include periodic aeroelastic behavior. A periodic response of the dynamic system is first obtained (dynamic solution n=0) from the CSD methodology based on a simple aerodynamic model, which provides a low fidelity input for the aerodynamic forces on the structural system. The CSD methodology might include an auto-pilot trimmer which is required to trim the rotor to target hub loads for an isolated rotor computation. A periodic aerodynamic response for the advanced CFD model is then obtained (aerodynamic solution n=0) with the periodic structural motion obtained from the initial CSD solution. The resulting periodic aerodynamic forces are then applied to the dynamic system to obtain a new periodic structural response (dynamic solution n=1). The next periodic aerodynamic solution is obtained with the updated structural motion (aerodynamic solution n=1). The process is repeated (n= 2,3,...) until a converged solution is obtained, where the periodic structural and aerodynamic loads do not change with further successive coupling iterations.

The methodology must be implemented in a manner that allows damping in each structural response calculation to avoid creating an ill-conditioned problem. The CFD airloads remain invariant during the trim procedure, hence the structural response computation becomes an ill-conditioned problem. This issue is addressed through the delta trimming methodology [54]. The aerodynamic force applied to the structural model in the n^{th} coupling iteration is shown in Eqn. (5.1), where F_n^{LL} is the aerodynamic force/moment computed from internal aerodynamics in the comprehensive solver. Aerodynamic damping in the system is associated with the F_n^{LL} term.

$$F_n^{CSD} = F_n^{LL} + \Delta F_n \tag{5.1}$$

The delta-airloads term, ΔF_n, represents the difference between the low and high fidelity airloads, and is calculated from the previous coupling iteration, as shown in Eqn. (5.2) .

$$\Delta F_n = F_{n-1}^{CFD} - F_{n-1}^{LL} \tag{5.2}$$

The term F_n^{LL} changes during the trimming process but the delta airloads term remains invariant. The combination of variant and invariant aerodynamic terms provides enough aerodynamic damping to the structural system. Initially the magnitude of ΔF_n is huge due to significant differences in fidelity between CFD and lifting line based solutions. As solution progresses though coupling iterations, F_{n-1}^{LL} and F_n^{LL} get closer to each other. Theoretically, the coupling process has converged when F_{n-1}^{LL} is equal to F_n^{LL} and the only forces now acting on the structural system are the high fidelity loads from CFD. This

methodology, in principle can be used only for steady flight conditions that have an inherent periodicity in the aerodynamic loading, but it can be extended for slow maneuvers as it shall be seen in the next chapter. The loose coupling methodology is automated through platform independent PERL and PYTHON scripts.

The loose coupling methodology between GT-Hybrid and DYMORE is shown in Figure 5.4. The coupling between DYMORE and GT-Hybrid used the Fluid Structure Interface (FSI) [116] format to exchange data. The non-rotating shaft frame was used as reference frame in both GT-Hybrid and DYMORE. Therefore, the airloads (Forces – Fx, Fy, Fz; Moments – Mx, My, Mz) from GT-Hybrid were computed as a function of radius and azimuth. In the current study, 49 CFD airloads stations and 81 lifting-line airloads stations were used. The airloads from GT-Hybrid were transferred in a shaft fixed frame as three components of forces and moments. Since rotor blades have very little elasticity in the chordwise direction, they can be modeled quite accurately in the CSD methodology using a 1-D beam representation with flap, lag, axial and torsion degrees of freedom. In contrast, the entire surface of the blade is represented in the CFD mesh within the limit of grid resolution. The difference in geometry description of the CFD and CSD models required specialized formulation for the transfer of loads and displacements. In this study, a rather simple approach of one-dimensional linear interpolation was used. Because of the structured nature of the grid, sectional aerodynamic loading can be easily determined using the pressure and shear stress distributions on the CFD surface grid. These were interpolated using linear interpolations to the control points of the CSD model.

5.3 CFD-CSD Tight Coupling (TC) Methodology

The flowchart for the TC methodology is shown in Figure 5.5. The fluid and structural equations are integrated using the conventional serial-staggered scheme (CSS). The CSS scheme was found to provide similar levels of accuracy as time accurate tight coupling (TA) [61] computations and is much faster. The procedure for tight coupling is as follows: The natural modes of the structural model in DYMORE are evaluated. The equilibrium positions of the blades are used as initial conditions for the forced response simulation. The initial forced response simulation is run without coupling to CFD solver where the airloads are computed using the internal aerodynamic model in DYMORE which uses 2-D aerodynamic coefficients table and dynamic inflow. The simulation is run for about 30 rotor revolutions to obtain periodic deformations. At this point, DYMORE writes out a semaphore file signaling the end of the CSD simulation for one time step. GT-hybrid monitors the availability of the semaphore and reads in the motions in the FSI format. DYMORE used a time step of 1° azimuth whereas the CFD code used a time step of 0.05° azimuth because CFD methodology needs a smaller time step to handle the flow transients. Once the CFD simulation is completed for 1°, the solver writes out the loads and a semaphore file asking DYMORE to read the data. The use of file I/O for tight coupling has many advantages. The solvers do not see each other directly; therefore the coupling process is modular and generic. No external script is required run the tight coupling process.

The initiation of the fluid-structure solution often creates large transients in both physical systems that can be amplified by the combined time integration procedure (because of its explicit nature) leading to destabilization. To prevent such destabilization

from occurring, the CFD based aerodynamic loading is slowly introduced into the CSD loading using a linear relaxation scheme. The aerodynamic model (lifting-line based) is maintained active in the CSD solver for the initiation. This model is fully-coupled in the sub-iteration level and does not cause destabilization. The aerodynamic loading from the CFD is slowly mixed with the lifting line aerodynamic loading over two revolutions. After the first 2 revolutions, the lifting line modeling is completely turned off and the CSD loading is exactly equal to the CFD aerodynamic loading. An auto-pilot trimming of a tight coupling scheme is not feasible because of the computationally intensive CFD process. Tight coupling methodology can be trimmed manually by estimating a trim Jacobian using CFD loads but the process is very time consuming. Therefore in this study, the trimmed control angles for the tight coupling simulation were obtained from the loose coupling simulations for all the flight conditions where both methodologies were tested. This approach was found to be adequate for steady, level flight conditions.

5.4 High Speed Flight c8534

This high speed case (μ=0.368) is characterized by high vibratory loading present on the advancing side of the rotor and reverse flow near the blade root on the retreating side. Both loosely coupled and tightly coupled simulations were run for this case. Baseline computational parameters specified in chapter 4 were chosen for the CFD simulations. For the high speed forward flight condition, the effects of the wake modeling are relatively unimportant. The inflow is dominated by the free stream component perpendicular to the rotor disk, owing to a large shaft tilt angle (8°). Therefore, the single tip vortex model was deemed to be sufficient for this case. Figure 5.6 shows the CFD hub loads convergence for the loose coupling process. The loose coupling methodology

shows good convergence to the target hub load values in about 10 iterations. The hub loads are generally over predicted for the first couple of iterations. This is because the aeroelastic motions obtained using lifting line aerodynamics and dynamic inflow, have high collective and cyclic angles. But as coupling iterations progress, the high fidelity CFD loads were slowly introduced onto the structural system and control angles converged towards the flight test values. This observation can also be inferred from pitch control convergence shown in Figure 5.7. The predicted pitch angles are marginally different from the flight test values. This has been observed in other computational work for the UH-60A rotor. This difference in pitch angles stems from the differences between the actual physical configuration and geometric representation of the helicopter control systems in CSD methodology.

The airload predictions from both the coupling methodologies were compared with flight test data at nine radial stations. The flight tests used pressure transducers to measure the surface pressures at these nine radial stations. The pressures were integrated to compute the normal forces and pitching moments. Figure 5.8 shows normal force coefficients which are non-dimensional sectional loads computed perpendicular to the local chord at each radial station. In Figure 5.9, the non-dimensional aerodynamic pitching moments computed about quarter chord are shown at each radial station. Pitching moment plots for all the UH-60A simulations have their means removed since earlier studies [54] have found faulty pressure taps in the dataset that cause considerable discrepancies in pitching moment mean values. It may be seen that the overall computed values are in excellent agreement with the test data. There is no significant difference in predictions obtained using loose and tight coupling methodologies. The peak-to-peak

magnitudes of the normal forces are well captured, though there is a small phase difference. The correlations are better on the outboard regions of the blade. The inboard regions have lower spanwise grid density and that may affect the correlations in this region. The results in the reverse flow region (r/R=0.225), where the angle of attack ranges from 0° to 180°, compare well with test data though there is a slight under-prediction in the pitching moments. This region is where the rotating velocity of the blades is not able to overcome the forward velocity of the rotor, resulting in a region where the flow is moving from the trailing edge to the leading edge of the blade airfoil sections. As the blade enters this region, the angles of attack change rapidly from close to 0° to close to 180°. As the blade moves away from this region it changes back as rapidly from 180° to 0°. So even though the blade pitch has not actually been rotated by such a large angle, the flow direction effectively forces this motion.

There is a small discrepancy in the prediction of the higher harmonic content in normal forces in the second quadrant at 67.5% R. To understand this discrepancy, the harmonic content in the loads need to be analyzed. Figure 5.10 shows the harmonic decomposition of flight test normal forces at four radial stations. The loads are decomposed into the 0-2 per rev non-vibratory loads and 3-10 per rev vibratory loads. It is seen that the vibratory loads determine the phase of the negative lift on the advancing side at 67.5%R and 77.5%R. Therefore, in order to capture the higher harmonic content, it is necessary to predict the correct vibratory lift. In the outboard regions, non-vibratory loads dominate and the predictions are much closer to test data. The vibratory loads are triggered by higher harmonics in elastic twist which is directly related to the pitching moments computed at quarter chord of the blade. The pitching moment predictions show

reasonable agreement with test data though some of the higher harmonics are not captured well. This is one of the primary reasons for slight discrepancies in normal force predictions. The pitching moments in the outboard regions are expected to be of unsteady transonic nature since moving shock waves are clearly visible in the surface pressure distributions (Figure 5.11) obtained from test data. To isolate the transonic effects, simulations were conducted reducing the tip Mach number and maintaining the same advance ratio. The converged blade motions from loose coupling simulations were used for all the tip mach number cases. The pitching moment waveforms for these cases are shown in

Figure 5.12. It is observed that as tip mach number decreases, the pitching moments vary drastically compared to flight test data indicating that the nose down pitching moments are due to transonic effects.

The structural loads computed at 30%R and 70% R are shown in Figures 5.13 and 5.14. The peak-to-peak torsional and flap bending moments compare well with test loads. Both the peak to peak magnitude and the higher harmonic waveform show similar trend as the test data. However, compared to the test data, the predictions appear to show a constant phase shift for both the radial stations. This is due to the small residual phase error in lift prediction on the advancing side. The negative lift on the advancing side is due the negative angle of attack produced by the transonic nose-down pitching moments. Therefore, phase lag in the pitching moment predictions creates the phase error in normal forces which affects the flapwise and torsional bending moments.

5.5 High Thrust Flight c9017

This counter is high thrust level (C_W/σ = 0.1325), and a moderate speed (μ = 0.237) flight condition. The moderate speed is high enough to prevent tip vortex inter-twinning but low enough to prevent the onset of strong transonic effects (M_{tip} = 0.77 in advancing side, with sweep). Even though the blade loading is not as high as that of the UTTAS maneuver, it is close to the McHugh's lift boundary. The vehicle experiences severe dynamic stall cycles in this flight condition, similar to what is observed in the UTTAS 11029 pull-up maneuver. Loose and tight coupling simulations were run for this flight condition. The CFD simulations used the baseline parameters except for the wake model. The shed wake model was shown to improve dynamic stall predictions; therefore it was used in the CFD simulations for this flight condition. The full span wake model has 15 trailers carrying 4 revs of trailed and shed wake. The wake model is updated every 5°. The coupling convergence for this flight condition is shown in Figures 5.16 and 5.17. The coupling process takes around 15 iterations to converge to the target values. The shaft moments are close to zero for this flight condition. The airloads obtained from loose and tight coupling simulations between DYMORE and GT-Hybrid for 9017 flight condition is shown in Figures 5.18 and 5.19. The difference between the coupling methodologies is almost negligible. Although dynamic stall is an unsteady phenomenon, loose coupling simulations seem to capture the stall loads reasonably. The normal forces and pitching moments are in good agreement with the flight test data. This flight condition is characterized by two distinct dynamic stall cycles on the retreating side. It appears that the first stall vortex starts accumulating and sweeping down the chord at around 250 degrees azimuth and leaves the airfoil at 270 degrees azimuth. This produces

the first lift stall. The second stall appears to occur around 320 degrees. The lift and moment stall cycles are captured well in phase but the magnitude of the second stall is slightly under-predicted.

The physics behind these stall cycles is understood by observing the geometric angle of attack on the outboard region. Figure 5.20 shows the contributions from pitch angle and elastic twist to the geometric angle of attack at 86.5% R (obtained from DYMORE). In general, the geometric angle of attack is dominated by the rigid pitch angles (control angles and rigid twist), which are of the order of 20 degrees on the retreating side. The elastic twist is of the order of -6 degrees. Its contribution is clearly visible in the fourth quadrant. Thus, the rise in angle of attack in the third quadrant is caused by the control angles. The rise in angle of attack in the fourth is caused by the elastic twist. This can be confirmed by a simple removal of higher harmonics from the elastic twist, as shown in Figure 5.21. Removing the 4 and 5/rev harmonics removes the twist oscillation in the fourth quadrant. Thus, to summarize, the first stall load is due to rotor trim. It remains unaffected by higher harmonics of twist. The second stall load is affected by 4 and 5/rev elastic twist. The 4 and 5/rev harmonics together produce the local angle of attack peak in the fourth quadrant. This peak determines the location and strength of the second stall load.

The trim condition and elastic twist was shown to have a direct influence on the dynamic stall cycles on the retreating side, but the effect of the wake is still unknown. Therefore CFD simulations were run using the single tip vortex and full span wake model (without the shed wake). The blade motions obtained from the converged loose coupling simulations were used in both the simulations. Figure 5.22 shows the normal force and

pitching moments for these two cases. The full span wake model correctly predicts the second dynamic stall but the single tip vortex fails to predict this phenomenon. Since both the cases use the same blade deformation file, the wake models predict the trim induced dynamic stall accurately. Therefore, the problem lies in the induced velocity field. The dynamic stall is a flow separation phenomenon that happens at high angles of attack. But if there is a high downwash in the vicinity, it reduces the effective angle of attack and the dynamic stall becomes weaker or the flow reattaches immediately after separation. The high inflow velocity can be attributed to a tip vortex that is stronger than the actual physical entity. To investigate this problem, the tip vortex strength was arbitrarily set to 70% of peak bound circulation instead of the original 100% value. The simulations were run again and the comparisons are seen in Figure 5.23. The tip vortex model with reduced strength is starting to predict the second dynamic stall. The tip vortex model assumes that all vorticity trailed behind the blade coalesces into the tip vortex. This assumption is applicable only for high speed flight, whereas 9017 is a moderate speed flight where the physical tip vortex is actually weaker than predicted strength. Therefore it can be concluded that the dynamic stall cycles in this flight condition are affected by trim, elastic motions and induced velocity field.

The structural loads computed at 30%R and 70% R are shown in Figures 5.24 and 5.25. The torsional moments show reasonable agreement with test data. The peak torsion loads are well predicted. The torsional moments are directly responsible for the higher harmonics of elastic twist and the predictions are consistent. The 4 and 5/rev harmonics that affect the elastic twist are the dominant components.

5.6 Low Speed Flight c8513

This flight condition ($\mu = 0.153$) is characterized by extensive wake interactions and a larger influence from the trailed vortex wake compared to high speed case. LC simulations for this flight condition were run using FSWM and shed wake model with 15 wake trailers. The hub loads and control convergence for the LC simulations is shown in Figures 5.26 and 5.27. The hub loads converge smoothly to target trim values in about 13 coupling iterations. The airloads obtained after convergence is compared with flight test data in Figures 5.28 and 5.29. BVI based impulsive loading is observed in the first and fourth quadrant of the normal forces that starts at the tip and extends up to 55% R inboard. The CFD predictions capture the BVI events reasonably well.

The BVI is due to the backwards tilt of the rotor shaft and low advance ratio in this flight condition. The older tip vortices from the blades convect above the rotor plane. As they gradually descend towards the rotor plane due to inflow, they start interacting with the flow over the blades. The low advance ratio also ensures that the wake is not quickly convected away from the blade. The vortex trailed from inboard regions is significant enough to affect the loading on the advancing blades. The FSWM predicts the strength and geometry of these inboard vortices effectively. The vehicle in this flight condition is known to experience significant vibration.

To understand the source of these vibrations, surface plot of normal forces with full test loads and vibratory loads (> 2 per rev) are plotted in Figures 5.30 and 5.31 respectively. It is clearly seen that the BVI impulse on advancing and retreating sides are the main source of vibratory loads in this flight condition. To gain insight into the mechanism of lift generation, the azimuthal variation of angle of attack is calculated. The

net angle of attack at a section consists of a combination of four factors: (i) collective and cyclic controls added to the rigid pre-twist, (ii) inflow distribution, (iii) blade flap and lag motion, and (iv) elastic torsion. The collective, cyclic, elastic twist angles, blade flap and lag motions are obtained from DYMORE. The downwash is computed at 75%R using the wake model. The induced velocity is computed using Biot-Savart's law at the leading edge of the airfoil.

Figure 5.32 shows the detailed angle of attack distribution for a spanwise station at 77.5% radius. The shape of both the angle of attack and the lift are dominated by the inflow component. The inflow contribution to the section lift clearly generates the impulsive lifts in the first and second quadrant. But the accuracy of the first impulse is affected by torsion response which shows a noticeable impact only on the advancing blade. Errors in torsion response can significantly contribute to the error in the prediction of the first impulse.

5.7 High Thrust Flight c9020

This flight condition is at a similar advance ratio as c9017 ($\mu = 0.245$) but at a lower thrust setting. Therefore, the vehicle experiences dynamic stall cycles on the retreating side similar to c9017 but the loading is less severe. Loose coupling simulations were run for this flight condition with full span wake model including shed wake. The convergence history of the coupling can be seen in Figures 5.33 and 5.34. The convergence history is reasonably smooth over 14 iterations. The effect of turbulence modeling on dynamic stall predictions was studied for this flight condition. The LC simulation was run using the SA-DES turbulence model. The converged blade motions

from the coupling were used for KES turbulence model. Using the same blade deformations eliminates the differences due to trim or elastic effects.

Figures 5.35 and 5.36 show the airload comparisons with flight test data. The KES turbulence model captures the second dynamic stall cycle reasonably well whereas SA-DES fails to model this phenomenon correctly. Earlier for the 9017 case, SA-DES was shown to model this phenomenon accurately. 2-D validation studies have shown that SA-DES over-predicts the peak lift magnitude before the airfoil stalls; compared to KES. This means that SA-DES predicts a high production of turbulent kinetic energy in the flow that prevents flow separation compared to KES model for the same angle of attack. The 9020 flight condition is less severe than 9017, hence the angle of attack around 300° azimuth is not sufficient for SA-DES to model the flow separation accurately. The pull up maneuver reaches a peak load factor of 2.1g, much higher than thrust requirement for 9017 flight condition. Even though SA-DES does not model the second stall accurately for 9020 flight condition, the local angles of attack in the maneuver are high enough to model the flow separation correctly. SA-DES, being a one equation turbulence model has a significantly smaller turnaround time than KES and therefore, the maneuver simulations are performed using SA-DES rather than KES.

5.8 Chapter Summary

Loose and tight coupling methodologies were implemented between GT-Hybrid CFD methodology and DYMORE CSD methodology to study the UH-60A rotor in steady flight conditions. Four varied flight conditions were chosen – c8534 (high speed), c9017 (high thrust), c8513 (low speed) and c9020 (medium thrust). The key mechanisms that affect a rotor in forward flight are free wake dynamics, unsteady transonic effects,

and dynamic stall. The flight conditions were chosen such that each counter represents a unique physical phenomenon. The evaluation of the CFD/CSD methodologies for these flight conditions is a precursor to extending the coupling methodology to maneuvering flight where all the aforementioned phenomena occur simultaneously.

Both loose coupling and serial staggered tight coupling was validated for 9017 and 8534 flight conditions and the differences in the airloads predictions were negligible. Since the loose coupling methodology has a robust trimming approach, this method is preferred over tight coupling for rotor aeromechanics studies in steady flight. Tight coupling might still be relevant for aeroelastic stability analysis where the phenomena are non-periodic and occurring on smaller time scales.

The analysis of 8534 flight condition revealed that vibratory loads (> 2 per rev) dominated the inboard region whereas the non-vibratory loads were the dominant component in the airloads on the outboard regions. Computational analysis revealed that nose down pitching moments which cause negative lift on the advancing side are due to transonic effects. Two characteristic dynamic stall cycles are observed on the retreating side in 9017 flight condition. It was concluded from the examination of blade local pitch angles that the first dynamic stall was induced by trim whereas the second one was due to elastic torsion caused by 5 per rev harmonics. The effect of the wake on dynamic stall was qualitatively assessed by testing the full span wake model and single tip vortex model. It was found that the vortex strength was too high in the single tip vortex model and that caused a huge downwash which decreased the local angle of attack and prevented the second dynamic stall cycle.

The analysis of 8513 flight condition indicated BVI events in the first and fourth quadrant that produced huge vibratory loads. The local angle of attack was examined and it was found that the inflow was the determining factor in the production of the impulsive loads. The 9020 flight condition exhibited the same underlying mechanisms that caused dynamic stall in flight counter 9017. SA-DES and KES turbulence models were compared for c9020 and it was concluded that SA-DES modeled a high production of turbulent kinetic energy that prevented the second dynamic stall whereas KES was able to model the phenomenon correctly. This behavior of SA-DES was not observed for c9017, and therefore is not expected to be an issue in the maneuvering analysis.

Table 5.1 UH-60A steady flight test conditions

Parameter \ Flight Counter →	FLT-8534	FLT-9017	FLT-8513	FLT-9020
Velocity, ft/sec	266.50	170.17	110.41	177.56
rotor speed, Hz	4.301	4.263	4.290	4.263
Vtip, ft/sec	725.16	718.65	723.20	718.65
density slug/ft^3	0.0020823	0.0013242	0.0021717	0.0014215
temp ^{o}F	71.81	24.76	66.62	29.99
Speed of sound, ft/sec	1129.97	1078.79	1124.43	1084.48
Advance Ratio, μ	0.368	0.237	0.153	0.245
M_{FLT}	0.236	0.158	0.098	0.164
M_{TIP}	0.642	0.666	0.643	0.663
Pitch Attitude, deg +'ve noseup	-4.310	2.801	3.754	3.515
α–shaft, deg (+ve tilt backward)	-7.310	-0.199	0.754	-0.515
C_T/σ	0.084	0.129	0.076	0.120
Thrust, lb	17665	16688	16302	16535
Pitch Moment, ft-lb, +'ve Nose up	-2583	112	-5470	-2176
Roll Moment, ft-lb, +'ve Rt.wing up	6884	-320	958	616

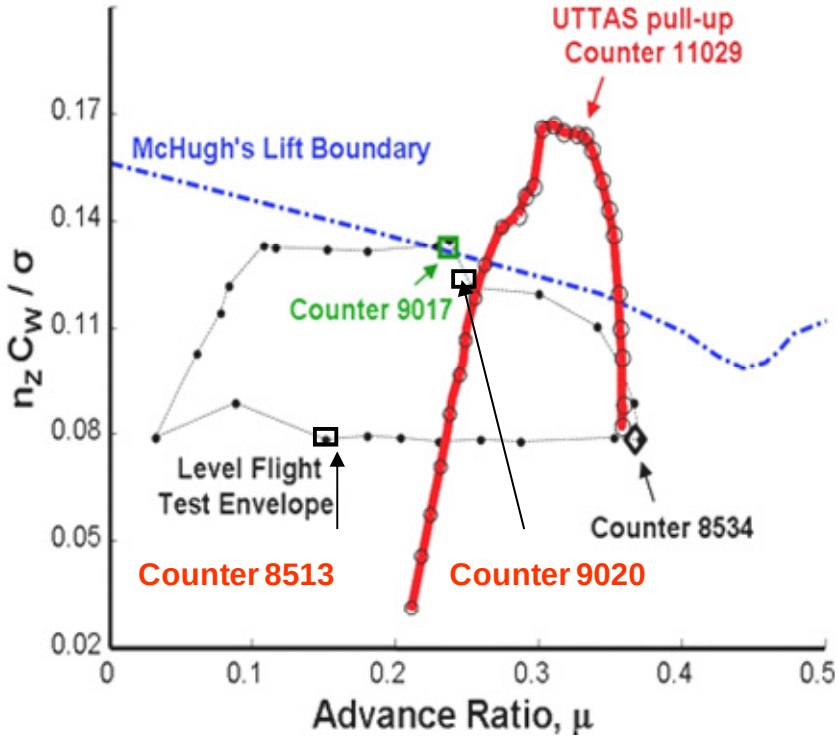

Figure 5.1 McHugh's lift boundary

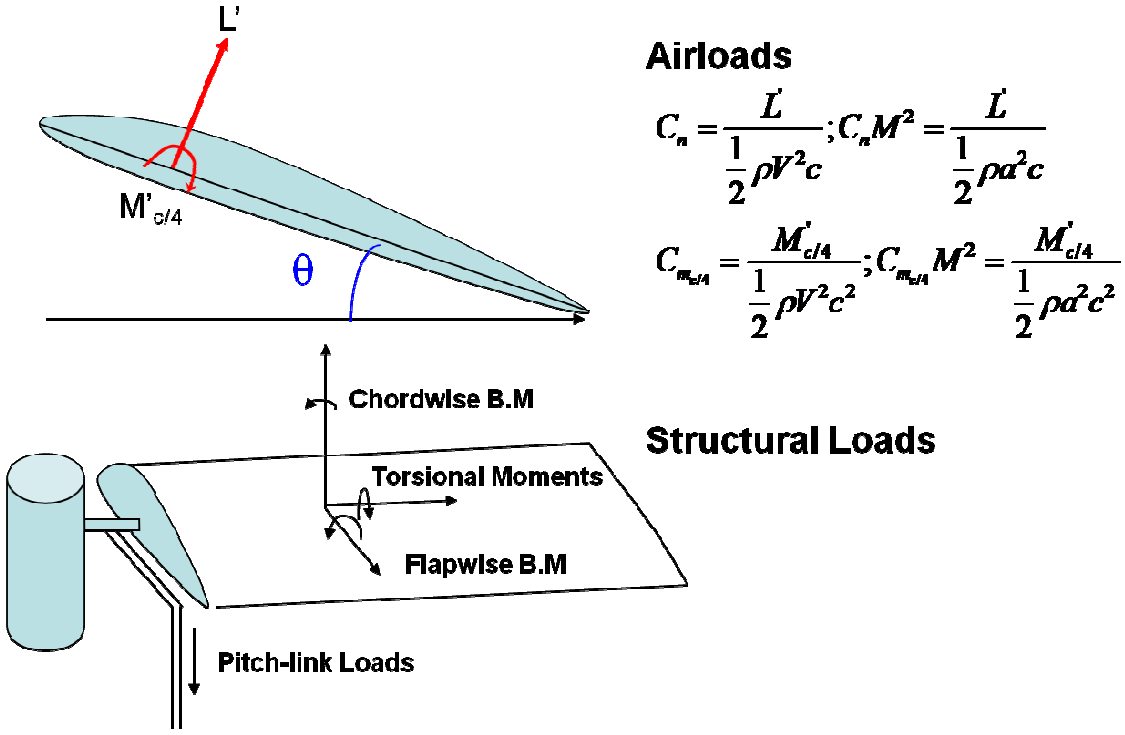

Figure 5.2 Schematic of airloads and structural loads for rotor blade

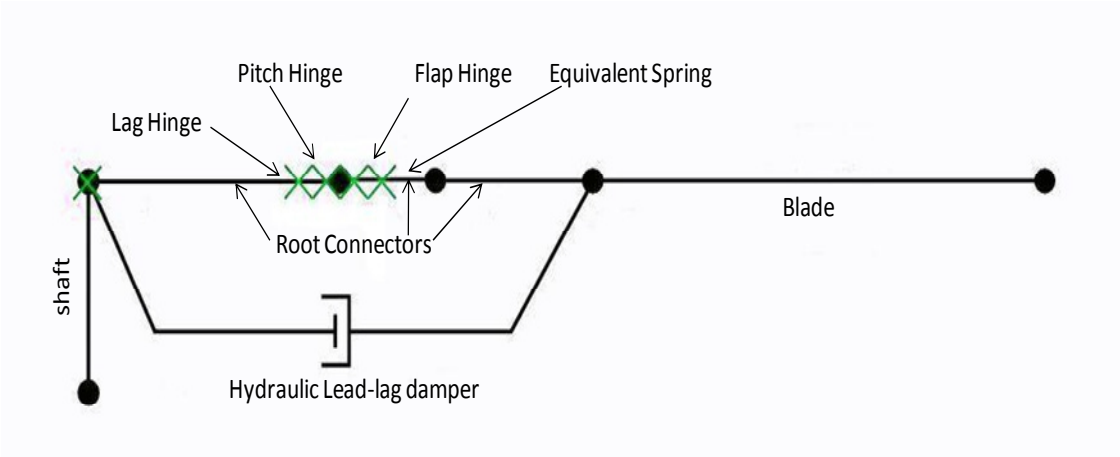

Figure 5.3 Schematic of UH-60A structural model

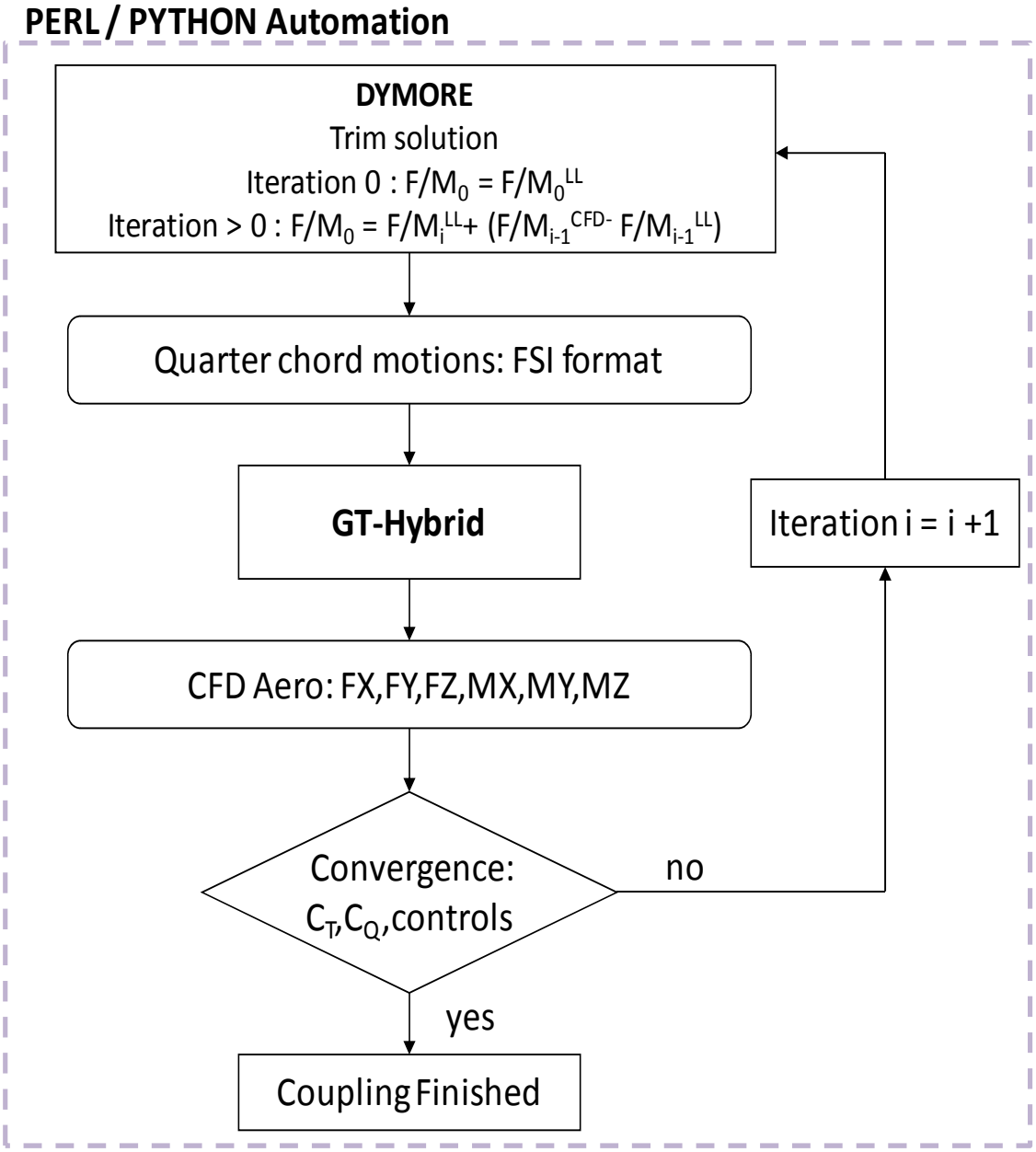

Figure 5.4 Loose coupling methodology between GT-Hybrid and DYMORE

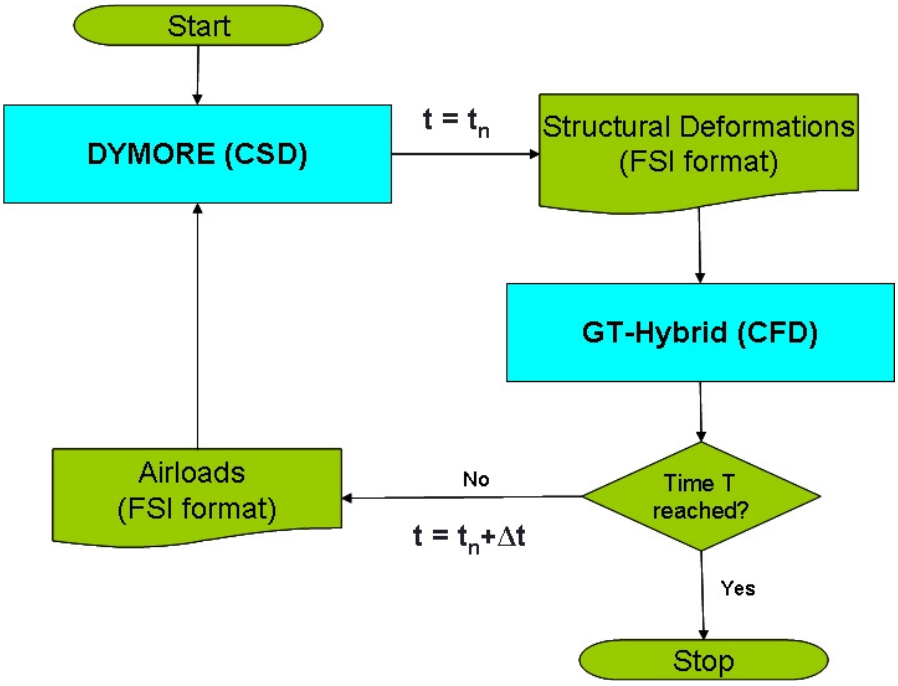

Figure 5.5 Tight coupling methodology between GT-Hybrid and DYMORE

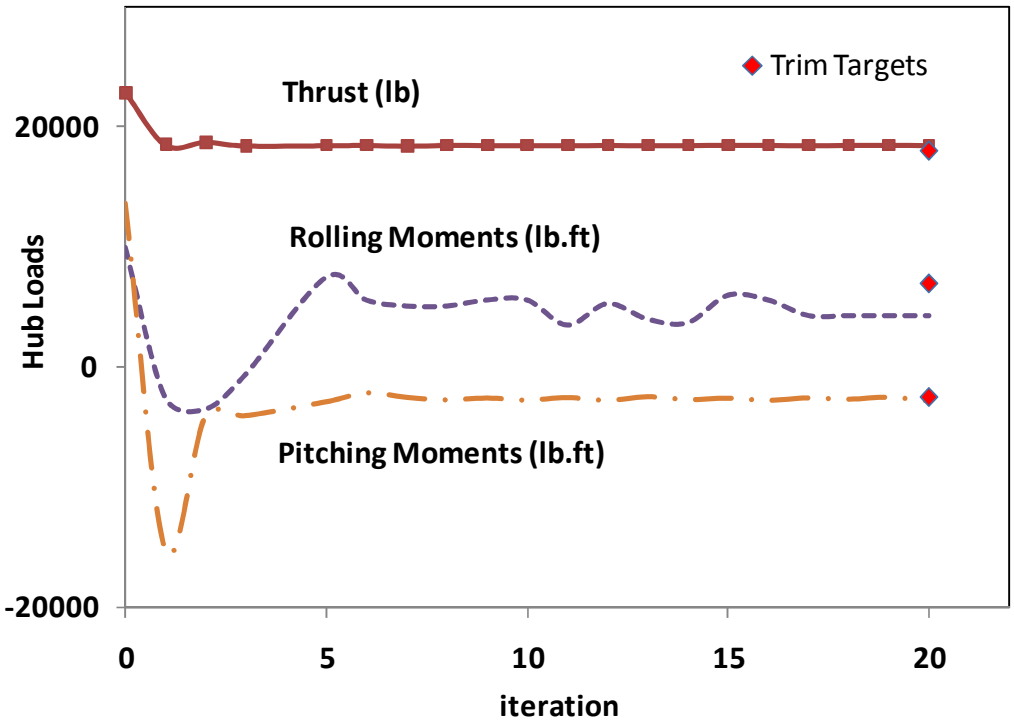

Figure 5.6 Flight counter 8534: Loose coupling hub loads convergence

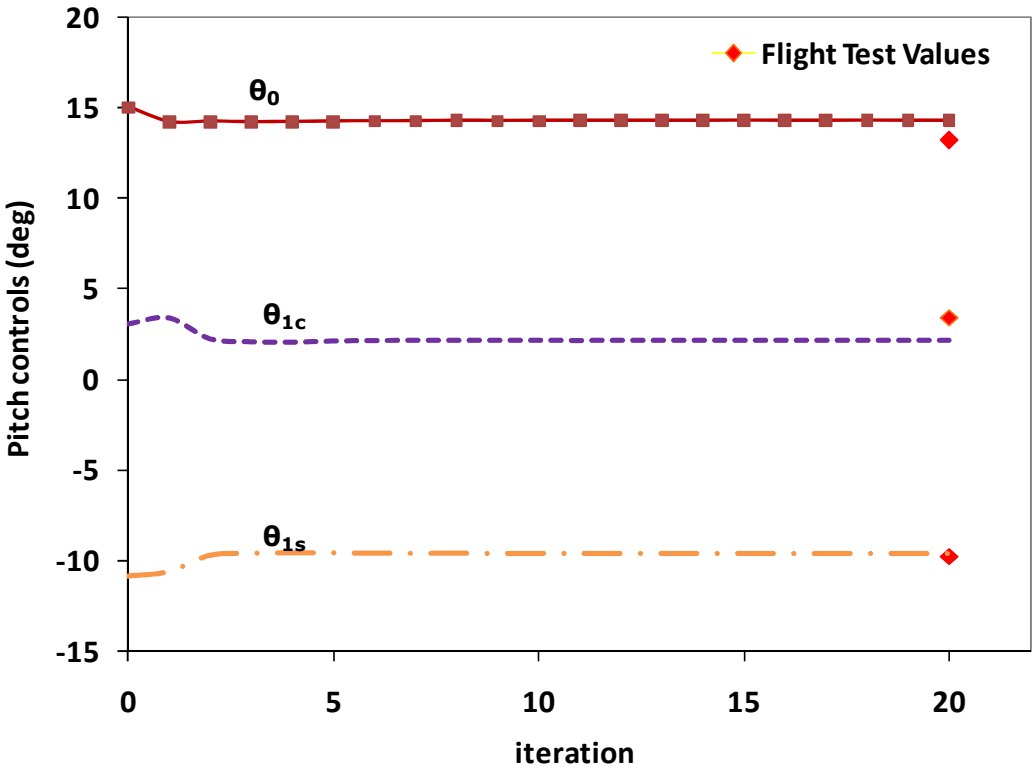

Figure 5.7 Flight counter 8534: Loose coupling pitch angle convergence

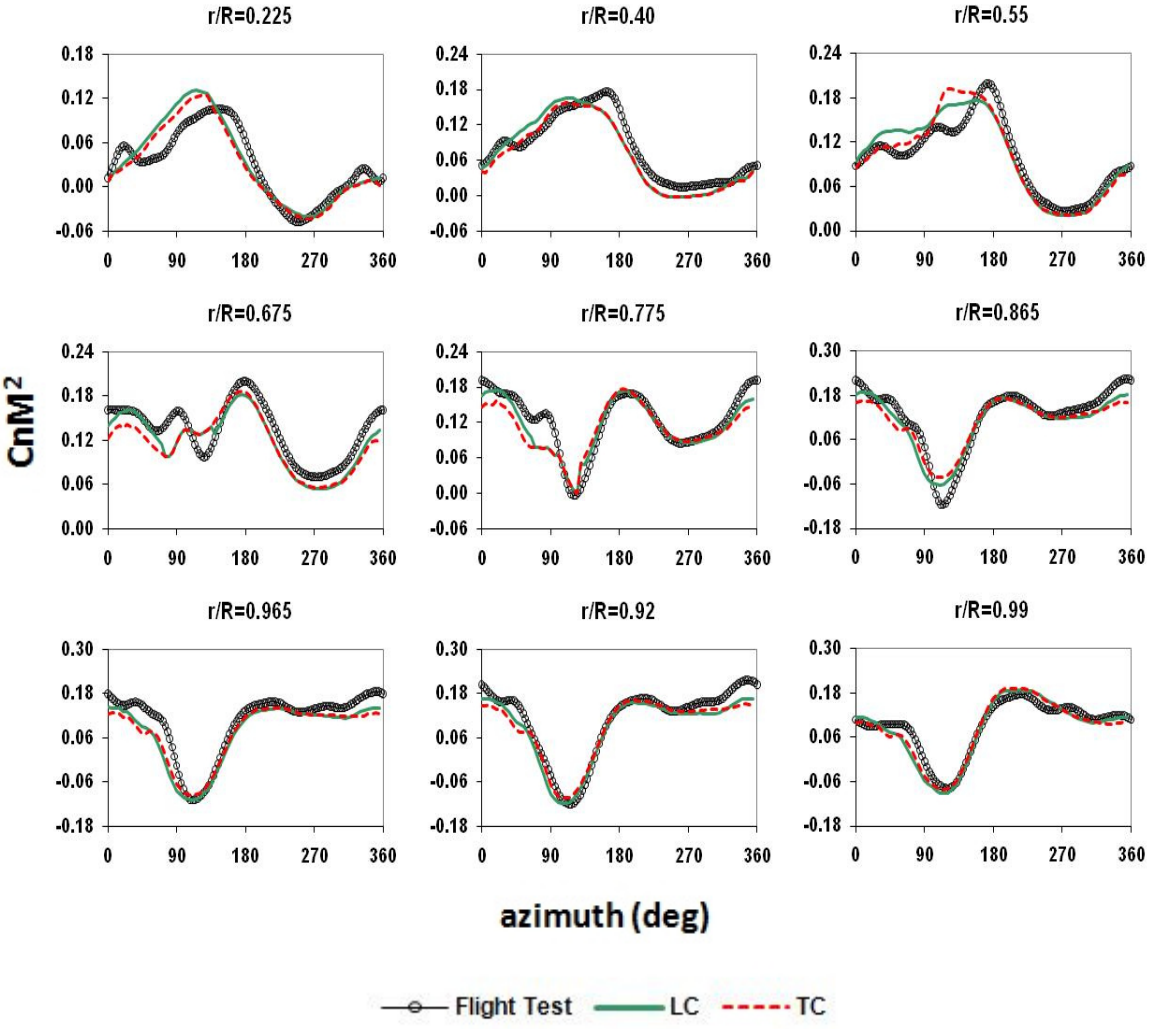

Figure 5.8 Flight counter 8534: Normal forces [TC vs. LC]

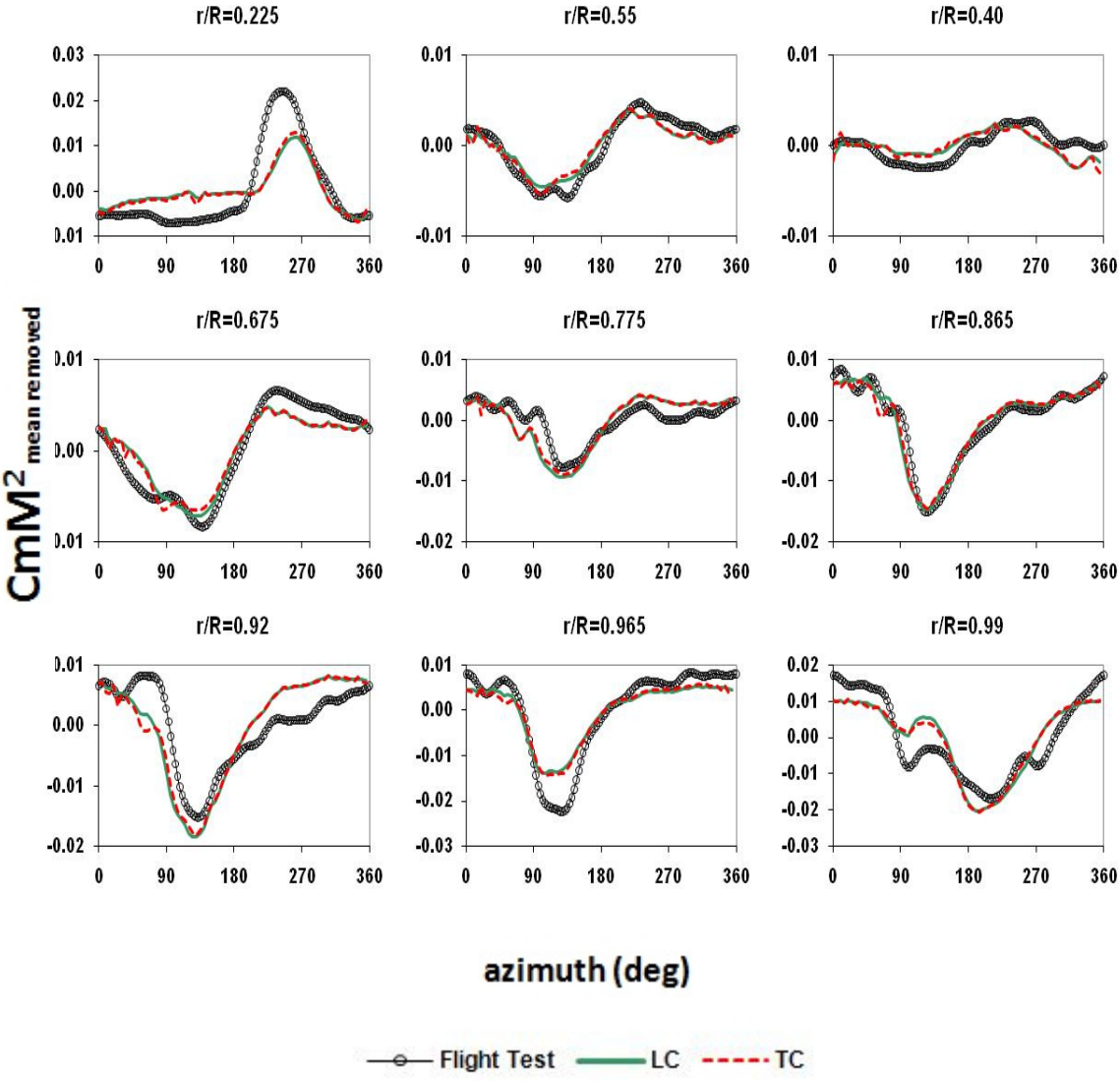

Figure 5.9 Flight counter 8534: Pitching moments (means removed) [TC vs. LC]

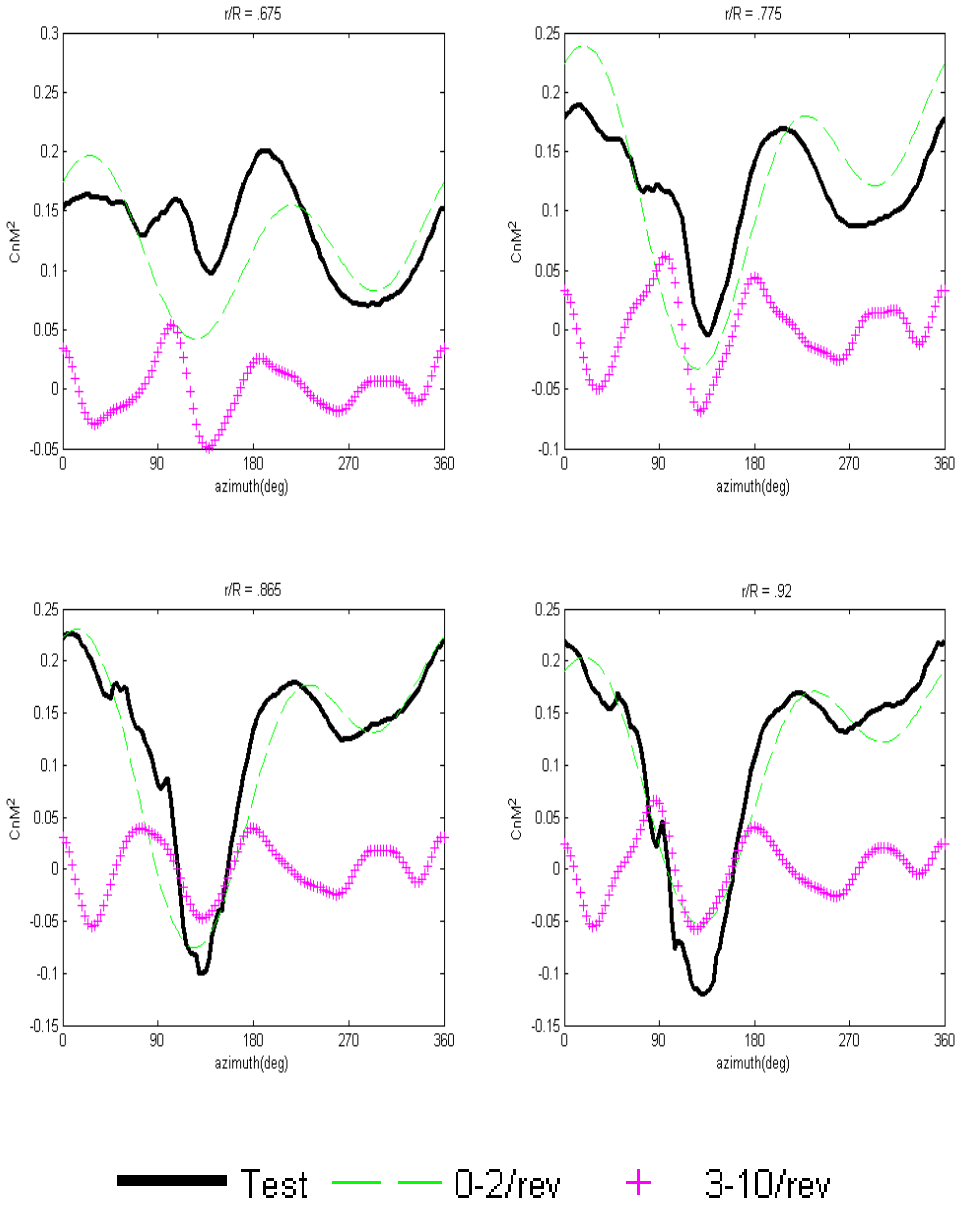

Figure 5.10 Flight counter 8534: Harmonic decomposition of normal forces

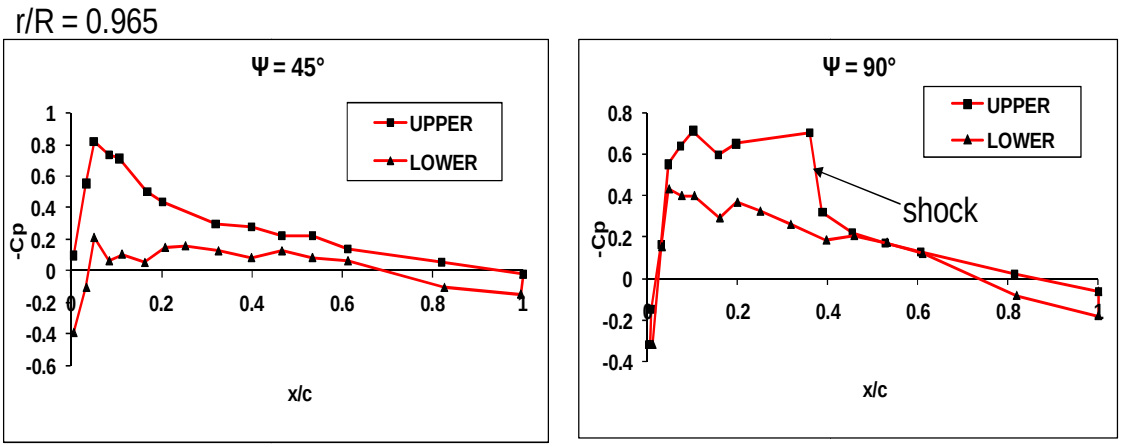

Figure 5.11 Flight counter 8534: Surface Pressure at 96.5%R (test data)

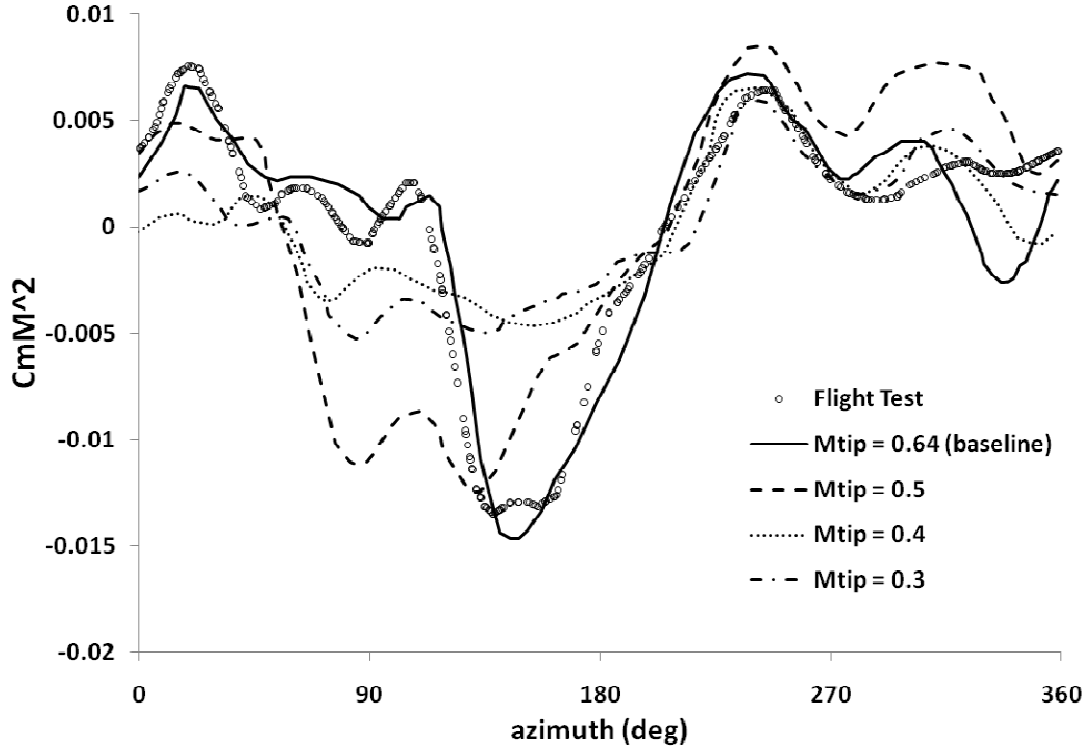

Figure 5.12 Flight counter 8534: Pitching moments (means removed) for different tip mach numbers at 86.5%R

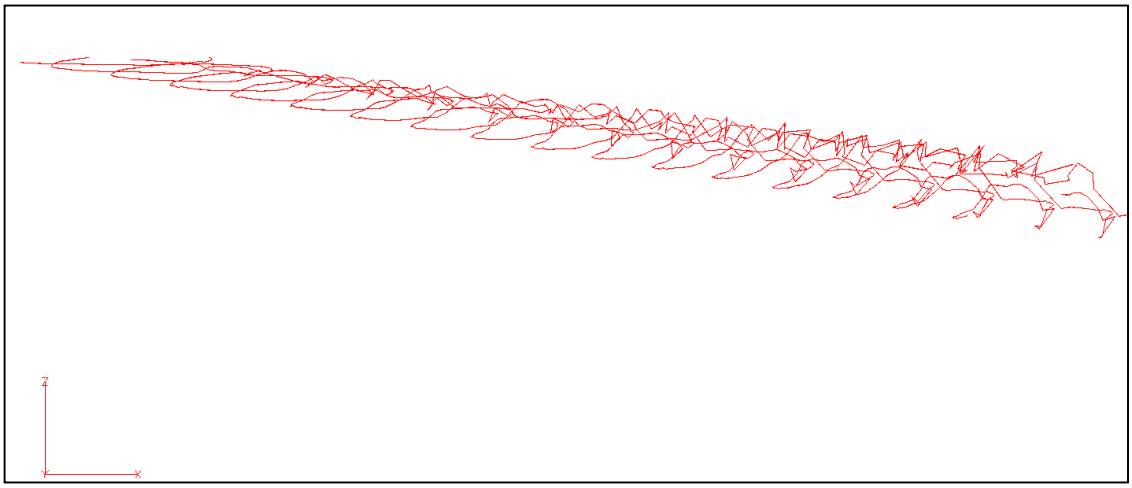

Figure 5.13 Flight Counter 8534: Wake geometry

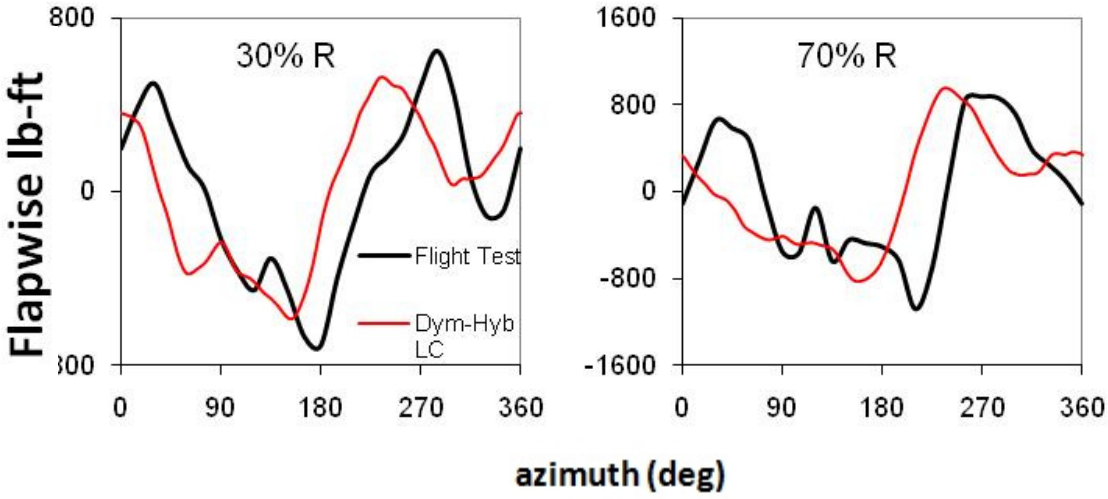

Figure 5.14 Flight counter 8534: Flapwise bending moments

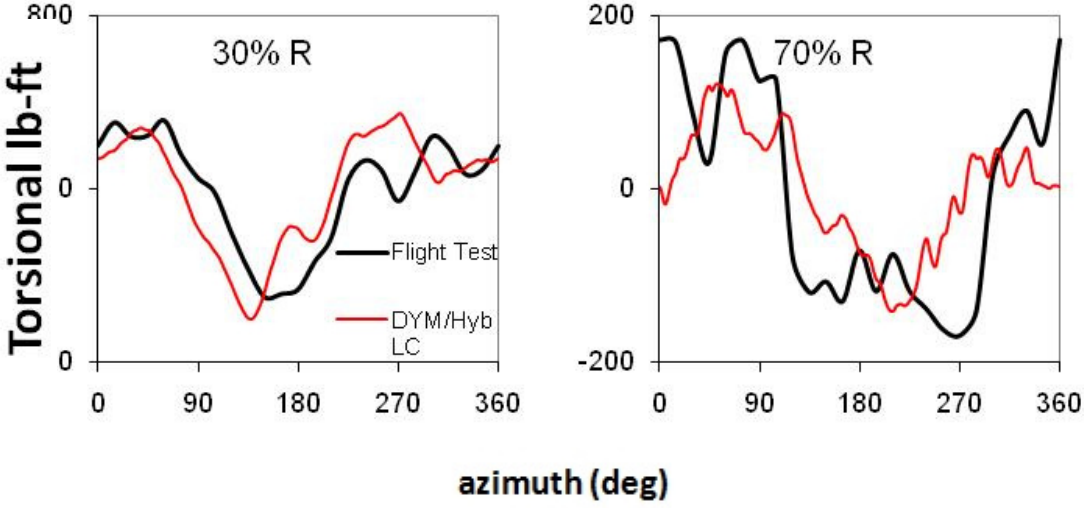

Figure 5.15 Flight counter 8534: Torsional bending moments

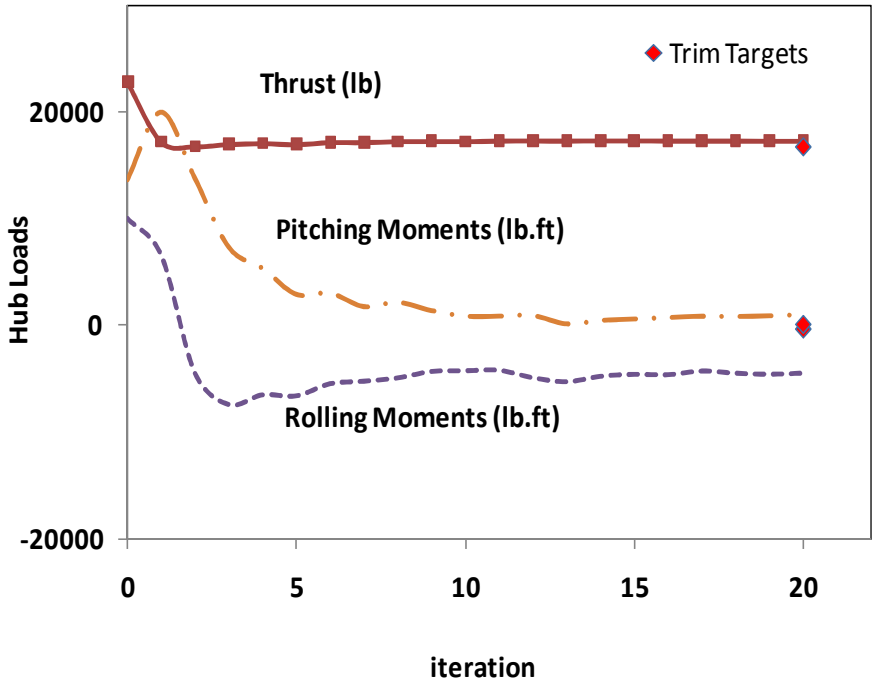

Figure 5.16 Flight counter 9017: Loose coupling hub loads convergence

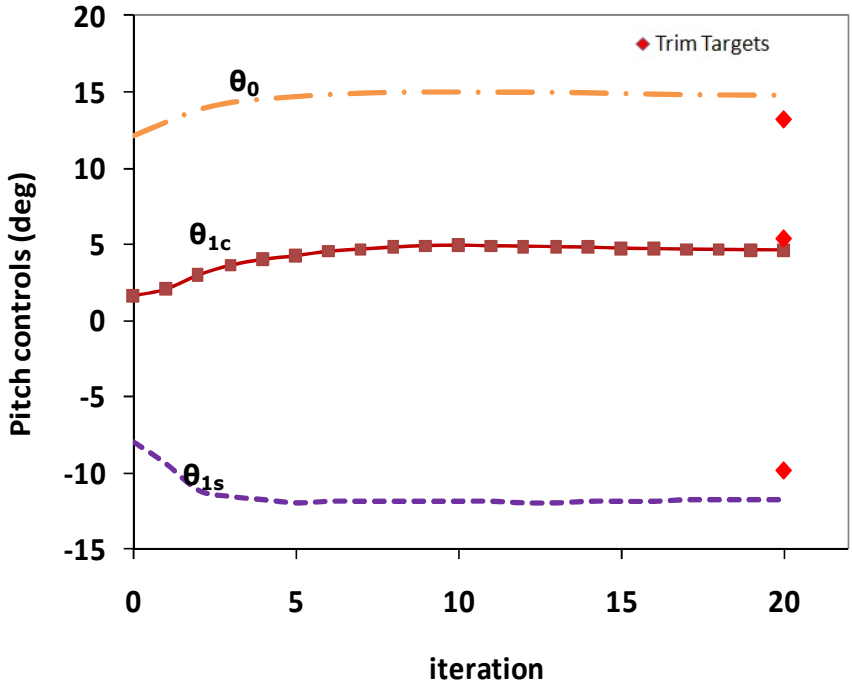

Figure 5.17 Flight counter 9017: Loose coupling pitch angle convergence

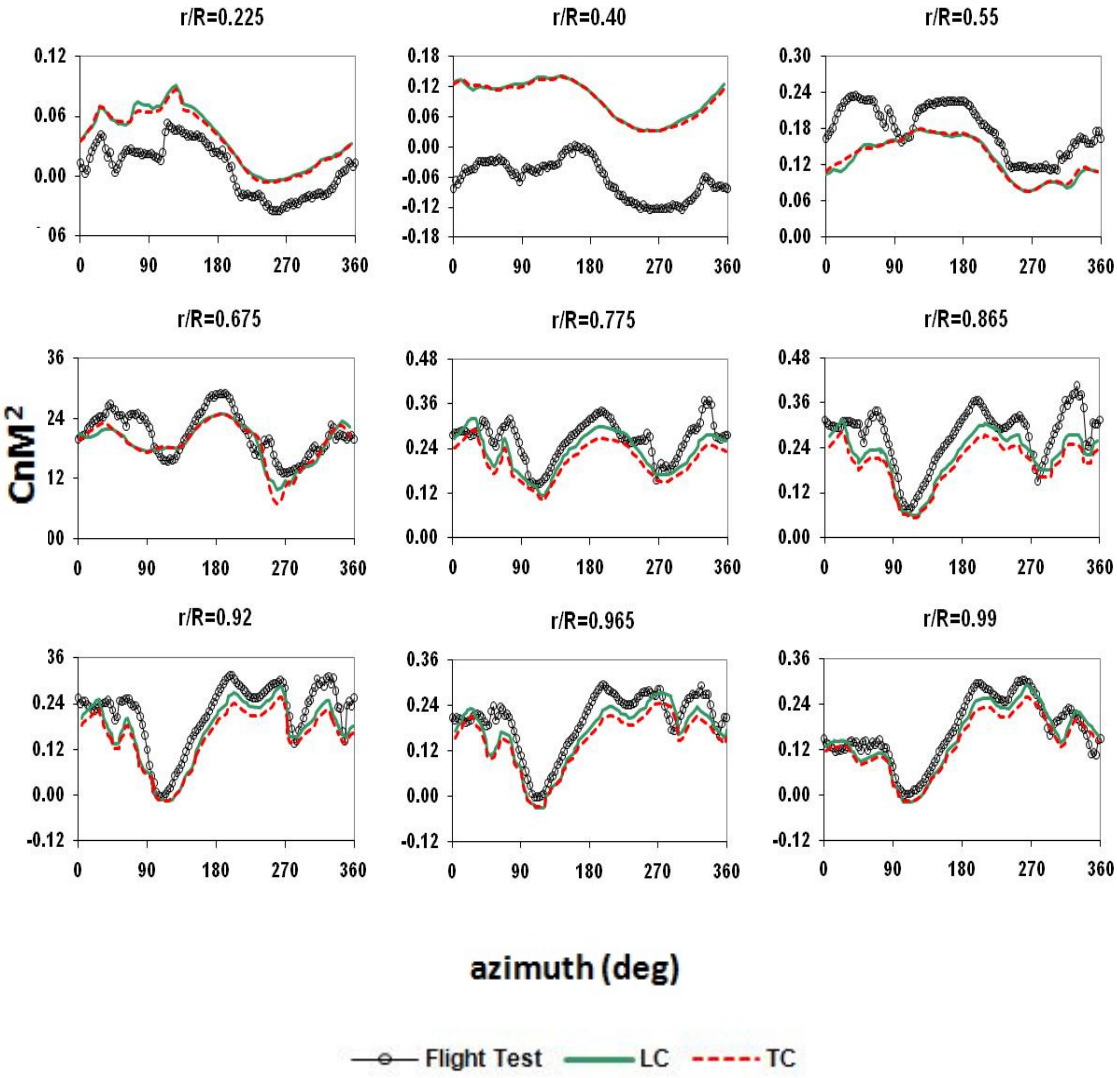

Figure 5.18 Flight counter 9017: Normal forces [TC vs. LC]

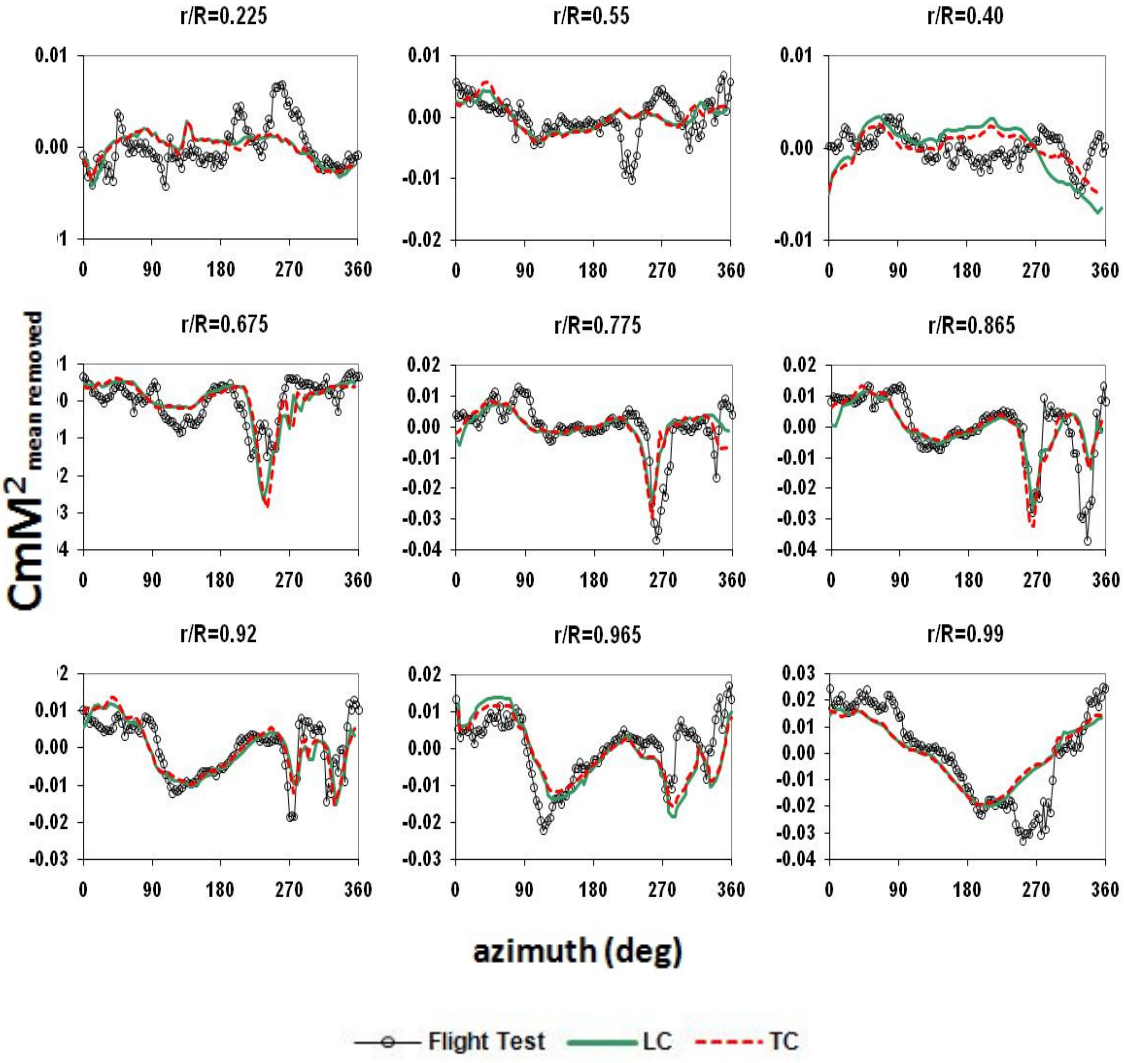

Figure 5.19 Flight counter 9017: Pitching moments (means removed) [TC vs. LC]

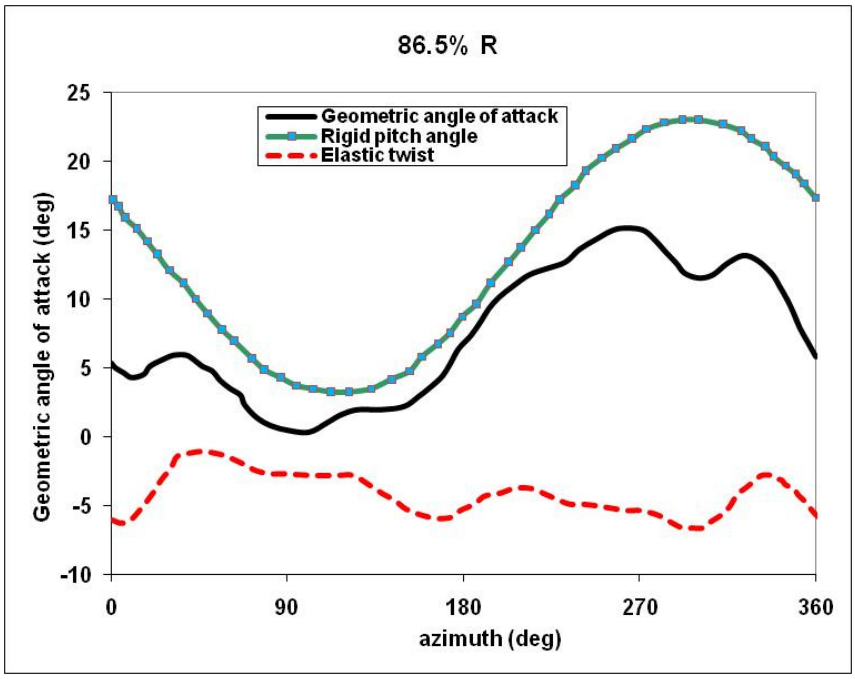

Figure 5.20 Geometric angle of attack at 86.5% R with contributions from pitch angle and elastic twist

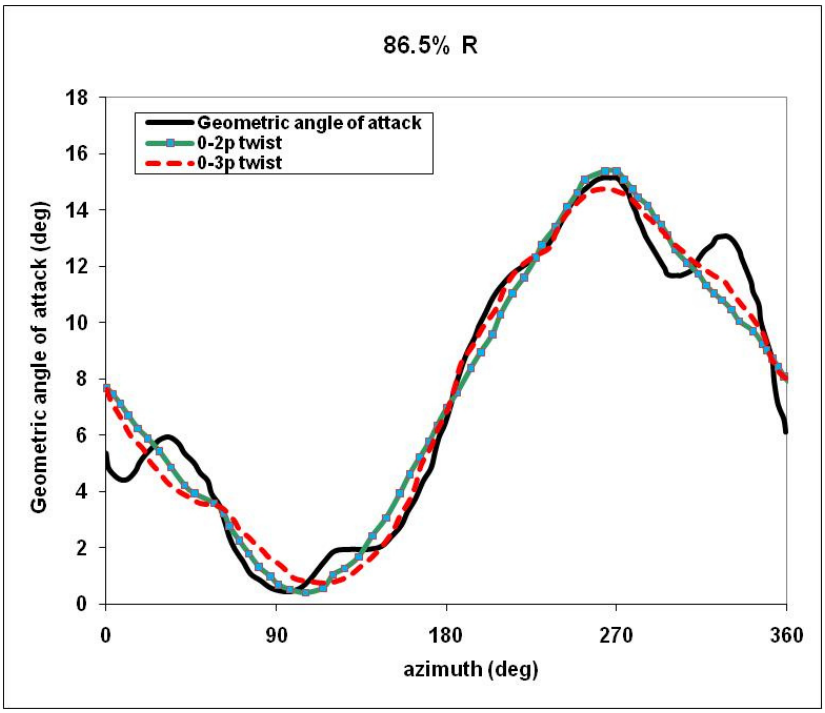

Figure 5.21 Geometric angle of attack at 86.5% R showing higher harmonic twist variation

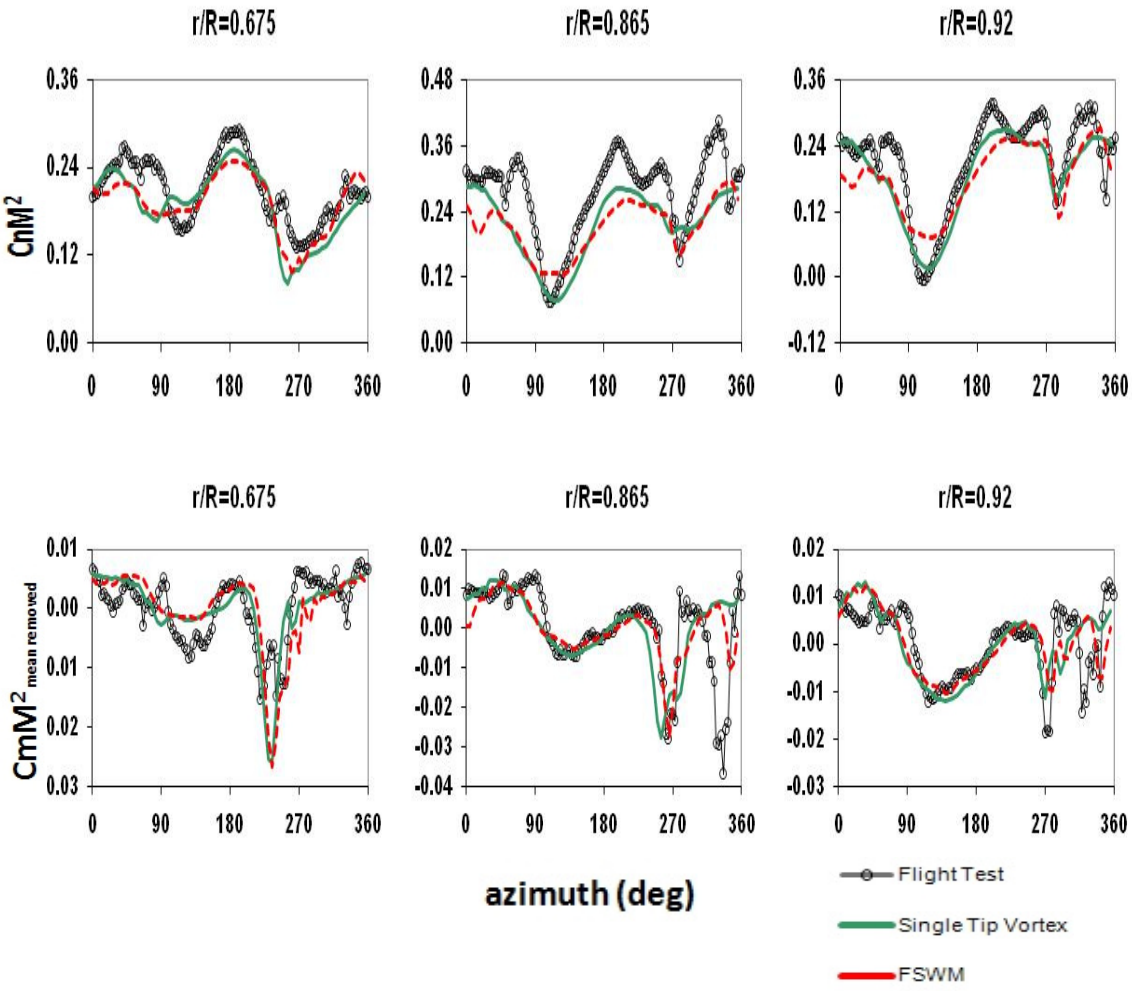

Figure 5.22 Flight counter 9017: Comparison between single tip vortex and full span wake models

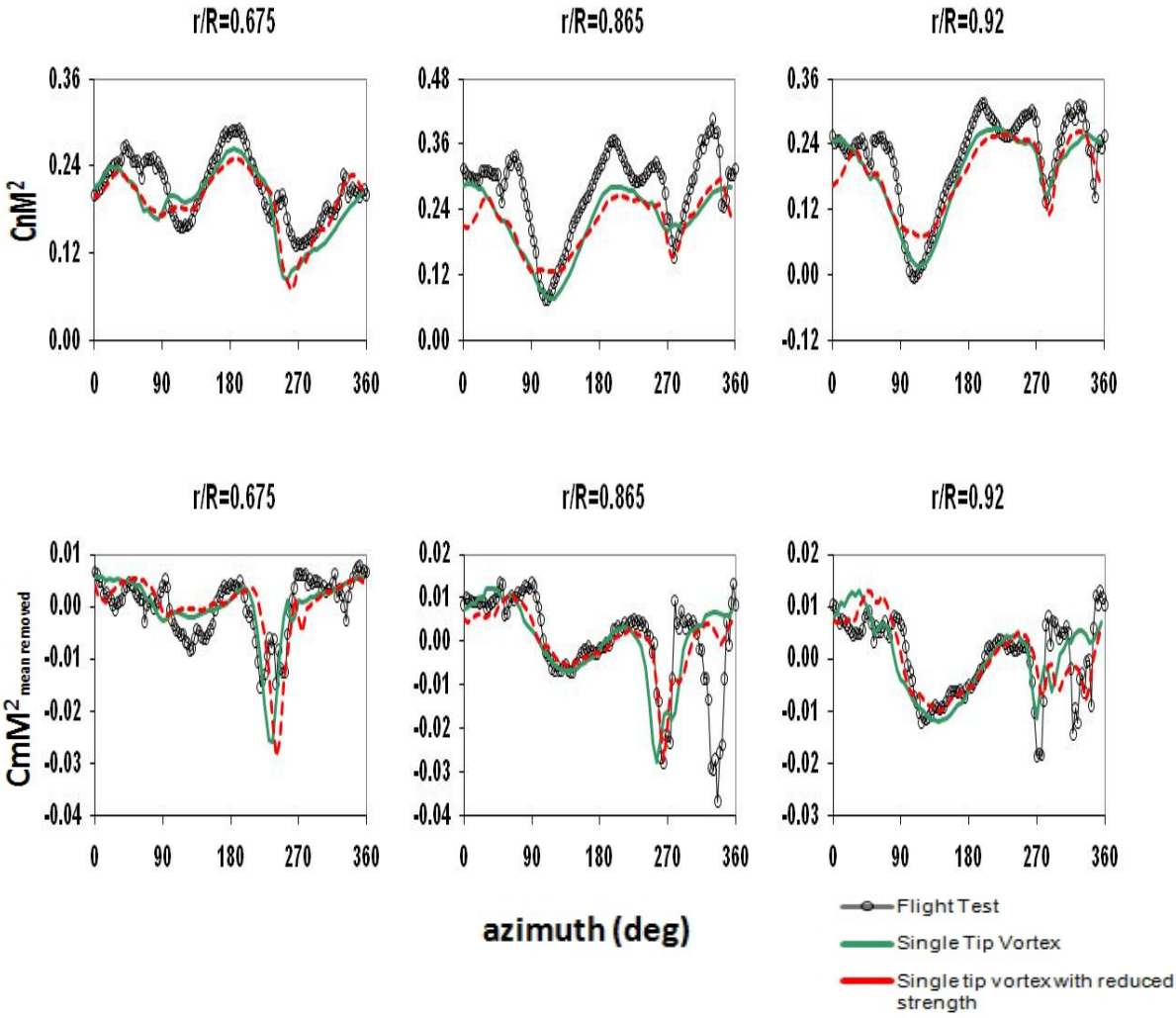

Figure 5.23 Flight counter 9017: Effect of tip vortex strength

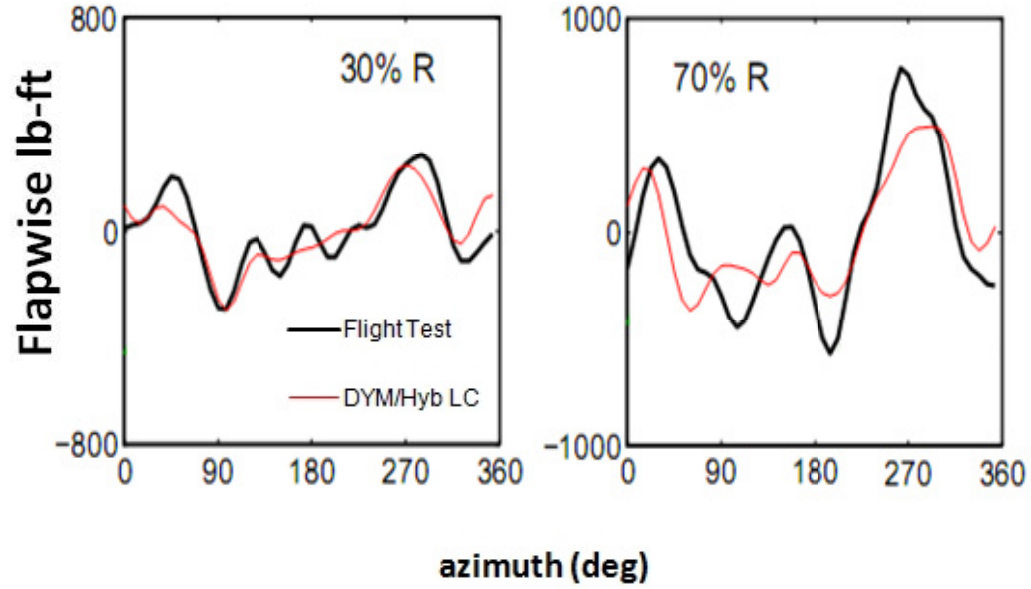

Figure 5.24 Flight counter 9017: Flapwise bending moments

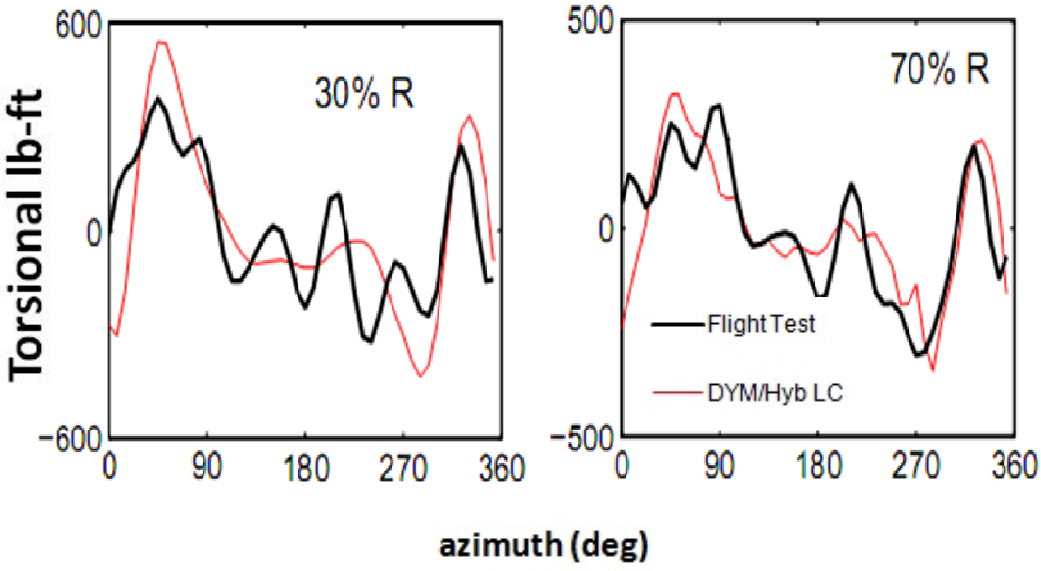

Figure 5.25 Flight counter 9017: Torsional moments

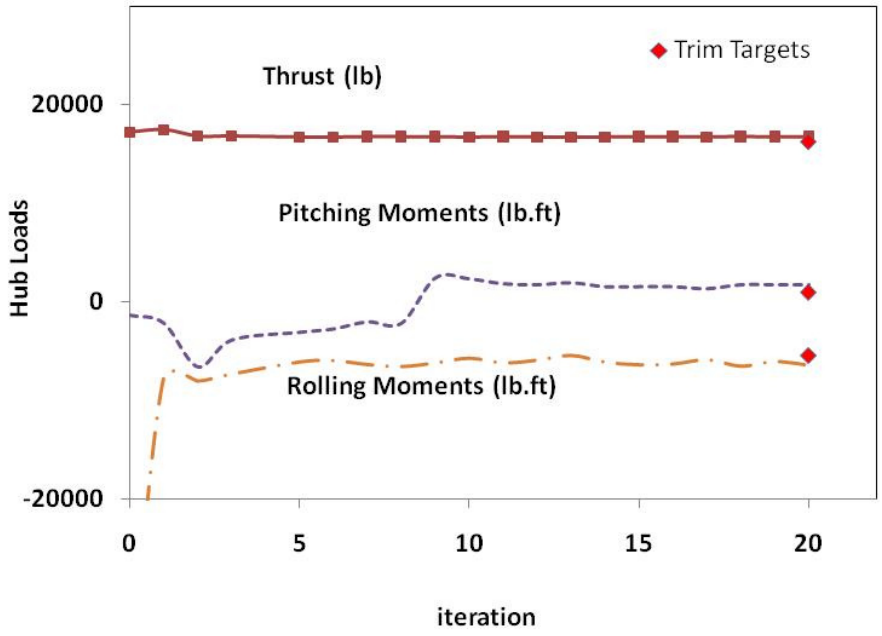

Figure 5.26 Flight counter 8513: Loose coupling hub loads convergence

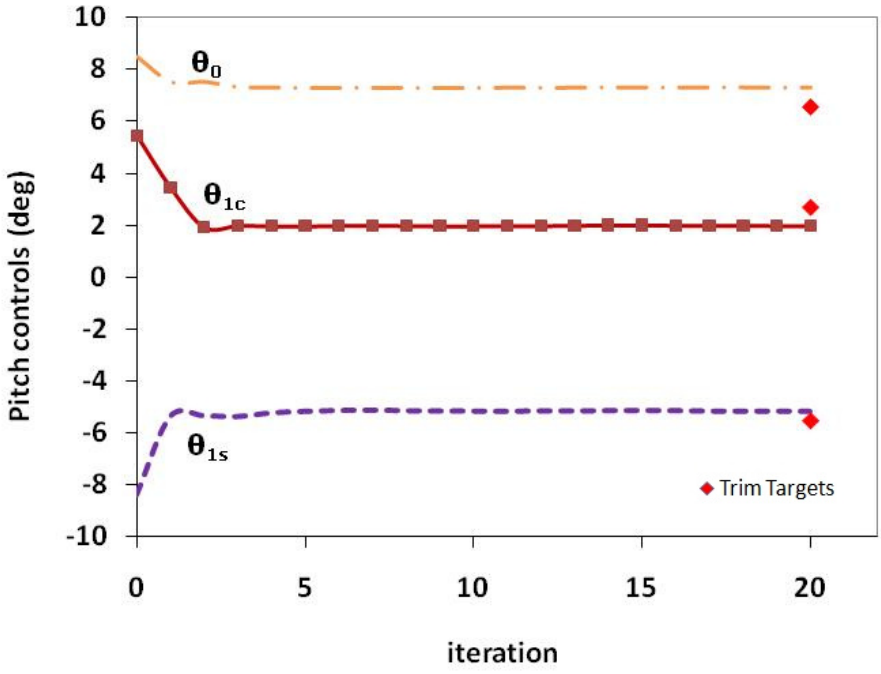

Figure 5.27 Flight counter 8513: Loose coupling pitch angle convergence

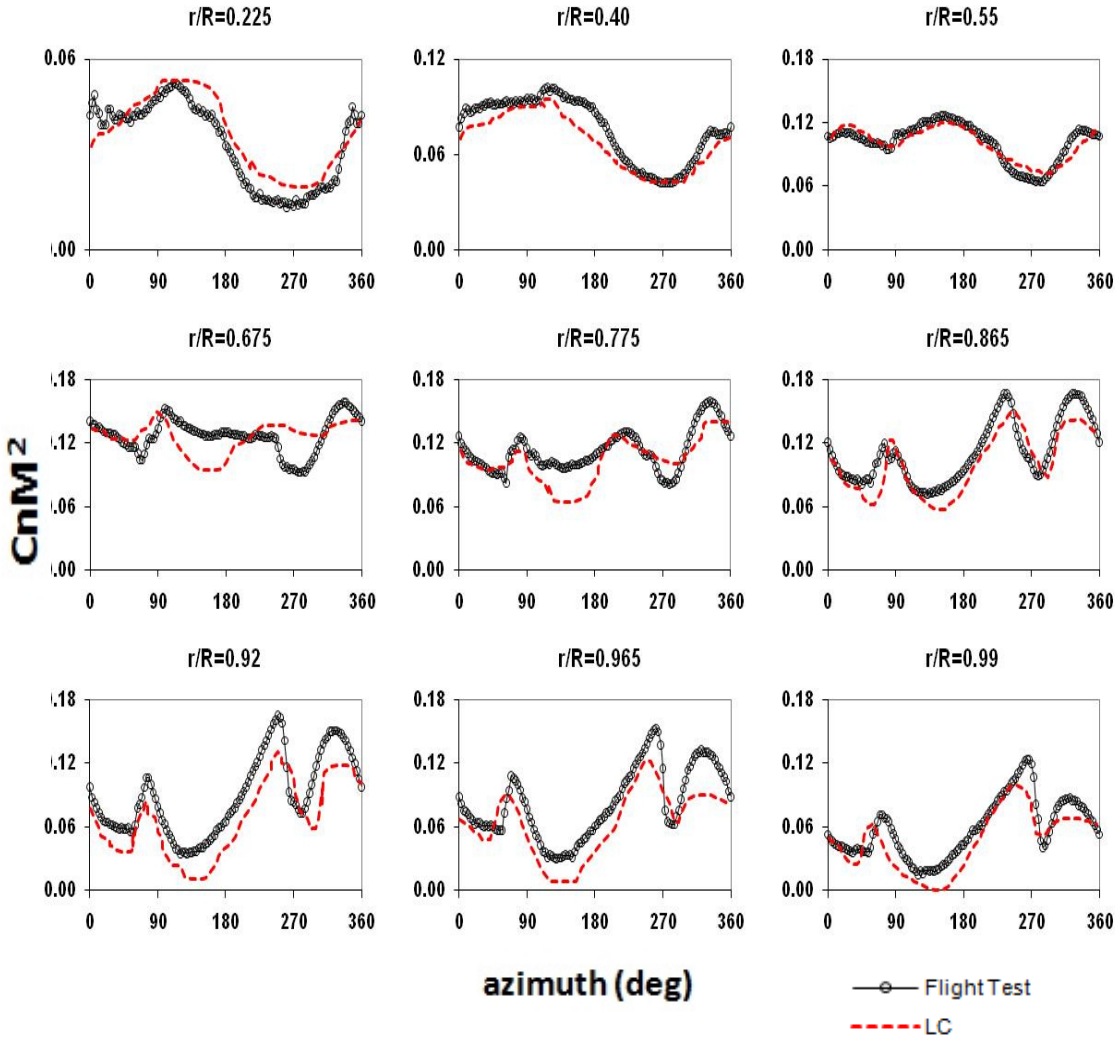

Figure 5.28 Flight counter 8513: Normal forces obtained using LC

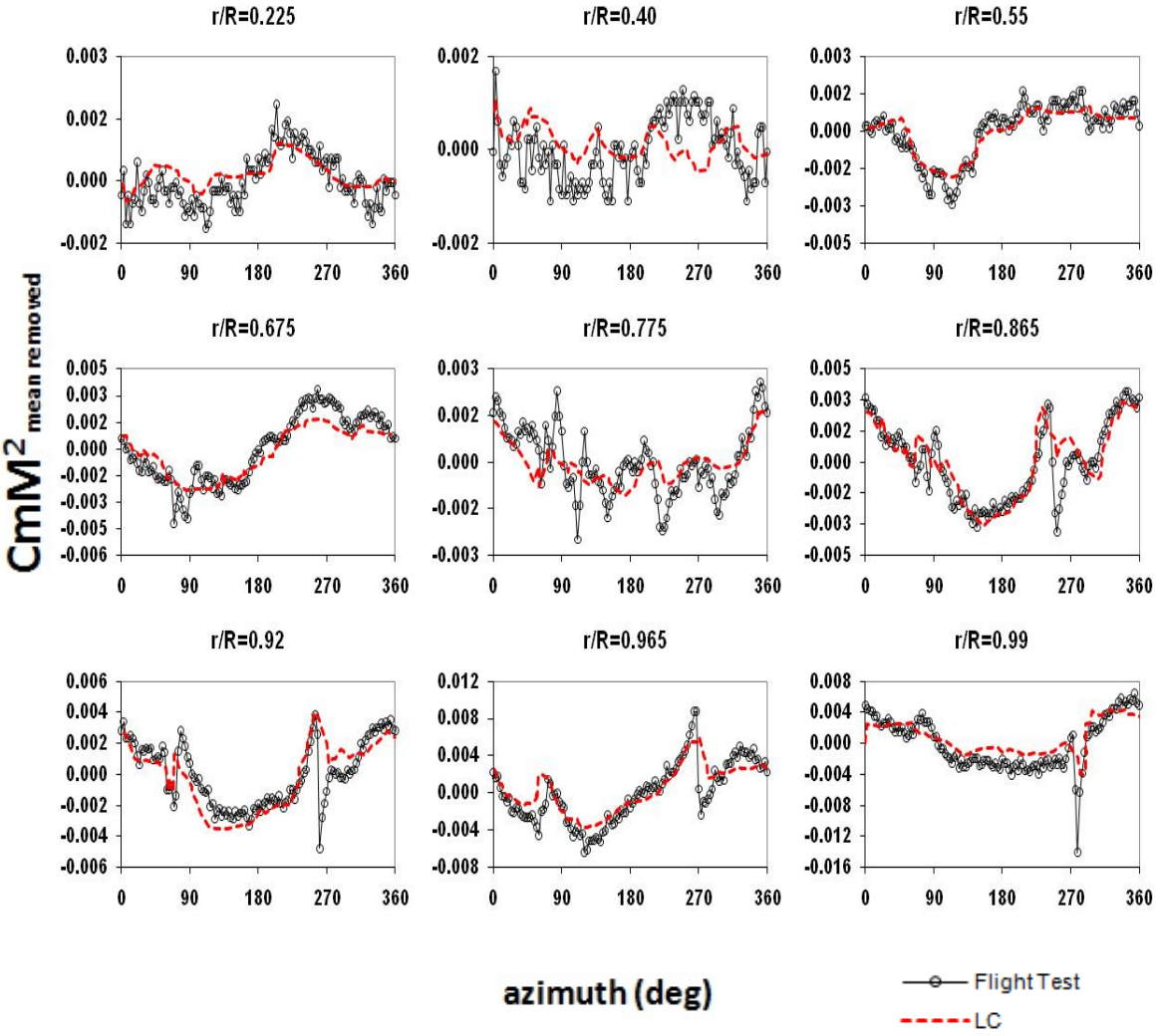

Figure 5.29 Flight counter 8513: Pitching moments (means removed) obtained using LC

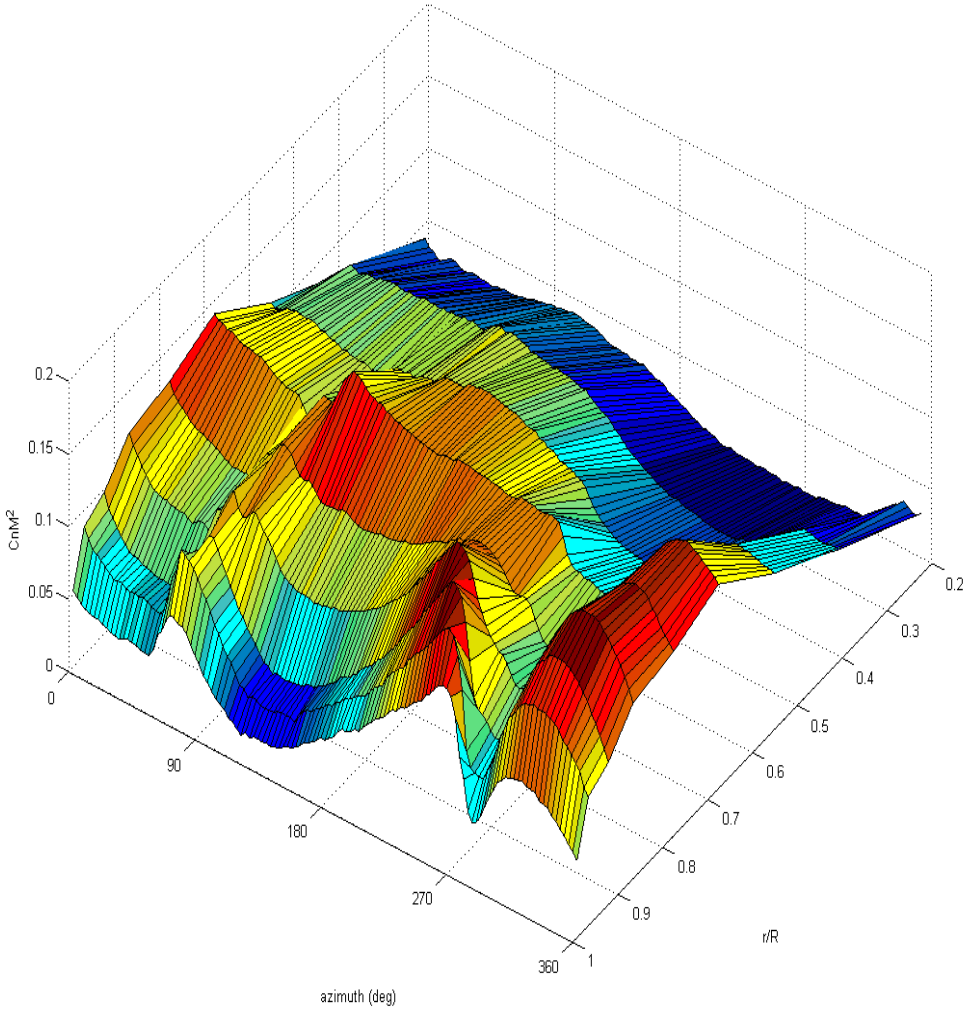

Figure 5.30 Flight counter 8513: Normal forces surface

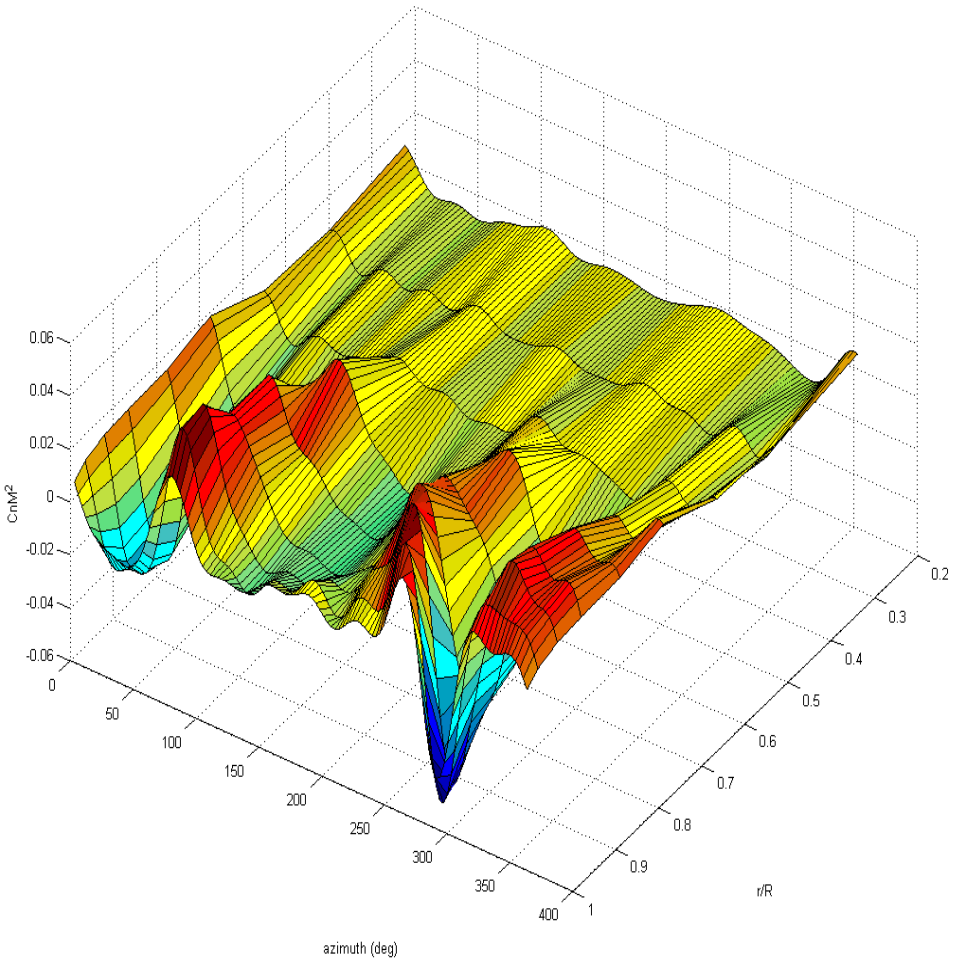

Figure 5.31 Flight counter 8513: Normal forces surface (3-10/rev)

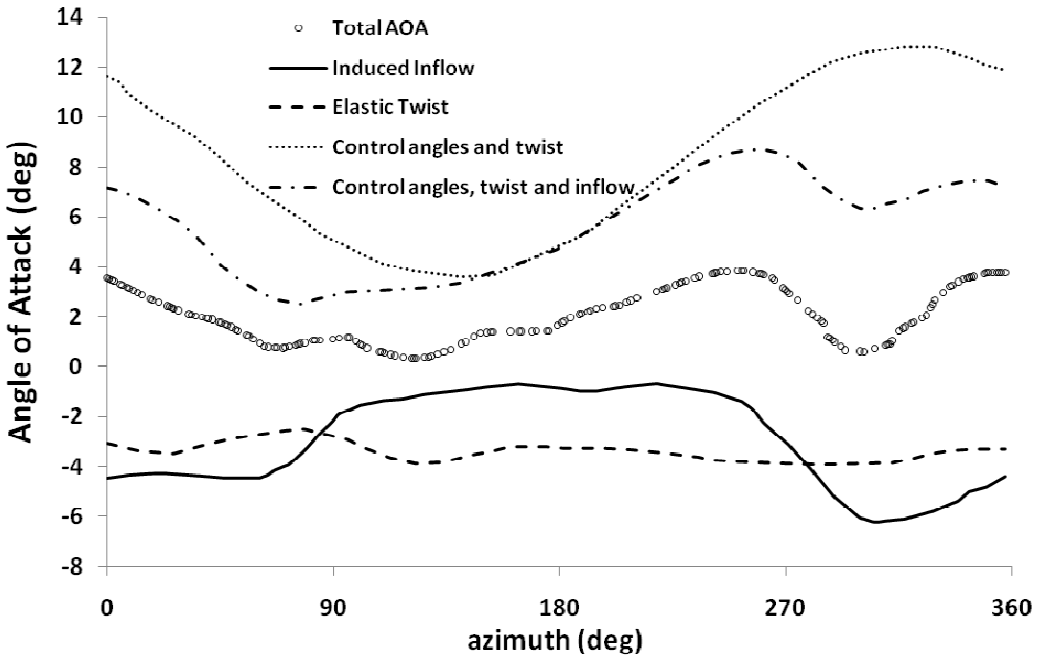

Figure 5.32 Flight counter 8513: Angle of attack at 77.5%R

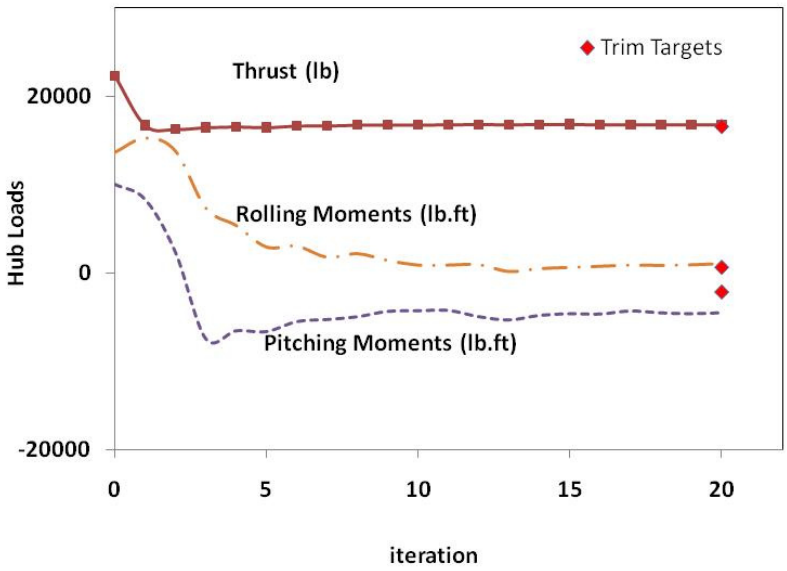

Figure 5.33 Flight counter 9020: Loose coupling hub loads convergence

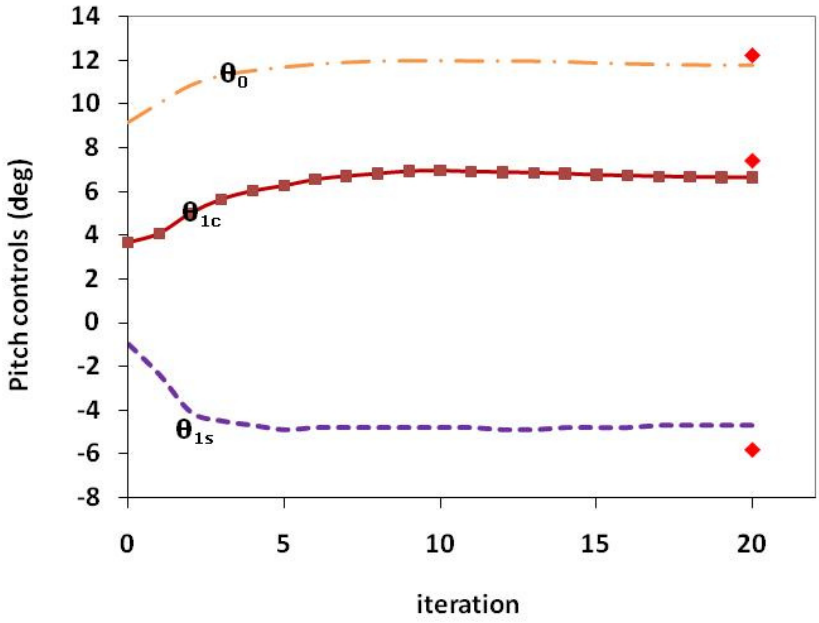

Figure 5.34 Flight counter 9020: Loose coupling pitch angle convergence

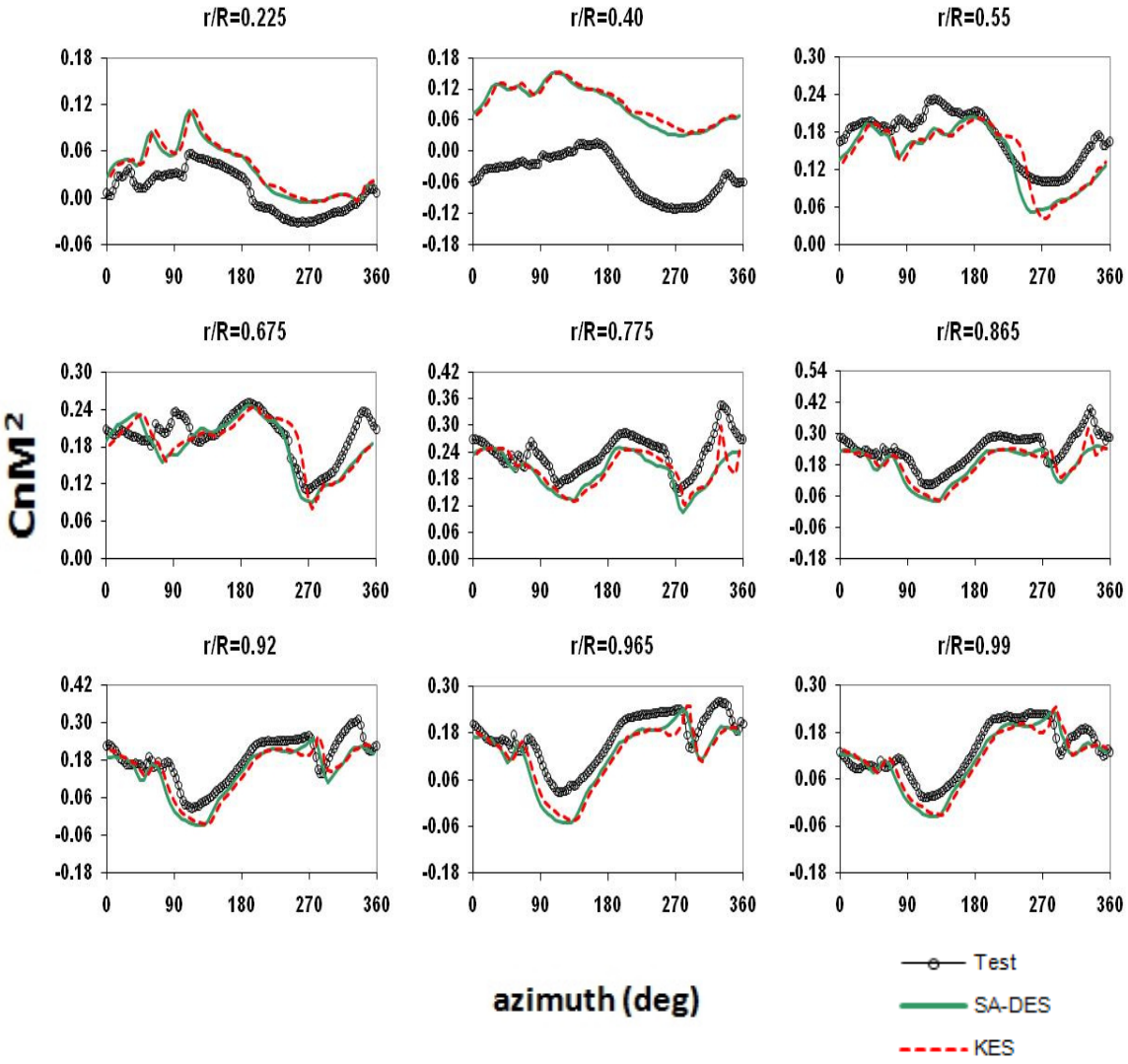

Figure 5.35 Flight counter 9020: Normal forces obtained using LC

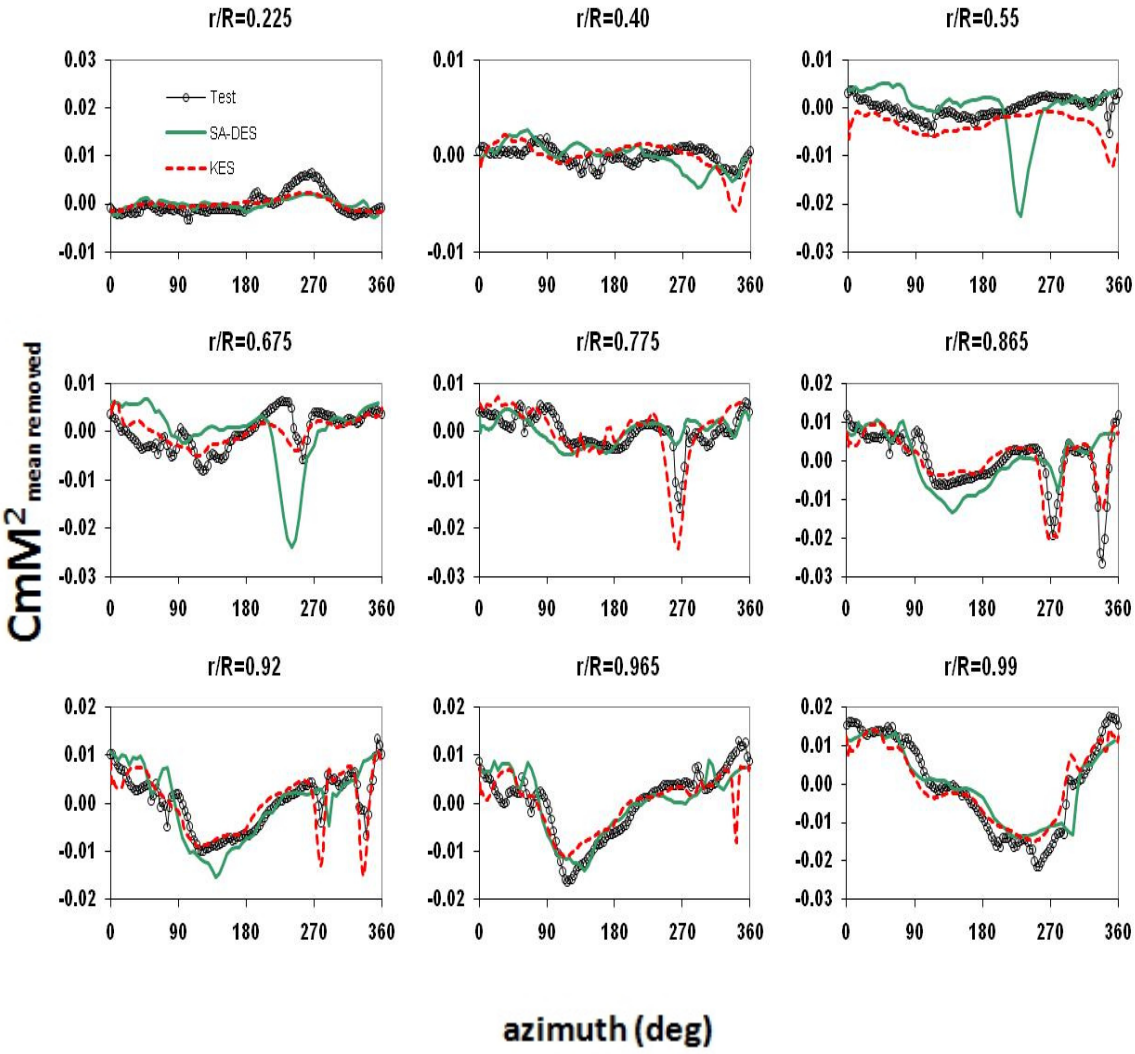

Figure 5.36 Flight counter 9020: Pitching moments (means removed) obtained using LC

CHAPTER 6

RESULTS PART II: CFD/CSD COUPLING FOR MANEUVERING FLIGHT CONDITIONS

The previous chapter studied the key phenomena characterizing some of the UH-60A steady flight conditions. The rotor experienced distinct phenomena in these flight conditions based on the speed regime and thrust settings. In this chapter, the validated loose and tight CFD/CSD coupling methodologies shall be extended to analysis of the UTTAS 11029 pull-up maneuver. The entire maneuver is over 40 rotor revolutions. In this study revs 1-5 and revs 15-17 have been chosen for analysis. Revs 1-5 represent high speed steady flight conditions whereas the helicopter experiences the maximum load factor during revs 15-17. Since the CFD and CSD methodologies are solved in a shaft frame, modifications are necessary to incorporate the translational and rotational motions of the hub, including the angular rates and accelerations. The maneuvering flight simulations are fundamentally different from steady flight simulations in the sense that the vehicle states are not known a priori. Therefore, the rotor blade pitch control angles either need to be estimated using an inverse flight simulation or should be available from flight test data. In this chapter, the flight test data is used to drive the coupling simulations. Some errors were observed in the flight test measurement which shall be addressed before attempting the maneuvering simulations.

6.1 UTTAS 11029 Maneuvering Flight Condition

A terrain avoidance maneuver was made part of the performance specification for the U.S. Army's procurement of the Utility Tactical Transport Aerial System (UTTAS)

program in the early 1970s. This procurement, which funded prototype aircraft from two manufacturers, led to the development of the UH-60A. The UTTAS maneuver was defined in two parts: a pull-up and a pushover. The specification for the UTTAS pull-up was that the maneuver was to be entered at maximum level flight speed and the pilot was to pull the aircraft's nose up to quickly obtain a load factor of 1.75g, and the load factor was to be held for three seconds without losing more than 30 knots of airspeed. The highest loaded maneuvers of the UH-60A helicopter have been studied in great detail by Bousman et al. [116,117]. Based on the criteria of six structural measurements: pitch-link load, torsion moment (30% R), and flap and chord bending moments (11.3% R and 60% R), they identified and ranked the severest maneuvers. Out of the two severest maneuvers, the second most severe maneuver, designated by Counter 11029, produces the highest root flap bending moment and the third highest oscillatory pitch-link load of all the UH-60A maneuvers. Therefore, this maneuver is a good candidate for aeromechanical studies.

The pull-up in the UTTAS 111029 maneuver was initiated when the helicopter was flying at 158 knots high-speed, level flight for a period of five rotor revolutions. The aggressive pull-up achieved a 2.1g normal load factor within approximately two sec. The pull-up was executed primarily as a longitudinal maneuver and concluded with a pushover recovery. After 40 rotor revolutions the aircraft returned to roughly 0.65g normal load factor with the entire maneuver lasting about 9.5 sec. Figure 6.1 includes a representative maximum thrust boundary as determined by the wind tunnel tests of McHugh. Also included is the time varying C_w/σ vs. μ values for the UTTAS pull-up maneuver. The maneuver begins near the maximum level flight speed of the aircraft and

achieves a significant normal load factor at 139 knots that significantly exceeds the steady state McHugh boundary ($n_Z C_W/ \sigma = 0.165$ vs. 0.12).

Figure 6.2 shows the vehicle attitude in the maneuver. The initial period of steady-state level flight extends for about four rotor revolutions before the aft longitudinal cyclic input is initiated. A small discrepancy (approximately 3 deg.) in vehicle angle of attack and pitch attitude is present which was corrected for the simulations. Theoretically, in level flight, angle of attack and pitch attitude should be identical. It is surmised that the angle of attack measurement may be influenced by the fuselage and rotor flow-field in high speed flight. Figure 6.3 shows the vehicle velocity components in the maneuver. Advance ratio decreased from 0.36 to 0.22 in the maneuver.

The pitch control time history is important to accurately calculate the rotor response. During the UH-60A flight tests, motion of each of the four blades was measured with specially designed instrumentation. The flapping, lead-lag, and pitch motion of the blade root is defined by rotations of the blade spherical elastomeric pitch bearing. These rotations were indirectly measured by a mechanical apparatus known as blade motion hardware (BMH) consisting of a system of links and rotary transducers. The blade pitch, flap, and lead-lag angles were obtained from a non-linear transformation of the BMH angle measurements. Since the transformation related all three BMH angles to all three blade motion angles, experimental error in a single BMH angle measurement propagated to all three transformed blade angles. In fact, several of the BMH angle data records for counter 11029 contained significant measurement errors for blades 1 and 4 [60]. Consequently, the rotor collective and cyclic pitch input time histories were based

on only the blade 2 and 3 pitch angles. A windowed FFT analysis of blade 2 and 3 pitch angle data was performed to determine the effective collective and cyclic time histories.

6.2 Extension of CFD/CSD Methodology for Maneuvering Flight Simulations

6.2.1 CFD Methodology

The CFD methodology needs to be modified for maneuvering flight analysis. A single blade grid was used for all the steady flight simulations. The effect of the other blades was simulated through the wake model. But this method will work only if the blade experiences the same flow conditions every revolution i.e. the flow is unsteady but periodic with a time period of one rotor revolution. The maneuvering flight simulation requires the flow to be solved over all the blades simultaneously to account for the time varying pilot input. Therefore, the CFD methodology was modified to handle multiple blade grids simultaneously. The hierarchical MPI parallelization was used to parallelize each blade grid independently. For steady flight simulations, a multi-blade simulation requires lower number of rotor revolutions to achieve flow-field periodicity since the vortex strengths of the wake from all the blades are being updated through N-S solution simultaneously. Therefore, for a rotor with N blades, a multi-blade simulation requires only 1/N times the number of revolutions required by the single blade simulation. This coupled with the fact that hierarchical MPI enables the parallelization of each blade grid simultaneously decreases the computational time by a factor of N. A four blade grid for the UH-60A rotor is shown in Figure 6.4.

The hybrid CFD methodology solves the flow-field over an isolated rotor in a non-rotating hub/shaft frame. This means that the motion of the hub in the maneuver needs to be applied to the CFD simulation in a hub fixed frame. This is achieved by

transforming all translational and rotational velocity components to the hub frame and adding them to the grid velocity terms in the CFD solver. The wake model is modified to account for the vehicle motion. Since the wake is shed from the blade and evolves in a hub fixed frame, the motion of the hub is simulated as a convection of the wake with respect to an observer placed on the hub.

The measured vehicle velocity was combined with the angle of attack and sideslip angle to calculate the three velocity components in vehicle body axes. An error in the angle of attack was noted in the previous section. The current analysis addresses this by applying a constant shift in the angle of attack measurements such that the initial pitch angle and angle of attack coincide. These velocity components were obtained in shaft frame through coordinate transformations accounting for 3 degree shaft tilt. Similarly, the angular velocity components in shaft coordinates were obtained from angular velocity components measured in vehicle body coordinates. The resulting hub translational and angular velocity components are shown in Figures 6.5 and 6.6, respectively. The angular velocity components are converted to grid velocity components through cross product of the angular velocity vector with the position vector of the grid point.

6.2.2 CSD Methodology

The rotor model for the CSD methodology includes a control system that is different from what was used for the steady flight conditions. The control system includes pushrods, pitch horns, rotating and fixed swashplates. The previous model applied the pitch control laws directly at the revolute joints whereas in this model, the control laws are applied at the swashplate. The reason for choosing a swashplate model was to analyze the pitch-link loads developed during the maneuver. Figure 6.7 shows a representation of

the UH-60 rotor modeled using DYMORE. The pitch-links were modeled as rigid elements connected to a prismatic joint with linear stiffness equal to 187792 lb/ft [60]. A swashplate mass of 75 kg (165 lb) was considered based on Ref. [119]. The determination of the swashplate and pitch-link properties can be found therein. The CSD model used for the steady flight conditions was built in the non rotating hub frame, identical to the CFD frame. Therefore, to simulate the translational and rotational dynamics of the hub in the maneuver, two revolute joints were added between the ground (clamped) and the rotor hub. The base of the hub has three degrees of freedom – vertical motion, pitching and rolling. In steady flight, the periodic motions of each blade are identical and a single blade's pitch angle is sufficient to define the rotor collective and cyclic pitch. During a transient maneuver, the blade motions are neither the same nor periodic; consequently collective and cyclic pitch are time varying and depend on the pitch of each blade. DYMORE provides the option to specify an arbitrary non-periodic time function to a control system. The model used in steady flight conditions used the intrinsic copy function in DYMORE to apply the same collective and cyclic angles to all the blades. This copy function was disabled for the control laws to achieve individual blade control. A pitch-link stiffness of 187792 lb/ft was chosen based on Ref. [60] and was the one used in the present analysis. The main effect of stiffening the pitch-link is to increase the first torsional frequency from about 3.8/rev to about 4.2/rev.

The structural model was validated using flight test airloads. The measured airloads problem (also termed as the mechanical airloads problem) allows one to assess the accuracy of the structural model separately from the airloads model, as the time varying measured airloads are no longer contaminated with the errors associated with the

predicted airloads. However, the airloads do not change with the structural response resulting in zero aerodynamic damping. This poses a significant difficulty in obtaining a periodic solution in level flight with little structural damping as the rotor frequencies, particularly 1/rev flapping, lies close to the rotor harmonics. Therefore, an additional damping, 0.02% of critical, had to be used throughout the analysis, requiring around 40 revs of maneuver initiation before the transient airloads are imposed. Figures 6.8 - 6.11 show the flapwise, chordwise, torsional and pitch-link loads obtained using the measured airloads problem for revs 15-17. The flapwise bending moment (BM) predictions compare well with test data. Both the peak to peak values and the phase are correctly captured in the measured airloads problem. These moments are directly affected by the lift acting on the blade. The predicted waveforms for chordwise BM compare reasonably well with test data though the magnitude is slightly under-predicted. The peak to peak values for torsional moments match the test values closely. The torsional moments are directly affected by the pitching moments. The pitch-link loads are also affected by torsional moments and the trends are similar. The effect of stall is clearly visible.

6.2.3 CFD/CSD Coupling

Both the loose coupling and tight coupling methodologies were implemented for this maneuvering study. The loose-coupling (LC) approach assumes that the flow-field is periodic in rotor rotational frequency and calculates a steady-state solution. Although this is not strictly valid in a time-varying non-periodic maneuver, it is nevertheless important to explore the feasibility of modeling the maneuver as a series of quasi-steady solutions. Moreover, the UTTAS 11029 maneuver time scales are slower compared to the rotor rotational time scales which make it more suitable for a quasi-steady analysis (the

maneuver lasts for about 10 seconds compared to 0.23 seconds taken by rotor to complete one revolution). All inputs were averaged over a revolution and all acceleration terms were set to zero to facilitate a quasi-steady analysis. Each rotor revolution was now treated as a separate coupling simulation and required 6-7 exchanges of loads and deflections for a converged solution. These LC maneuver calculations were performed in a manner similar to the steady-level trimmed flight calculations, with the controls held fixed. The results from these runs were then compared with the tight coupling computations.

Tight coupling simulations were performed in the same manner as before. The trim conditions to be used in the TC simulations for the initial steady flight regime were estimated through the loose coupling simulations, though both the CFD and CSD simulations were started from rest. But the tight coupling simulations cannot be started from rest at rev 15 because of the time varying non-periodic flow conditions that will prevent the numerical errors from dissipating. Therefore, loose coupling simulations were run for rev 14 and the flow-field and structural modes served as initial condition for both loose coupling and tight coupling simulations starting at rev 15. The simulations were run continuously from revs 15 to 17. Both the methodologies were implemented using file I/O in the FSI format to transfer airloads and blade deformations between the CFD and CSD solvers, though the vehicle motion data was input independently.

6.3 UTTAS 11029 Maneuver Simulations: Revolutions 1-5

The pull-up maneuver is preceded by steady level flight at an advance ratio, μ of 0.357 with a blade loading coefficient, C_T/σ of 0.0793. The pull-up is initiated during rev 5 by a gradual increase in longitudinal cyclic. Both loose and tight coupling simulations

were run for this region, with the trim conditions from the loose coupling used to drive the tight coupling runs. This flight condition is very similar to counter 8534 hence the baseline computational parameters were used for the CFD simulations.

Table 6.1 shows the collective and cyclic angles obtained at the end of converged loose coupling simulations. These angles were different from flight test data, therefore adjustments were made to the three rotor pitch controls based on trim solutions obtained with loose coupling computations. These adjustments were then added to the maneuver control input time history. Figure 6.12 shows the adjusted control time histories that were used for the maneuver analyses along with the unadjusted measurements. The normal forces and pitching moments obtained for this region is shown in Figures 6.13 and 6.14. It can be seen that the two key physical phenomena identified during previous investigations of flight counter 8534 are also evident here, namely the impulsive negative pitching moment and normal force occurring on the advancing side of the disk ($\psi \approx 120°$). The predictions from TC simulations and LC simulations for revolutions 1-5 are very comparable. The normal force predictions match well with test data for most of the radial stations. The impulsive negative loads due to wake interactions on the advancing side are captured well in phase and magnitude. The computed forces are marginally lower in magnitude on the retreating side probably due to small inaccuracies in modeling the fuselage and tail download effects on the thrust targets. The pitching moment trends show good agreement with test data. The unsteady transonic pitching moment phenomenon on the advancing side is captured well. Accurate prediction of sectional pitching moment leads to improved prediction of the elastic torsional response leading to improved prediction of effective angle of attack (which is a combination of control pitch, elastic

torsion and inflow) at each blade section. Improved prediction of effective angle of attack in turn leads to improved prediction of advancing blade lift waveform. A small impulsive behavior appears before the onset of the transonic pitching moments that is seen in both test and computed results. This behavior was not seen for the steady flight condition.

The tight coupling predictions of structural loads at 50%R are shown in Figure 6.15. The normal bending moments compare well with test data. The peak to peak torsional moments are slightly higher though the waveform correlates well with test data. The normal bending moments are directly affected by lift predictions and torsional moments are affected by pitching moment predictions. Therefore, good correlation in lift and pitching moments improves the correlation of torsional and normal bending moments. A steady magnitude difference is observed in the edgewise bending moments though the phase correlates well with test data. The peak to peak pitch-link loads are higher than observed values and this trend is consistent with correlation of torsional moments since torsion directly affects the loads on the pitch-link.

6.4 UTTAS 11029 Maneuver Simulations: Revolutions 15-17

The coupling simulations for revs 15-17 were run using the corrected pitch control angles shown in Figure 6.12. The tight coupling simulations cannot start from rest at the beginning of rev 15; therefore loose coupling simulations were run for rev 14 and the converged flow-field and structural states were used as initial condition for the tight coupling simulations. Although the loose coupling simulations were run separately for revs 15, 16 and 17 as independent cases, to accelerate convergence, rev 15 was used as initial condition for rev 16 and in the same manner for rev 17. This reduced the number

of coupling iterations for revs 16 and 17 to four updates. The full span wake model with shed wake is used for these maneuvering simulations.

6.4.1 Second Order Temporal Accuracy

In section 3.6, the second order temporal accuracy was tested for a steady flight condition. The higher order temporal accuracy did not impact the loads significantly, therefore the first order temporal accuracy with 0.05 degrees azimuthal time step was chosen as the baseline computational parameter for steady flight simulations. The flow conditions in a maneuver could vary rapidly that the first order temporal accuracy might be insufficient to capture the flow phenomena accurately. Therefore, the higher order temporal accuracy is tested with the azimuthal time step of 0.05 degrees. Figures 6.16 and 6.17 show the pitching moment coefficients at 86.5%R and 92%R respectively. The first order and second order temporal accuracy simulations are compared with each other and test data. The differences between predictions obtained using the two temporal schemes are minimal on the advancing side but on the retreating side, the second dynamic stall is better predicted by second order temporal accuracy simulation. Dynamic stall is an unsteady phenomenon which is directly dependent on the local angle of attack. Since the local angle of attack is transient due to the maneuver, the second order temporal accuracy captures the second stall better. Therefore, the second order temporal accuracy is chosen for this region of the maneuver.

6.4.2 Coupling Results

Figures 6.18 and 6.19 show the normal forces and pitching moment coefficients in this region at four radial stations. Two distinct stall events are clearly seen in the normal forces and pitching moments obtained from flight test data. As the aircraft engages on the

longitudinal pull-up, the pitch attitude and aircraft angle of attack increase leading to an increased thrust. The helicopter attains the highest thrust condition in this region of the maneuver. The high sectional angle of attack caused by the combination of control pitch, aircraft pitch rate and inflow transients causes flow separation and eventual stall on the retreating side of the rotor The high frequency torsional response caused by the impulsive nose down pitching moments causes an elastic torsional response which relieves the high angle of attack momentarily causing the flow to reattach. However, within a few degrees of azimuthal sweep the elastic torsional response becomes out of phase with the control pitch inducing a higher sectional angle of attack and leading to another stall event. This behavior is very similar to the stall events observed in the 9017 flight condition. The tight coupling analysis captures the stall behavior correctly but there is under-prediction in the magnitude of the stall. There is a third stall event clearly visible in the experimental data on the advancing side of the rotor disk. The location of the stall and high Mach number on the advancing side (M_{tip} = 0.82) indicate that this phenomenon is a transonic stall.

Unlike the steady flight conditions, loose coupling and tight coupling methodologies differ in their predictions significantly on the retreating side. The tight coupling analysis shows better stall predictions. The loose coupling analysis shows weak stall behavior on the retreating side though the advancing transonic stall prediction is reasonable. The stall recovers earlier than what is observed in the tight coupling simulations. Since both loose and tight coupling simulations use the same initial conditions at the start of rev 15, the differences arise primarily from the differences in unsteady and quasi-steady analysis. The pitch attitude increases rapidly in this region and averaging the pitch rate lowers the physical angle of attack which affects the prediction of

dynamic stall on the retreating side. The advancing transonic stall is less dependent on angle of attack and therefore, the phase and magnitude of the stall compare well with each other.

The tip wake geometry predicted at the end of rev 5 and rev 17 is shown in Figure 6.20. The inboard and shed wake has been removed and the wake geometry has been smoothed for clarity and emphasis. Predicted wake geometry follows expected qualitative trends corresponding to the prescribed flight dynamics and computed aeromechanics. At the initiation of the maneuver (rev 5), the operating condition is very close to steady high speed forward flight where the wake is convected away from the rotor system in the horizontal direction. Returning wake effects are minimal at this condition. The aircraft angle of attack rapidly changes from nose-down to nose-up in the next 16 revolutions with the maximum angle of attack attained at the time level of about 20 revolutions. The vortex wake convects very close and even cuts through the rotor disk during this process. Therefore large unsteadiness can be noticed in the wake dynamics at rev 17. The combination of high thrust, higher climb rate and decreased forward speed at around revolution 17 causes increased vertical convection of the wake.

The structural loads obtained using tightly coupled simulations are compared with test data in Figure 6.21. The torsional moments correlate well in phase but the peak to peak magnitude is slightly under-predicted. This observation is consistent with the pitching moment predictions where the stall cycles are slightly under-predicted. The pitch-link loads show good agreement in phase but peak to peak is not adequately captured. Since the blade does not offer much inertia in the pitching axis, the pitching moments significantly affect the pitch-link loads explaining the observed trends. The

normal bending moments show good agreement with test data. The edgewise moments show poor correlations and more studies are required to address this issue.

6.5 Chapter Summary

The loose and tight coupling methodologies developed and validated for steady flight conditions were extended for analysis of maneuvering flight. The UTTAS 11029 maneuver was chosen as the test case of the analysis. This flight counter was the second most severe maneuver that was tested in the UH-60A flight test program. The maneuver is performed over 40 rotor revolutions but most of the critical phenomena occur between revs 15-17 where the vehicle experiences the maximum load factor. Therefore, the coupling simulations were run for revs 1-5 and 15-17. The loose coupling methodology was used for a quasi-steady analysis whereas the tight coupling was used for an unsteady simulation of the maneuver.

The CFD and CSD methodology had to be modified for maneuvering flight simulations. The non-periodic nature of the maneuvering simulations required a multi-blade CFD simulation. The vehicle velocity components had to be transformed to a hub fixed frame and applied as grid velocity components to avoid reorienting the computational grid. A swashplate model was added to the existing CSD model and hub motions were simulated through revolute joints added the base of the shaft. A non-periodic time function was defined for the control system to simulate the time varying blade control angles.

The analysis of revs 1-5 showed that the airloads are characterized by transonic nose-down pitching moments and negative lift on advancing side, similar to 8534 flight condition. The coupling analyses compared well with each other and flight test data.

The analysis of revs 15-17 indicated a dual stall phenomenon on the retreating side due to a very high thrust condition and rapidly increasing pitch attitude. An advancing blade stall was observed which indicated strong transonic effects. The tight coupling simulations showed reasonable agreement with test data though the stall magnitudes were slightly under-predicted. The loose coupling simulations compared well with tight coupling on advancing side but the predictions were poor on the retreating side primarily due to the quasi-steady nature of the analysis. The angular velocity components in the longitudinal direction are averaged therefore the angle of attack is lower than observed value which affects the stall predictions.

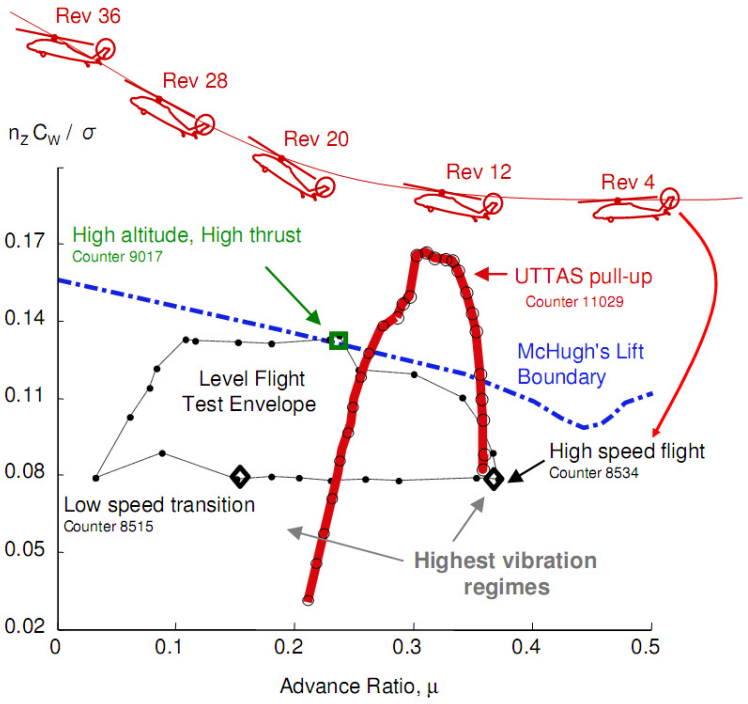

Figure 6.1 UTTAS 11029 maneuver trajectory and flight envelope (Reference [60])

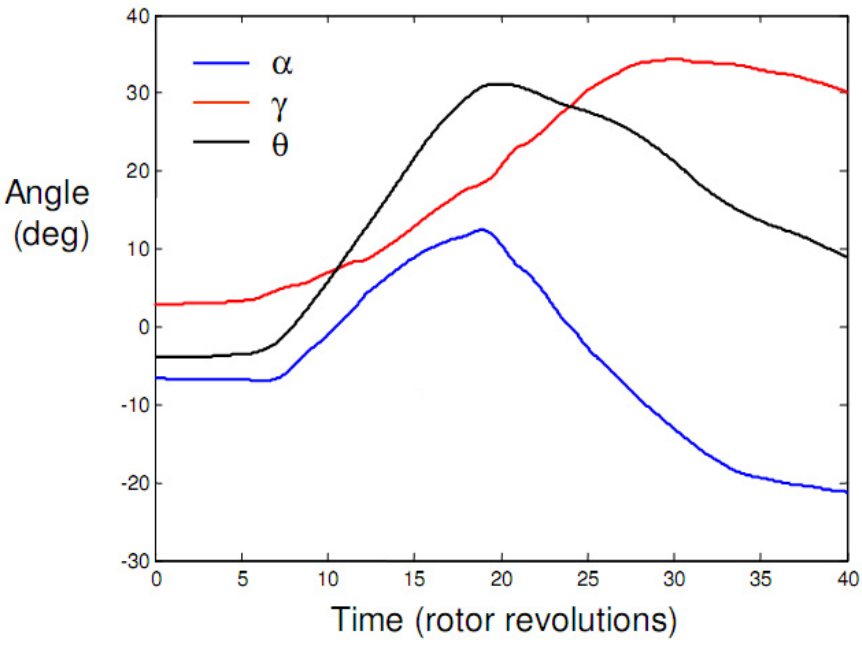

Figure 6.2 UTTAS 11029 maneuver: Vehicle attitude

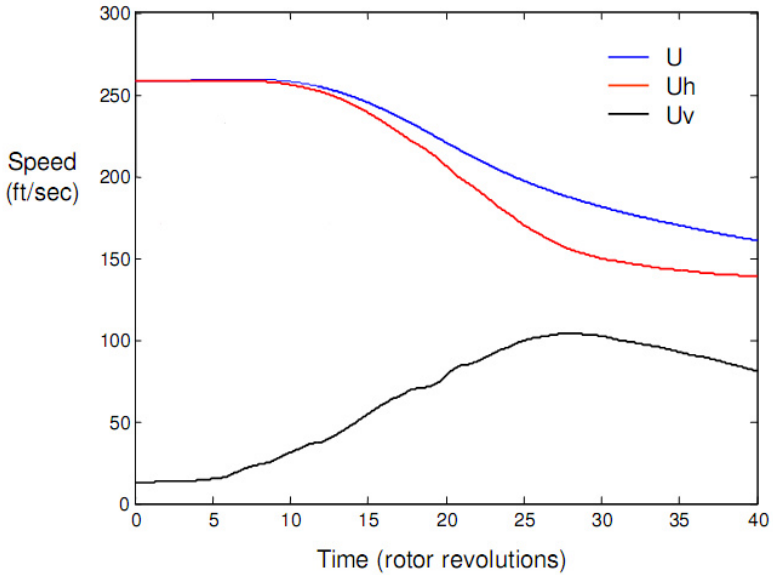

Figure 6.3 UTTAS 11029 maneuver: Flight path angle

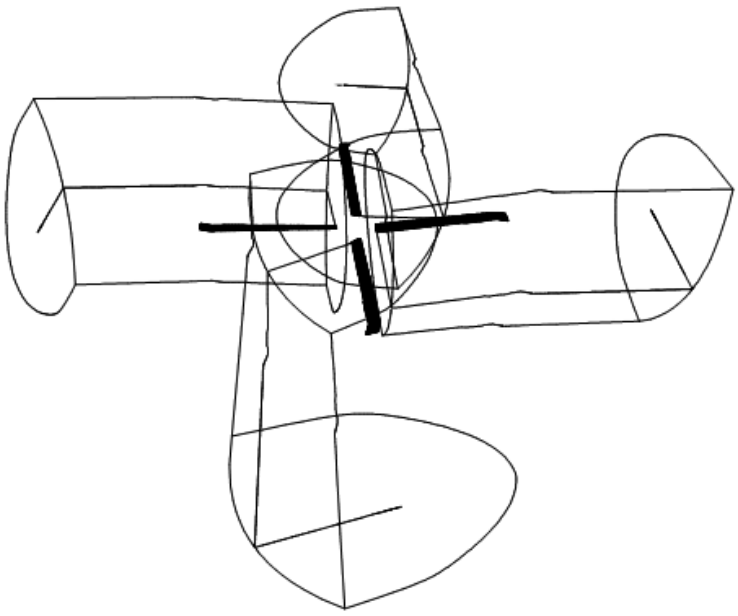

Figure 6.4 CFD multi-blade grid for maneuvering analysis

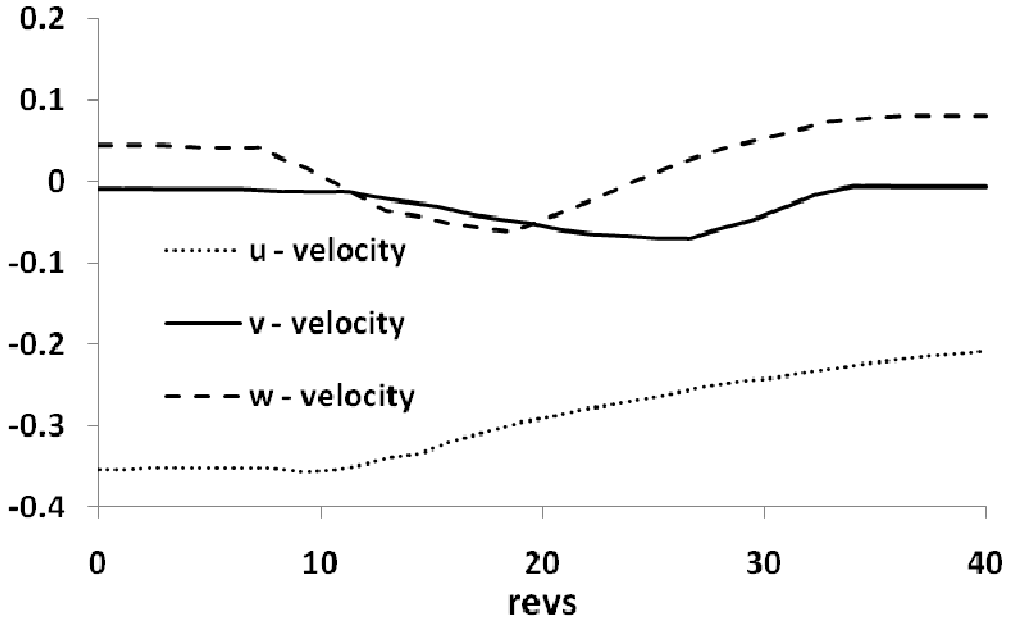

Figure 6.5 Hub velocity normalized by tip speed

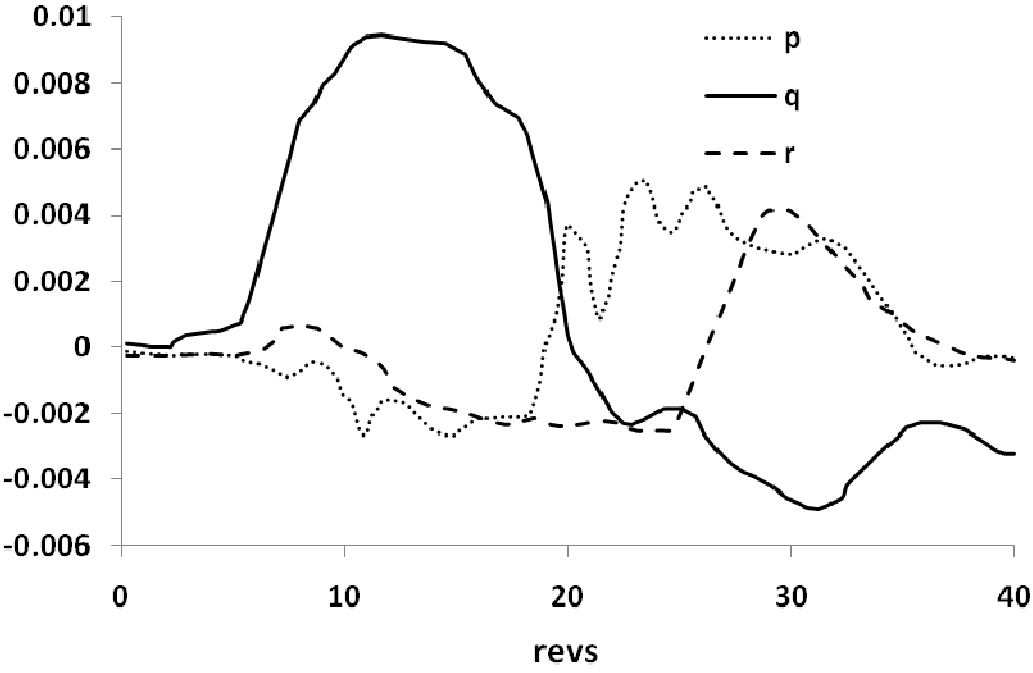

Figure 6.6 Hub angular velocity normalized by tip speed

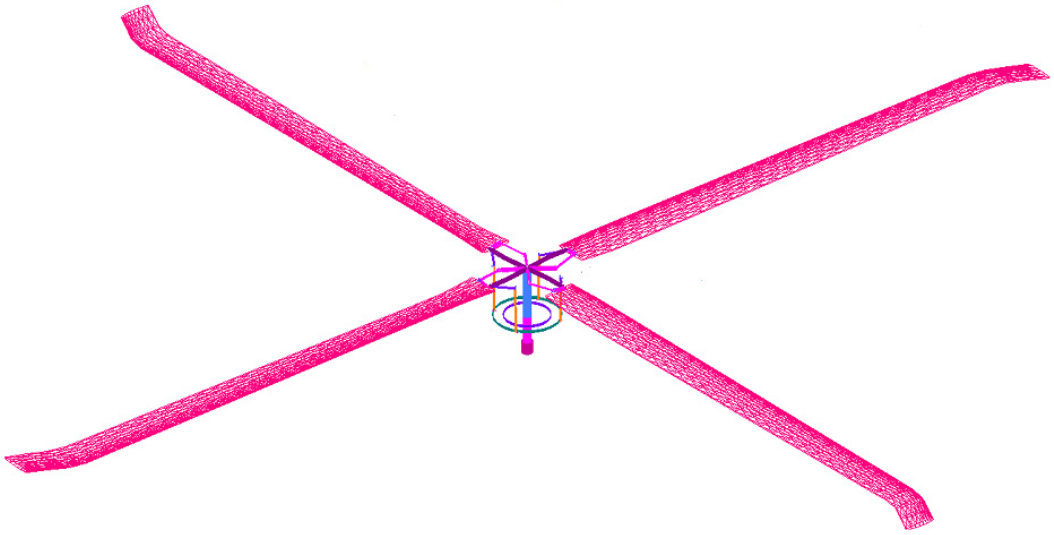

Figure 6.7 DYMORE UH-60A model with swashplate

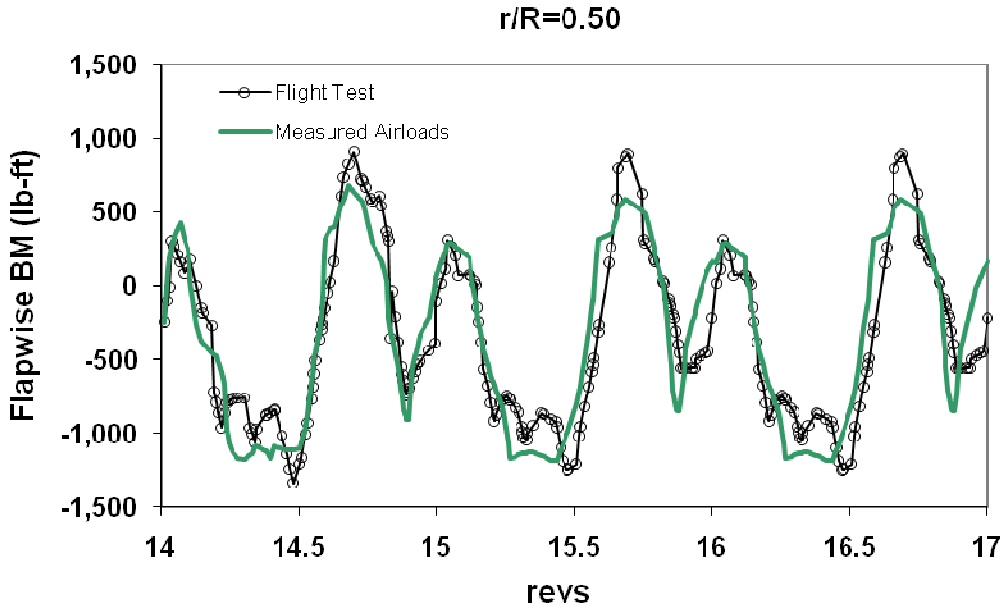

Figure 6.8 UTTAS 11029 Maneuver Revs 15-17: Flapwise BM with measured airloads

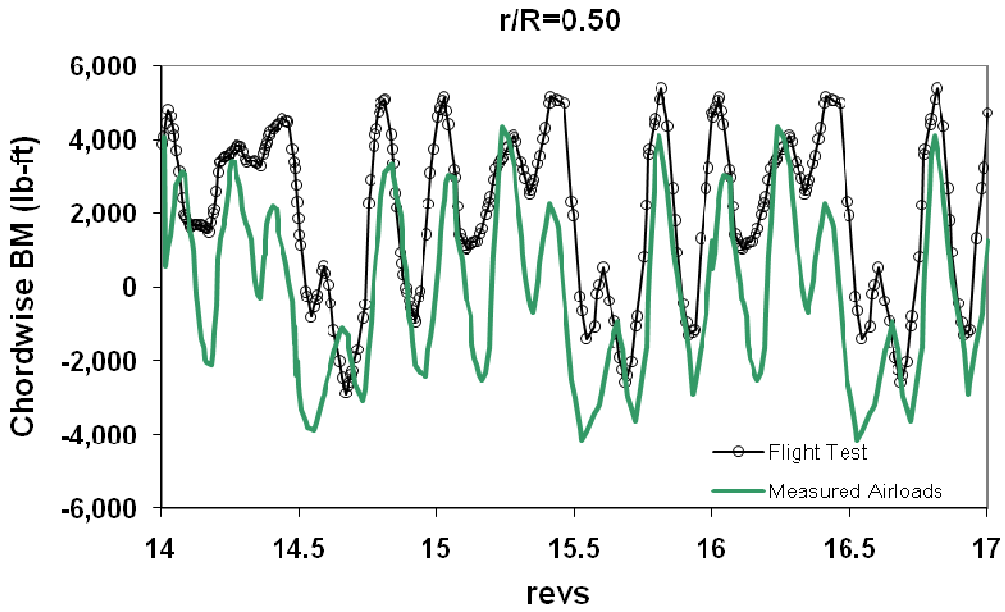

Figure 6.9 UTTAS 11029 Maneuver Revs 15-17: Chordwise BM with measured airloads

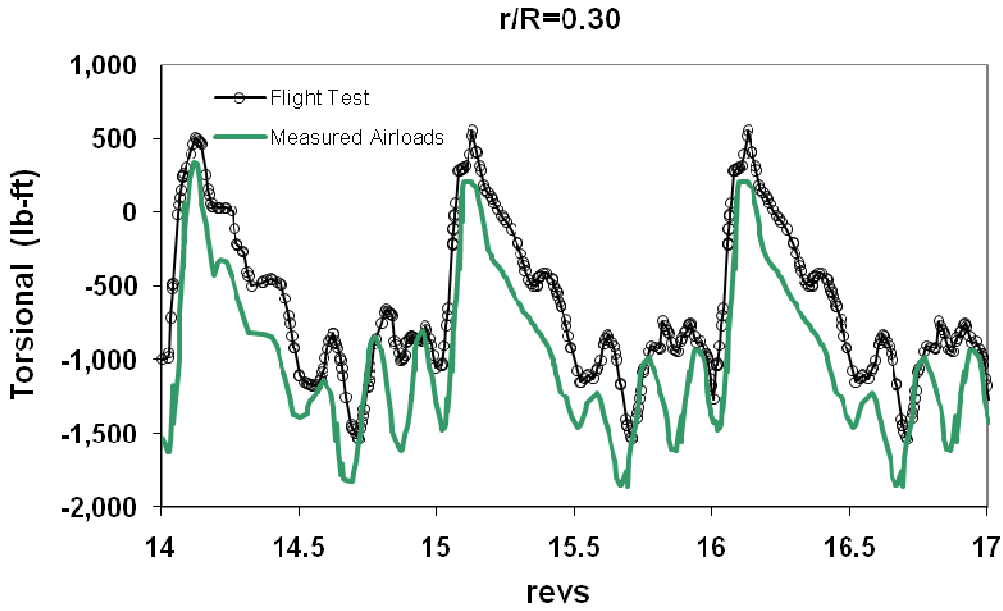

Figure 6.10 UTTAS 11029 Maneuver Revs 15-17: Torsional moments with measured airloads

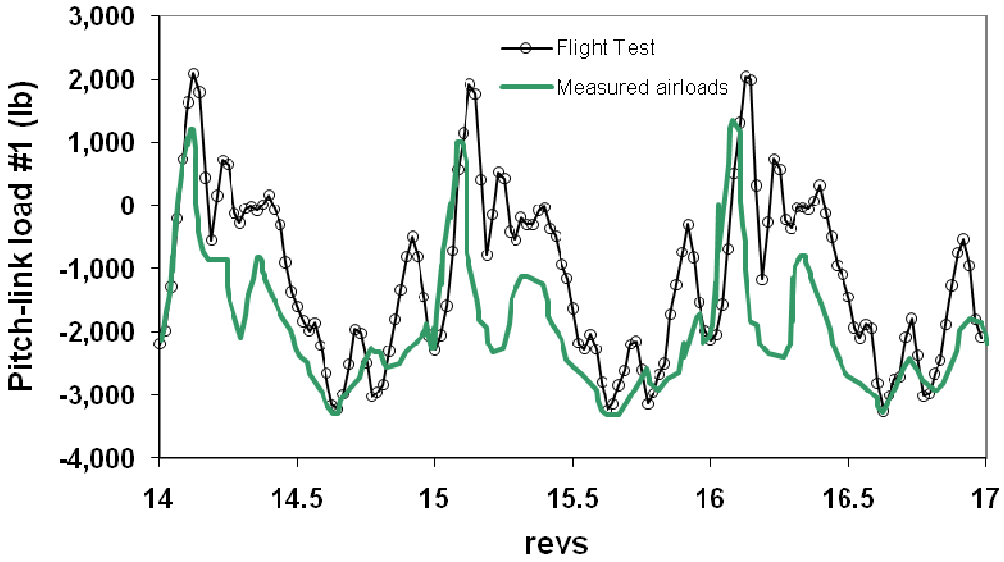

Figure 6.11 UTTAS 11029 Maneuver Revs 15-17: Pitch-link loads with measured airloads

Table 6.1 UTTAS 11029 Revs 1-5: Pitch control angles comparison

	Flight Test	GT-Hyb / DYM LC
θ_0	12.45°	14.18°
θ_{1c}	4.63°	3.98°
θ_{1s}	-9.68°	- 9.3°

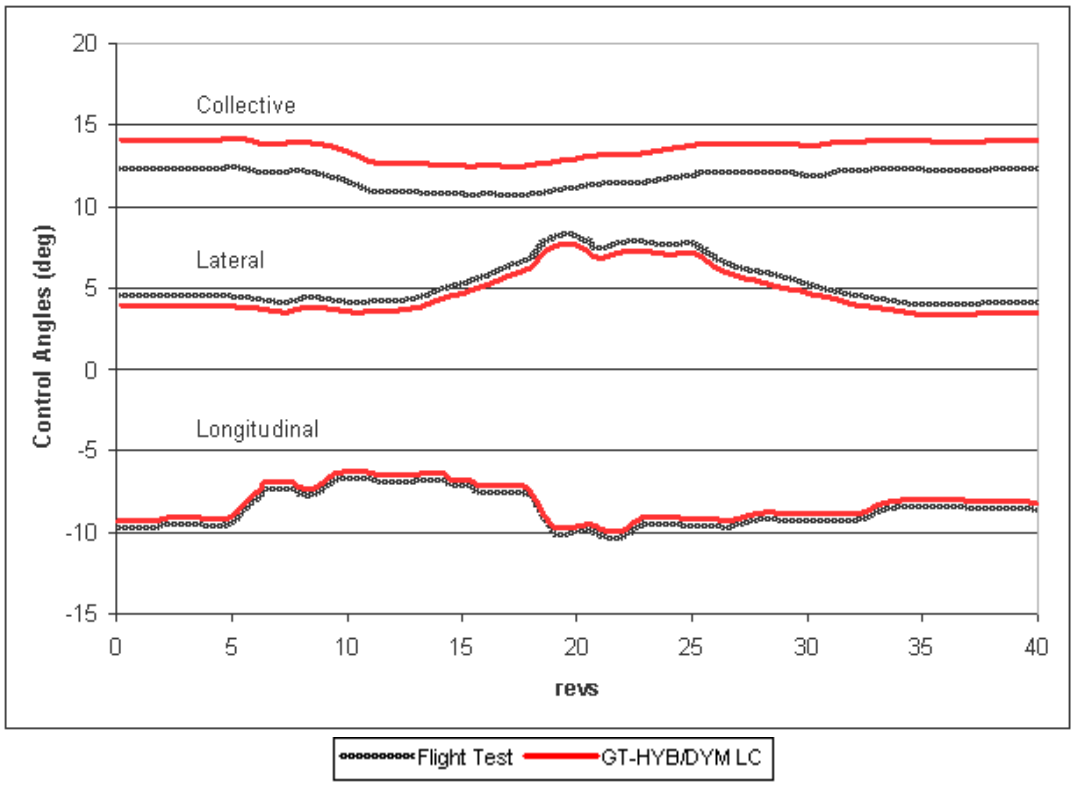

Figure 6.12 Pitch control input time history for UTTAS 11029 maneuver

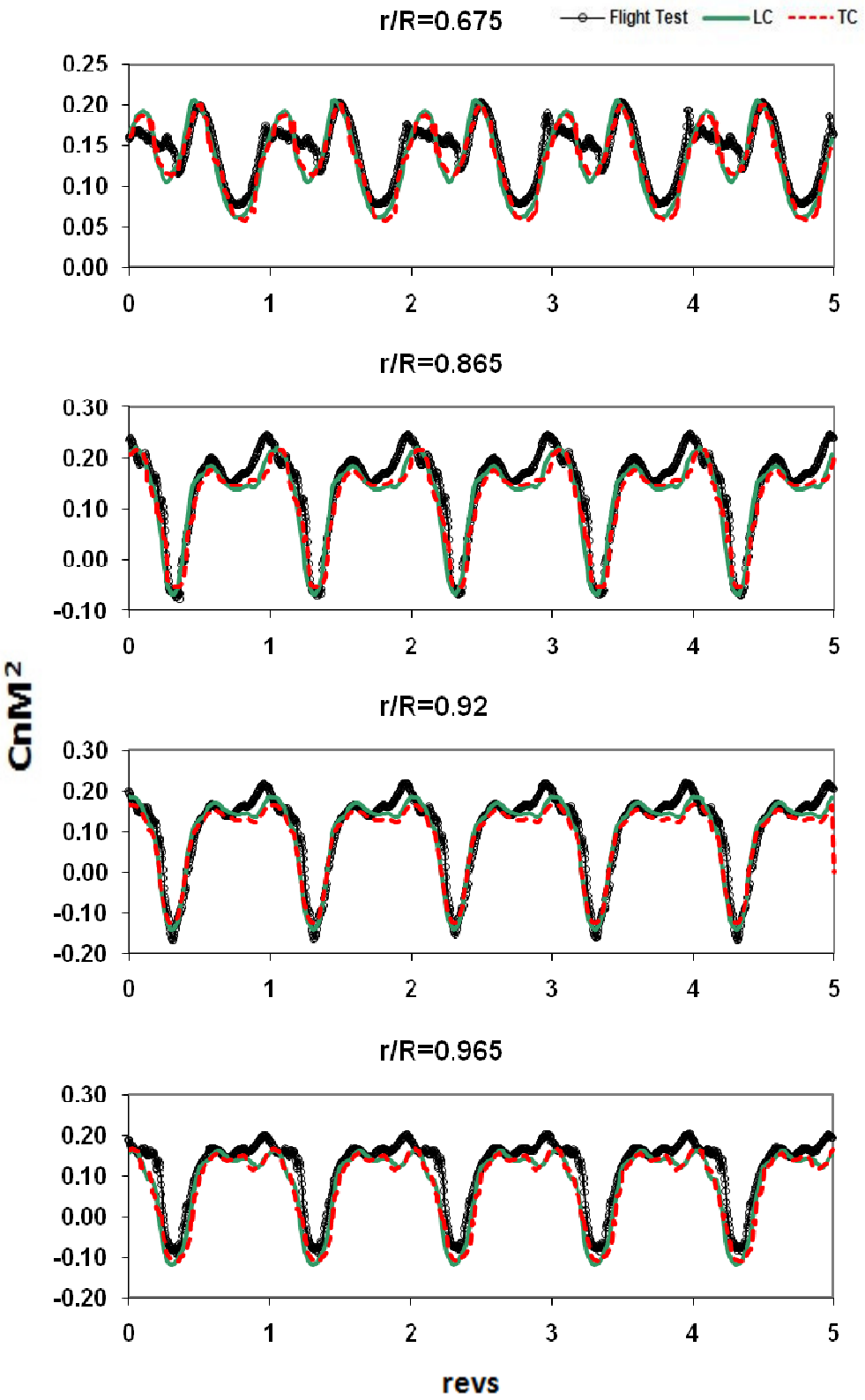

Figure 6.13 UTTAS 11029 maneuver revs 1-5: Normal forces

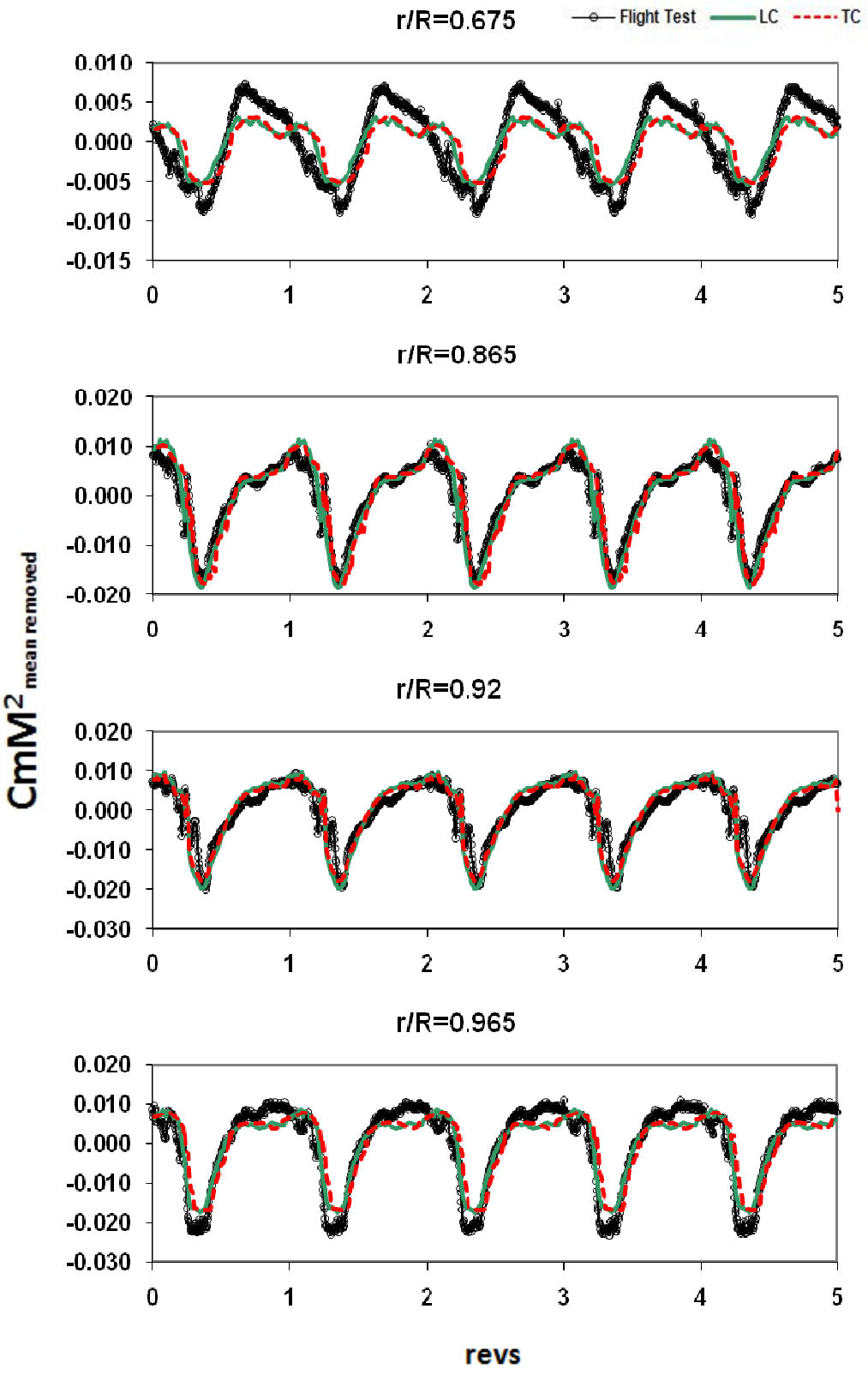

Figure 6.14 UTTAS 11029 maneuver Revs 1-5: Pitching moments (means removed)

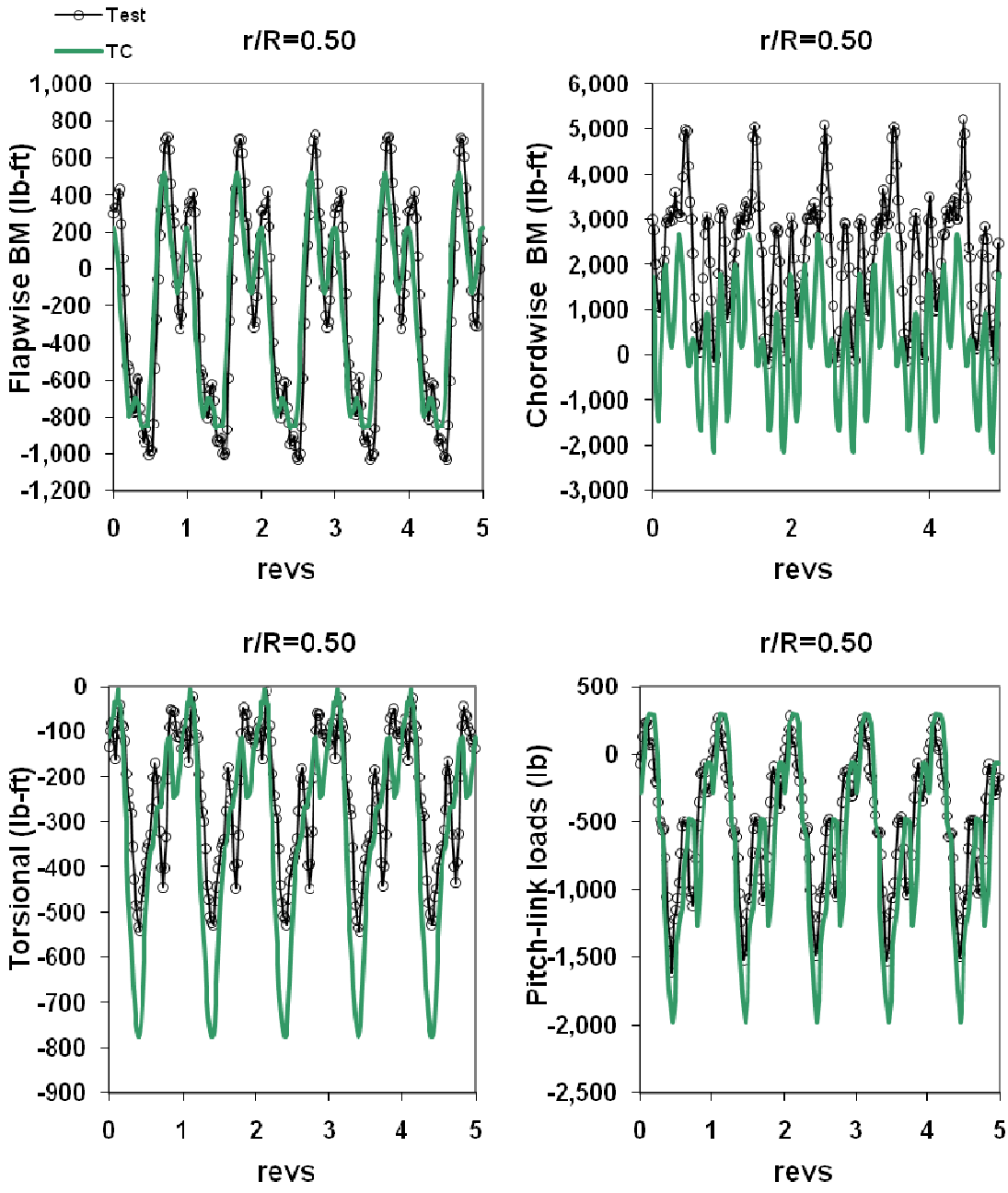

Figure 6.15 Structural loads at 50%R for 11029 maneuver: Revs 1-5

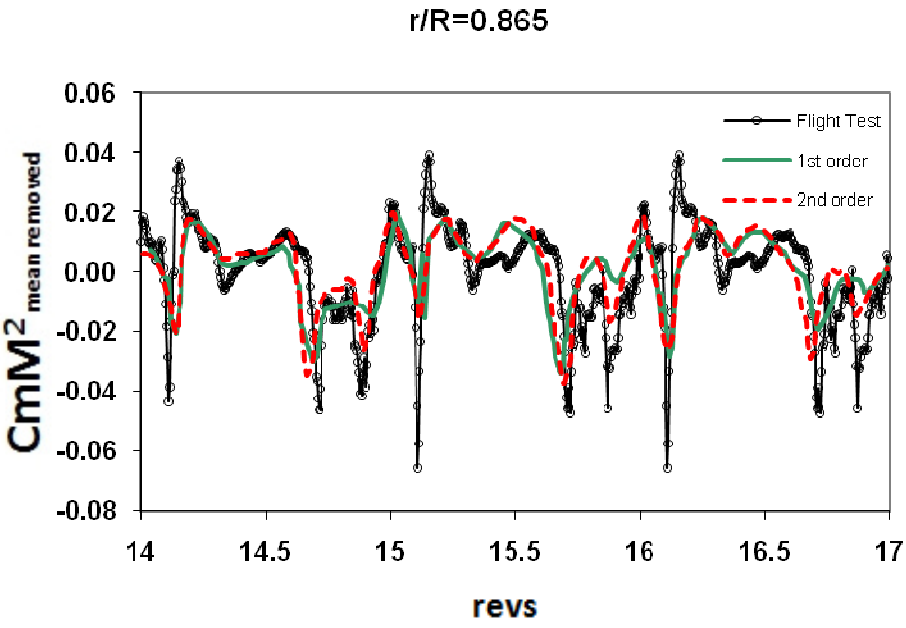

Figure 6.16 Effect of temporal accuracy: Pitching moments at 86.5%R (means removed)

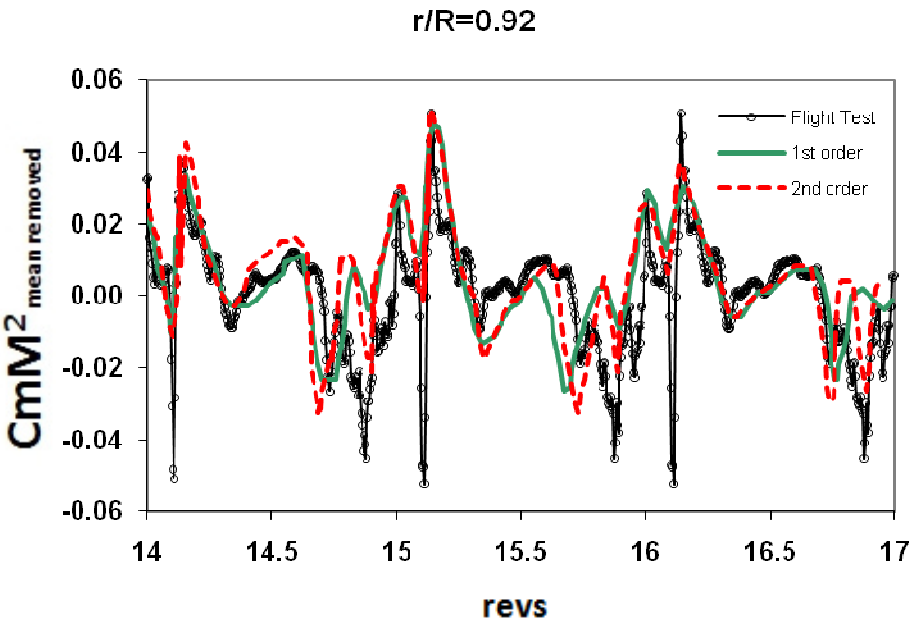

Figure 6.17 Effect of temporal accuracy: Pitching moments at 92%R (means removed)

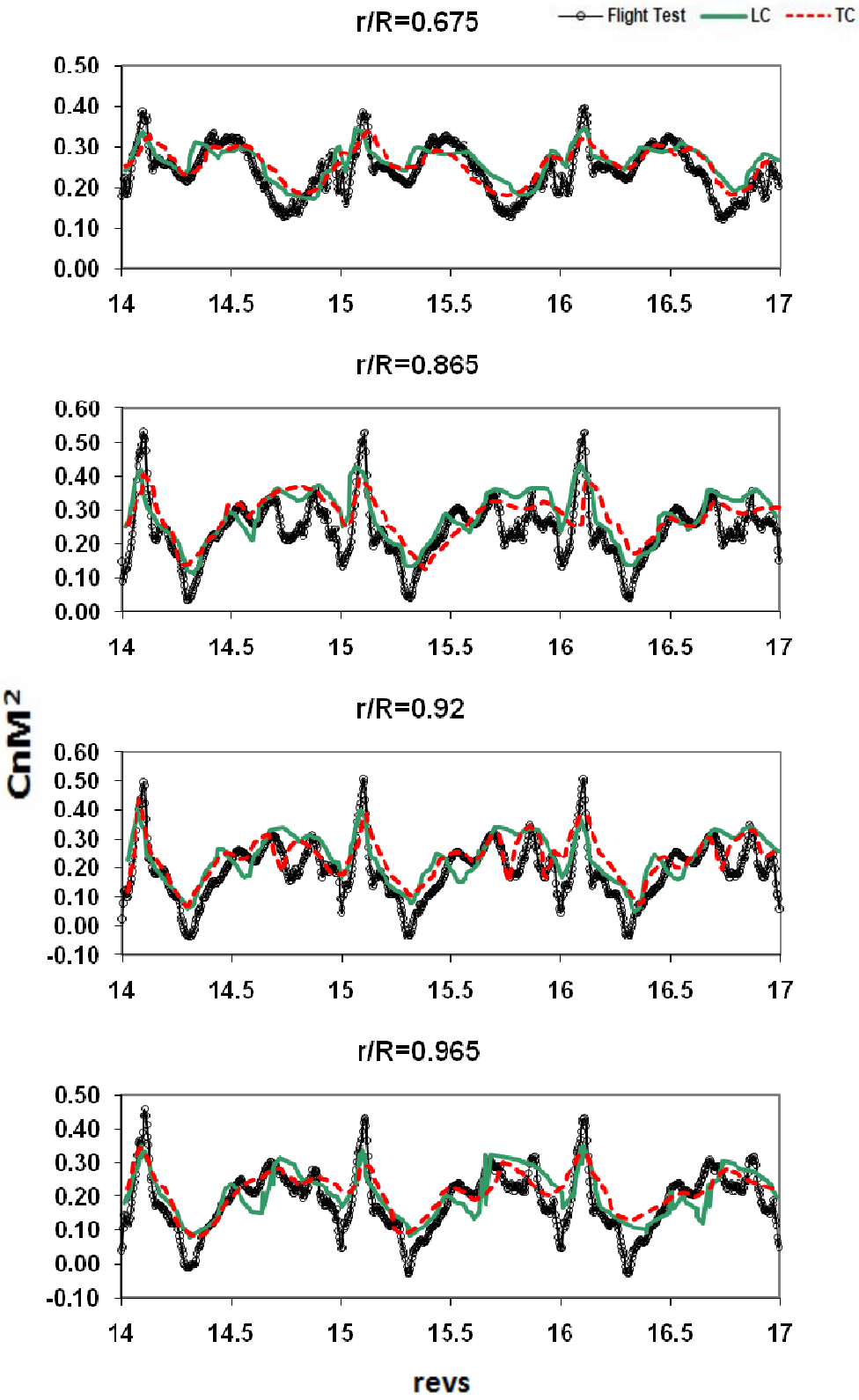

Figure 6.18 UTTAS 11029 maneuver Revs 15-17: Normal forces

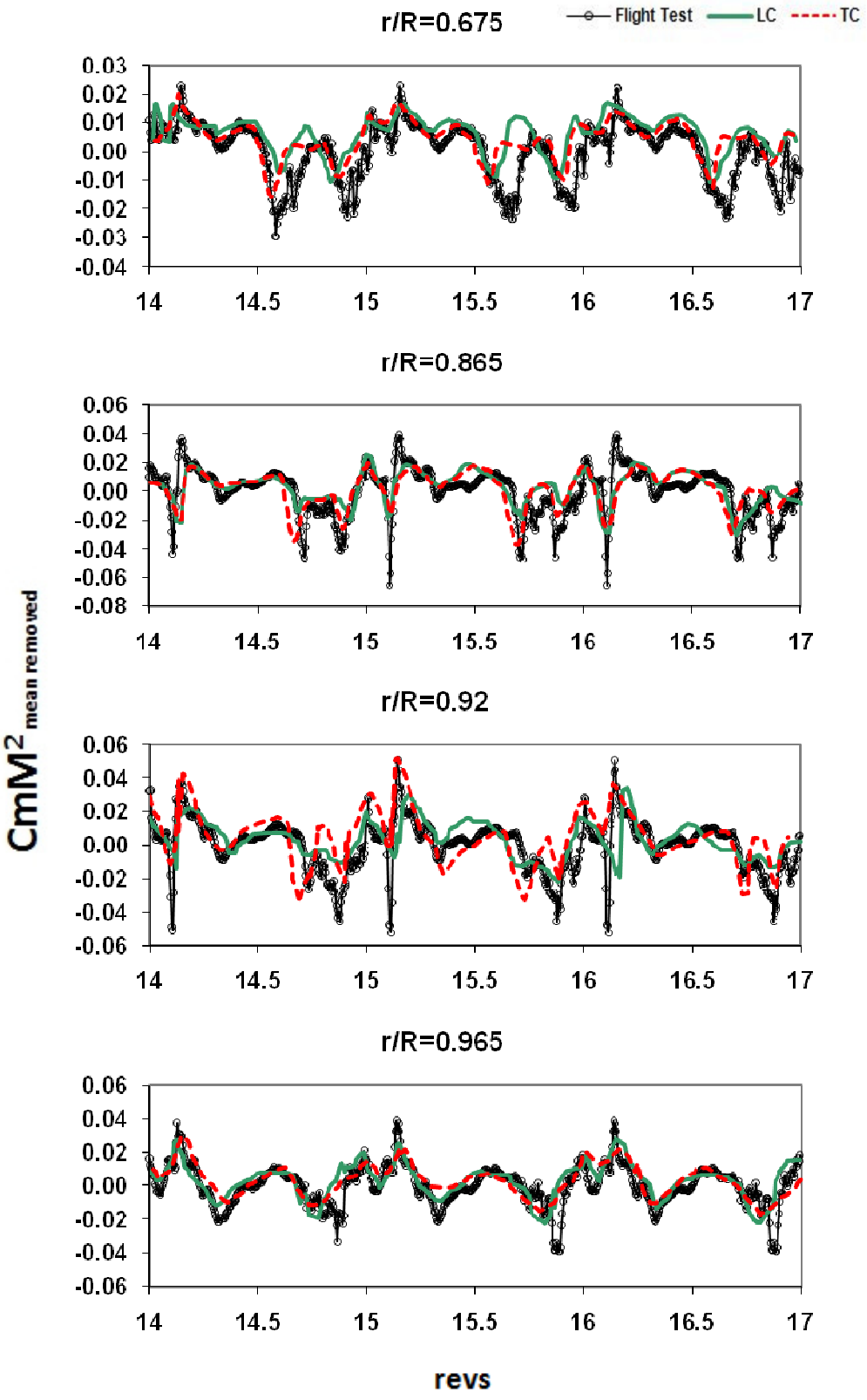

Figure 6.19 UTTAS 11029 maneuver Revs 15-17: Pitching moments (means removed)

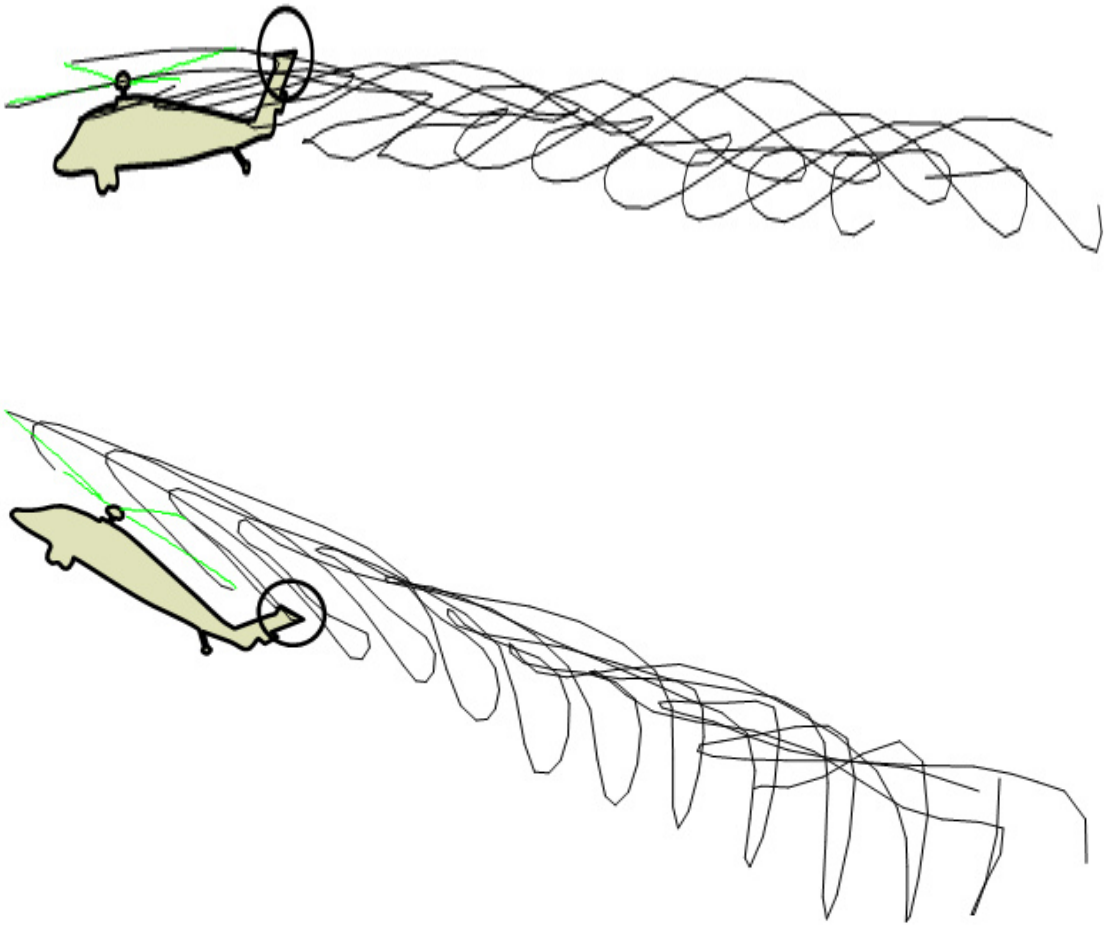

Figure 6.20 Tip wake geometry at end of rev 5 (upper) and rev 17 (lower)

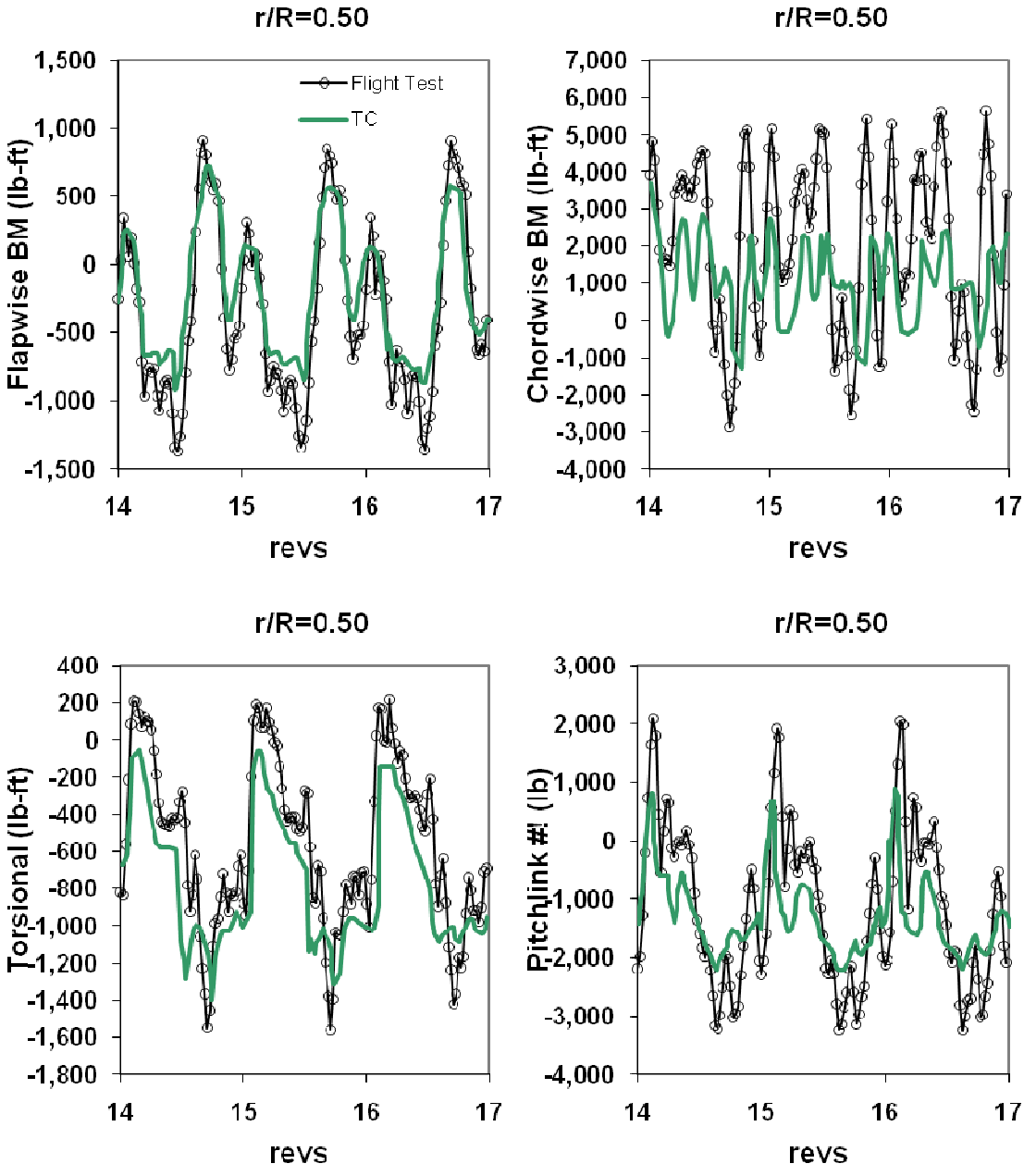

Figure 6.21 Structural loads at 50%R for 11029 maneuver: Revs 15-17

CHAPTER 7

AEROMECHANICS/FLIGHT MECHANICS COUPLING METHODOLOGY

In the previous chapter, the aeromechanics of the UTTAS 11029 maneuver was studied using the loose and tight coupling methodologies. The blade collective and cyclic inputs from the flight test database were used to drive the CFD/CSD coupling simulations. To study the rotor aeromechanics in a maneuver that has not been flown, the pilot input needs to be estimated using a mathematical technique known as inverse simulation. In this chapter, a methodology is developed to couple the CFD/CSD coupling framework with inverse simulation so that the CFD airloads in the maneuver can be estimated without using the flight test data for pitch inputs. The methodology shall be referred to as AFMC in this chapter.

7.1 Flight Mechanics Simulation

7.1.1 UH-60A Black Hawk Helicopter Model

This section describes the general characteristics of the Black Hawk helicopter and the model configuration used for the flight dynamics and inverse simulations. The helicopter configuration is based on the Sikorsky UH-60A, which has a fully-articulated rotor system with 4 blades of 26.83 feet radius rotating at 27 rad/sec or 260 RPM and a forward shaft tilt of 3 degrees. The blade airfoil section is the SC1095, for which aerodynamic data is extracted from look-up tables. The tip of the blade is swept by 20 degrees over the outboard 1.90 feet of the radius. The hinge offset is 1.25 feet and the

cuff extends outboard for another 3.83 feet. The blade has a chord length of 1.73 feet and an equivalent linear twist of about 18 degrees, although the blade is twisted only outboard of the cuff. The actual blade twist from the root to tip is 14 degrees (without the inclusion of the swept tip).

The tail rotor has a cant angle of 20 degrees, and therefore it generates relatively strong couplings between longitudinal and lateral directional dynamics. It has the same airfoil section and blade twist as the main rotor, although with a smaller radius and chord (5.5 feet and 0.81 feet, respectively). The horizontal stabilizer uses the NACA 0014 airfoil and has an area of 45 square feet and an aspect ratio of 4.6. Its incidence is adjustable by the flight control system as a function of speed. The vertical stabilizer, which uses the NACA 0021 airfoil, has a surface area of 32.3 square feet and an aspect ratio of 1.92. Table 7.1 summarizes the configuration of the UH-60A articulated rotor helicopter used in this study. The majority of the UH-60A parameters and non-linear functions and data tables have been adapted from an existing UH-60A simulation model (Ref. [120]). Further details of the implementation of the fuselage, empennage and tail rotor models for the UH-60A helicopter can be found in the GENHEL theory manual (Ref. [120]). Figures 7.1 - 7.3 show the lift, drag and moment coefficients, as a function of angle of attack and Mach number for the airfoil of the U-60A as obtained from the data in Ref. [120].

7.1.2 Mathematical Formulation

In order to simulate the UH-60A to obtain control inputs for a given trajectory, the Black Hawk helicopter is modeled as a rigid body with six degrees of freedom. An overview of the simulation structure is shown in Figure 7.4. The vehicle state vector

consists of the position and velocity of the vehicle center of mass, and the vehicle attitude and angular rates, all with respect to the inertial frame. The rigid body equations of motion are shown below:

$$\begin{Bmatrix}\dot{x}\\ \dot{y}\\ \dot{z}\end{Bmatrix}=\begin{bmatrix} c_\theta c_\psi & c_\theta s_\psi & -s_\theta \\ s_\phi s_\theta c_\psi - c_\phi s_\psi & s_\phi s_\theta s_\psi + c_\phi c_\psi & s_\phi c_\theta \\ c_\phi s_\theta c_\psi + s_\phi s_\psi & c_\phi s_\theta c_\psi - s_\phi c_\psi & c_\phi c_\theta \end{bmatrix}\begin{Bmatrix}u\\ v\\ w\end{Bmatrix} \tag{7.1}$$

$$\begin{Bmatrix}\dot{\phi}\\ \dot{\theta}\\ \dot{\psi}\end{Bmatrix}=\begin{bmatrix} 1 & s_\phi t_\theta & c_\phi t_\theta \\ 0 & c_\phi & -s_\phi \\ 0 & s_\phi / c_\theta & c_\phi / c_\theta \end{bmatrix}\begin{Bmatrix}p\\ q\\ r\end{Bmatrix} \tag{7.2}$$

$$\begin{Bmatrix}\dot{u}\\ \dot{v}\\ \dot{w}\end{Bmatrix}=\begin{Bmatrix}X/m\\ Y/m\\ Z/m\end{Bmatrix}+\begin{bmatrix} 0 & -r & q \\ r & 0 & -p \\ -q & p & 0 \end{bmatrix}\begin{Bmatrix}u\\ v\\ w\end{Bmatrix} \tag{7.3}$$

$$\begin{Bmatrix}\dot{p}\\ \dot{q}\\ \dot{r}\end{Bmatrix}=[I_H]^{-1}\left[\begin{Bmatrix}L\\ M\\ N\end{Bmatrix}-\begin{bmatrix} 0 & -r & q \\ r & 0 & -p \\ -q & p & 0 \end{bmatrix}[I_H]\begin{Bmatrix}p\\ q\\ r\end{Bmatrix}\right] \tag{7.4}$$

where <x,y,z> is position vector, <φ,θ,ψ> are euler angles defining vehicle attitudes, <u,v,w> are vehicle velocity components, <p,q,r> are vehicle angular rates, s_α = sin(α), c_α = cos(α) and t_α = tan(α).

The forces on the helicopter (X, Y, Z) consist of components from the main rotor thrust, tail rotor thrust, helicopter weight, and aerodynamic forces on the fuselage, vertical tail, and horizontal tail. The moments on the helicopter (L, M, N) are due to pure moments about the various components, as well as moments due to the relative position of application of the forces from the vehicle center of mass. Aerodynamic forces and moments from the fuselage, vertical tail, and horizontal tail are obtained using table lookup.

The rotor aerodynamics is computed using combined blade-element momentum theory (BEMT) with an assumption of first harmonic quasi-steady flapping. In this approximation, the blade flapping is assumed to reach steady state much more quickly than the helicopter can react to the application of forces or moments resulting from flapping. Thus, only the steady state flapping must be computed, therefore the flapping equations become algebraic in nature. The flapping dynamic equation is shown below:

$$\ddot{\beta} + \omega_N^2 \beta = M_F \tag{7.5}$$

where ω_N is given by

$$\omega_N = \Omega \sqrt{1 + \frac{m_B e R}{2 I_B}} \tag{7.6}$$

The steady state flapping angle is assumed to be of the form:

$$\beta = \beta_0 + \beta_{1C} \cos\psi_{MR} + \beta_{1S} \sin\psi_{MR} \tag{7.7}$$

By substituting this solution into Eqn. (7.6), the steady state coning angle, longitudinal flapping angle, and lateral flapping angle are determined for a given control input of the form:

$$\theta_{pitch} = \theta_0 + \theta_{1C}\cos\psi_{MR} + \theta_{1S}\sin\psi_{MR} \tag{7.8}$$

7.2 Inverse Flight Mechanics Simulation

In order to compute the controls required to fly a given trajectory, an inverse simulation of the flight dynamic model must be performed. The inverse simulation technique has been explained in the work by Thomson et al. [69]. Extensive methods have been proposed to accomplish this, including differentiation methods, integration methods, and two-time scale methods. In this work, a feedback linearization controller is used to track given states. Feedback linearization is an approach to nonlinear control design where the central idea is to algebraically transform nonlinear systems dynamics into (fully or partly) linear ones, so that linear control techniques can be applied.

The helicopter dynamic model developed above can be written as the following:

$$\begin{aligned} \dot{\vec{x}} &= f(\vec{x},t) + g(\vec{x},t)\vec{u} \\ \vec{y} &= \vec{x} \end{aligned} \tag{7.9}$$

where $\vec{x}$ is the state vector, $\vec{u}$ is the control vector, and $\vec{y}$ is the state, which is to be tracked. Since there are four controls (θ_0, θ_{1c}, θ_{1s}, θ_{TR} - main rotor collective and cyclic, tail rotor collective) available, four vehicle states may be tracked. The time derivatives of

the corresponding outputs to these states are taken until any one of the four controls appears in the derivative. This procedure results in the following equation:

$$\begin{Bmatrix} \frac{d^{\rho_a} y_a}{dt^{\rho_a}} \\ \frac{d^{\rho_b} y_b}{dt^{\rho_b}} \\ \frac{d^{\rho_c} y_c}{dt^{\rho_c}} \\ \frac{d^{\rho_d} y_d}{dt^{\rho_d}} \end{Bmatrix} = F_{4\times1}(\vec{x},t) + E_{4\times4}(\vec{x},t) \begin{Bmatrix} \theta_0 \\ \theta_{1C} \\ \theta_{1S} \\ \theta_{TR} \end{Bmatrix} \tag{7.10}$$

Setting Eqn. (7.10) equal to a pseudo control, $\vec{\gamma}$ the controls become:

$$\begin{Bmatrix} \theta_0 \\ \theta_{1C} \\ \theta_{1S} \\ \theta_{TR} \end{Bmatrix} = \left[E_{4\times4}(\vec{x},t)\right]^{-1} \left(\vec{\gamma}(y_a, y_b, y_c, y_d, y_a^c, y_b^c, y_c^c, y_d^c) - F_{4\times1}(\vec{x},t)\right) \tag{7.11}$$

The pseudo control is designed in the linear domain to stabilize the following system:

$$\begin{Bmatrix} \frac{d^{\rho_a} y}{dt^{\rho_a}} \\ \frac{d^{\rho_b} y}{dt^{\rho_b}} \\ \frac{d^{\rho_c} y}{dt^{\rho_c}} \\ \frac{d^{\rho_d} y}{dt^{\rho_d}} \end{Bmatrix} = \vec{\gamma}(y_a, y_b, y_c, y_d, y_a^c, y_b^c, y_c^c, y_d^c) \tag{7.12}$$

where y_i^c is a known state variable to be tracked, and y_i is the actual state variable. If the error dynamics in γ are set to converge at a much faster rate than the system dynamics, then the controls can be calculated with Eqn. (7.11) so that the system tracks the desired states with a very small lag. The inverse simulation used in this study was developed by Abraham and Costello [121]. The inverse simulation uses a 4th order implicit Runge-Kutta time marching approach. A schematic of the feedback linearization technique is shown in Figure 7.5.

7.3 Inverse simulation of UTTAS 11029 maneuver

The inverse simulation is run for the UTTAS 11029 maneuver using the internal aerodynamic model. The pilot controls (θ_0, θ_{1c}, θ_{1s}, θ_{TR}) are determined for the entire maneuver using the vehicle states (u,v,w – translational velocity components, q - pitch rate). A time step of 0.001 seconds is used for the time marching. The maneuver covers a time frame of 9.5 seconds, therefore the entire simulation is run over 9500 time steps. The inverse simulation uses the state tracking approach to compute the pilot controls required to track the particular trajectory. Since the simulation is primarily in the longitudinal direction, the pedal is used primarily to counter pitch-yaw coupling. The

excursions in the lateral direction are very small compared to the movement in the longitudinal direction. The computed controls are shown in Figure 7.7. The controls are not compared with flight test values, since those values had experimental errors. Therefore, the adjusted control angles computed in the last chapter are used as the benchmark. The general trends are predicted reasonably though the magnitudes are different. The higher collective angle predictions are primarily because of the high inflow predicted by the BEMT model. Similarly, the longitudinal cyclic shows a higher value than readjusted controls because the aerodynamic model produces a lower thrust than CFD, hence higher control angles are required to produce the same amount of thrust. These pilot controls are used to fly the maneuver using the 6 DOF flight dynamics model. The altitude variation is shown in Figure 7.8 compared to the actual flight trajectory. The predicted trajectory shows a steeper pull-up than the actual flight trajectory.

7.4 Coupling of Aeromechanics and Flight Mechanics (AFMC)

The inverse simulation uses blade element momentum theory (BEMT) to evaluate aerodynamic loads. The use of a low fidelity method to predict rotor aerodynamics reduces the accuracy of the simulation. CFD/CSD coupling tools have known to capture the flow physics accurately. The idea is to replace the low fidelity aerodynamics with high fidelity CFD loads. The method employed to introduce the CFD loads into the flight mechanics system is similar in principle to the delta trimming methodology used in CFD/CSD loose coupling.

A flowchart of the methodology is shown in Figure 7.6. The steps involved in the aeromechanics / flight mechanics coupling are enumerated as follows:

a) The vehicle state vector in a chosen section of the maneuver is provided as an input to the inverse simulation. These states include <X, Y, Z> coordinates of the vehicle c.g. in the inertial frame, <φ, θ, ψ> euler angles denoting vehicle attitudes in inertial frame, <u, v, w> translational velocity components of the vehicle c.g. in global frame, <p, q, r> angular velocity components about the vehicle c.g in the global frame. The inverse simulation can track only four states corresponding to four pilot inputs, therefore these four states are chosen depending on the dominant motion of the vehicle. For ex: if the vehicle is pulling up in a longitudinal maneuver, the pitch rates along with translational velocity components are the most relevant states that are chosen for tracking.

b) The inverse simulations are run for this portion of the maneuver using BEMT for airloads computation. The pilot controls $<\theta_0, \theta_{1c}, \theta_{1s}, \theta_{TR}>$ are estimated for this maneuver.

c) The CFD-CSD coupling tools use the main rotor pitch input $<\theta_0, \theta_{1c}, \theta_{1s}>$ from the inverse simulation to perform a tight coupling simulation for that portion of the maneuver. The main rotor forces and moments (F_X, F_Y, F_Z, M_X, M_Y, M_Z) obtained from CFD simulations are transformed to the global frame and transferred to the inverse simulation. The CFD hub loads are not applied directly, but the difference between CFD and BEMT loads from previous iteration are computed which is denoted as Δ_{loads}. The Δ_{loads} are added to the loads calculated by the quasi-steady blade-element momentum theory model within the flight dynamics solver. Thus, for the same state and control input, the flight dynamic simulation now sees a correction

of the airloads using CFD loads. This Δ_{loads} approach provides the aerodynamic damping for the flight dynamic model.

d) The inverse simulation now results in a new set of states and controls, which is again fed into the CFD-CSD framework. This iterative process is continued until the loads computed by BEMT do not change with iteration at which stage the BEMT loads from 2 successive iterations cancel each other and only CFD loads are applied on the main rotor. Once the simulation has converged for a revolution, the next revolution is started using the current states and controls as initial conditions.

7.4.1 AFMC Results for Revs 1-5

The inverse simulation was coupled with CFD hub loads for the first five revolutions of the maneuver. Since this is a steady flight region, the coupling between inverse simulation and CFD solver happens only at the end of 5 revolutions. The inverse simulation was run using its internal aerodynamic model for the first iteration denoted as iteration 0. The control angles obtained from the inverse simulation were used to drive the first iteration of the tight coupling simulations. The CFD/CSD simulations were started from “no flow” initial conditions, therefore 3 revs of tight coupling simulations were performed for the transients to decay before transferring five revolutions of hub loads as delta loads to the inverse simulation. This process was repeated till convergence was achieved in the control angles. The flight conditions at beginning of rev 1 and end of rev 5 are almost identical, therefore the states computed at end of rev 5 can be used as initial conditions in inverse simulation. In the same manner, the tight coupling simulations can restart from flow conditions at end of rev 5. The restart option accelerates the coupling convergence between the inverse simulation and CFD/CSD methods. The

convergence of the blade control angles are shown in Figures 7.9 – 7.11. Convergence is achieved in about 6 iterations and control angles are within 10% of the trim values predicted by loose coupling simulations. When the delta hub loads are provided as an input to the inverse simulation, there is a steep change in the pitch control prediction, primarily because of the difference in fidelity between CFD and internal aerodynamic model. As the simulation progresses, the trends get smoother and they finally converge to a value that is closer to the trim predictions.

7.4.2 AFMC Results for Revs 15-17

Revs 15-17 represent the high load factor region of the pull-up maneuver. Since the vehicle is already undergoing maneuvering flight in this region, neither the inverse simulation nor the CFD/CSD coupling simulation can be started from 'no flow' ambient conditions. The loose coupling simulations performed for the quasi-steady analysis of rev 14 of the maneuver were used as initial conditions for the tightly coupled simulations. The controls determined using the loose coupling simulations were used as initial condition for the inverse simulation. The main difference between the simulations for steady flight and maneuvering flight is that the applied pilot control inputs are time varying for the maneuvering flight. As observed in the previous section, the inverse simulation generally predicts a spike in the control angles when the CFD hub loads are initially applied to the vehicle model. This sharp variation in control angles produces large grid deformations which affects the CFD/CSD coupling solution. To address this problem, a relaxation factor was used during the application of Δ_{loads} on the vehicle model for rev 15. The relaxation factor of 0.1, primarily estimated through trial and error was used in this study. The relaxation factor prevents large variation in controls but also

adversely affects the convergence. The control angle convergence for revs 15-17 is shown in Figures 7.12 - 7.14. The coupling is performed for each revolution in a serial fashion. The first AFMC simulations are performed for rev 15. The initial pilot controls for the inverse simulation correspond to a trim solution achieved using loose coupling simulations. Therefore, the zeroth interation of the AFMC methodology shows huge variation in control predictions. The Δ_{loads} were introduced with relaxation and convergence was achieved in about 17 iterations. The converged controls, flow information and blade deformations were used as initial conditions for rev 16. Since the inverse simulation has converged with CFD loads in previous revolution, delta loads can be directly applied and the inverse simulation with BEMT loads can be skipped. The control angle predictions for rev 16 converge in about 5 iterations, much faster than what was observed in the previous revolution. This is primarily because the inverse simulation starts from the converged controls from previous revolution. The convergence for rev 17 exhibits the same kind of behavior. The predicted control angles at end of convergence are very close to the adjusted test data for all the revs.

The converged set of control angles were used to run the tight coupling simulations for revs 15, 16 and 17. The normal force and pitching moment coefficients are plotted in Figure 7.15. A steady magnitude difference between the CFD/CSD TC simulation with flight test controls and AFMC methodology is observed in the normal force predictions. This steady displacement stems from the difference in collective. The lower harmonics in the predictions match reasonably well with test data though the stall loads are under-predicted.

7.4.3 Effect of Inflow Model

The blade element momentum theory (BEMT) model used in the inverse simulation provides a radial variation of the induced inflow distribution depending on the operating thrust and properties of the blade, such as the sectional chord, the blade twist, and the airfoil characteristics. Although, the BEMT approach has proved to be a very successful and reliable engineering tool, it is based on assumptions that make it insufficient to model critical physical phenomena. The BEMT does not account for wake contraction which affects the loading significantly in high thrust conditions. It does not account for the compressibility or dynamic stall effects which are critical physical phenomena affecting rotors in maneuvering flight. The Lagrangean wake model in the hybrid CFD solver is based on Prandtl lifting line theory. The wake strengths are obtained from CFD airloads using Kutta Joukowski theorem. This vortex wake model is a better physical representation of the rotor wake and therefore, the computed induced velocity field is more accurate. This vortex wake geometry is available in the hybrid CFD method. Therefore, it is beneficial to use this wake model to replace the BEMT model in the inverse simulation. The wake geometry is preserved from the CFD simulation but the wake strengths are obtained from the circulation computed by internal aerodynamic model in the inverse simulation tool. The enhanced inflow model in the inverse simulation is mainly used to improve the convergence of the coupling between CFD airloads and vehicle model. The AFMC simulations were performed for rev 15 with enhanced inflow model in inverse simulation. The difference in lifting line loads between successive iterations is computed as an l^2-norm and is plotted as function of coupling iterations for rev 15. The simulation with enhanced inflow model converges in about 8

iterations whereas the simulation with BEMT model takes about 17 iterations to converge.

7.5 Chapter Summary

A methodology was developed to couple the CFD/CSD coupling framework with inverse simulation so that the CFD airloads in the maneuver can be estimated without using the flight test data for pitch inputs. The methodology is used to study the rotor aeromechanics, as in previous chapters, for Revs 1-5 and Revs 15-17 of the UTTAS 11029 maneuver.

The inverse simulation convergence for steady flight revs 1-5 was smooth and the predicted control angles were within 10% of test data. The convergence for revs 15-17 was slower because of the under-relaxation of the Δ_{loads} that was required for numerical stability. The stability issues were primarily because of difference in fidelity of hub loads prediction which caused large variation in predicted control angles. To address this issue, the CFD wake geometry was used to compute the inflow in the internal aerodynamic table lookup model used by the inverse simulation. The enhanced inflow predictions improved the convergence characteristics of the methodology.

Table 7.1 UH-60A Black Hawk vehicle parameters

MAIN ROTOR	
Number of blades	4
Radius R, ft	26.833
Blade Chord c, ft	1.73
Rotational Speed Ω, rad/s	27.01
Tip Speed ft/sec	724.41
Longitudinal Shaft Tilt, deg	-3.0
Linear Blade Twist , deg	-18.0
Solidity	0.083
Lock Number	5.11

FUSELAGE	
Gross Weight, lbs	16000
Pitch Inertia, lbs-ft^2	38512
Roll Inertia, lbs-ft^2	4659
Yaw Inertia, lbs-ft^2	36800
I_{xz}, lbs-ft^2	1882
Horizontal tail surface area (ft^2)	45

TAIL ROTOR	
Number of blades	4
Radius, ft	5.5
Blade Chord	0.81
Rotational speed, rad/sec	124.62
Tip speed, ft/sec	685.41
Rotor shaft cant angle, deg	20.0

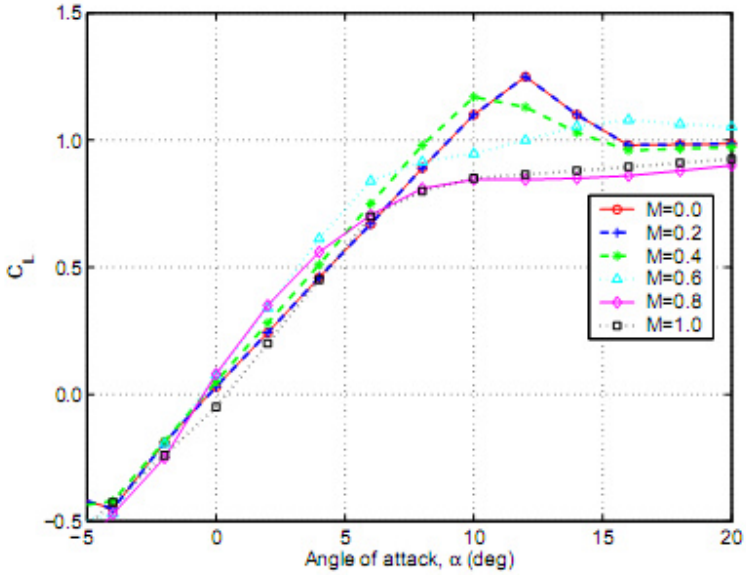

Figure 7.1 Lift Coefficient vs. angle of attack and Mach number for SC1095

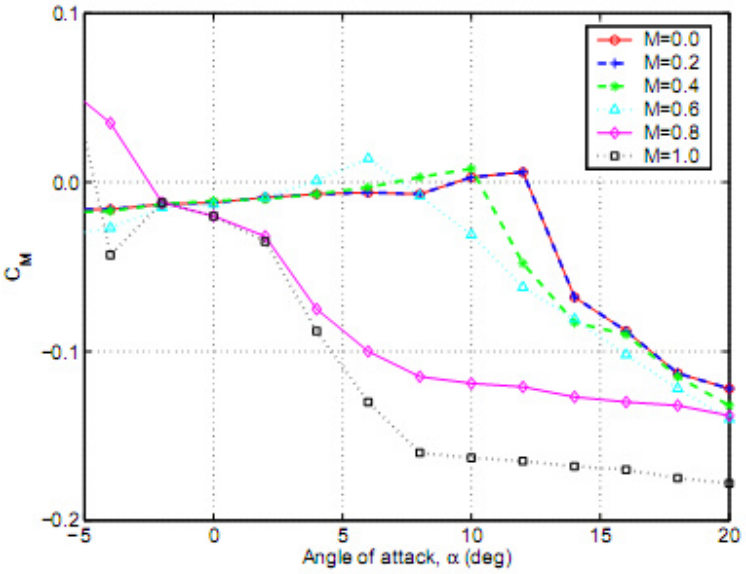

Figure 7.2 Moment Coefficient vs. angle of attack and Mach number for SC1095

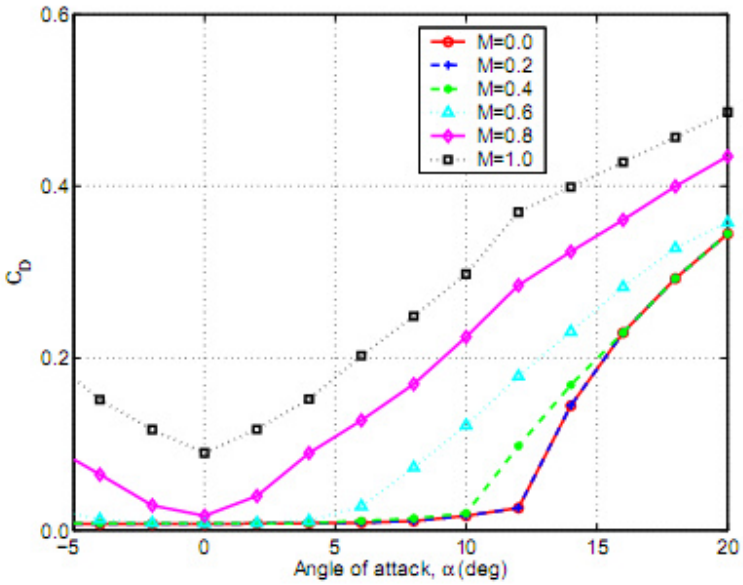

Figure 7.3 Drag Coefficient vs. angle of attack and Mach number for SC1095

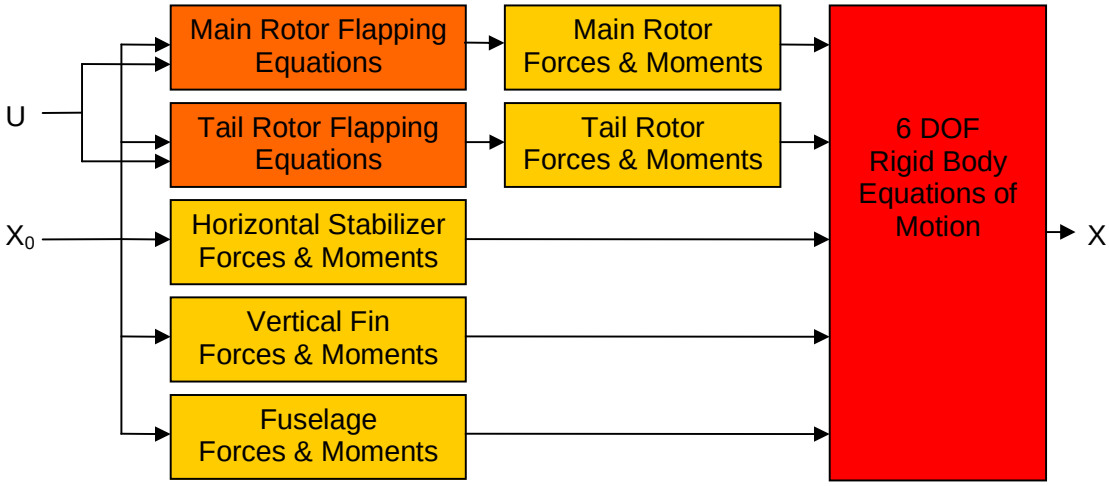

Figure 7.4 Schematic of UH-60A flight dynamics model

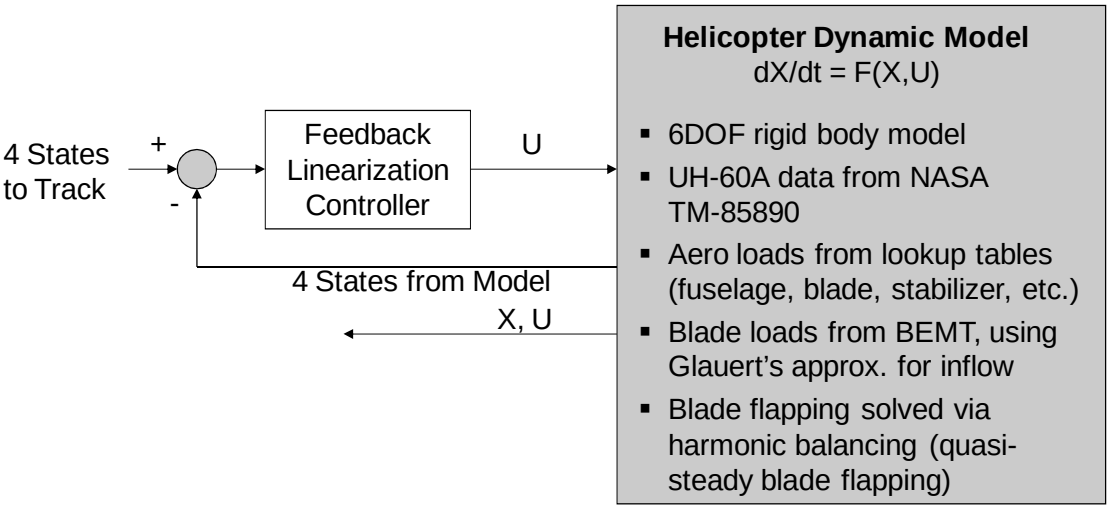

Figure 7.5 Schematic of feedback linearization technique

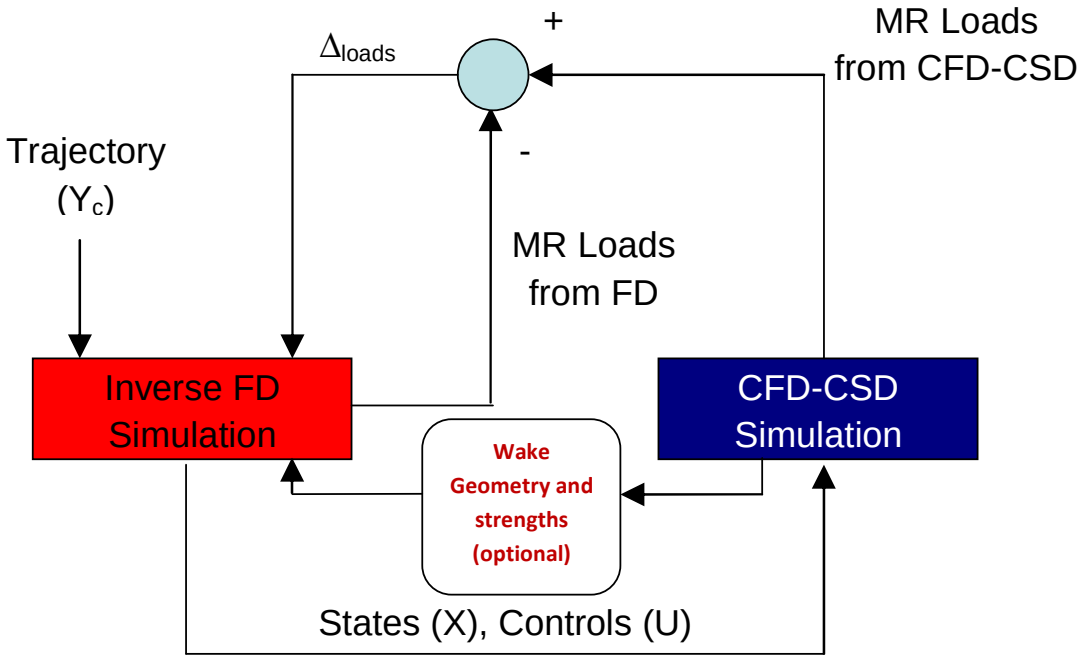

Figure 7.6 Schematic of Aeromechanics / Flight Mechanics Coupling Methodology

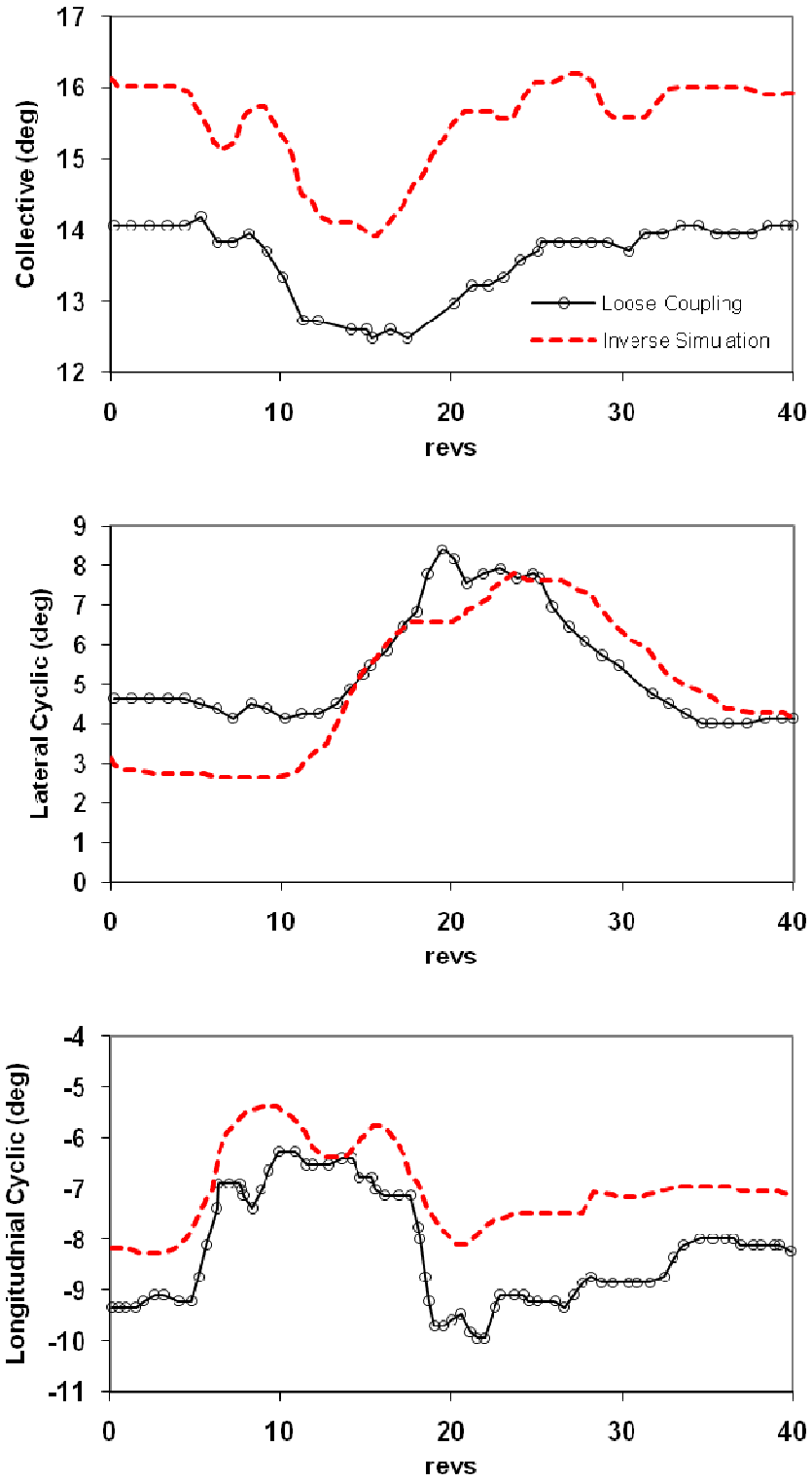

Figure 7.7 Inverse simulation for UTTAS 11029 maneuver

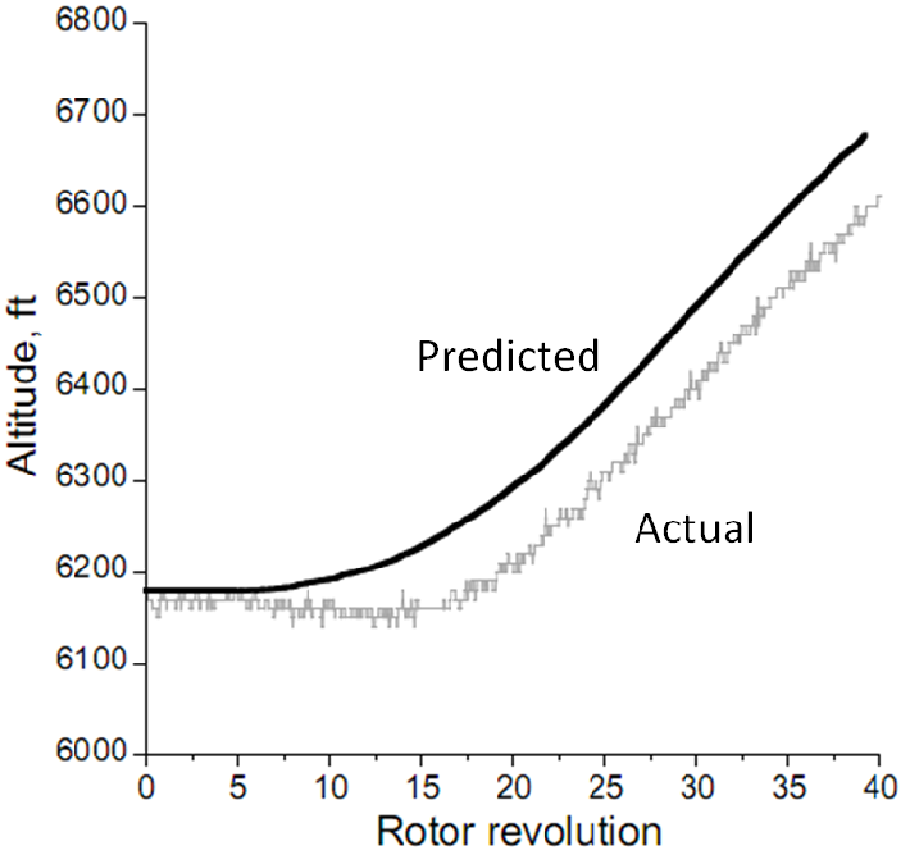

Figure 7.8 UTTAS 11029 Trajectory – real vs. predicted

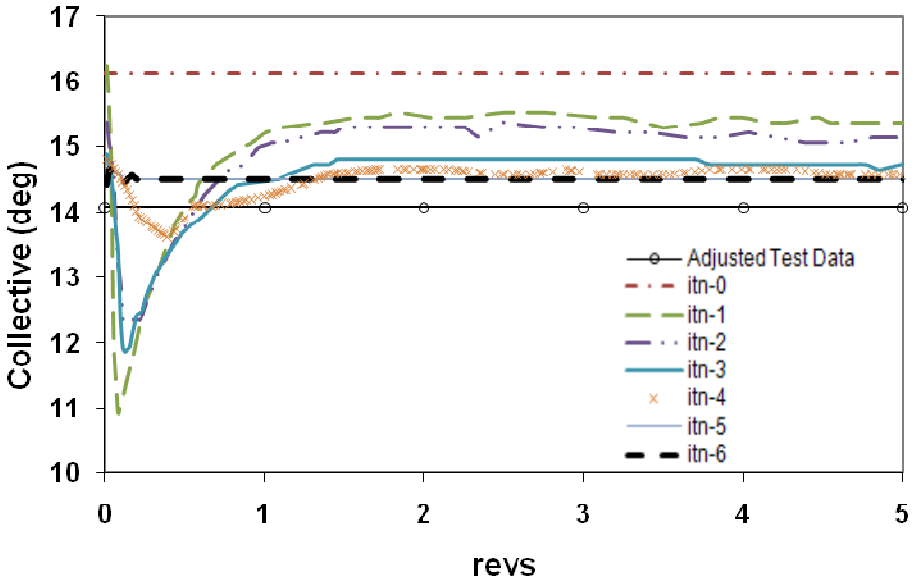

Figure 7.9 UTTAS 11029 Revs 1-5: Blade collective convergence

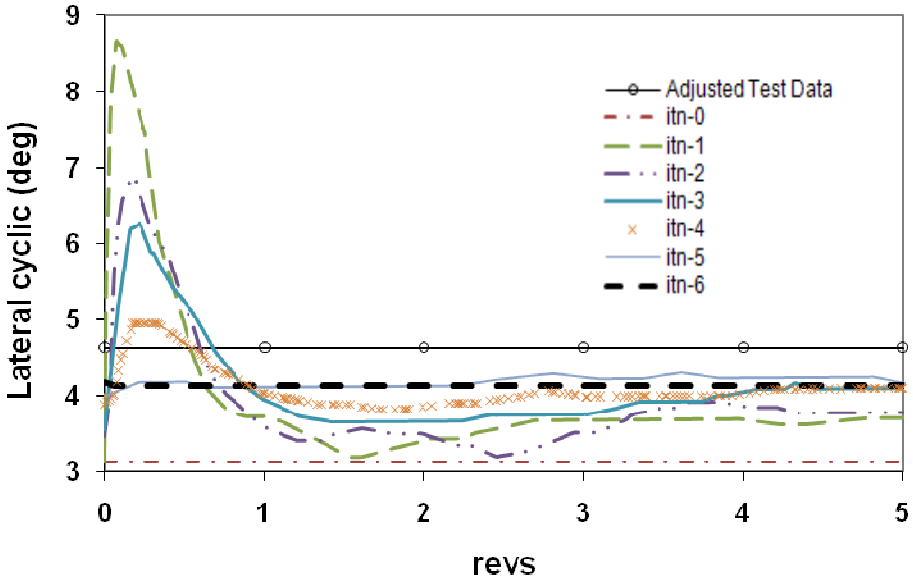

Figure 7.10 UTTAS 11029 Revs 1-5: Blade lateral cyclic convergence

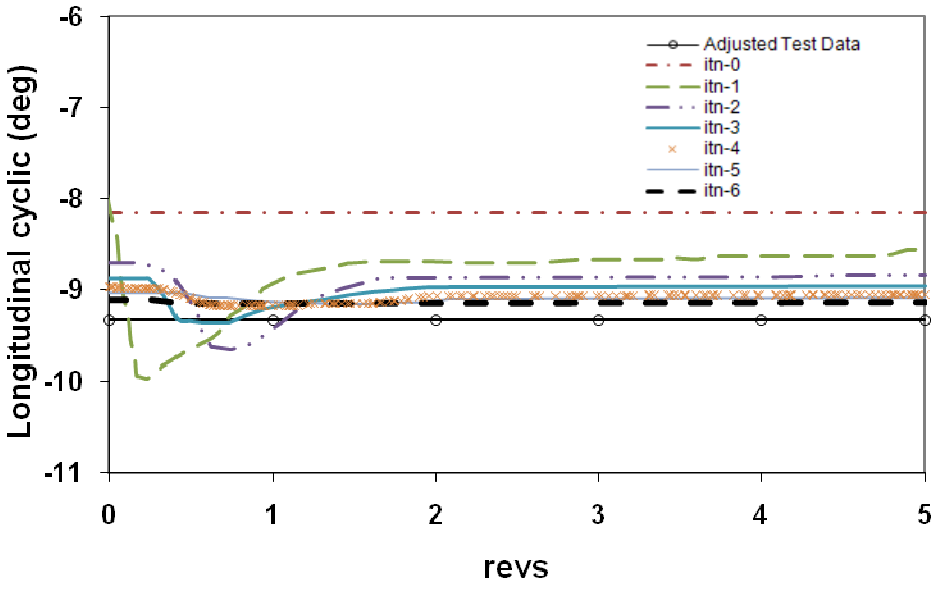

Figure 7.11 UTTAS 11029 Revs 1-5: Blade lateral cyclic convergence

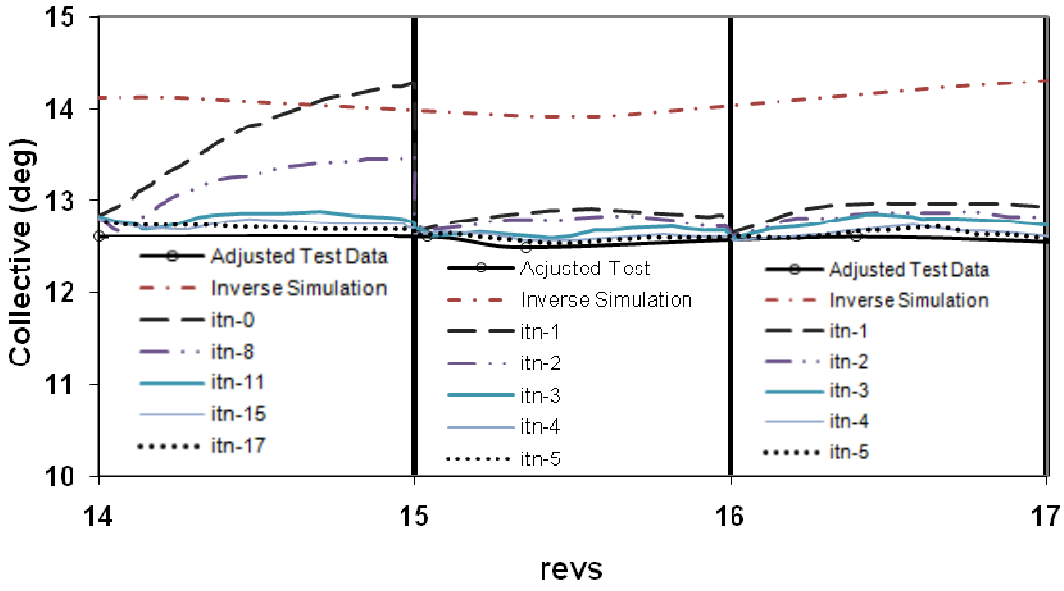

Figure 7.12 UTTAS 11029 Revs 15-17: Blade collective convergence

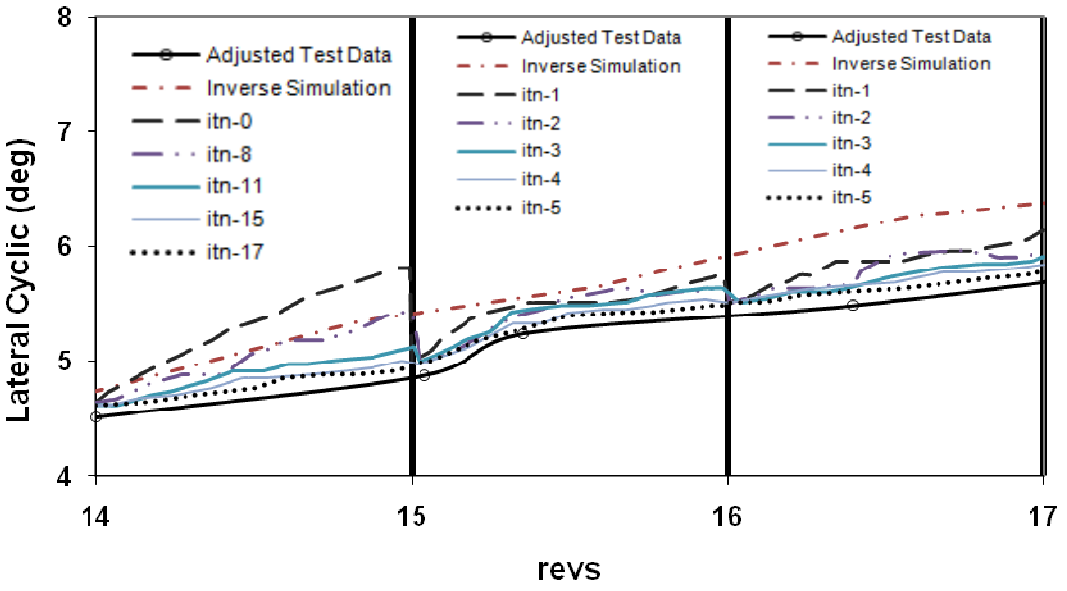

Figure 7.13 UTTAS 11029 Revs 15-17: Blade lateral cyclic convergence

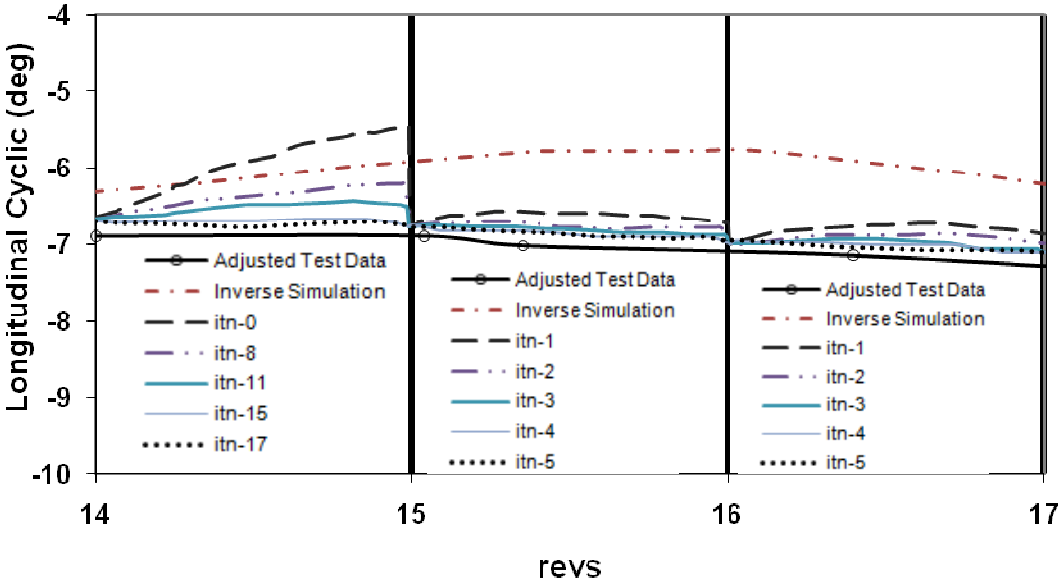

Figure 7.14 UTTAS 11029 Revs 15-17: Blade longitudinal cyclic convergence

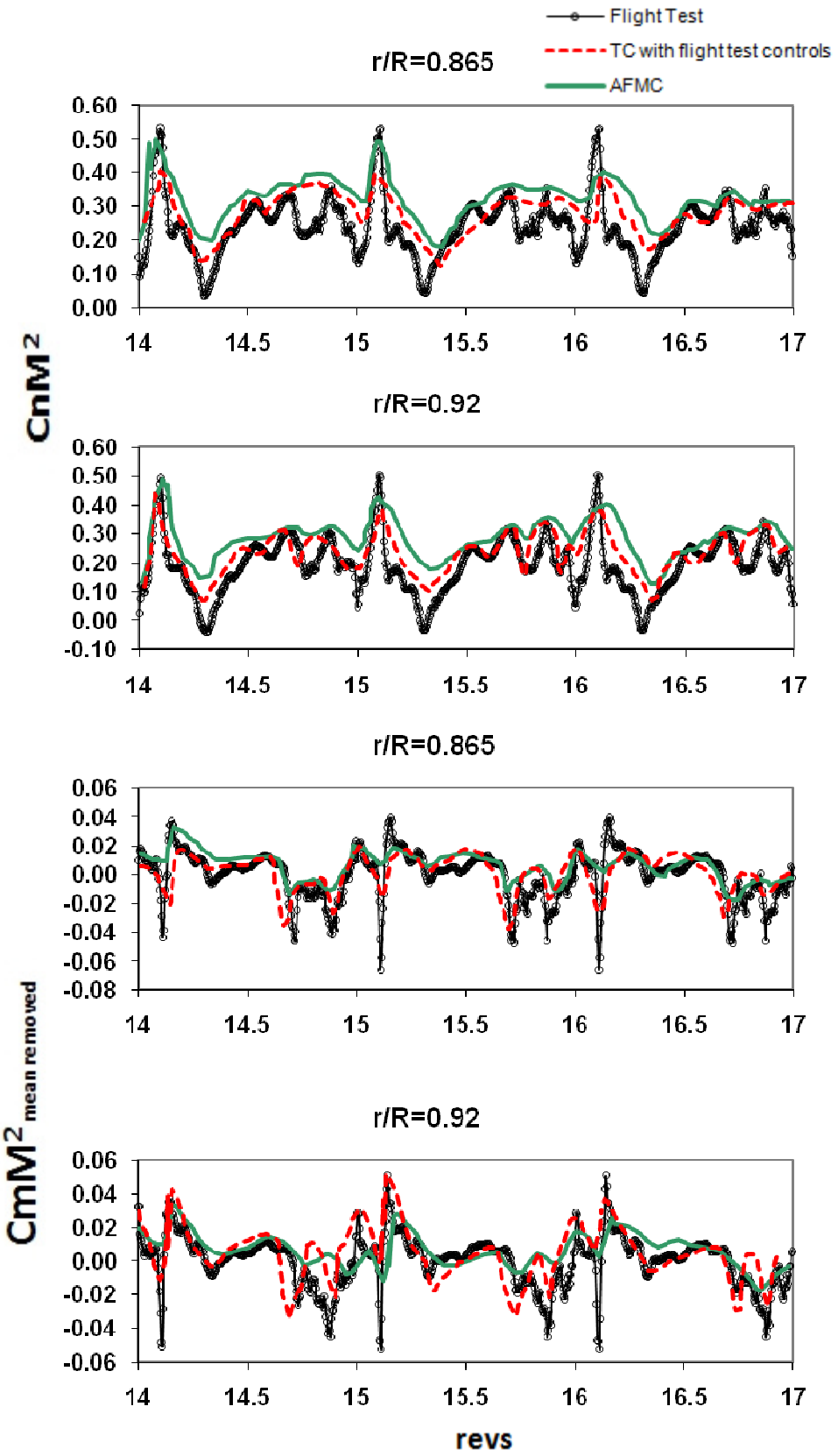

Figure 7.15 UTTAS 11029 Revs 15-17: AFMC results

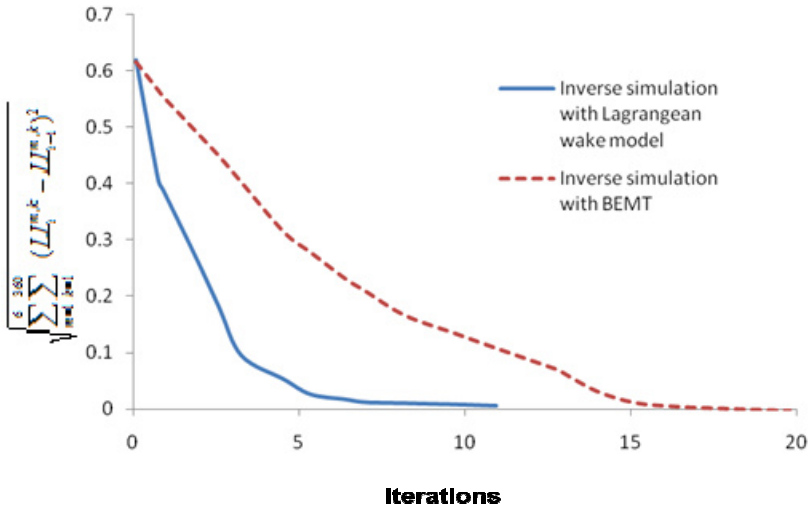

Figure 7.16 Effect of inflow model on AFMC convergence

CHAPTER 8

CONCLUSIONS AND RECOMMENDATIONS

The helicopter is one of the most complicated vehicles to design because of the myriad of flight modes that need to be considered and the complex multidisciplinary coupling that causes various physical phenomena during operation. The study of rotorcraft aeromechanics using efficient, high fidelity computational tools is therefore very important to the rotorcraft community. In this research, an enhanced hybrid Navier-Stokes / free wake methodology was developed to study rotor aeromechanics in a computationally efficient manner. The Navier-Stokes solver was coupled to a free wake model to take into account the rotor wake that is not captured by the solver. Enhancements made to the hybrid CFD methodology improved the prediction of complex aerodynamic phenomena and further increased the efficiency of the methodology. These enhancements include parallelization of the solver, implementation of full span wake and shed wake models, implementation of geometric conservation law and higher order spatial and temporal schemes. The enhancements were validated for 3-D rotor simulations using prescribed aeroelastic deformations.

The CFD methodology was coupled to CSD methodology to perform a trimmed aeroelastic analysis of a rotor in forward flight. The coupling analyses, both loose and tight were used to identify the key physical phenomena that affect rotors in different flight regimes. The coupling methodology was extended to maneuvering flight analysis by enhancing the computational and structural models to handle non-periodic flight

conditions and vehicle motions. The flight test measured control angles were used to drive the maneuvering flight analysis.

Finally, a methodology was developed to couple the CFD/CSD simulation with an inverse flight mechanics simulation to perform the maneuver analysis without using the flight test control input. The UH-60A rotor was used as test case for all these studies and the flight conditions were chosen from the UH-60A Airloads Program database.

8.1 Conclusions

Based on the aforementioned studies, the following conclusions may be drawn:

1. It was found that the satisfaction of Geometric Conservation Law in CFD methodology could remove non-physical mass and momentum accumulation at the far-field where the cell size and deformation is large.
2. A 5^{th} order ENO scheme did not significantly improve the prediction of rotor airloads over a 3^{rd} order MUSCL scheme on a highly stretched baseline grid. The second order temporal scheme did not significantly impact the airload predictions over a first order temporal scheme for steady flight conditions given the small time step (0.05 degrees azimuth) used in this study.
3. The full span wake model captures the effect of inboard vorticity and was shown to be essential to capture the effects of BVI in a low speed flight condition.
4. The shed wake is significant in separated flow regions. The shed wake model enhanced the induced velocity field and improved the prediction of dynamic stall loads on retreating side.

5. There was no particular benefit to using tightly coupled CFD/CSD predictions for steady flight conditions. Loosely coupled methods were shown to be adequate for these cases.
6. An aeroelastic coupling analysis of c8534 high speed flight condition revealed that vibratory loads (> 2 per rev) dominated the inboard region whereas the non-vibratory loads were the dominant component in the airloads on the outboard regions. Further analysis showed that nose down pitching moments causing negative lift on the advancing side are due to transonic effects.
7. An aeroelastic coupling analysis of 9017 high thrust flight condition predicted two dynamic stall cycles on the retreating side. It was concluded from the examination of blade local pitch angles that the first dynamic stall was induced by trim whereas the second one was due to elastic torsion caused by 5 per rev harmonics. The effect of the wake on dynamic stall was qualitatively assessed by testing the full span wake model and single tip vortex model. It was found that the vortex strength was too high in the single tip vortex model and that caused a huge downwash which decreased the local angle of attack and prevented the second dynamic stall cycle.
8. The coupling simulations of low speed 8513 flight condition indicated BVI events in the first and fourth quadrant that produced huge vibratory loads. The local angle of attack was examined and it was found that the inflow was the determining factor in the production of the impulsive loads.
9. The high thrust 9020 flight condition exhibited dynamic stall cycles similar to what was observed in flight counter 9017. SA-DES and KES turbulence models were compared for c9020 and it was concluded that SA-DES modeled a high production

of turbulent kinetic energy that prevented the second dynamic stall whereas KES was able to model the phenomenon correctly. This behavior of SA-DES was not observed for c9017.

10. The coupling analysis of revs 1-5 of UTTAS 11029 maneuvering flight condition showed that the airloads are characterized by transonic nose-down pitching moments and negative lift on advancing side, similar to high speed 8534 flight condition. The loose and tight coupling analyses predictions were comparable to each other.
11. The analysis of revs 15-17 of UTTAS 11029 indicated a dual stall phenomenon on the retreating side due to a very high thrust condition and rapidly increasing pitch attitude. A strong transonic blade stall was observed on the advancing side. The loose coupling simulations compared well with tight coupling on advancing side but the predictions were poor on the retreating side primarily due to the quasi-steady nature of the loose coupling analysis. The angular velocity components in the longitudinal direction were averaged; therefore the angle of attack is lower than observed value which affects the stall predictions.
12. A second order temporally accurate scheme predicted better stall loads compared to a first order scheme for maneuvering flight conditions. The second order scheme is able to capture the transient flow information better than first order temporal scheme.
13. A new methodology was developed to couple the CFD/CSD framework with an inverse flight simulation method for maneuvering analysis without using blade pitch angles from test data. The methodology showed reasonable convergence in steady flight regime and control angles predictions compared reasonably well with test data.

In the maneuvering flight regions, the convergence was slower due to relaxation techniques used for stability. The predicted control angles in this region compared well with test data. The enhancement of the rotor inflow computations in the inverse simulation through implementation of a Lagrangean wake model accelerated the convergence of the coupling methodology.

8.2 Recommendations for Future Work

Based on the computational studies and the conclusions drawn from them, the following recommendations are made for future research:

1. The airload correlations for steady flight conditions were found to be better in the blade outboard regions than inboard regions. The effect of spanwise grid density and other factors on airload predictions for inboard regions should be investigated.
2. This work studied only selected critical regions in the UTTAS 11029 maneuver. The coupling methodology should be applied to other regions of the maneuver. The methodology should also be used for analyzing other types of severe maneuvers in the UH-60A Airloads Program.
3. The hybrid CFD methodology was extensively validated for the UH-60A rotor. The methodology needs to be further evaluated for rotor configurations like Apache, MDART and HART to fully evaluate the capabilities of the methodology.
4. The aeromechanics / flight mechanics coupling methodology should be further evaluated for other types of maneuvers. The methodology uses a generic framework, therefore other CFD, CSD and flight simulation tools can be applied to study the rotor loads in arbitrary trajectories.

5. The hybrid CFD methodology was shown to incorporate the blade to blade interactions in an efficient manner through the wake model. Therefore, this methodology must be further explored for interactional aerodynamics studies like coaxial rotors, tandem rotors, main rotor / tail rotor interactions etc.
6. The hybrid CFD methodology can be coupled to structured overset solvers like OVERFLOW or unstructured Cartesian solvers like NASCART-GT [122] to perform rotor-airframe interactional studies in a computationally efficient manner.
7. The CFD/CSD coupling methodologies should be extended to the analysis of rotor aeroelastic stability including, but not restricted to the study of phenomena like transonic flutter, stall flutter and ground resonance.
8. Blade on-board control is a critical area of research where active control devices like trailing edge flaps, morphing airfoils, gurney flaps etc. are used to mitigate vibratory loads, avoid BVI events and reduce the acoustic signature of the rotor. These on-board control devices can be effectively simulated in the hybrid CFD methodology through blade deformations providing an efficient method to study the active control of rotor blades.

APPENDIX A

COMPUTATIONAL TIMING ANALYSIS

The computational timing analysis enumerates the computational expense of each modeling enhancement in the hybrid CFD methodology as a percentage of the baseline condition turnaround time. The analysis is based on performance benchmarks on a Intel® Core™ 2 Quad 2.4GHz cluster with 8 processors. The analysis is presented in the table below:

Table 8.1 Computational Timing Analysis

Type of enhancement	**Baseline Scheme / Model**	**Enhancement**	**Computational Time Increase**
Spatial accuracy	3rd order MUSCL	5th order ENO	53%
Temporal accuracy	1st order time accuracy	2nd order time accuracy	45%
Turbulence modeling	SA-DES	KES	34%
Wake model	Single tip vortex model	Full Span Wake Model (n = 10 trailers)	49%
Wake model	Single tip vortex model	Full Span Wake Model (n = 10 trailers) with shed wake	52%

REFERENCES

[1] Landgrebe, A. J., "New Directions in Rotorcraft Computational Aerodynamics Research in the U.S.," *AGARD-CP-552*, August 1995.

[2] Johnson, W., "Helicopter Theory," Princeton University Press 1998

[3] Loewy, R. G., "A Two Dimensional Approach to the Unsteady Aerodynamics of Rotor wings," *Journal of Aerospace Science*, Vol.24, 1957, pp.81-98.

[4] Leishman, J. G. and Beddoes, T. S., "A Semi-Empirical Model for Dynamic Stall," *Journal of the American Helicopter Society*, Vol.34, No.3, July 1989, pp.3-17.

[5] Johnson, W., "Development of a Comprehensive Analysis for Rotorcraft I. Rotor Model and Wake Analysis", *Vertica*, Vol.5, 1989, pp.90-130.

[6] Johnson, W., "Development of a Comprehensive Analysis for Rotorcraft II. Aircraft Model, Solution Procedure and Applications", *Vertica*, Vol.5, 1989, pp.185-216.

[7] Stephens, W. B., Rutkowski, M. J., Ormiston, R. A., and Tan, C. M., "Development of the Second Generation Comprehensive Helicopter Analysis System (2GCHAS)," Proceedings of the AHS National Specialists' Meeting on Rotorcraft Dynamics, Arlington, TX, Nov. 1989.

[8] Sopher, R. and Hallock, D. W., "Time-History Analysis for Rotorcraft Dynamics Based on a Component Approach," *Journal of the American Helicopter Society*, Vol.31, No.1, Jan. 1986, pp.43-51.

[9] Johnson, W., "Technology Drivers in the Development of CAMRAD II," in Aeromechanics Specialists Conference, (San Francisco, CA), American Helicopter Society, January 1994.

[10] Johnson, W., "Rotorcraft Dynamics Models for a Comprehensive Analysis," Proceedings of the 54th Annual Forum, (Washington D.C.), American Helicopter Society, May 1998.

[11] Bauchau, O. A., Botasso, C. L., and Nikishkov, Y. G., "Modeling Rotorcraft Dynamics with Finite Element Multibody Procedures," *Mathematical and Computer Modeling*, vol. 33, pp. 1113–1137, 2001.

[12] Bir, G. and Chopra, I., "Development of UMARC (University of Maryland Advanced Rotorcraft Code)," in Proceedings of the 46th Annual Forum, (Washington D.C.), American Helicopter Society, May 1990.

[13] Ormiston, R. A., “An Investigation of the Mechanical Airloads Problem for Evaluating Rotor Blade Structural Dynamics Analysis," American Helicopter Society 4th Decennial Specialists Conference on Aeromechanics, San Francisco, CA, January 2004.

[14] Benoit, B., Dequin, A.M., Kampa, K., Grunhagen,W., Basset, P.M., and Gimonet, B., “HOST: A General Helicopter Simulation Tool For Germany and France,” in Proceedngs of the 56th Annual Forum, (Virginia Beach, VA), American Helicopter Society, May 2000.

[15] Caradonna, F. X. and Isom, M. P., “Subsonic and Transonic Potential Flow over Helicopter Rotor Blades,” *AIAA Journal*, No.12, December 1972, pp.1606-1612.

[16] Chattot, J. J., “Calculation of Three-dimensional Unsteady Transonic Flows Past Helicopter Blades,” NASA Technical Paper 1721, Oct. 1980.

[17] Sankar, L. N. and Prichard, D., “Solution of Transonic Flow Past Rotor Blades using the Conservative Full Potential Equation,” AIAA Paper 85-5012, October 1985.

[18] Sankar, L. N. and Malone, J. B., “Unsteady Transonic Full Potential Solutions for Airfoils Encountering Vortices and Gust,” AIAA paper 85-1710, July 1985.

[19] Hassan, A., Tung, C., and Sankar, L. “An Assessment of Full-Potential and Euler Solutions for Self-Generated Rotor Blade-Vortex Interactions,” 46th AHS Annual Forum Proceedings, Washington, D. C., May 1990.

[20] Tadghighi, H., Hassan, A., and Charles, B., “Prediction of Blade-Vortex Interaction Noise Using Airloads Generated by a Finite-Difference Technique,” 46th AHS Annual Forum Proceedings, Washington, D. C., May 1990.

[21] Sankar, L.N. and Tung, C., “Euler Calculations for Rotor Configurations in Unsteady Forward Flight,” Proceedings of the 42nd Annual Forum of the American Helicopter Society, Washington, DC, June 1986.

[22] Sankar, L. N., Wake, B. E., and Lekoudis, S. G., “Solution of the Unsteady Euler Equations for Fixed and Rotor Wing Configurations,” *Journal of Aircraft*, Vol.23, No.4, April 1986, pp.283-289.

[23] Roberts, T. W. and Murman, E. M., “Solution Method for a Hovering Helicopter Rotor Using the Euler Equations,” AIAA paper 85-0436.

[24] Agarwal, R. and Deese, J., “An Euler Solver for Calculating the Flow-field of a Helicopter Rotor in Hover and Forward Flight,” AIAA 19th Fluid Dynamics, Plasma Dynamics, and Laser Conference, June 1987.

[25] Chang, I-C., “Unsteady Euler Solution of Transonic Helicopter Rotor Flow,” AHS Specialists Meeting on Aerodynamics and Aeroacoustics, Feb. 1987.

[26] Srinivasan, G. R., Baeder, J. D., Obayashi, S. and McCroskey, W. J., "Flow-field of a Lifting Rotor in Hover: A Navier-Stokes Simulation," *AIAA Journal*, Vol.30, No.10, Oct. 1992, pp.2371-2378.

[27] Srinivasan, G. R. and Baeder, J. D., "TURNS: A Free Wake Euler/Navier-Stokes Numerical Method for Helicopter Rotors," *AIAA Journal*, Volume 31, Number 5, May 1993, pp.959-962.

[28] Wake, B. E., "A Solution Procedure for the Navier-Stokes Equations Applied to Rotors," Ph.D. Dissertation, Georgia Institute of Technology, 1987.

[29] Srinivasan, G. R. and McCroskey, W. J., "Navier-Stokes Calculations of Hovering Rotor Flow-fields," *Journal of Aircraft*, Vol.25, No.10, Oct. 1988, pp.865-874.

[30] Agarwal, R. K. and Deese, J. E., "Navier-Stokes Calculations of the Flow-field of a Helicopter Rotor in Hover," AIAA Paper 88-0106, 1988.

[31] Wake, B. and Baeder, J., "Evaluation of a Navier-Stokes Analysis Method for Hover Performance Prediction," *Journal of the American Helicopter Society*, Vol.41, No.1, Jan. 1996, pp.1-17.

[32] Hariharan, N. S. and Sankar, L. N., "First-Principle Based High Order Methodologies for Rotorcraft Flow-field Studies," 55th Annual Forum of the American Helicopter Society, Montreal, Canada, May 25-27, 1999.

[33] Bangalore, A. and Sankar, L. N., "Forward Flight Analysis of Slatted Rotors Using Navier-Stokes Methods," AIAA Paper 96-0675, Jan. 1996.

[34] Ahmad, J., Duque, E. P. N., and Strawn, R. C., "Computations of Rotorcraft Aeroacoustics with a Navier-Stokes/Kirchhoff Method," 22nd European Rotorcraft Forum, Brighton, UK, Sept. 17-19, 1996.

[35] Ekaterinaris, J. A., Srinivasan, G. R., and McCroskey, W. J., "Present Capabilities of Predicting Two-Dimensional Dynamic Stall," AGARD CP-552, Oct. 1994.

[36] Narramore, J., Sankar, L. N., and Vermeland, R., "An Evaluation of a Navier-Stokes Code for Calculations of Retreating Blade Stall on a Helicopter Rotor," Proceeding of the 44th Annual Forum of the American Helicopter Society, Washington, D. C., June 1988.

[37] Sankar, L. N., Bharadwaj, B. K., and Tsung, F. L., "A three-dimensional Navier-Stokes/full-potential coupled analysis for viscous transonic flow," AIAA 10th Computational Fluid Dynamics Conference, Honolulu, HI, June 24-27, 1991.

[38] Berezin, C. R. and Sankar, L. N., "An Improved Navier-Stokes/Full Potential Coupled Analysis for Rotors," Mathematical Computational Modeling, Vol.19, No.3/4, 1994, pp.125-133.

[39] Berkman, M. E., Sankar, L. N., Berezin, C.R., and Torok, M. S., " Navier-Stokes/Full Potential/Free-Wake Method for Rotor Flows" *Journal of Aircraft*, Vol.34, No.5, 1997, pp.635-640.

[40] Yang, Z., Sankar, L. N., Smith, M. J., and Bauchau, O., "Recent Improvements to a Hybrid Method for Rotors in Forward Flight," *Journal of Aircraft*, Vol. 39, No. 5, 2002, pp. 804-812.

[41] Yang, Z., Sankar, L., "A Hybrid Flow Analysis for Rotors in Forward Flight," Ph.D. Dissertation, Georgia Institute of Technology, 2001.

[42] Peters, D. A., Boyd, D. D., and He, C. J., "Finite-State Induced-Flow Model for Rotors in Hover and Forward Flight," *AHS Journal*, Vol.34, No.4, October 1989, pp.5-17.

[43] Tung, C., Caradonna, F., X. and Johnson, W., "The Prediction of Transonic Flows on an Advancing Rotor," *Journal of American Helicopter Society*, Vol. 32, No. 7, 1986, pp. 4-9.

[44] Strawn, R.C. and Tung, C., "Prediction of Unsteady Transonic Rotor Loads with a Full-Potential Rotor Code," American Helicopter Society, 43rd Annual Forum, St. Louis, MO, May 18-20, 1987.

[45] Strawn, R.C. and Tung, C., "The Prediction of Transonic Loading on Advancing Helicopter Rotors," NASA TM-88238, 1986.

[46] Yamauchi, G.K., Heffernan, R.M., and Gaubert, M., "Correlation of SA349/2 Helicopter Flight Test Data with a Comprehensive Rotorcraft Model," *Journal of American Helicopter Society*, Vol. 33, No. 2, 1988, pp. 31-42.

[47] Murthy, H., Bottasso, C., Shephard M. P. M., and Bauchau, O., "Aeroelastic Analysis of Rotor Blades Using Nonlinear Fluid/Structure Coupling," Proceedings of the 53rd Annual AHS Forum, Virginia, April 1997.

[48] Bauchau, O. A. and Ahmad, J. U., "Advanced CFD and CSD Methods for Multidisciplinary Applications in Rotorcraft Problems", Proceedings of the AIAA/NASA/USAF Multidisciplinary Analysis and Optimization Symposium, Bellevue, WA, Sep. 4-6, 1996, pp.945-953.

[49] Torok, M. S. and Chopra, I., "Hingeless Rotor Aeroelastic Stability Analysis with Refined Aerodynamic Modeling," *Journal of the American Helicopter Society*, Vol.36, No.4, October 1991, pp.48-56.

[50] Kim, K. C., Desopper, and Chopra, I., "Blade Response Calculations Using Three Dimensional Aerodynamic Modeling," *Journal of the American Helicopter Society*, Vol.36, No.1, Jan. 1991, pp.68-77.

[51] Sitaraman, J., "CFD Based Unsteady Aerodynamic Modeling for Rotor Aeroelastic Analysis," Ph. D. Dissertation, University of Maryland, 2003.

[52] Datta, A., Sitaraman, J., Chopra, I., Baeder, J. D., "CFD/CSD Prediction of Rotor Vibratory Loads in High-Speed Flight," *Journal of Aircraft*, Vol.43, No.6, 2006

[53] Datta, A., Chopra, I., "Prediction of UH-60A Dynamic Stall Loads in High Altitude Level Flight using CFD/CSD Coupling," American Helicopter Society 61st Annual Forum, Grapevine, TX, June 2005.

[54] Potsdam, M., Yeo, H., Johnson, W., "Rotor Aerodynamic Prediction using Loose Aerodynamic/Structural Coupling," American Helicopter Society 60th Annual Forum, Baltimore, MD, June 2004.

[55] Phanse, S., Sankar, L. N., Bauchau, O., "An Efficient Tightly Coupled Fluid-Solid Interaction for Modeling Rotors in Forward Flight," 2nd International Basic Research Conference on Rotorcraft Technology, Nanjing, China, November 7- 9, 2005.

[56] Phanse, S., Sankar, L. N., Charles, B. D., "Efficient Coupled Fluid Structure Interaction Approach for Analysis of Rotors in Forward Flight," American Helicopter Vertical Lift Aircraft Design Conference, San Francisco, California, January 18-29,2006

[57] Makinen, S., Reed, E., Egolf, A., Rajmohan, N., Sankar, L.N., "Vibratory Load Correlation for the UH-60A Rotor in a High Thrust Forward Flight Condition," AHS 64th Annual Forum, Montreal Quebec, Canada, April 29 - May 1

[58] Makinen, S., Reed, E., Egolf, A., Rajmohan, N., Sankar, L.N., "Initial Development of a Methodology for Quantitative Load Prediction Over the Aircraft Flight Envelope," AHS Specialist's Conference on Aeromechanics, San Francisco, CA, Jan. 23-25, 2008

[59] Duque, E., Sankar, L. N., Menon, S., Bauchau, O., Ruffin, S., Smith, M., Ahuja, K., Brentner, K., Long, L., Morris, P., and Gandhi, F., "Revolutionary Physics-Based Design Tools for Quiet Helicopters," 44th AIAA Aerospace Sciences Meeting and Exhibit, AIAA, Reno, NV, January 2006, AIAA 2001-1068.

[60] Bhagwat, M. J., Ormiston, R. A. ,Saberi, H. A. and Hong, X., "Application of CFD/CSD Coupling for Analysis of Rotorcraft Airloads and Blade Loads in Maneuvering Flight," AHS 63rd Annual Forum, Virginia Beach, VA, 2007

[61] Silbaugh, B., Baeder, J.D., "Coupled CFD/CSD Analysis of a Maneuvering Rotor Using Staggered & Time-Accurate Coupling Scheme," AHS Specialist's Conference on Aeromechanics, San Francisco, CA, Jan. 23-25, 2008.

[62] Abhishek, A., Datta, A., Chopra, I., "Comprehensive Analysis, Prediction, and Validation of UH-60A Blade Loads in Unsteady Maneuvering Flight," AHS Specialist's Conference on Aeromechanics, San Francisco, CA, Jan. 23-25, 2008.

[63] Fusato, D., Celi, R., "Multidisciplinary Design Optimization for Aeromechanics and Handling Qualities," *Journal of Aircraft*, Vol. 43, No. 1, January–February 2006

[64] Bottasso, C.L., Croce, A., Leonello, D., Riviello, L., "Unsteady Trim for the Simulation of Maneuvering Rotorcraft with Comprehensive Models," Scientific Report DIA-SR 05-02, Dip. Ingegneria Aerospaziale, Politecnico di Milano, 2005.

[65] Bottasso, C.L., Croce, A., Leonello, D., "Procedures for enabling the simulation of maneuvers with comprehensive codes," 31st European Rotorcraft Forum, Firenze, Italy 2005.

[66] Bauchau, O., Bottasso, C., Nikishkov, Y., "Modeling Rotorcraft Dynamics with Finite Element Multibody Procedures," *Mathematical and Computer Modeling*, 33, pp 1113-1137, 2001

[67] Bridges, D.O., Horn, J.F., Alpman, E., Long, L.N., "Coupled Flight Dynamics and CFD Analysis of Pilot Workload in Ship Airwakes," AIAA Atmospheric Flight Dynamics Conference, Hilton Head, SC, Aug 2007

[68] O'Neill, C.R., Arena , A.S., "Aircraft Flight Dynamics with a Non-Inertial CFD Code," 43rd AIAA Aerospace Sciences Meeting and Exhibit, Jan. 10–13, Reno, NV

[69] Thomson, D. G., and Bradley, R., "Development and Verification of an Algorithm for Helicopter Inverse Simulation," Vertica, Vol. 14, No. 2, 1990, pp. 185-200.

[70] Bradley, R., and Thomson, D. G., "Handling Qualities and Performance Aspects of the Simulation of Helicopters Flying Mission Task Elements," Proceedings of the Eighteenth European Rotorcraft Forum, Avignon, France, Sep 1992, pp. 139.1-139.15.

[71] Whalley, M. S., "Development and Evaluation of an Inverse Solution Technique for Studying Helicopter Maneuverability and Agility," NASA TM 102889 and USAAVSCOM TR 90-A-008, July 1991.

[72] Kato, O., and Sugiura, I., "An Interpretation of Airplane General Motion and Control as Inverse Problem," *Journal of Guidance, Control, and Dynamics*, Vol. 9, No. 2, Mar-Apr 1986, pp. 198-204.

[73] Hess, R. A., Gao, C., and Wang, S. H., "Generalized Technique for Inverse Simulation Applied to Aircraft Maneuvers," *Journal of Guidance, Control, and Dynamics*, Vol. 14, No. 5, Sep-Oct 1991, pp. 920-926.

[74] Bousman, W.G. and Kufeld, R.M., "UH-60A Airloads Catalog," Aeroflightdynamics Directorate (AMRDEC), U.S. Army Research, Development, and Engineering Command, Ames Research Center, Moffet Field, California, August 2005, NASA-TM-2005-212827, AFDD/TR-05-003

[75] Yeo, H., Shinoda, P.M., "Investigation of Rotor Loads and Vibration at Transition Speed," Presented at the American Helicopter Society 58th Annual Forum, Montreal, Canada, June 11-13, 2002

[76] Liou, M.-S. and Steffan, C., "A New Flux Splitting Scheme," NASA TM-104404, 1991.

[77] Godunov, S. K., "A Finite-Difference Method for the Numerical Computation and Discontinuous Solutions of the Equations of Fluid Dynamics," *Matematicheskii Sbornik,* Vol. 47, 1959, pp.271-306.

[78] Roe, P. L., "The Use of the Riemann Problem in Finite-Difference Schemes," *Lecture Notes in Physics*, Vol. 141, Springer-Verlag, New York, 1980, pp. 354-359.

[79] Roe, P. L., "Approximate Riemann Solvers, Parameter Vectors, and Difference Schemes," *Journal of Computational Physics*, Vol. 43, 1981, pp. 357-372.

[80] Osher, S., "Riemann Solvers, Entropy Conditions and Difference Approximations," *SIAM Journal on Numerical Analysis*, Vol. 21, 1984, pp. 217-235.

[81] Roe, P. L. and Pike, J., "Efficient Construction and Utilization of Approximate Riemann Solutions," *Computing Methods in Applied Sciences and Engineering*, R. Glowinski and J. L. Lions, eds., North Holland, Amsterdam, 1985.

[82] Vinokur, M. and Liu, Y., "Equilibrium Gas Flow Computations II: An Analysis of Numerical Formulations of Conservation Laws," AIAA Paper 88-0127, 1988.

[83] Roe, P. L. and Pike, J., "Efficient Construction and Utilization of Approximate Riemann Solutions," *Computing Methods in Applied Sciences and Engineering*, R. Glowinski and J. L. Lions, eds., North Holland, Amsterdam, 1985.

[84] Van Leer, B., "Upwind Difference Methods for Aerodynamic Problems Governed by the Euler Equations," *Lectures in Applied Mathematics*, Vol. 22, 1985.

[85] Van Albada, G. D., Van Leer, B., and Roberts, W.Jr., "Comparative Study of Computational Methods in Cosmic Gas Dynamics," *Astronomy and Astrophysics*, Vol. 108, 1982, pp. 76-84.

[86] Pulliam, T. H. and Steger, J. L., "Implicit Finite Difference Simulations of Three Dimensional Compressible Flow," *AIAA Journal*, Vol. 18, No. 2, 1980, pp. 159-167.

[87] Yoon, S. and Jameson, A., “Lower-Upper Symmetric-Gauss-Seidel Method for the Euler and Navier-Stokes Equations,” *AIAA Journal*, Vol. 26, No. 9, Sep. 1988, pp. 1025-1026.

[88] Spalart, P. R. and Allmaras, S. R., "A One-Equation Turbulence Model for Aerodynamic Flows," *La Recherche Aerospatiale*, 1994.

[89] Spalart, P. R., Jou, W-H., Strelets, M., and Allmaras, S. “Comments on the Feasibility of LES for Wings and on a Hybrid RAN/LES Approach,” Proceeding 1st AFOSR Int. Conf. on DNS/LES, Ruston, LA. 1997.

[90] Fang, Y., and Menon, S., "A Two-Equation Subgrid Model for Large-Eddy Simulation of High Reynolds Number Flows," AIAA paper 2006-116, 44th AIAA Aerospace Sciences Meeting and Exhibit, Reno, Nevada, 9-12 January, 2006.

[91] Mello, O. A. F., Prasad, J. V. R., Sankar, L. N., and Tseng, W., "Analysis of Helicopter/Ship Aerodynamic Interactions", American Helicopter Society Aerodynamics Specialists Conference, San Francisco, California, Jan. 19-21, 1994.

[92] Hoffmann, K. A. and Chang, S. T., *Computational Fluid dynamics Volume II, Fourth Edition*, Engineering Education System, Wichita, Kansas, 2000.

[93] Bauchau, O., DYMORE: A Finite Element Based Tool for the Analysis of Nonlinear Flexible Multibody Systems. Georgia Institute of Technology.

[94] Bauchau, O., “Computational schemes for flexible, nonlinear multi-body systems,” Multibody System Dynamics, vol. 2, pp. 169–225, 1998. 186

[95] Bauchau, O. and Bottasso, C., “On the design of energy preserving and decaying schemes for flexible, nonlinear multi-body systems,” *Computer Methods in Applied Mechanics and Engineering*, vol. 169, pp. 61–79, 1999.

[96] Rankine, W. J. M., Manual of Applied Mechanics, C. Griffen Co., London, 1858.

[97] Scully, M. P., “Computation of Helicopter Rotor Wake Geometry and Its Influence on Rotor Harmonic Airloads,” Massachusetts Institute of Technology Report No. ASRL TR 178-1, March 1975.

[98] Oseen, C. W., “Uber Wirbelbewegung in Einer Reibenden Flussigkeit,” Ark. J. Mat. Astrom. Fys., Vol. 7, 1912, pp. 14–21.

[99] Vatistas, G. H., Kozel, V., and Mih, W. C., “A Simpler Model for Concentrated Vortices,” *Experiments in Fluids*, Vol. 11, 1991, pp. 73–76.

[100] Vatistas, G. H., “New Model for Intense Self-Similar Vortices,” *Journal of Propulsion and Power*, Vol. 14, No. 4, April 1998, pp. 462–469.

[101] Bhagwat, M. J., Leishman, G., “Generalized viscous vortex model for application to free-vortex wake and aeroacoustic calculations”, American Helicopter Society 58th Annual Forum, Montreal, Canada, June 2002.

[102] Kuethe, A.M., Chow, C., and Fung, Y. C., Foundations of Aerodynamics, Bases of Aerodynamics Design, Fourth edition, *Journal of Biomech. Eng.* 109, 178 (1987)

[103] Message Passing Interface Forum, “MPI: A message-passing interface standard,” International Journal of Supercomputer Applications, 8(3/4), 1994.

[104] Thomas, P.D., Lombard, C.K., “Geometric Conservation Law and its Application to Flow Computations on Moving Grids”, AIAA Journal, Vo. 7, No.10, 1979, pp.1030-1037

[105] Harten, A., "High Resolution Schemes for Hyperbolic Conservation Laws."Journal of Computational Phvsics. Vol.49, 1983, pp. 357-393.

[106] Harten, A., Engquist, B., Osher, S., Chakravarthy, C. R., "Uniformly High Order Accurate Essentially Non-oscillatory Schemes, III."Journal of Computational Physics. Vol.71, 1987,pp. 231-303

[107] Harten, A., Chakravarthy, C. R., "Multi-Dimensional ENO Schemes for General Geometries", NASA CR-187637, Sep. 1991.

[108] Hariharan, N., “High Order Simulation of Unsteady Compressible Flows Over Interacting Bodies with Overset Grids”, Ph. D. Dissertation, School of Aerospace Engineering, Georgia Institute of Technology, Atlanta, GA, 1995.

[109] Cook, P. H., McDonald, M. A., and Firmin, M. C. P., "Aerofoil RAE 2822 - Pressure Distributions, and Boundary Layer and Wake Measurements," *Experimental Data Base for Computer Program Assessment*, AGARD Report AR 138, 1979.

[110] McAlister, K. W., Pucci, S. L., McCroskey, W. J., and Carr, L. W., “An Experimental Study of Dynamic Stall on Advanced Airfoil Sections, Volume2. Pressure and Force Data,” NASA TM 84245, Sep. 1982.

[111] Lorber, P.F., “Aerodynamic Results of Pressure Instrumented Model Rotor Test at the DNW,” *Journal of the American Helicopter Society*, Vol. 36, No. 4, 1991, pp. 66-76.

[112] McHugh, F. J., “What Are the Lift and Propulsive Force Limits at High Speed for the Conventional Rotor?” American Helicopter Society 34th Annual National Forum, Washington, D.C., May 15-17, 1978.

[113] Liu, H., “Interfacing Comprehensive Rotorcraft Analysis with Advanced Aeromechanics and Vortex Wake Models,” Phd Dissertation, Georgia Institute of Technology, 2008

[114] Bauchau, O. A. and Liu, H., "On the Modeling of Hydraulic Components in Rotorcraft Systems," *Journal of the American Helicopter Society*, vol. 51, no. 2, pp. 175–184, 2006.

[115] Abras, J., "Enhancement of Aeroelastic Rotor Airload Prediction Methods," Ph.D Dissertation, Georgia Institute of Technology, 2009

[116] Nygaard, T. A., Saberi, H., Ormiston, R. A., Strawn, Roger C., Potsdam, M., and Johnson, W., "Fluid Structure Interface for Rotorcraft Aeromechanic Computations," Unpublished Report, ELORET Corp., Advanced Rotorcraft Technology, AMRDEC, NASA-Ames Research Center, May 3, 2005

[117] Bousman, W. G., "A Qualitative Examination of Dynamic Stall from Flight Test Data," *Journal of the American Helicopter Society*, Vol. 43, (4), October 1998, pp. 279–295.

[118] Kufeld, R. M., "High Load Conditions Measured on a UH-60A in Maneuvering Flight," *Journal of the American Helicopter Society*, Vol. 43, (3), July 1998, pp.202–211.

[119] Abhishek, A., Datta, A., and Chopra, I., "Prediction of UH-60A Structural Loads Using Multibody Analysis and Swashplate Dynamics," *Journal of Aircraft*, Vol. 46, (2), March, 2009.

[120] Howlett, J. J., "UH-60A Black Hawk Engineering Simulation Program - Volume II - Mathematical Model," NASA CR-166309, December 1981.

[121] Abraham, M., Costello, M., "In-Flight Estimation of Helicopter Gross Weight and Mass Center Location," *Journal of Aircraft*, Vol. 46, No. 3, May–June 2009

[122] Ruffin, S. M., O'Brien, D. O., Smith, M. J., Hariharan, N., Lee, J. D., Sankar, L. N., "Comparison of Rotor-Airframe Interaction Predictions Utilizing Overset and Unstructured Grid Techniques," AIAA Paper 2004-0046, Jan., 2004.

VITA

NISCHINT RAJMOHAN

Nischint Rajmohan was born in Chennai, situated in the state of Tamil Nadu in India on January 13th, 1983. He did his schooling at Padma Seshadri Bala Bhavan Senior Secondary School, K.K.Nagar. He finished high school in 2000 and joined the Indian Institute of Technology, Madras to purse his bachelor degree in Aerospace Engineering. He interned at National Aerospace Laboratories, Bangalore in the summer of 2003 where he worked on experimental aerodynamics. He graduated with a Bachelor of Technology in 2004 and came to Georgia Institute of Technology, Atlanta to purse his doctoral program. He obtained his Masters in Aerospace Engineering in Fall 2006. His research interests include rotary wing computational aeromechanics and software development. During his Ph.D. program, he collaborated with Bell, Boeing and Sikorsky to develop simulation tools to study rotorcraft aeromechanics in a computationally efficient manner. He is a student member of the American Institute of Aeronautics and Astronautics, and the American Helicopter Society. He is currently starting his career at Advanced Rotorcraft Technology, Inc. as an aerospace engineer.